

## METHOD FOR NITRATE DETERMINATION IN WATER IN THE PRESENCE OF NITRITE

Maria Sandu<sup>a\*</sup>, Tudor Lupascu<sup>b</sup>, Anatol Tarita<sup>a</sup>, Tatiana Goreacioc<sup>a</sup>,  
Sergiu Turcan<sup>a</sup>, Elena Mosanu<sup>a</sup>

<sup>a</sup>Institute of Ecology and Geography, A.S.M., 1, Academiei str., Chisinau MD-2028, Republic of Moldova

<sup>b</sup>Institute of Chemistry, A.S.M., 3, Academiei str., Chisinau MD-2028, Republic of Moldova

\*e-mail: sandu\_mr@yahoo.com; phone: (+373 22) 73 15 50; 72 17 74

**Abstract.** The study relates to determination of nitrate in presence of nitrite in water and can be used in the quality monitoring of natural water (surface and groundwater), drinking water, water from fish farms and public aquaria where autonomous filters is used. The nature and quantity of reagents used have insignificant impact on natural waters and sewages. According to the investigation, the method includes the removal of nitrite from the solution/water with sulfaminic acid, the nitrate ion reduction to nitrite using a reducing mixture that contains Na<sub>2</sub>SO<sub>4</sub> and zinc dust in ratio of 100:5 and determining the nitrite with the Griess reagent.

**Keywords:** water, nitrate determination, nitrites, sulfaminic acid, Griess reagent, reducing mixture.

### Introduction

Water quality in wells and often in centralized distribution systems, almost on all over the country territory don't correspond to the standard for drinking water even after nitrate content. Analysis of groundwater quality monitoring results conducted by the Agency for Geology and Mineral Resources of the Republic of Moldova (AGRM) shows that the most artesian water contains ammonium ions, nitrate and nitrite in considerable amounts, sometimes exceeding the maximum allowable concentration (MAC) for drinking purposes. In Ialoveni district, for example, about 32% of the wells contain 69-280 mg/dm<sup>3</sup> NO<sub>3</sub><sup>-</sup> [1].

The process of nitrification in natural waters has mandatory stage the appearance of nitrite content of which in surface waters in Moldova ranges from 0-0.4 mg/dm<sup>3</sup> to tens of mg/dm<sup>3</sup> in small rivers water downstream of sewage discharges, insufficiently treated in biological purification plants type. During of 2002-2004 years, in the river Bac downstream of Chisinau city it was registered 1.2 -16.8 mg/dm<sup>3</sup> NO<sub>2</sub><sup>-</sup>; in river Lunga (village Lunga) - of 3.6 till 12.6 mg/dm<sup>3</sup> NO<sub>2</sub><sup>-</sup> and nitrates content ranged from 0.8 to 18.7 mg/dm<sup>3</sup> [2].

Thus the assessment of nitrate and nitrite content (NO<sub>3</sub><sup>-</sup> in the presence of NO<sub>2</sub><sup>-</sup>) in the aquatic medium, performed by analytical services for monitoring of natural, drinking, waste waters, food and soil is of real importance.

This highlights the necessity to develop the simple methods for determining nitrate in presence of nitrite in water and to identify those which are not presented in the normatives for drinking water.

### Experimental

#### Apparatus

Visible spectrophotometer (Model HACH) with 2 cm matching cells was used for the absorbance measurements. A pH-ionometer I-120.1 was used for pH measure.

#### Reagents and Solutions

All chemicals used were of analytical reagent grade, and double distilled water was used in the preparation of all solutions for the experiments.

Nitrite solution (20 mg/cm<sup>3</sup>) was prepared by dissolving 3.0 g sodium nitrite in water and diluting to 100 cm<sup>3</sup>. Nitrate solution (1000 mg/dm<sup>3</sup>) was prepared by dissolving 1.371 g sodium nitrate in water and diluting to 1000 cm<sup>3</sup>. Working standard nitrate solutions were prepared by appropriate dilution. Sulfaminic acid solution was used of 3 mg/cm<sup>3</sup> (0.3 g in 100 cm<sup>3</sup>) and Griess reactive – of 3% (3g in 100 cm<sup>3</sup>). To adjust the value of pH the solutions of HCl and NaOH (0.1 mol/dm<sup>3</sup>) were used.

### Results and discussion

Allowable levels for drinking water, which are binding in the Republic of Moldova by Government Decision no. 934 of 15.08.2007 is of 50 mg/dm<sup>3</sup> for nitrate and 0.5 mg/dm<sup>3</sup> for nitrite. Thus the problem of nitrate and nitrite monitoring in waters intended for human consumption (drinking water, water for foods preparation etc.) is in attention of specialized institutions [3].

There are various methods for nitrate and nitrite determining, including spectrometric, fluorometric, luminescent, electrophoretic, electrochemical and chromatographic.

To determine nitrites it is widely used the photometric method with Griess reagent proposed in 1879 year [4] with sensitivity of 0.001 mmol/dm<sup>3</sup>. The sensitivity, simplicity of the method, the accessibility of Griess reagent permits to use them for nitrate determination after its reduction to nitrite, but it is necessary to remove nitrites present in the water/solution.

There is also the method for the determination of NO<sub>3</sub><sup>-</sup> ions with sulfosalicylic acid, but the process is influenced by the presence of more than 2 mg/dm<sup>3</sup> of nitrites and consists of several steps which hinder the analytical work (boiling, evaporation, dissolving the shift quantity of the solution in the other vessel, etc.) [5].

Determination of nitrates may be carried out also by reaction with diphenylamine, but in the presence of nitrite method can not be applied, since they formed with diphenylamine colour compound [6].

Widely for nitrate determination there are used methods based on the principle of nitrate to nitrite preventive reduction, those latter being determined by Griess reaction. The reduction NO<sub>3</sub><sup>-</sup> → NO<sub>2</sub><sup>-</sup> is carried out by cadmium column [7-9], vanadium compounds (+3 and +4) [10], zinc and manganese sulphate [11, 12]. In all cases nitrites influence the process. Since the determination of nitrate in the presence of nitrites has limitations [13], it has been proposed solution to remove preventative nitrite with sodium azide in the reduction system Zn-Fe (III)-Ferozin (sodium salt of p, p'-disulphonic hydrate, 3 - (2-pyridyl) -5,6-diphenyl-1,2,4-triazine acid) [14].

***Determination of nitrate in presence of nitrite using the existing methods has the following disadvantages:***

- For analysis of several samples of water, there are required simultaneously multiple columns with cadmium. A large amount of metallic Cd and cadmium column passes through several stages of preparation (Cd metal preparation, washing the column before and after the reduction of NO<sub>3</sub><sup>-</sup> ions), that takes time. Cadmium is a relatively non-specific reductant and methods of its utilization are inefficient at lower concentrations of nitrate [15].

- Cadmium is a toxic element with a low limit of exhaust in wastewater treatment system and the environment (0.1 mg/dm<sup>3</sup>). In some countries, the production and cross-border movement of cadmium and its compounds are prohibited by law.

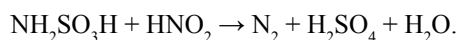
- In the case of vanadium, its compounds (+3 and +4 forms) are reduced by magnesium metal in an acid medium, and the solution is kept under argon, into the same flask.

- Vanadium is included in the families and groups of substances which have a deleterious effect on the aquatic medium [16].

- The disadvantage of the process of nitrite removal with sodium azide is that the reagent is toxic, including discharge into the natural water and sodium salt of p, p' - disulphonic acid hydrate 3 - (2- pyridyl) -5.6 – diphenyl - 1,2,4 - triazine acid is a shortage reagent and it is not known impact on the environment.

Pre-treatment of water with sulfaminic acid (ASA) allows the removal of the nitrite and nitrosating agents before nitrates determination after their reduction to nitrite [5, 17].

Sulfaminic acid reacts with nitrite and forms free nitrogen, water and sulphuric acid:



The advantage of sulfaminic acid using consists in economy, efficiency and ease of use.

In the passport of Security according Document 1907/2006/EC, art. 31(24/09/2013, version 3) it is mentioned that sulfaminic acid has insignificant effect in waste water canalization.

There are international standard methods taken by the Republic of Moldova for separate nitrates and nitrites determination in the water [18, 19]. But it is missing the standard for determining of nitrate in presence of nitrite.

The purpose of the present study is to develop a simple method for determination of nitrate in the presence of nitrite in aqueous solutions and natural waters using a reducing mixture Na<sub>2</sub>SO<sub>4</sub>:Zn, Griess reagent and sulfaminic acid.

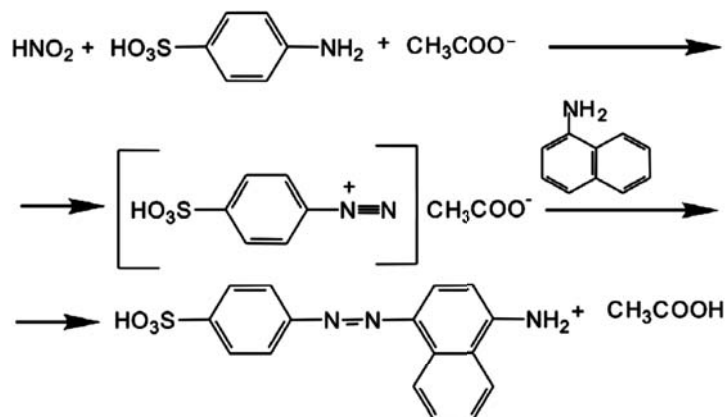
The most appropriate method to determine nitrates in the presence of nitrites is the process for removal of nitrite from the solution/water using sulfaminic acid [5] and the process of nitrate to nitrite reduction with a reducing mixture MnSO<sub>4</sub>:Zn = 100:2 and determination of formed NO<sub>2</sub><sup>-</sup> ions with Griess reagent [12]. The disadvantage of the method is the use of MnSO<sub>4</sub> (300 mg for a sample), which is more expensive, and Mn<sup>2+</sup> has a low permissible content to discharge into canalization system (1 mg/dm<sup>3</sup>) and the environment.

Sodium sulphate, proposed as reducing mixture component Na<sub>2</sub>SO<sub>4</sub>:Zn = 100:5, is used in amounts of 2.5 times lower (120 mg for a sample) as MnSO<sub>4</sub>, which is about two times cheaper and has a much higher discharge into waste water system or the environment (200 mg/dm<sup>3</sup>).

The process is characterised by simplicity, given the opportunity to perform simultaneous analysis of large numbers of samples, using efficient and accessible reagents that have a minimal negative effect on wastewater treatment technology and the environment to their discharge into drains and the environment. Zinc dust, which is not consumed in the reaction, is collected, washed with distilled water, dried and subsequently used for obtaining the reducing mixture Na<sub>2</sub>SO<sub>4</sub>: Zn.

The process consists in nitrite removal from natural waters and aqueous solutions to free nitrogen (N<sub>2</sub>) by ASA (NH<sub>2</sub>SO<sub>3</sub>H + HNO<sub>2</sub> → H<sub>2</sub>O + N<sub>2</sub> + H<sub>2</sub>SO<sub>4</sub>), reduction of nitrate to nitrite with a mixture consisting of sodium sulphate and zinc powder in ratio of components Na<sub>2</sub>SO<sub>4</sub>:Zn = 100:5. The chemistry of the reaction is in the process of reducing

of nitrates  $Zn + NO_3^- = NO_2^- + Zn^{2+}$  (1 mg  $NO_3^-$  is reduced by 1.08 mg of metallic Zn). The reduction of nitrates from 10 cm<sup>3</sup> water/solution with concentration of 0.2-10 mg/dm<sup>3</sup> consumed about 0.005-0.1 mg of zinc. Nitrite formed in the reaction is determined by Griess reagent widely used in the present and enough sensitive for routine use:



To establish the conditions for removal of nitrite it was estimated the quantity of sulfaminic acid, the time and the value of pH necessary for nitrite transformation to free nitrogen. In order to elucidate the conditions for reduction of nitrates in water it was evaluated the quantity of reducing mixture, the time of there contact with nitrate ions and those for formed nitrite with Griess reagent.

The results indicate that the removal of nitrite from sulfaminic acid solution takes place during of 25-30 minutes (Figure 1).

Obtained data reveal that 3 mg of sulfaminic acid remove nitrite in solution containing of 20 mg/dm<sup>3</sup>  $NO_2^-$  (Figure 2).

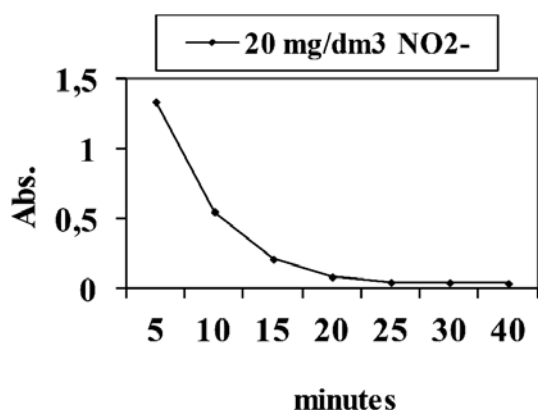


Figure 1. The amount of  $NO_2^-$  ion oxidation with sulfaminic acid by adding reduction mixture  $Na_2SO_4$ ; Zn = 100:5.

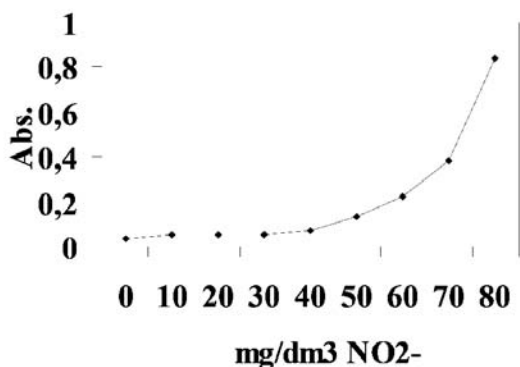
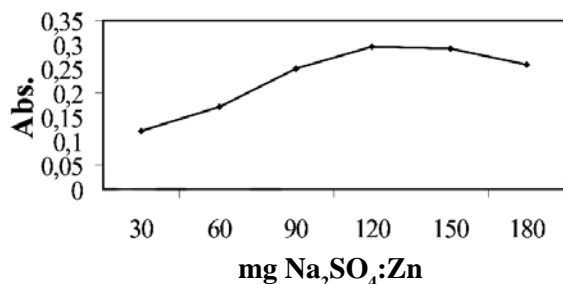


Figure 2. The absorbance of the solution containing 20 mg/dm<sup>3</sup> of  $NO_2^-$  contacted with 3 mg of ASA in the conditions of  $NO_3^-$  ions determination.

Thus, by adding 3 mg of sulfaminic acid, to 10 cm<sup>3</sup> of solution, it can be determined nitrate (less 10 mg/dm<sup>3</sup>) in the presence of nitrites (less 20 mg/dm<sup>3</sup>).

The effect of nitrate to nitrite reduction is optimal by using 120 mg of reduction mixture for one sample (Figure 3). The effect of nitrite removal from solution before nitrates determination is optimal at pH 1-2.5 (Figure 4). The results show that reduction mixture (120 mg) convert nitrate to nitrite in the solution during of 10 minutes (Figure 5).



**Figure 3.** The absorbance of solutions containing 20 mg/dm<sup>3</sup> of NO<sub>2</sub><sup>-</sup> and 2 mg/dm<sup>3</sup> of NO<sub>3</sub><sup>-</sup> ions contacted with 3 mg of sulfaminic acid in function on the amount of reduction mixture.

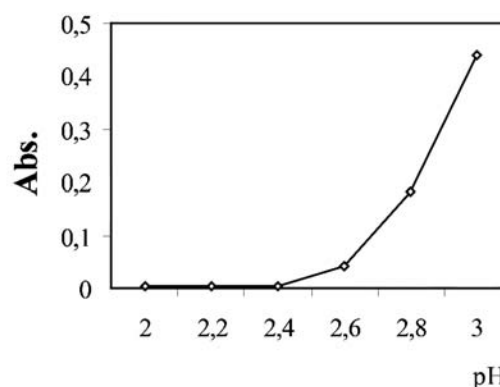


**Figure 4.** Solutions absorbance with contain nitrites (20 mg/dm<sup>3</sup>) and sulfaminic acid (3 mg) in dependence on the pH.

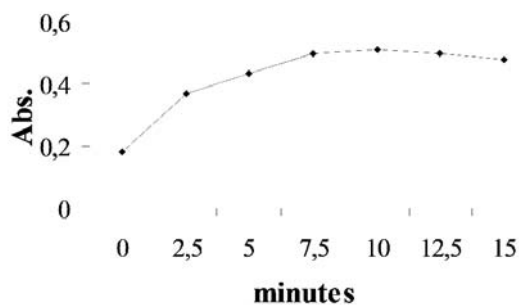


**Figure 5.** Time dependence of absorbance for NO<sub>3</sub><sup>-</sup> ions reduction with mixture Na<sub>2</sub>SO<sub>4</sub> Zn = 100:5 in the presence of nitrite and ASA.

So, it was obtained the following method for nitrate determination in presence of nitrite.

**The method for nitrate determination in presence of nitrite**

In the calibrated flask of 10 cm<sup>3</sup>, an aliquot of solution for analysis is used (0.1-10 mg/dm<sup>3</sup> of NO<sub>3</sub><sup>-</sup> and not more than 20 mg/dm<sup>3</sup> of NO<sub>2</sub><sup>-</sup>), then 0.3 cm<sup>3</sup> of sulfaminic acid solution with a concentration of 10000 mg/dm<sup>3</sup> (3 mg/sample) is added. The volume is bringing up to 10 cm<sup>3</sup> with distilled water, stirred after each 5 minutes during of 30 minutes (6 times). Then (after 30 minutes) 120 mg of reduction mixture Na<sub>2</sub>SO<sub>4</sub>:Zn = 100:5 is added and is stirred for 3 times during of 10 min. After the nitrate reduction period (10 min) in the solution is poured 1 cm<sup>3</sup> of 3% solution of Griess reagent, 30 minutes later the absorbance of the red solutions is measured at the wavelength of 520 nm. As a comparison it is use a solution containing reagents used properly: to 9.7 cm<sup>3</sup> of distilled water, 0.3 cm<sup>3</sup> sulfaminic acid and 1 cm<sup>3</sup> of 3% Griess reagent to meet stages and time mentioned.

The calibration curve is obtained using a standard solution of NaNO<sub>3</sub> with concentration of NO<sub>3</sub><sup>-</sup> ions from 0.5 to 10 mg/dm<sup>3</sup>, adding reagents, and required time following the steps described in the method (Figure 6).

Nitrate and nitrite standard solutions are stored in a refrigerator at 4°C.

**Result of the study and novelty criterion consists of the following:**

1. In the process of nitrates determination in the presence of nitrites into aqueous solutions and natural waters the sulfaminic acid is used for removal of the nitrites and creation of appropriate pH of the reaction, reduction mixture consisting in chemical available substances (Na<sub>2</sub>SO<sub>4</sub> and Zn powder in the ratio of 100:5) for the reduction of nitrates to nitrites and Griess reagents for the determination of formed nitrites.

2. The result of proposed method consists in minimizing of analysis cost and use of efficient reagents which have a minimal negative effect on wastewater treatment technology and the environment as a result of discharge into drains or the environment.

3. The procedure has a sensitivity of  $0.1 \text{ mg/dm}^3 \text{ NO}_3^-$  in the presence of  $20 \text{ mg/dm}^3$  of  $\text{NO}_2^-$  ions. Relative error of the method is from 0.21 to 1.5% and relative standard deviation - within the limits of 0.2 - 3.0%.

4. The removal of nitrite with ASA ensures the value of pH essential for process, the  $\text{Na}_2\text{SO}_4$  - stable ionic strength in solutions with the effectiveness determination of nitrate in the presence of nitrite in ratio  $\text{NO}_2^- : \text{NO}_3^- = 20:(0.1-10)$ , by using a reducing mixture  $\text{Na}_2\text{SO}_4 : \text{Zn} = 100:5$  and Griess reagent, reagents having a little impact on waste water sewage and the environment.

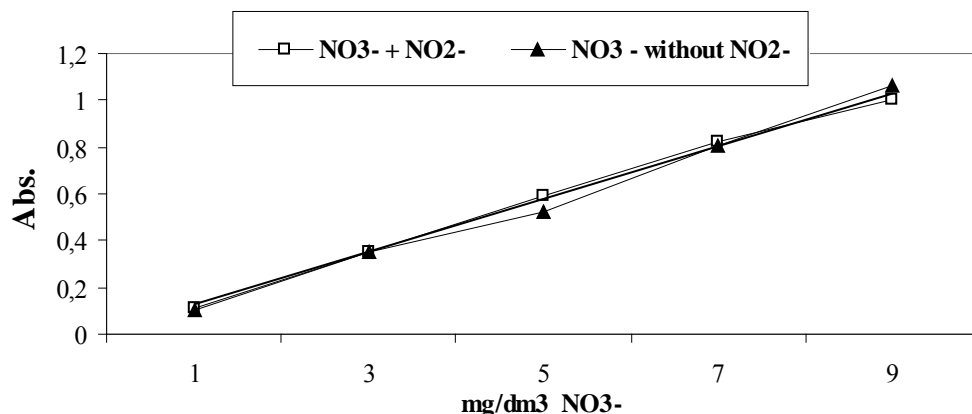


**Figure 6. The calibration curve for nitrates determination in the absence ( $y = 0.2362x - 0.3748$ ,  $R^2 = 0.9955$ ) and presence ( $y = 0.2249x - 0.3216$ ,  $R^2 = 0.9975$ ) of nitrites.**

The solution which contains  $1 \text{ mg/dm}^3$  ( $0.016 \text{ mol/dm}^3$ ) in 2 cm cuvette has a media absorbance of  $0.114 \pm 0.010$  at 520 nm. So the molar extinction coefficient is of  $3.56 \pm 0.09 \cdot 10^3 \text{ (cm}^{-1}\text{M}^{-1})$  and the sensibility of  $\text{NO}_3^-$  determination reaction - of  $0.1 \text{ mg/dm}^3$ , relative standard deviation - within the limits of 0.2 - 3.0%.

A number of ions potentially present in natural, drinking waters, in public aquariums and fish farms do not affect the determination of nitrate in presence of nitrite under the conditions of the present method (Table 1).

Table 1

**Ions that not affect nitrate determination in the presence of nitrite.**

Ions	The tolerance ( $\text{mg/dm}^3$ )
$\text{Al}^{3+}$	150
$\text{Ba}^{2+}$	100
$\text{Ca}^{2+}$	300
$\text{Cd}^{2+}$	1000
$\text{Cu}^{2+}$	15
$\text{Fe}^{3+}$	15
$\text{K}^+$	2000
$\text{Mg}^{2+}$	350
$\text{Mn}^{2+}$	1000
$\text{Na}^+$	2000
$\text{Pb}^{2+}$	20
$\text{C}_2\text{O}_4^{2-}$ (oxalate)	300
$\text{CH}_3\text{COO}^-$ (acetate)	2000
$\text{C}_6\text{H}_5\text{O}_7^{3-}$ (citrate)	100
$\text{C}_4\text{H}_4\text{O}_6^{2-}$ (tartrate)	500

## Conclusions

The procedure has a sensitivity of  $0.1 \text{ mg/dm}^3 \text{ NO}_3^-$  in the presence of  $20 \text{ mg/dm}^3$  of  $\text{NO}_2^-$  ions, and allows a large number of analyses simultaneously.

The removal of nitrite with sulfaminic acid is ensured of the value of pH essential for process, the  $\text{Na}_2\text{SO}_4$  - stable ionic strength in solutions, all reagents having a little impact on waste water sewage and the environment.

Due to the use of zinc dust and  $\text{Na}_2\text{SO}_4$  it is minimized the cost of the analysis, the level of water pollution from sewage system and the environment, compared to the use of cadmium metal, vanadium and manganese compounds, etc. for nitrates reduction.

The simplicity of the process steps allows of carrying out the analysis of a large number of samples simultaneously, including for evaluation of the error and the standard deviation of nitrate content in the presence of nitrite.

## References

1. Mustea, M.; Boian, I.; Galca, G.; Sandu, M.; Tarita, A.; Zubcov, E.; Sireteanu, D.; Gladchi, V.; Prepelita, A.; Jeleapov, V.; Serenco, L. State of water resources. In: National Report on the Environment State in the Republic of Moldova, 2007–2010. Nova-Imprimi: Chisinau, 2011, pp. 75-80 (in Romanian).
2. Galca, G.; Cunician, L.; Sandu, M. et al. State of water resources. In: National Report on the Environment State in the Republic of Moldova, 2004. Nova-Imprimi: Chisinau, 2005, pp. 48-53 (in Romanian).
3. Government Decision of Republic of Moldova, 15.08.2007/934, on automated information system establishment, State Register of natural mineral waters, drinking water and bottled soft drinks. Official Monitor no. 131-135, Art. No. 970 (Published: 24.08.2007) (in Romanian).
4. Bol'shova, T.A.; Brykina, G.D.; Garmash, A.V. et al. Fundamentals of analytical chemistry. Akademija: Moscow, 2012; 384 p. (in Russian).
5. Novikov, Iu.V.; Lastocichina, K.O.; Boldina, Z.N. The methods for investigation of reservoirs water quality. Medicina: Moscow, 1990, 321 p. (in Russian).
6. Basarghin, N.N.; Oscotscaia, E.R.; Iuscova, E.Iu.; Rozovschii, Iu.G. Individual concentration and spectrometric determination of nitrate ions in natural and waste waters. Factory laboratory. Diagnostics of Materials, 2006, 72(7), pp. 16-18 (in Russian).
7. Eaton, A.D.; Clesceri, L.S.; Greenberg, A.E.; Eds. Standard methods for the examination of water and wastewater; 20<sup>th</sup> Ed., American Public Health Association: Washington, 1995, 988 p.
8. Cortas, N.K.; Wakid, N.W. Determination of inorganic nitrate in serum and Urine by a kinetic cadmium-reduction method. Clinical Chemistry, 1990, 36(8), pp. 1440-1443.
9. Schneider, N.R.; Yeary, R.A. Measurement of nitrite and nitrate in blood. American Journal of Veterinary Research, 1973, 34, pp. 133-135.
10. Miranda, V.; Espey, M.G.; Wink, D.A. A rapid, simple spectrophotometer method for simultaneous detection of nitrate and nitrite. Nitric Oxide, 2001, 5(1), pp. 62-71.
11. Mir, S.A. Extraction of  $\text{NO}_x$  and Determination of Nitrate by Acid Reduction in Water, Soil, Excreta, Feed, Vegetables and Plant Materials. Journal of Applied Sciences & Environmental Management, 2009, 13(3), pp. 57-63.
12. Lozan, R.; Ropot, V.; Sandu, M. Determination of nitrate and nitrite in natural waters. Journal of Water Chemistry and Technology, 1989, 11(2), pp. 120-122 (in Russian).
13. Mir, S.A. An improved zinc reduction method for direct determination of nitrate in presence of nitrite, Asian Journal of Chemistry, 2007, 19(7), pp. 5703-5710.
14. Stanley, J.B.; Bruno, J. Spectrometric determination of nitrate and nitrite in natural water and sea-water. Talanta, 1985, 32(2), pp. 115-118.
15. Marzinzig, M.; Nussler, A.K.; Stadler, J.; Marzinzig, E. et al. Improved methods to measure end products of nitric oxide in biological fluids: Nitrite, nitrate, and S-nitrosothiols. Nitric oxide, 1997, 1(2), pp. 177-189.
16. Government Decision of Republic of Moldova, 2013/950, Regulation concerning the collection, treatment and discharge of wastewater into the sewer system and/or bodies of water for urban and rural areas. Official Monitor no. 284-289, Art. No. 1061 (Published: 06.12.2013) (in Romanian).
17. Mir, S.A. A rapid technique for determination of nitrate and nitric acid by acid reduction and diazotization at elevated temperature. Analytica Chimica Acta, 2008, 620(1-2), pp. 183-189.
18. SM SR EN 26777:2006. Water Quality. Determination of nitrite. - Molecular absorption spectrometric method (in Romanian).
19. SM SR ISO 7890-3:2006 Water Quality. Determination of nitrate. Part 3: Spectrometric method using sulfosalicylic acid (in Romanian).
20. Safety data sheet according to 1907/2006/EC, Article 31 (24/09/2013 version 3). [http://ec.europa.eu/enterprise/sectors/chemicals/documents/classification/archives/safety-data-sheet/index\\_en.htm](http://ec.europa.eu/enterprise/sectors/chemicals/documents/classification/archives/safety-data-sheet/index_en.htm).

## STUDY OF SOME ARCHAEOMETRIC CHARACTERISTICS USED IN PANEL PAINTING ICONS AUTHENTICATION

Raluca Anamaria Cristache\*, Ana Maria Budu, Petronela Spiridon,  
Viorica Vasilache, Ion Sandu

*Interdisciplinary Research and Education Platform ARHEOINVEST, Laboratory of Scientific Investigation and Conservation of Cultural Heritage, Alexandru Ioan Cuza University of Iasi, 11, Carol I blvd., Iasi 700506, Romania*  
\*e-mail: raluca\_cristache@yahoo.com; phone: +40 0766 407927

**Abstract.** The authentication of cultural heritage assets is a complex process of scientific investigation which regards obtaining information about: author (painter), the period when it was made, the owners and other data related to the main contexts of their evolution in time (routes travelled). In fact, the identification of specific archaeometric features is aimed, in determining the materials composition and the patina, then the study of artistic techniques and technology used in the making process of a work of art. Latest serves to define the patrimonial elements and the role of the artifact in time. The expertise of old panel painting icons requires an interdisciplinary approach, correlating the artistic style with technique and materials used. In this regard, the specific techniques of microscopy and spectroscopy are very useful tools for determining the composition of structural elements and their deterioration / degradation state. This work presents a comparative study of the paper used in the preparation layer of three icons painted in Russian style. As an analysis techniques were used the micro and macro photography assisted by Optical Microscopy (OM), SEM-EDX and micro-FTIR. Based on the experimental data obtained, it was found that the icons belong to the first half of the 19<sup>th</sup> century.

**Keywords:** icon, historic paper, SEM-EDX, micro-FTIR.

### Introduction

Icons are works of art painted, in general, on wood (lime wood, fir, oak). In their creation process painters used different materials, organic and inorganic. Usually, canvas was glued on the panel made of one or more planks. After that, a ground layer, obtained from animal glue and calcium sulfate or calcium carbonate, was applied. Sometimes, instead of canvas, paper was used, glued on the entire surface or only on certain area of planks joint or on the margins. After finishing the ground, the drawing was made and painting was made with tempera or oil. Many times the background of the icon was made with golden or silver leaf which was covered with a colored varnish (shellac), to give the impression of gold [1].

The characteristics of the materials used in creating these icons may help in their dating and authentication. For example, the structure of the paper glued on the wooden support can offer information. The paper was created first by Chinese people in the 3<sup>rd</sup> century BC, from ground and macerated rags and reeds until they become a paste. Europeans began to make paper from 11<sup>th</sup> century (Spain and Italy) [2].

Until 1800 the paper continued to be made of hemp and flax rags, their selection depending on material texture. The paste obtained by mechanical processing was diluted with water and then left for drying on a wire net. Because water could contain iron oxides which gave paper a red shade, calcium carbonate was added in the paste. For a higher resistance of paper it was used gelatin and alum ( $KAl(SO_4)_2 \cdot 12H_2O$ ), that had a conservation role [3].

From the beginning of 19<sup>th</sup> century there are used colored rags which usually are bleached. The blue paper, made of rags from the navy uniforms, was the cheapest [4].

At the same time, the gelatin is replaced by rosin treated with soda or combined with paraffin. Aluminum sulfate was added in the mixture to increase adhesion. Since 1826 rosin is generally used. After 1840, mechanically or chemically processed wood is used in paper production.

Chemical processing of wood developed around 1850. This type of paper didn't contain lignin, which was dissolved by chemical substances. 50% of wood mass was lost this way. In 1874, and in 1878 chemical procedures that involved sulfites, respectively sulfates were introduced. In 1867 paper was made by mechanical processing. It contained the principal components of wood: lignin, cellulose and hemicelluloses but it was low quality, used mainly for newspapers [5]. The wood pulp paper also contains additives like coloring agents, coagulants and protective layers [6]. One of the differences between rags paper and wood pulp paper is that the rags fibers are made from linear long cellulose fibers [7].

The aim of this paper is the authentication and dating of three panel painting icons by analyzing the natural materials used in the making process: paper made from rags with cellulosic fibers and binding materials.

### Materials and techniques

For analysis we used three samples of paper taken from three orthodox icons painted in Russian style, tempera on wood: Saint Nicholas - SN (Figure 1), The Holy Virgin of Kazan, copy - HVK (Figure 2), and Saint Anastasia – SA

Presented at the International Conference dedicated to the 55<sup>th</sup> anniversary from the foundation of the Institute of Chemistry of the Academy of Sciences of Moldova

(Figure 3). The paper was glued by the original artist on the entire panel surface or on the margins, after that ground was applied over it. The samples were taken from the lacunae and analyzed by different techniques in order to obtain information regarding the methods and materials used.



**Figure 1. Icon of St. Nicholas:  
a- front view; b- lacunae detail.**

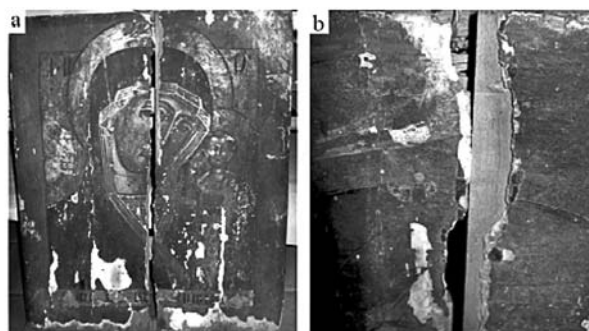


**Figure 2. Icon Holy Virgin of Kazan:  
a- front view; b- lacunae detail.**

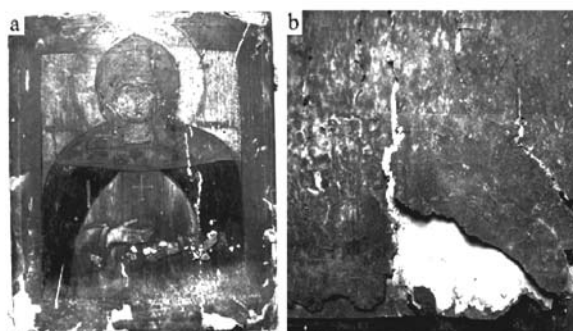


**Figure 3. Icon St. Anastasia:  
a- front view; b- lacunae detail.**

First all samples were analyzed by light microscopy by reflection CARL ZEISS AXIO IMAGER A1m, with attached camera AXIOCAM, images being increased between 50x and 500x. To identify the chemical elements, we have used an electron microscope (SEM-EDX), model VEGA II LSH, made by TESCAN Czech Republic, coupled with an X-ray spectrometer QUANTAX QX2, produced by BRULER/PROENTEC Germany. FT-IR spectra were recorded with a FT-IR spectrometer coupled with a microscope HYPERION 1000, both from Brüker Optic Equipment, Germany.

### Results and discussion

The samples were first analyzed with the help of optical microscopy (OM) by reflection, ranged between 50x and 500x, and photographed. The most edifying images (at magnifications of 50x and 200x) were chosen, so we could have a clear image of the papers structures.

The paper used for SN icon has a dark blue-grey color (Figure 4). As we can see in the images obtained by OM, the paper paste is a mixture of white and long, dark blue fibers. The paper sample from HVK is white-yellow, with a fine texture (Figure 5). The microscopic images show that the fiber net is much tighter, the paste being more processed.

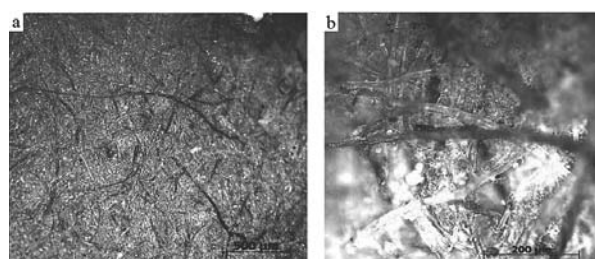


**Figure 4. Images of paper sample from SN icon,  
obtained by OM: a- 50x; b-200x.**

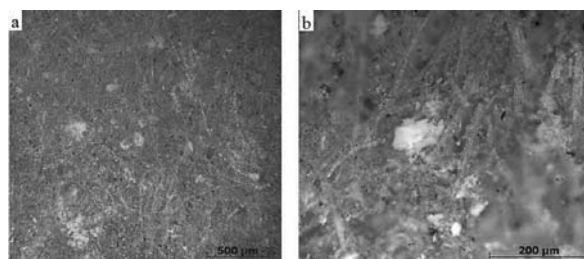


**Figure 5. Images of paper sample from HVK icon,  
obtained by OM: a- 50x; b-200x.**



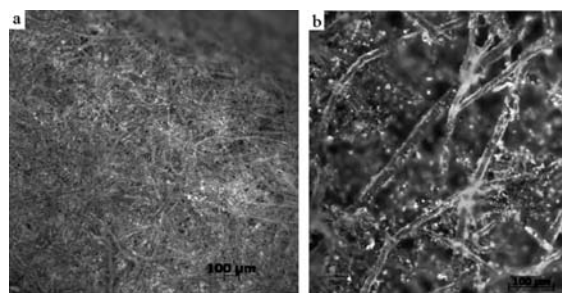


Figure 6. Photos of paper samples from SA icon, by OM: a-50x, b-200x.

For the identification of elemental composition of paper samples electronic microscopy was used (SEM-EDX) and also Micro-FTIR. Regarding the elemental composition of papers, SEM-EDX analysis identified a series of chemical elements which correspond to the substances mentioned in the manufacturing of historic paper.

Table 1

Elemental composition of the paper samples (wt.%).													
Sample	C	Ca	S	Si	Fe	K	Al	Mg	Na	P	Cl	Pb	O
SN	16.97	1.86	1.64	0.76	-	0.62	0.23	0.28	0.85	-	0.79	-	75.96
HVK	15.44	3.19	2.17	1.36	0.52	0.47	0.62	0.39	0.57	0.33	0.36	3.64	70.88
SA	13.12	3.47	0.49	1.83	0.86	0.75	0.84	0.32	0.71	0.14	0.44	-	76.98

SEM-EDX analysis of paper samples from SN, HVK and SA icons revealed that Ca, Na, Si, K, Al and Mg are in higher quantities and are representative for all the samples. Fe and P appear only in two samples (HVK and SA) (Figure 7). All samples contain Si, Cl, and S. The results are given as percents, but they are only relative percents which include the organic part (C, H, and O).

Calcium is present in paper composition. Calcium carbonate, which is a universal filler is present in all three samples analyzed and was used not only for the degree of white, but for the brightness that gives to the paper. Its major advantage is that it does not decrease the mechanical strength of the paper, as do other fillers [9]. The presence of K, Al, S in all the samples, in different quantities, suggests the use of alum in paper processing. It also shows the paper belongs to the 19<sup>th</sup> century. Fe, Ba, Mg, Na and K may appear in the samples as impurities from alum or water [10].

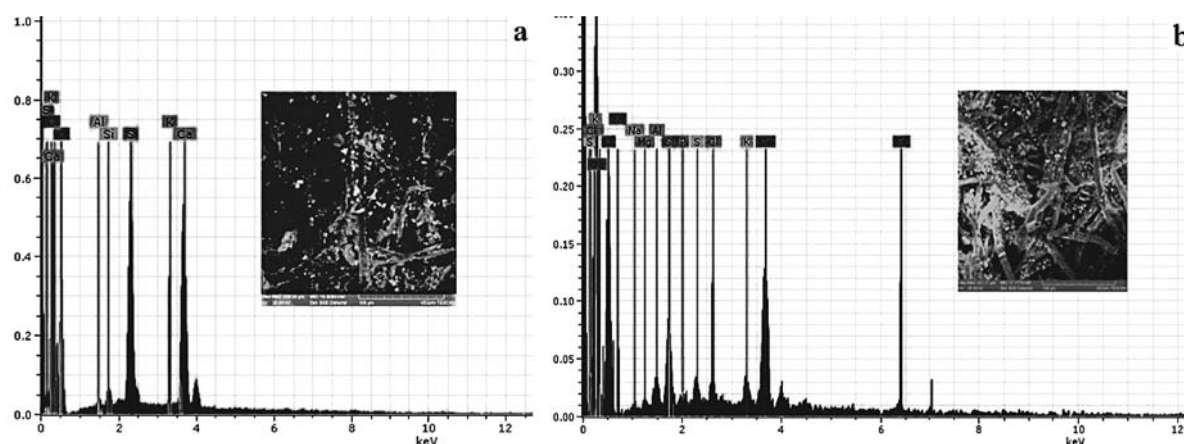


Figure 7. Microphotos and EDX spectra of samples: a- HVK, b- SA.

The presence of Mg in small quantities also may suggest that talcum ( $3\text{MgO}\cdot 4\text{SiO}_2\cdot \text{H}_2\text{O}$ ) was used as filler. Because talcum is soft and greasy it made the paper opaque and soft.

The sulfur is one of the chemical elements that appear in all samples, HVK paper having the biggest quantity (2.17%), while SA paper has the smallest sulfur percentage (0.49%). The high quantity of S from HVK and SN samples is given by the presence of ground, which contains  $\text{CaSO}_4$ . The smaller mass of S in the third sample might be explained by a smaller concentration of ground or alum.

Also, traces of Cl were found in the samples, due to the fact that sodium hypochlorite was used as a bleaching agent [10]. The percentage of Cl is higher in the SN sample (0.79%), where are more blue fibers.

The books which contain recipes for paper manufacturing indicate the use of phosphates as fillers (e.g. calcium phosphate), which explains the presence of P in the samples [11]. The phosphorus quantity in HVK sample is 0.33%, and only 0.14% in SA sample.

Pb is the only element which appears only in the HVK sample and in high concentration (3.64%). This fact helps us to date the paper sample from the first half of 19<sup>th</sup> century, because since 1827 the paper was covered with a few layers of lead white ( $2\text{PbCO}_3 \cdot \text{Pb(OH)}_2$ ), enamel paper was made with lead white, isinglass, gum, and animal size [12]. After that the paper sheets were burnished by plating or by rolling with a steel plate [12-14]. The lead white was forbidden since the beginning of 20<sup>th</sup> century, due to its toxicity.

The results obtained by SEM-EDX were compared with FTIR spectra of paper samples (Figure 8).

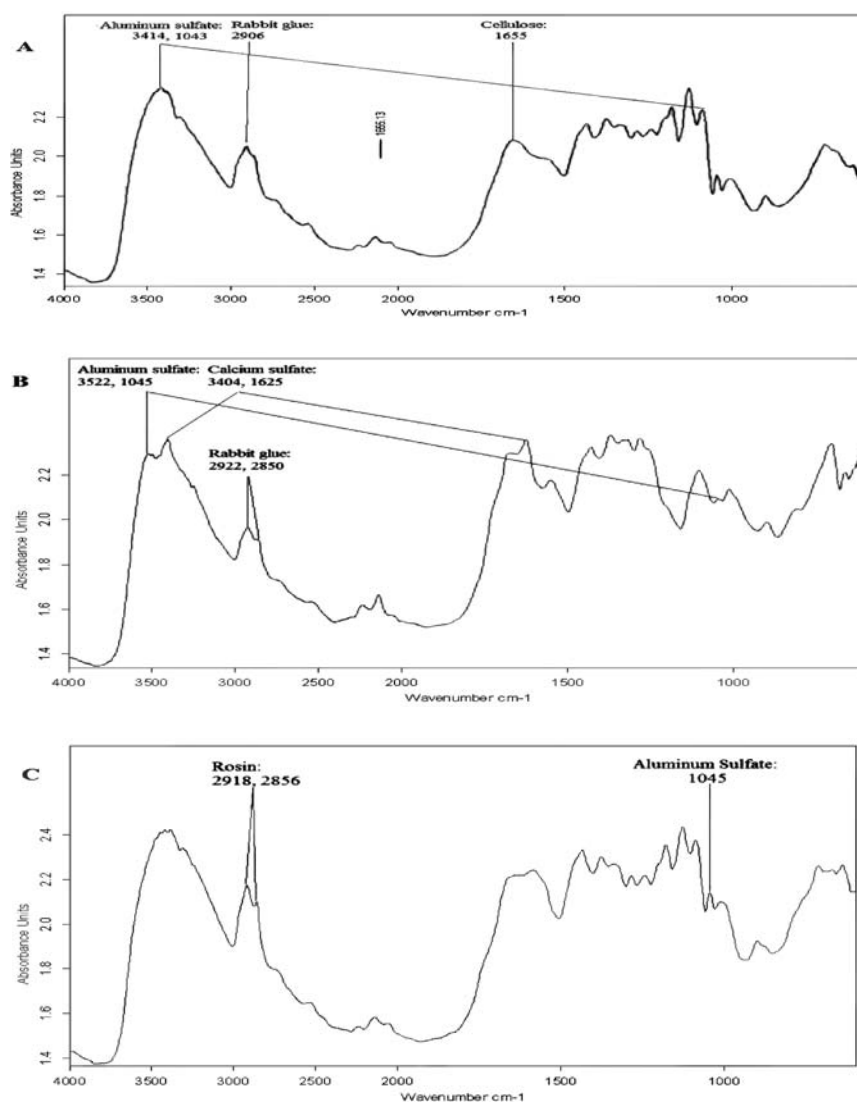


**Figure 8. FTIR spectra: A - SN, B - HVK, C – SA.**

The fillers were identified as calcium sulfate dihydrate ( $\text{CaSO}_4 \cdot 2\text{H}_2\text{O}$ ), aluminum sulfate ( $\text{Al}_2(\text{SO}_4)_3 \cdot 18\text{H}_2\text{O}$ ), talcum ( $3\text{MgO} \cdot 4\text{SiO}_2 \cdot \text{H}_2\text{O}$ ), rosin and rabbit glue. These substances present specific absorption bands:  $\text{CaSO}_4 \cdot 2\text{H}_2\text{O}$  -  $3404 \text{ cm}^{-1}$ ,  $1685 \text{ cm}^{-1}$ ,  $1625 \text{ cm}^{-1}$ , and  $666 \text{ cm}^{-1}$ , talcum-  $1045 \text{ cm}^{-1}$  and  $669 \text{ cm}^{-1}$ , and  $\text{Al}_2(\text{SO}_4)_3$ -  $3522 \text{ cm}^{-1}$  and  $1045 \text{ cm}^{-1}$  (Table 2) [15].

Rosin has absorption bands at  $2922 \text{ cm}^{-1}$ ,  $1697 \text{ cm}^{-1}$ ,  $1365 \text{ cm}^{-1}$ ,  $1275 \text{ cm}^{-1}$ ,  $1106 \text{ cm}^{-1}$ ,  $809 \text{ cm}^{-1}$ ,  $707 \text{ cm}^{-1}$  [16]. The peaks from  $1550 \text{ cm}^{-1}$  and  $1656 \text{ cm}^{-1}$  are representative for proteins, but they are superimposed on the representative band for cellulose ( $1635 \text{ cm}^{-1}$ ). Their presence might be observed at  $1625 \text{ cm}^{-1}$  and  $1551 \text{ cm}^{-1}$  [17].

The HVK paper sample, which has in composition white lead mixed with rabbit glue has representative peaks at  $2922 \text{ cm}^{-1}$ ,  $2850 \text{ cm}^{-1}$  and  $1739 \text{ cm}^{-1}$  (Figure 8, Table 2) [18].

Table 2

**Identified peaks by micro-FTIR for the three paper samples, between 4000 cm<sup>-1</sup> and 600 cm<sup>-1</sup>.**

Sample	Peaks, cm <sup>-1</sup>
SN	3414 3304 2906 2541 2124 1655 1434 1375 1283 1241 1179 1127 1088 1043 1005 898
HVK	3522 3404 2922 2234 2136 1625 1551 1429 1317 1320 1283 1106 1045 1012 899 707 666 619
SA	3387 3309 2918 2855 2541 2233 2135 2060 1582 1431 1374 1336 1282 1241 1177 1125 1086 1043 1009 898 712 671 638

**Conclusions**

The microscopic structure of paper (textile fibers) suggests that the icons belong to the first half of the 19<sup>th</sup> century. The presence of blue fibers in the SN paper sample shows us the icon belongs to the beginning of 19<sup>th</sup> century. Also the chemical composition allows us to approximate the period when the paintings were realized. For example, the lead content of HVK paper corroborated with the fibers aspect indicates us the icon was painted in the first half of the 19<sup>th</sup> century, when the paper was coated with lead. The fillers in all the icons were identified as calcium sulfate dihydrate, aluminum sulfate (alum), talcum, rosin and rabbit glue. These materials can help in the authentication and dating of art works, especially because they are an inner part of the icons, an intermediate layer between the support and the ground.

**References**

- Espinola, V.B.-B., Russian Icons: Spiritual and Material Aspects. *Journal of the American Institute for Conservation*, 1991-1992, 31 (1), pp. 17-22.
- Radu, M.; Repanovici A., A history of printing and prints. Transilvania: Brasov, 2004, (in Romanian) <http://www.unitbv.ro/faculties/biblio/istoria/my%20web/pdf/Cap%204.pdf>
- Barrett, T., European Papermaking Techniques 1300–1800. <http://paper.lib.uiowa.edu/european.php>
- Paper, <http://comminfo.rutgers.edu/~lesk/spring06/lis556/P-paper.pdf>
- Graphic Documents, [http://webworld.unesco.org/safeguarding/en/pdf/txt\\_grap.pdf](http://webworld.unesco.org/safeguarding/en/pdf/txt_grap.pdf)
- Laguardia, L.; Vassallo, E.; Cappitelli, F.; Mesto E.; Cremona, A.; Sorlini, C.; Bonizzoni, G. Elemental identification of document paper by X-ray fluorescence spectrometry. *Applied Surface Science*, 2005, 252, pp. 164-170.
- Manso, M.; Costa, M.; Carvalho, M.L. Comparison of elemental content on modern and ancient papers by EDXRF. *Applied Physics A*, 2008, 90, pp. 43–48.
- Brückle, I., The Role of Alum in Historical Papermaking. *Abbey Newsletter*, 1993, 17(4), pp. 53-57.
- Espadaler, I.; Sistach, M.C.; Cortina, M.; Eljarrat, E.; Alcaraz, R.; Cabañas, J.; Rivera, J.; Organic and inorganic components of manuscript inks. *Anales de Quimica*, 1995, 91, pp. 359-364.
- Roberts, J.C. *The Chemistry of paper*. RSC PAPERBACKS, Cambridge, 1996, 190 p.
- Wagner, B.; Bulska, E.; Hulanicki, A.; Heck, M.; Ortner, H. M. Topochemical investigation of ancient manuscripts. *Fresenius' Journal of Analytical Chemistry*, 2001, 369, pp. 674-679.
- van der Reyden, D.; Mosier, E.; Baker, M.; Pigment-coated papers I & II: history and technology, Triennial meeting (10th), Washington, DC, 1993, 498 p.
- Hunter, D. *Papermaking: The History and Technique of an Ancient Craft*, Dover Publications: New York, 1978, 611 p.
- Maclead, M., Early History of Coated Papers-How They Came of Age. *Paper Trade Journal*, 1972, pp. 170-175.
- Zhbankov, R.G.; Firsov, S.P.; Buslov, D.K.; Nikonenko, N.A.; Marchewka, M.K.; Ratajczak, H. Structural physico-chemistry of cellulose macromolecules. Vibrational spectrum and structure of cellulose. *Journal of Molecular Structure*, 2002, 614, pp. 117-125.
- Derrick, M.R.; Stulik, D.; Landry, J.M.; *Infrared Spectroscopy in Conservation Science*. The Getty Conservation Institute, Los Angeles, 1999, 251 p.
- Baker, M.; Van der Reyden, D.; Ravenel, N. FTIR Analysis of Coated Papers, *The Book and Paper Group*, 1989, Vol. 8, (<http://cool.conservation-us.org/coolaic/sg/bpg/annual/v08/bp08-01.html>)
- Vetter, W.; Schreiner, M.; Characterization of Pigment-Binding Media Systems - Comparison of Non-Invasive in-Situ Reflection FTIR with Transmission FTIR Microscopy. *e-PRESERVATION Science*, 2011, 8, pp. 10-22.

## DISTRIBUTION OF SOLUBLE AND INSOLUBLE CHEMICAL SPECIES OF CHROMIUM (III) AND (VI) IN AQUEOUS SOLUTIONS

Oxana Spinu

*Institute of Chemistry of Academy of Sciences of Moldova, 3, Academiei str., Chisinau, MD 2028, Republic of Moldova  
e-mail: oxana\_spinu@yahoo.com; phone (+373 22) 73 97 81*

**Abstract.** On the basis of currently revised thermodynamic data for Cr(III) and Cr(VI) hydrolysis and photolytic equilibria in addition to original thermodynamic and graphical approach, used in this paper, the repartition of their soluble and insoluble chemical species has been investigated. By means of the diagrams “ $\Delta G - pH$ ”, the areas of thermodynamic stability of chromium(III) hydroxide have been established for a number of the analytical concentration of Cr(III) in heterogeneous mixtures. The degree of polynuclearity for Cr (III) and Cr(VI) has been calculated for different initial composition of aqueous solutions. The diagrams of heterogeneous and homogeneous chemical equilibria have been used for graphical representation of complex equilibria in aqueous solutions containing Cr(III) and Cr(VI). The obtained calculated results correlate well with existing experimental data.

**Keywords:** chemical equilibrium, chromium complexes, distribution diagram, Gibbs energy.

### Introduction

The increased knowledge regarding the behavior of chromium in natural waters and soils is essential for the complete and accurate determination of its possible toxicity to the particular ecosystem, as well as for the development of methods which minimize the risk of pollution areas. Due to the complex, heterogeneous nature of the soil and surface waters, the determination of the chromium behavior may be a very difficult task. Only by understanding the specific mechanism of the reactions, in which chrome may participate, one can expect a truthful forecast of its behavior.

Chromium (Cr) is one of the most strategically important materials in the world, having a wide range of applications in metallurgy and chemical industry. Alloys containing chromium metal enhance such properties as the resistance, stability to corrosion and oxidation. Furthermore, chromium is used as an additive in the production of stainless steel, in the treatment of leather, metal plating, in the production of catalysts and in other industries [1].

Chromium is rarely found in nature as a free metal. Chromium can exist in all degrees of oxidation from 0 to VI. The most typical chromium degrees of oxidation are +2, +3 and +6, but +3 and +6 are most stable ones, while the oxidation states +1, +4 and +5 are rare found in nature. Cr(III) is much less toxic than Cr(VI) [3]. Cr(III) is the most stable form in the environment and biological systems. It is an essential trace element in the human body and participates, in combination with various enzymes, in the metabolism of sugars, proteins and fats. The recommended daily dose for an adult is between 0.5 to 1.0 mg/day [4].

According to the World Health Organization (WHO) and the International Agency for Research on Cancer Cr(VI) is a carcinogen form. The inhalation of Cr(VI) can cause irritation of the nose and nosebleeds. After the contact of Cr(VI) with the human body, skin rashes, indigestion and ulcers, respiratory diseases, weakness of immune system, kidney and liver damage, alteration of genetic material, lung cancer and death may appear or be caused [5]. The WHO considers Cr(VI) as a pollutant of main concern. The concentration of 0.05 mg/L for Cr(VI) has been adopted as the maximum allowable concentration (MAC) for drinking water. That is why a constant monitoring and analysis of chromium in the environment is becoming a requirement. The natural sources of chromium in natural waters are such processes as erosion of rocks and run-off from the land-based systems. The chromium concentration in rivers and lakes is generally limited to 0.5 – 100.0  $\mu\text{g/L}$  [6], while in marine waters it ranges between 0.156-0.260  $\mu\text{g/L}$  [7].

The concentration of chromium in contaminated area may be much higher. The local increase in the concentration of chromium in waters (mainly in rivers) is due to wastewater discharges from the metallurgy, electroplating, chemical and leather industries, as well as the health leach dumps etc. The concentration and type of substances present in the effluent depend on the nature of industrial processes using chromium [8].

In natural waters, chromium exists in only two stable states, Cr(III) and Cr(VI). The presence and the ratio between these two forms dependent on the various processes that include chemical, photochemical, and redox processes, reactions of precipitation/dissolution and adsorption/desorption. The high concentrations of chromium in the nature cause mutagenic, teratogenic or carcinogenic effects.

The highest concentration of chromium in the Chisinau city was found in samples of snails collected in the industrial zone, indicating a strong pollution of nearby territory by this metal (snails were collected in the vicinity of the factory of leather processing “Piele SA”) and near the gas station [9]. A relatively high concentration of chromium was detected in immature specimens of *Helix Lutescens* (2.0  $\mu\text{g/g}$ ). The Cr concentration in the soil in the industrial area was particularly high - 1079.7  $\mu\text{g/g}$ .

The aim of this paper is the thermodynamic analysis, based on the selected recent experimental data, and graphical representation of the distribution of various soluble and insoluble chemical forms of chromium (III) and (VI) for different concentrations in a wide range of pH values.

### Theoretical part

#### **Thermodynamic calculations and graphic representation of the distribution of chemical forms of Cr(III) and Cr(VI)**

In this paper the diagrams of heterogeneous chemical equilibria (DHCE) have been used for graphical representation of complex equilibria in aqueous solutions containing Cr(III) [10]. Their construction is based on the determination of the thermodynamic stability areas of the solid phase [11-13], derived by the method of residual concentrations (RC) [14, 15]. The biphasic systems consisting of the soil solution and minerals, in which a number of chemical reactions occur simultaneously, are heterogeneous systems. These diagrams are similar in appearance to the distribution diagram in the case of homogeneous (single-phase) systems [16], however, the principle of their construction differs significantly from the past ones.

Besides the process of chromium hydroxide  $Cr(OH)_{3(S)}$  dissolution (the subscript symbol "S" denotes solid phase):



the hydrolysis reaction with the formation of mono- and polynuclear hydroxocomplexes  $Cr_i(OH)_j^{3i-j}$  are taken into account [17]:



Near to the equations of reactions their corresponding equilibrium constants  $K_s$  and  $K_{ij}$  are written.

The conditions of mass balance (MB) in this system are formulated on the basis of residual concentrations, RC [14, 15]:

$$C_{Cr}^0 = C_{Cr}^r + \Delta C_{Cr} = \sum_{i=1} \sum_{j=0} i[Cr_i(OH)_j] + \Delta C_{Cr} \quad (3)$$

$$C_H^0 = C_H^r + \Delta C_H = [H] - [OH] - \sum_{i=1} \sum_{j=1} j[Cr_i(OH)_j] + \Delta C_H \quad (4)$$

For convenience, the notation of species charges is omitted. The quantities  $C_i^0$  and  $C_i^r$  in Eq.(3) and Eq.(4) represent, respectively, the analytical (total) and residual concentrations of the "i" component in the heterogeneous system under consideration. In Eq.(3) and Eq.(4) by  $\Delta C_i$  the amount of solid phase in one liter of solution is denoted. In Eq.(4),  $C_H^0$  symbolizes the excess of the  $H^+$  ions towards the hydroxyl ions in the two-phase mixture,  $C_H^0 = -C_{OH}^0$ . From the stoichiometric composition of chromium hydroxide  $Cr(OH)_{3(S)}$ , the following relation is derived:

$$1/3\Delta C_{OH} = \Delta C_{Cr} \quad (5)$$

Moreover, in the framework of the RC method, it can be written:  $\Delta C_{OH} = -\Delta C_H$  and  $C_{OH}^r = -C_H^r$ . The equilibrium concentration of chromium ion  $[Cr^{3+}]$  is determined from the equilibrium constant  $K_s$  (Eq.(1)). In view of the law of mass action (LMA) and relation (5), from the mass balance (3) and (4) at a given pH, we obtain an equation with one unknown -  $\Delta C_{Cr}$ , which can be easily solved by the known numerical methods. From the combined aforementioned equations of LMA and MB, one can calculate the distribution diagram of the chromium ion in the solid phase and complex species in the liquid phase (aqueous solution), i.e. the DHCE. The following equations for calculating the partial molar fraction of species  $f_i$  in the heterogeneous system, wherein the reactions (1) and (2) proceed simultaneously, have been used:

$$f_S = \frac{\Delta C_{Cr}}{C_{Cr}^0}, \quad f_{tot} = \frac{C_{Cr}^r}{C_{Cr}^0}, \quad f_{Cr} = \frac{[Cr]}{C_{Cr}^0}, \quad f_{ij} = \frac{i[Cr_i(OH)_j]}{C_{Cr}^0} \quad (6)$$

Here the subscript "tot" means the sum of the molar fractions of all the soluble species. On the basis of Eq.(3), Eq.(5) and Eq.(6) the validity of the following equation can be verified:

$$f_S + f_{tot} = f_S + f_{Cr} + \sum_{i=1} \sum_{j=1} f_{ij} \quad (7)$$

When  $i > 1$  for the hydroxo-complexes of type  $Cr_i(OH)_j$ , the polynuclear complexes are formed. In order to appreciate their amount, the degree of the polynuclear hydroxo-complex formation has been calculated [18]:

$$P = \sum_{i=1} \sum_{j=0} i f_{ij} \quad (8)$$

If  $P > 1$ , then the polynuclear hydroxo-complexes are present in the solution.

In appearance DHCE are similar to the diagrams of distribution of the species in homogeneous solution. The latter are usually built in the coordinates  $f_i(\text{pH})$ , as in the absence of polynuclear complexes, the molar fractions of species  $f_i$  in aqueous solution are a function of the solution pH and do not depend on the initial concentrations of components. In the case of heterogeneous equilibria, the molar fractions of species depend also on the initial composition of the mixture, being at a given pH a function of one variable  $f_i = f(C^0(\text{Cr}))$ . In this case, it is desirable to build the diagrams in the coordinates  $(f_p, \text{pH})$ , fixing the values of other variables. The procedure for constructing DHCE includes the following successive steps:

1) Thermodynamic calculation of the  $\text{Cr}(\text{OH})_{3(S)}$  stability area. The authors [9-13] derived the equation for calculating the Gibbs energy of complex process  $\Delta G_{S,tot}$ , in which reactions (1) and (2) occur simultaneously:

$$\Delta G_{S,tot} = -RT \ln \frac{C_{Cr}^r}{C_{Cr}^0} \quad (9)$$

The solid phase  $\text{Cr}(\text{OH})_{3(S)}$  is stable if  $\Delta G_{S,tot} > 0$ . The condition  $\Delta G_{S,tot} = 0$  corresponds to the beginning of its dissolution (or precipitation).

2) Subsequently, the molar fractions  $f_i$  of all the chemical species containing chromium ion are calculated by the Eq.(6) within the stability area of  $\text{Cr}(\text{OH})_{3(S)}$  defined in the previous stage.

3) For completeness, outside this area, i.e. for homogeneous aqueous solutions, the molar fractions are calculated by the usual equations for the distribution diagrams [16]. In this case, the  $f$  value does not depend on the initial concentrations of examined components under the conditions of formation of only mononuclear complex species.

Distribution diagrams of chemical forms Cr(VI) are calculated by the usual equations for the distribution in the homogeneous systems. The chemical equilibria and their equilibrium constants, used in this paper, are given in Table 1.

Table 1

Equilibrium constants used for calculations in this work.

Chemical reactions	$\log K$	Source
$\text{Cr}^{3+} + \text{H}_2\text{O} = \text{CrOH}^{2+} + \text{H}^+$	-3.57	[17]
$\text{Cr}^{3+} + 2\text{H}_2\text{O} = \text{Cr}(\text{OH})_2^+ + 2\text{H}^+$	-9.84	[17]
$\text{Cr}^{3+} + 3\text{H}_2\text{O} = \text{Cr}(\text{OH})_{3(aq)}^0 + 3\text{H}^+$	-16.19	[17]
$\text{Cr}^{3+} + 4\text{H}_2\text{O} = \text{Cr}(\text{OH})_4^- + 4\text{H}^+$	-27.65	[17]
$2\text{Cr}^{3+} + 2\text{H}_2\text{O} = \text{Cr}_2(\text{OH})_2^{4+} + 2\text{H}^+$	-5.00	[19]
$3\text{Cr}^{3+} + 4\text{H}_2\text{O} = \text{Cr}_3(\text{OH})_4^{5+} + 4\text{H}^+$	-10.75	[19]
$4\text{Cr}^{3+} + 6\text{H}_2\text{O} = \text{Cr}_4(\text{OH})_6^{6+} + 6\text{H}^+$	-13.86	[20]
$\text{Cr}(\text{OH})_{3(S)} + 3\text{H}^+ = \text{Cr}^{3+} + 3\text{H}_2\text{O}$	9.35	[19]
$\text{CrO}_4^{2-} + \text{H}^+ = \text{HCrO}_4^-$	6.55	[19]
$\text{CrO}_4^{2-} + 2\text{H}^+ = \text{H}_2\text{CrO}_4$	6.31	[19]
$2\text{CrO}_4^{2-} + 2\text{H}^+ = \text{Cr}_2\text{O}_7^{2-} + \text{H}_2\text{O}$	14.7	[19]

## Results and discussion

The data regarding the thermodynamic stability of the chromium (III) hydroxide, calculated by Eq.(9), are depicted graphically on the Figure 1. As one can see, the area of predominance of the solid phase diminishes noticeably with decreasing the analytical concentration of Cr(III) in the heterogeneous mixture.

According to the thermodynamic calculations in this paper, depending on the total (analytical) concentration of chromium and acidity of solutions, Cr (III) can exist in aqueous solution as hydroxo complexes, such as  $\text{Cr}(\text{OH})^{2+}$ ,  $\text{Cr}(\text{OH})_2^+$ ,  $\text{Cr}(\text{OH})_3$ ,  $\text{Cr}(\text{OH})_4^-$ ,  $\text{Cr}_2(\text{OH})_2^{4+}$  and  $\text{Cr}_3(\text{OH})_4^{5+}$ . Figure 2 shows DHCE for  $C^0(\text{Cr}) = 10^{-6}$  M. Hence one can conclude that  $\text{Cr}^{3+}$  exists only in highly acidic environments,  $\text{Cr}(\text{OH})^{2+}$  predominates at the pH values of 3.7 – 6.0, while the solid phase  $\text{Cr}(\text{OH})_{3(s)}$  is prevailing at  $\text{pH} > 6.0$ . In highly alkaline solutions, at  $\text{pH} > 12$ , chromium in the solution is in the anionic form of hydroxocomplex  $\text{Cr}(\text{OH})_4^-$ .

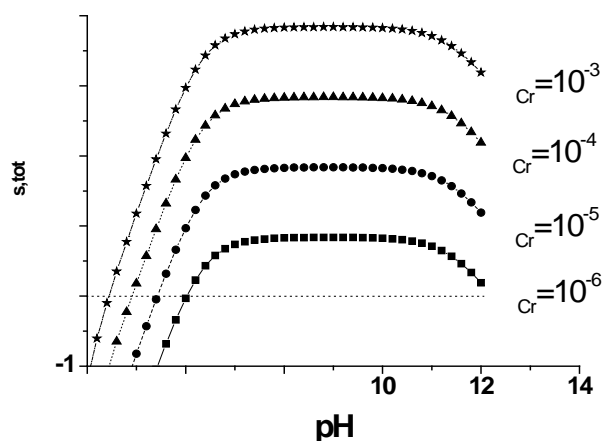


**Figure 1. The total Gibbs energy versus pH for the system “saturated aqueous solution – Cr(III) hydroxide” for different analytical concentrations of Cr(III).**

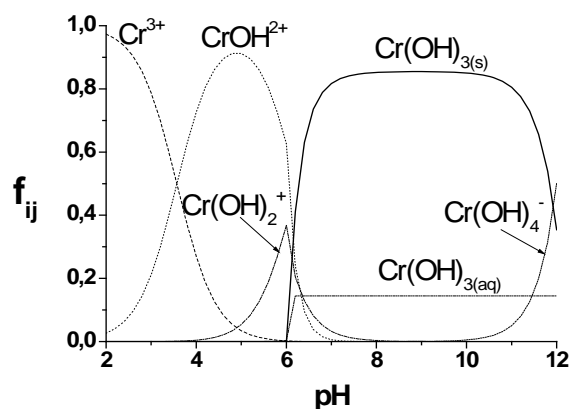


**Figure 2. The curves of distribution of the Cr(III) hydroxocomplexes as a function of pH for  $C^0(\text{Cr}) = 10^{-6}$  M.**

By increasing the analytical concentration of Cr(III) the amount of its polynuclear hydroxocomplexes grows substantially (Figures 3 and 4). By comparison Figures 3 and 4 one can deduce that the complex  $\text{Cr}_2(\text{OH})_2^{4+}$  for the pH range between 4 and 6 is formed. The larger pH area between 2 and 9 corresponding to the formation of polynuclear complexes  $\text{Cr}_2(\text{OH})_2^{4+}$ ,  $\text{Cr}_3(\text{OH})_4^{5+}$  and  $\text{Cr}_4(\text{OH})_6^{6+}$  is found for  $C^0(\text{Cr}) = 0.1$  M.

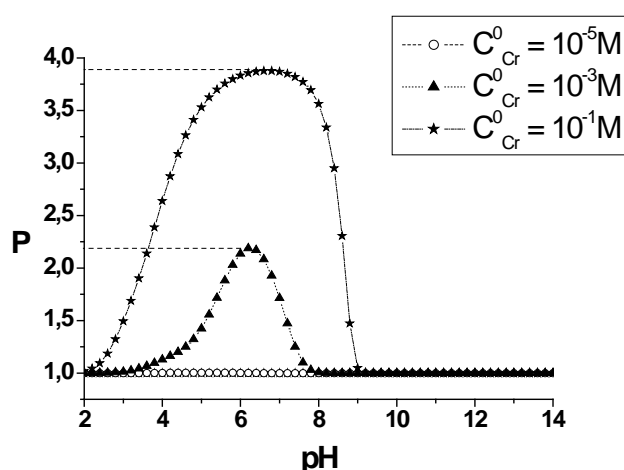


Figure 3. The degree of polynuclearity for hydroxocomplexes of Cr(III) versus pH at different analytical concentrations of Cr(III).

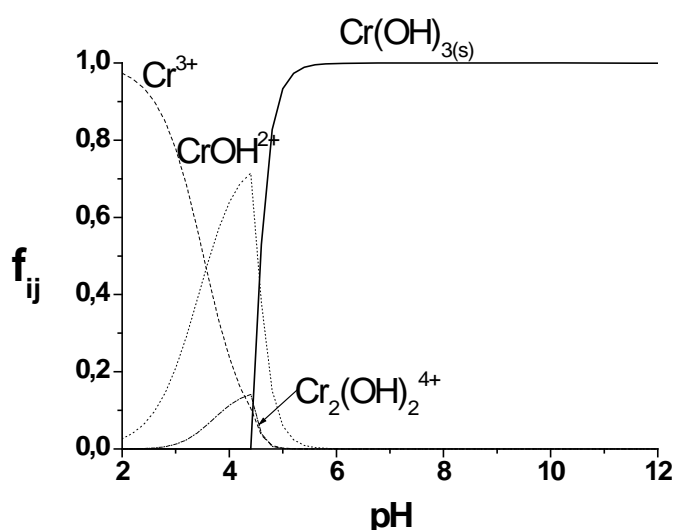


Figure 4. The curves of distribution of the Cr(III) hydroxocomplexes as a function of pH for  $C^0(\text{Cr}) = 10^{-3} \text{ M}$ .

On the Figure 5 the degree of polynuclear complex formation for Cr(VI) at its different analytical concentrations is represented. As one can see, the polynuclear Cr(VI) species are not formed at the concentration  $C^0(\text{Cr}) \leq 10^{-5} \text{ M}$ .

Cr(VI) may be present in the aqueous solution mainly in the form of chromate, dichromate, hydrogen chromate, chromic acid and hydrogen dichromate. The last two species were found only in the strongly acidic solutions. In typical surface waters, when the concentration of chromium is less than  $5.0 \mu\text{g/L}$ , only  $\text{HCrO}_4^-$  and  $\text{CrO}_4^{2-}$  can be found. The soluble chromium species  $\text{CrO}_4^{2-}$  and  $\text{Cr}(\text{OH})_3$  are bio-accumulated as phyto- and zooplankton readily absorb chromium in all its forms. Nevertheless, the slow water flow and reducing bandwidth can cause adsorption of chromium on the surface of suspended particles in water and thus its deposition occurs.

Figure 6 shows DHCE of the chemical forms of Cr(VI) for its different total concentrations in aqueous solution. In contrast to Cr(III), DHCE for Cr(VI) are changed to a much lesser extent with the change in the total concentration of the metal ion in solution.



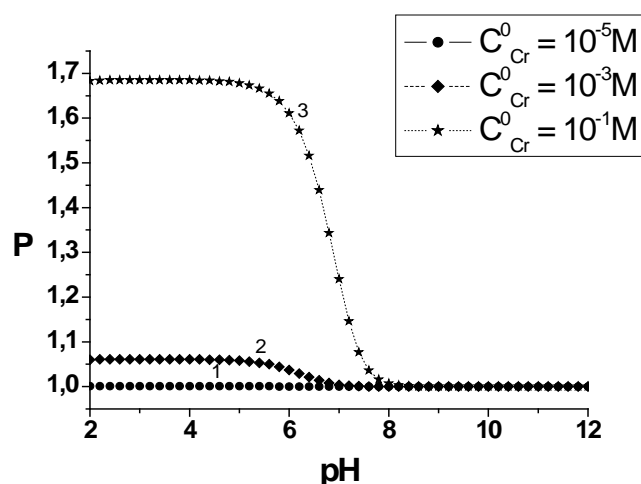


Figure 5. The degree of polynuclearity of the Cr(VI) species versus pH at different analytical concentrations of Cr(VI).

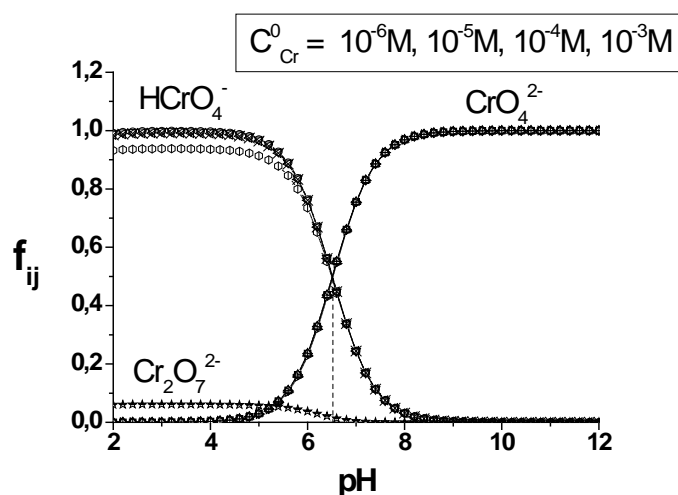


Figure 6. The curves of distribution of the complexes of Cr(VI) as a function of the pH solution at different analytical concentrations of Cr(VI).

## Conclusions

It is worthy to note that our results, based on the thermodynamic analysis and graphic design of the calculated data in the form of the diagrams of heterogeneous chemical equilibria, are in good agreement with the available experimental data.

## Acknowledgement

Author thanks to the Professor Igor Povar for his kind support, help and encouraging this research.

## References

1. Guertin, J.; Jacobs, J.A.; Avakian, C.P. Chromium (VI) Handbook. CRC Press: Boca Raton, USA, 2004, 800 p.
2. Kohl, W. Handbook of Materials and Techniques for Vacuum Devices. Reinhold Publishing: New York, 1967, 161 p.
3. Grevatt, P.C. Toxicological review of trivalent chromium. U.S. Environmental Protection Agency: Washington, 1998, 44 p.
4. Vincent, J.B. The Nutritional Biochemistry of Chromium (III). Elsevier: Amsterdam, 2011, 292 p.
5. Zhitkovich, A. Chromium in Drinking Water: Sources, Metabolism, and Cancer Risks. Chemical Research in Toxicology, 2011, 24(10), pp. 1617-1629.

6. Beaublen, S.; Nriagu, J.; Blowes, D.; Lawson, G. Chromium speciation and distribution in the great lakes. *Environmental Science & Technology*, 1994, 28, pp. 730-736.
7. Richard, F.C.; Bourg, A.C.M. Aqueous geochemistry of chromium: a review. *Water Research*, 1991, 25, pp. 807-816.
8. Nriagu, J. Production and uses of chromium. *Chromium in Natural and Human Environments*. Wiley Interscience: New York, 1988, pp. 81-104.
9. Andreev, N.; Zubcov, E. The content of heavy metals (Cd, Cu, Cr and Pb) in terrestrial snail body (helix, gastropoda, pulmonata) and health standards for food. *Collection of Scientific Articles: Tighina, Eco-Tiras*, 2006, pp. 43-46 (in Romanian).
10. Povar, I.; Rusu, V. Aluminium heterogeneous speciation in natural waters. *Canadian Journal of Chemistry*, 2012, 90, pp. 326- 332.
11. Fishtik, I.; Povar, I.; Vataman, I. Thermodynamics of Complex Equilibria in Salt Deposit-Aqueous Solution Systems. Estimation of Polynuclear Particle Formation. *Journal of General Chemistry*, 1987, 57, pp. 736-742 (in Russian).
12. Povar, I. Thermodynamic calculation of pH of the minimum solubility of slightly soluble oxides and hydroxides under metal ion polynuclear hydrolysis conditions. *Ukrainian Chemistry Journal*, 1994, 60, pp. 371-376 (in Russian).
13. Povar, I. Potentiometric determination of solubility products of poorly soluble hydroxides and acids. *Journal of Analytical Chemistry*, 1998, 53, pp. 1113 -1119 (in Russian).
14. Povar, I. Buffer properties of heterogeneous systems containing sparingly soluble acids and metal hydroxides. *Russian Journal of Inorganic Chemistry*, 1996, 41, pp. 1167-1172.
15. Povar, I. Buffer properties of heterogeneous water-salt systems in relation to the components of a low-solubility precipitate. *Russian Journal of Inorganic Chemistry*, 2000, 45, pp. 1632-1636.
16. Kragten, Y. Atlas of metal-ligand equilibria in aqueous solutions. Halsted Press: New York, 1978, 781 p.
17. Rai, D.; Sass, B. M.; Moore, D.A. Cr(III) hydrolysis constants and solubility of Cr(III) hydroxide. *Inorganic Chemistry*, 1987, 26, pp. 345-349.
18. Fishtik, I. et al. On the polynuclearity degree in solution complexation reactions. *Russian Journal of Inorganic Chemistry*, 1987, 32(8), pp. 2061-2064 (in Russian).
19. Ball, J. W.; Nordstrom, D. K. Critical Evaluation and Selection of Standard State Thermodynamic Properties for Chromium Metal and Its Aqueous Ions, Hydrolysis Species, Oxides, and Hydroxides. *Journal of Chemical and Engineering Data*, 1998, 43, pp. 895-918.
20. Stunzi, H. et al. Early stages of the hydrolysis of Cr(III) in aqueous solution. 4. Stability constants of the hydrolytic dimer, trimer and tetramer at 25 °C and I = 1 M. *Inorganic Chemistry*, 1989, 28, pp. 66-71.

## ECOLOGICAL CLEANING SYSTEMS FOR OLD ICONS PAINTED IN TEMPERA

Silvea Pruteanu, Petronela Spiridon, Viorica Vasilache, Ion Sandu\*

„Alexandru Ioan Cuza” University of Iasi, Interdisciplinary Research Platform ARHEOINVEST,  
Laboratory of Scientific Investigation and Conservation of Cultural Heritage,  
11, Carol I blvd., Iasi 700506, Romania,

\*e-mail: sandu\_i03@yahoo.com; phone: 040 232 201662; fax: 040 232 214816

**Abstract.** Old icons, especially those involved in liturgical rituals are affected in time by external agents factors (temperature, humidity, light, pollution, microbiological attack, abrasion etc.), resulting changes of the appearance and of the structural integrity, dirt deposits, altered varnish and painting layer, cracks, material loss etc. In order to remove the dirt deposits, there are used cleaning systems with dry wiping, vacuuming, scraping, washing with organic solvents, ion exchange solutions, polyelectrolyte, surfactants, and so on, by enzymatic systems or by laser pyrolysis. The last two processes being considered aggressive and highly invasive, although they do clean very well adherent dirt deposits, which strongly degraded the varnish to total blackening (the iconographic image cannot be seen). Based on the literature in the field, regarding the nature of the materials used during the painting process and of the types and structures of the deposits, a series of alcoholic solutions of different concentrations were made, as such or basified, which were compared with ecologic synergic systems based on organic uncolored vegetable juices and decoctions from dried plants. The cleaning effectiveness was done by visual analysis and CIE  $L^*a^*b^*$  reflection colorimetry, space proposed by the CIE (International Commission on Illumination) in 1976, was used. This technique permitting to determine by color deviations the critical point where the patina and polychromes layer.

**Keywords:** degraded varnish, deposits of dirt on tempera, wash tests, solvents, vegetable extracts, decoction of dried plants, CIE colorimetry reflection  $L^*a^*b^*$ .

### Introduction

To restore the aesthetics of an old icon, blackened in time and to improve the age patina “the golden halo” of an artifact [1-3] requires some cleaning procedures compatible and highly specific for adherent deposits. These operations consider a number of issues related to the value of the artifact, the age, the nature of the materials used in the making process, the effects of deterioration and degradation and the nature and aggressiveness of dirt deposits (loose, clogged - strongly adherent). These deposits lead to the darkened varnishes or bleaching of the paintings, along with the burns, blisters, varnish and paint layer warping, greatly affect the integrity and aesthetics, leading to their removal from the liturgical and museum circuit [4-6].

Cleaning dirt deposits includes dry physical and mechanical processes, wet physicochemical and enzymatic cleanings, or thermal processes by laser pyrolysis. The first group of methods is based on dust removal processes (vacuum), brushes, scraping (with knife), removal or dry polishing which is used for thick adherent deposits (wax, bitumen, paint and other fatty deposits accidentally splashed, or other type of contact etc.). The wet cleaning is applied frequently when using conventional washing solutions by using water or organic solvents in the form of a synergistic washing complex systems (emollients, surfactants or additives, surfactants, enzymes etc.) [7].

Lately, there have been increasingly studied the ecological systems based on uncolored fruit extracts and decoctions of dried herbs, freshly prepared [8-10]. The idea of using systems based on fresh colorless juices extracts (garlic, white onion, cabbage, zucchini, parsley, celery etc.) and decoctions of dried plants (corn silk, cobs containing alkali and furfural with moisturizing role, basil etc.) was often used in the past for cleaning carpets, upholstery and old icons blackened. In this regard, it was agreed a systematic reanalysis of them because they have a number of advantages related to the ecology of work (minimum aggression, high synergy, low cost, zero toxicity etc.).

Thus, the paper presents the results obtained by washing of old icons in tempera, using a series of synergistic natural systems based on extracts and decoctions. As a reference we used an aqueous solution based on alcohol, which was first optimized in relation to the old tempera painting, by varying the concentrations and slight alkalisation or adding ammonia. For application, first wash test were performed on very small surfaces with representative degradation of the painting, with standard solutions, choosing the most effective formula. Then, wash tests were applied to systems based on natural extracts and decoctions. After every cleaning application processes the efficiency of cleaning was analyzed as well as the side effects on varnish and patina, using the visual and colorimetric analysis [11] by reflection CIE  $L^*a^*b^*$ .

### Experimental

The study is made on an icon of from XIX<sup>th</sup> century, from a private collection, representing the Three Hierarchs Basil, Gregory and John, made in tempera on lime wood, by an anonymous painter (Figure 1). The pigments used are colored earths blinded with egg yolk.

Presented at the International Conference dedicated to the 55<sup>th</sup> anniversary from the foundation of the Institute of Chemistry of the Academy of Sciences of Moldova



**Figure 1. Icon Three Holy Hierarchs Basil, Gregory and John (front/back).**

By using visible reflectography, in UV and IR were observed on both the front and on the back a series of degradation and progressive deterioration, of the paint layer and of the wood panel from handling and careless or improper use or storage in unsuitable conditions, previously cleaned very aggressive, inappropriate, which led to the loss of varnish. Also other physical deterioration can be seen, cracking, wood plank separation, multiple and profound gaps in the paint layer, unevenness and small, recent hatch openings by borer insect attack (Figures 2 and 3).



**Figure 2. Degradation of the paint layer and the substrate, no varnish on the right of the icon.**

Regarding the dirt deposits, the paint layer were found adherent deposits, clogged are as on the golden cloak from the central area, yellowing and opacifying of the varnish, early micro fissures on the entire surface of the icon (Figures 1-3).



**Figure 3. Cracks, separation, multiple and profound gap sin the paint layer to support wood nun even small.**

#### **Cleaning systems, washing tests**

The washing tests were performed with cotton pads (100%) wound on wood sticks, soaked in solutions or mixtures of various solvents. For establishing the optimum cleaning standard system compatible with the old tempera painting, we studied the ability of washing small areas of homogeneous and uniform dirt, i.e. the same colors, with the following classical solutions based on ethanol or alkalinized:

**E1** – aqueous 60% ethanol and 40% distilled water;

**E2** – aqueous 70% ethanol and 30% distilled water;

**E3** – aqueous 80% ethanol and 20% distilled water;

**E4** – aqueous 90% ethanol and 10% distilled water;

**E5** -100% absolute ethanol;

**E6** - The aqueous solution obtained by mixing 6.5 mL distilled water with 2.8 mL ethanol and three drops of ammonia.

In order to achieve synergistic mixtures based on colorless vegetable extracts and of dried decoctions of fresh herbs prepared (which were previously selected and studied in [8-10]) were tested in the following washing systems:

**S1** – 200 mL of 10g decoction of dried corn silk,

**S2** – 10 mL juice zucchini,

**S3** – 10 mL white onion juice,

**S4** - 10 ml carrot juice,

**S5** – 10 mL celery juice,

**S6** – 10 mL cabbage juice,

**S7** – 200 mL 10g decoction of dried basil,

**S8** – 10 mL parsley juice,

**S9** – 10 mL cucumber juice pulp (unshelled),

**S10** – 10 mL broth Hustle wheat bran.

The extracts of succulent vegetables (pumpkin, white onion, carrot, cabbage and cucumber) were obtained by blending and then spinning them. The vegetables which are not so juicy (roots of parsley, celery) were finely milled and dispersed in distilled water in 1:1 weight ratio. Corn silk decoctions and dried basil were obtained by boiling 10 g of dry plant in 200 mL of distilled water for 5 minutes. From the corn silk only the cornhusk was used. Tests were conducted on very small areas, about 1cm<sup>2</sup>, delimited and marked with special pencils Ceracoat type.

#### **Evaluation of cleaning efficiency**

The cleaning efficiency is highlighted by comparison system, by direct observation with a magnifying glass and by colorimetric CIE L\*a\*b\* using a colorimeter LOVIBOND 300 Reflectance Tinctometer, by comparing the cleaned areas with alcoholic solution using the standard systems S1 - S10.

For graphical representation of colorimetric values of the samples analyzed the CIE L\*a\*b\* space proposed by the CIE (International Commission on Illumination) in 1976, was used. The hue in this space (represented by basic colors: red, green, blue etc.), brightness or clarity (color ranging from black to white) and color (the color purity through its saturation, meaning its maximum brightness that appears for given added color), is analyzed on three axes: L\*, a\* and

b\*. The axis OX, noted a\*, it represents chromatic variation from red to green (a\* axis it refers to the chromatic red - a\* > 0 and green - a\* < 0), while b\* represents the axis OY, the other two chromatic stimuli, yellow (b\* > 0), and blue (b\* < 0), and L\* represents the axis OZ, the brightness. This method of representation of color [11] by means of Cartesian coordinates is based on the consideration that no color can be red or green and yellow and blue at the same time (so it is assumed that there is a complementary red/green and blue/yellow). At the painting cleaning the basic principles of intervention were respected [12, 13], by testing the solutions on different types of deposits, and according to their state of preservation.

In this way, the colour parameters L\*, a\*, b\*, h\* as well as the colour differences  $\Delta E$  [11-13] were determined. The colour difference was computed with Eq.(1):

$$\Delta E = [(\Delta L)^2 + (\Delta a)^2 + (\Delta b)^2]^{1/2} \quad (1)$$

where:  $\Delta$  indicates the difference between the batch sample in the present case the tinctorial determinations as compared and a witness sample;  $\Delta L$  represents the lightness difference (%) between batch and witness. If  $\Delta L > 0$ , then the sample which reproduces (batch) is lighter than the witness; if  $\Delta L < 0$  the sample which reproduces (batch) is darker than the witness.

## Results and discussion

After analyzing the conservation state of the icon the cleaning processes were done, initially by brushing and gentle aspiration, and then washing using various solvents, besides the usual and with some fruit juices and teas. For each system used, first a wash test was performed on a very small surface with painting representative degradation (Figure 4).

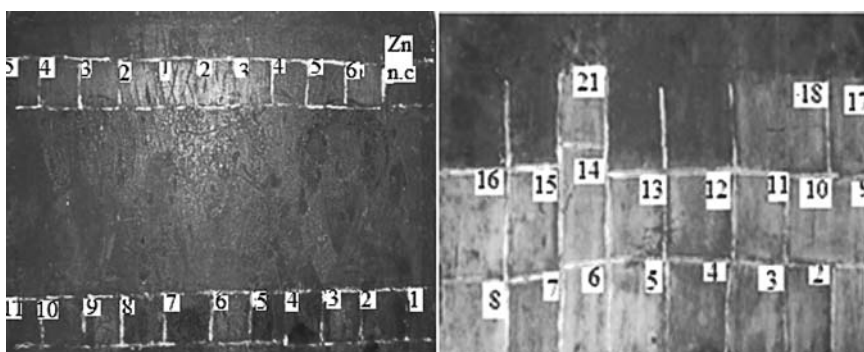


**Figure 4. Washing tests (front /back) on small surfaces with aqueous alcoholic E1-E6 (top row), natural vegetable extracts and decoctions of herbs freshly prepared: S1-S10 (bottom row).**

As mentioned, the wet cleaning operations, focused on two groups of systems:

-Five standard aqueous ethanol solutions (E1 - E5) with different concentrations from 60% to 100% (absolute ethylic alcohol) and the optimum solution E6 used later as a reference, which was obtained by basification with three drops of 25% aqueous ammonia solution E2 (70% ethanol solution).

-Seven uncolored vegetable extracts, two dried plants decoctions and a weak solution of lactic acid produced by the maceration wheat bran.

First of all the aqueous alcoholic solutions were tested, which are known in the literature for their cleaning properties on oil paintings but not on tempera. After each washing and after the surface was dried, the surface was inspected by direct visual observation or with a magnifying glass for increased comparing with the adjacent areas and that of the standard (E6), it was concluded that:

- E1 solution (60% ethanol) did not remove any adhering dirt, even in a greater period of time with 5 minutes.
- E2 solution (70% alcohol) removed easily greasy dirt and without affecting the varnish or age patina, in an emolliating time smaller than 2 minutes.
- E3 solution (alcohol 80%) permits removal of adhering dirt without affecting the varnish or patina, in an emolliating time of 3 minutes.
- E4 solution (90% ethanol) removed the less adherent in 4 minutes.
- E5 solution (100% ethanol) removed just the less adherent, in an emolliating time of 3 minutes.
- E6 standard solution removed all dirt adhesion, even the sturdy one and cleaning effect was better than other alcoholic solutions used without affecting the pigments, varnish and age patina.

It should be noted that no metal leaf was affected (Figures 5, a and b).

Figure 6 shows the reflectance colorimetry data obtained by the CIE L\*a\*b\* on the six test areas with alcoholic solutions, confirming that the E4 solution (obtained by 80% E3 solution with ethanol, alkalizing it with three low drops of ammonia 25%) is the most effective, not affecting the varnish or age patina.

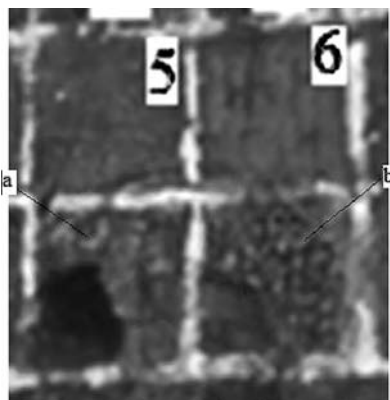


Figure 5. Details of areas cleaned using standard reference solution.

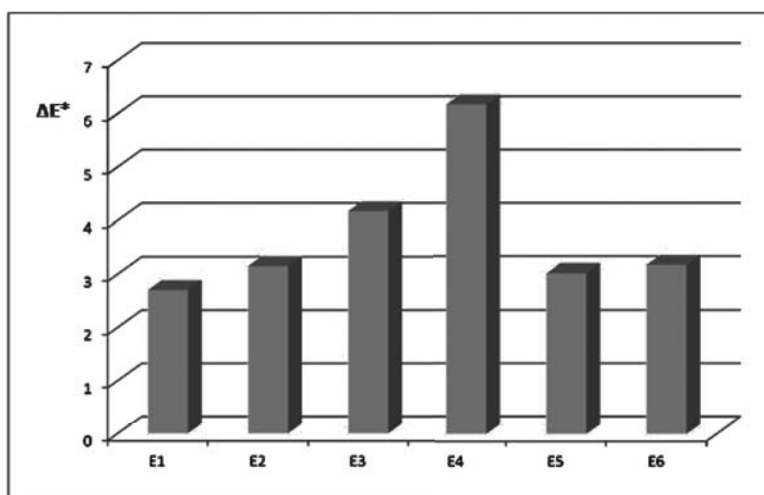


Figure 6. Colorimetric analysis CIE L\*a\*b\* of the areas cleaned with alcoholic solutions E1-E6.

The cleaning efficiency of the ten natural systems was highlighted by visual comparison with the standard clean areas and the good system efficiency was noted S3-S9 (Figure 7).

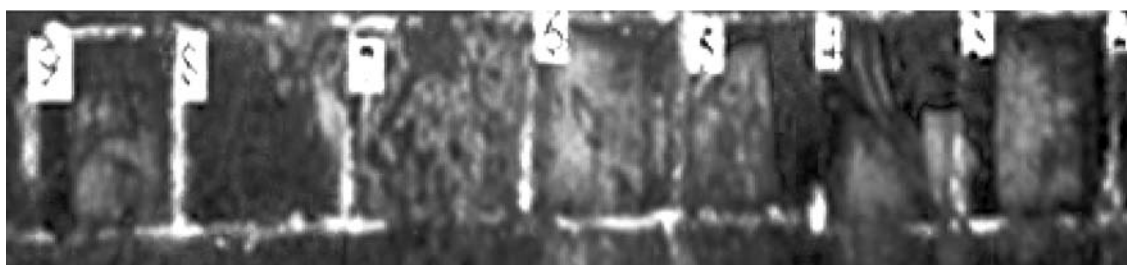


Figure 7. Details of the areas cleaned with natural extracts vegetables: S3-S9.

Figure 8 shows the reflectance data obtained by colorimetry CIE L\*a\*b\* on the ten areas tested, washed with ecological systems, where it is clear that S6 - cabbage extract behaved most effectively, then S3 system based on white onion extract, S4 - colorless carrot extract, and S9 - cucumber juice gave a weaker result, and S7 - decoction of basil.

In the ecological systems - freshly prepared, used in the washing tests, is a very important observation to mention, about the behavior of these cleanings for a longer period of time and after second varnishing, is a subject for further research.

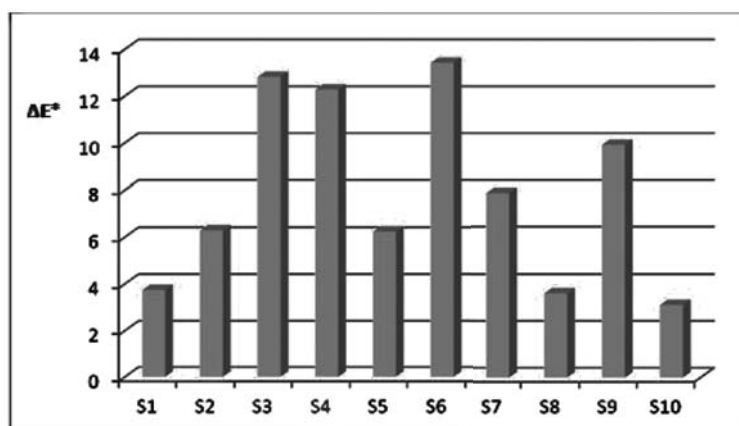


Figure 8. CIE L\*a\*b\* colorimetric analysis of cleaned areas with ecological systems S1-S10.

### Conclusions

To cleaning of the studied icons were used extracts of green plants and vegetables, dried herbs decoction that formed synergistic solutions, noted from S1 to S10 and a reference: the classical solution ethyl alcohol of various concentrations, or slightly alkalinized E1 - E6. From the alcoholic solutions tested were chosen only the ones with effective cleaning on degraded varnish layer and deposits of dirt, which was alkalinized with three drops of 25% ammonia (E6). Using visual analysis and the CIE colorimetric reflectance L\*a\*b\* was observed that the best results were obtained with S6, S3, S4 and S9 systems, which provided: a quick and effective cleaning; paint layer, varnish and age patina were not affected; pigments have not changed color; detachments or flaking didn't occur.

### References

- Vasilache, V.; Sandu, I.; Luca, C.; Sandu I.C.A. News in scientific preserve of old wood polychrome; Univ. "Al.I.Cuza": Iasi, 2009, 282 p. (in Romanian).
- Sandu, I.C.A.; Bracci, S.; Sandu, I.; Lobefaro, M. Integrated analytical study for the authentication of five Russian icons (XVI–XVII centuries). *Microscopy Research and Technique*, 2009, 72, pp. 755–765.
- Sandu, I.C.A. GILT-Teller: An interdisciplinary multiscale study of gilding techniques and materials in Portugal 1500-1800. *Proceeding. VIII Jornadas de Arte e Ciência - Conservação e Restauro de Artes Decorativas de Aplicação Arquitectónica*, Porto, 2013, pp. 127-142.
- Sandu, I. Degradation and deterioration of the Cultural Heritage; Univ. "Al.I.Cuza": Iasi, vol. I, 2008, 462 p.
- Sandu, I. Degradation and deterioration of the Cultural Heritage; Univ. "Al.I.Cuza": Iasi, vol. II, 2008, 538 p.
- Sandu, I.C.A.; Luca, C.; Sandu, I.; Vasilache, V.; Hazashi, M. Authentication of ancient easel-paintings through materials identification from polychrome layers. II. FTIR Spectroscopy. *Revista de Chimie, Bucuresti*, 2008, 59(4), pp. 384-387.
- Feller R. *Conservation and Restauration of Pictorial Art*, London: Butterworths, 1976, 158 p.
- Pruteanu, S.; Sandu, I.; Vasilache, V.; Gherman, L.G.; Sandu, I.C.A.; Cristache, R.A. Integrated analytical study for the evaluation of cleaning effectiveness on Old Wood Romanian Icons, *PRO LIGNO*, 2013, 9(4), pp. 242-250.
- Pruteanu, S.; Gherman, L.G.; Sandu, I.; Hayashi, M.; Cozma, D.G.; Vasilache, V.; Sandu, I.C.A. Ecological materials used in preservation and restoration on New Wood. *PRO LIGNO*. 2013, 9(4), pp. 265-275.
- Budu, A.M.; Pruteanu, S.; Vasilache, V.; Sandu, I. Investigation methods and techniques for analysis of panel paintings state of conservation. *The Annals of "Dunarea de Jos" University of Galati, Fascicle IX. Metallurgy and Materials Science - Special Issue*, 2013, pp. 191-196.
- Sandu, I.; Sandu, I.C.A.; Sandu, I.G. *Colorimetry in the art*. Corson: Iasi, 2002, 273 p. (in Romanian).
- Brandi, C. *Restoration Theory. History and Literature*: Roma, 1963, (reedited by G. Einaudi, Torino, 1977) (in Italian).
- Baldini, U. *Restoration Theory and Integrate Methodology*. vol. II, Nardini: Firenze, 1981, pp. 136 -142 (in Italian).



## APPLICATION OF FLOW-THROUGH THREE-DIMENSIONAL ELECTRODES FOR REGENERATION OF PLATING IRON ELECTROLYTES: 1. MATHEMATICAL MODEL

Alexandr Koshev<sup>a</sup>, Olga Covaliova<sup>b\*</sup>, Valery Varentsov<sup>c</sup>

<sup>a</sup>*Penza State University of Architecture and Construction, 28, G. Titova str., Penza 440028, Russian Federation*

<sup>b</sup>*State University of Moldova, Research Center of Applied and Ecological Chemistry, 60, A. Mateevici str., Chisinau MD 2009, Republic of Moldova*

<sup>c</sup>*Institute of Solid and Mechanochemistry of the Siberian Branch of RAS, 18, Kutateladze str., Novosibirsk 630128, Russian Federation*

\**e-mail: covaleva.olga@yahoo.com; phone / fax: (+373 22) 57 75 56*

**Abstract.** The mathematical model of electrochemical processes distribution within the three-dimensional flow-through electrode for the system Fe(III)/Fe(II)/Fe is described in this paper, considering also the electrochemical reactions of hydrogen and molecular oxygen reduction. Possible dynamic changes in the parameters of electrode, electrolyte and the process are taken into account in the mathematical model, such as electro-conductivity of electrode material, electrolyte flow rate, material porosity and specific electrode surface, concentrations of electro-active substances and other characteristics within the local volume of electrode. Electrode and process characteristics are treated as time and coordinate functions within the electrode volume. The results of calculations and experimental studies of iron electro-reduction are given, the analysis of the numerical modeling is provided.

**Keywords:** electro-reduction, three-dimensional flow-through electrodes, electro-active components, numerical calculations of electrolysis processes.

### Introduction

During the electrochemical reduction of iron ions from the different electrolytes, relatively rapid oxidation of Fe(II) ions to Fe(III) occurs, so the preparation of good quality uniform coatings becomes difficult. Therefore, the problem of iron and its alloys electroplating and regeneration of “oxidized” electrolytes has not lost its actuality. The specifics of cathode processes in these electrolytes are connected with the formation and excessive accumulation of OH<sup>-</sup> ions in the vicinity of cathode. This causes the pH local shift to the alkaline area, in regard to the acidity in the bulk of solution. Apparently, in the presence of both Fe(II) and Fe(III) species in the iron plating solution, considering the different pH of their hydroxides formation ( $\text{Fe(II)}_{\text{hydr.}} = 6.5\div 9.7$ ;  $\text{Fe(III)}_{\text{hydr.}} = 1.5\div 4.1$ ), Fe(III) hydroxide is initially formed. A certain role in the redox-processes is also played by the other factors, specifically, anodic oxidation, effect of oxygen in the near-surface electrolyte layers, with subsequent diffusion of oxidation products into the bulk of solution, etc. In these cases, forming colloidal particles of Fe(III) hydroxide will most probably be included into the electrochemically plated coatings, provoking the deterioration of their physical-mechanical properties [1].

To ensure the stable operation of iron-containing electrolytes, a series of methods has been proposed, including the introduction of various stabilizing additives of organic or inorganic nature, membrane separation of anode and cathode compartments, etc. The conventional electrochemical pre-treatment of oxidized iron electrolytes is both energy- and time consuming. Hydrogen emission on the cathode is one of the factors promoting the reduction of iron in such electrolytes. We have proposed the reagent-free electrochemical technology of stabilizing the composition of iron-containing electrolytes with low concentrations of electro-active components [2], based on the application of flow-through three-dimensional electrodes (FTE), specifically, carbon-graphite fibrous materials (CFM), which make it possible to intensify electrochemical processes [3].

### Experimental

Our polarization studies, compared to the current efficiency data [4], have demonstrated (Figure 1) that the current efficiency of the reaction  $\text{Fe(III)} \xrightarrow{+e} \text{Fe(II)}$  is close to 100%, while using the Pt electrode under the potentials from +0.6 to (-0.2) ÷ (-0.3) V. With further cathode polarization, this value starts to decrease. At the same time, hydrogen emission begins (at  $E \approx 0\text{V}$ ), which amount is increasing. Consumption of current quantity is thus determined by these two competing processes, up to the potential of metal deposition beginning.

In addition to that, certain increase in the current efficiency value of the reaction  $\text{Fe(III)} \xrightarrow{+e} \text{Fe(II)}$  was marked on this electrode, reaching above 100%. The possible reason of this may be catalytic properties of Pt surface, which facilitates the formation of atomic hydrogen, which is a reducing agent with regard to Fe(III) ions. However, the share of this reaction is low, compared to the pure electrochemical reaction  $\text{Fe(III)} \xrightarrow{+e} \text{Fe(II)}$ , which, according to our estimation, lays within the limits of 5 ÷ 7%.

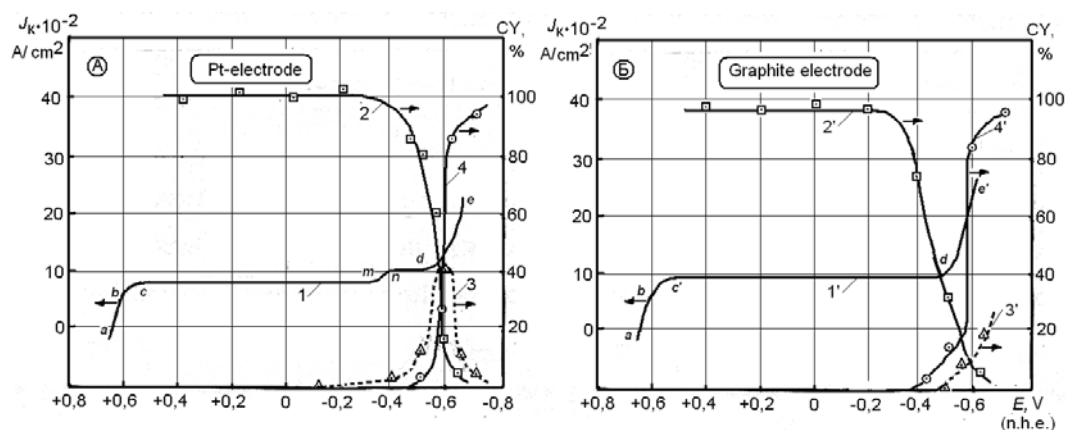


**Figure 1. Potential evolution (1, 1') on platinum (A) and graphite (B) electrodes, and current efficiency (CY) of the reactions:  $\text{Fe(III)} + e \rightarrow \text{Fe(II)}$ , (curves 2,2');  $2\text{H}^+ + 2e \rightarrow \text{H}_2$  (curves 3,3');  $\text{Fe(II)} - 2e \rightarrow \text{Fe}^0$  (curves 4,4').**

The dependence of current efficiency of the reaction  $\text{Fe(III)} \xrightarrow{+e} \text{Fe(II)}$  from the potential on graphite electrode is decreasing sharply. This is apparently connected with the fact, that on the graphite surface no effect is observed, resulting in iron reducing due to hydrogen, and the current efficiency of the process  $\text{Fe(III)} \xrightarrow{+e} \text{Fe(II)}$  within the potentials area up to the beginning of metal iron deposition, is close to 100%.

With the beginning of metal iron deposition under the potentials  $(-0.43) \div (-0.45)\text{V}$ , the current efficiency of  $\text{Fe(III)}$  ions is sharply decreased, remaining only within the limits of several percents, as soon as the basic reaction of  $\text{Fe(II)}$  ions reduction to metal prevails. The curve of the hydrogen current efficiency on Pt-electrode passes through the maximum and also decreases to the values of  $5 \div 10\%$ , as the potentials are shifted to the electronegative area.

Therefore, the succession of the reactions running during the cathode treatment of iron-containing electrolyte within the studied potential area can be presented in the following way. Under the  $E \approx +0.64\text{V}$ , the transition  $\text{Fe(III)} \xrightarrow{+e} \text{Fe(II)}$  starts, which occurs with the current efficiency close to 100%. In the more negative field than  $E \approx 0\text{V}$ , hydrogen emission starts on platinum surface, which begins more and more intensive, up to the beginning of the metal iron deposition. On graphite electrode, unlike the Pt one, hydrogen emission begins much later (under the potential more negative than  $-0.4\text{V}$ ). Presence of the broad area of potentials (about  $1\text{V}$ ), where the target reaction  $\text{Fe(III)} \xrightarrow{+e} \text{Fe(II)}$  runs with the high current efficiency, close to 100%, testifies on the possibility of the efficient application of carbon-graphite three-dimensional electrodes for carrying out of this process in the iron plating electrolytes [5].

The work of three-dimensional electrodes is affected at the same time by the number of interconnected factors, specifically: the kinetic parameters of the process, hydrodynamic conditions, specifics of the CFM applied and other factors, which complicates the study of the electrochemical processes' regularities. The method of mathematical modeling is one of the efficient ways to explore the regularities of the three-dimensional electrodes operation [6-8], making it possible to describe the processes occurring within these electrodes. In addition, with the help of this method it becomes possible to predict the changes of the basic technological parameters, influencing the studied process, and to optimize the electrolysis conditions.

Electrochemical processes occurring within the studied FTE during the regeneration of iron plating solutions – electroreduction of  $\text{Fe(III)}$  ions to  $\text{Fe(II)}$  and  $\text{Fe(II)}$  ions to metal, are as a rule accompanied by the secondary electrochemical reactions with participation of hydrogen ions and molecular oxygen.

The scope of this work was to create the mathematical models of electrochemical processes occurring within the flow-through three-dimensional electrode during the simultaneous reduction  $\text{Fe}^{+3} \rightarrow \text{Fe}^{+2}$  and  $\text{Fe}^{+2} \rightarrow \text{Fe}$ , considering the electrode reactions of hydrogen and molecular oxygen reduction, as well as the change in the electrode electroconductivity, the electrolyte flow rate, concentrations of electroactive substances and other parameters of electrode and electrolyte along the electrode depth. Apart from this, the scope of this work was to carry out the numerical studies of the above electrode processes within the FTE made of the carbon-graphite fibrous materials.

#### **Elaboration of the mathematical model of electrolysis in the polycomponent electrolyte within the FTE**

The mass balance within the flow of the charged particles involved in the electrode process can be described by the Eq. (1) [9]:

$$\frac{\partial C_i}{\partial t} = -\text{div}(z_i \mu_i F C_i \text{grad}(U) + C_i v) \quad (1)$$

Here and later  $z_i, C_i$  (mol/cm<sup>3</sup>),  $\mu_i$  – charge, concentration and mobility of  $i$ -th electroactive component ( $i=1, \dots, 4$ ) in the pseudo-homogeneous medium, accordingly;  $F$  (C mol<sup>-1</sup>) – Faraday's number,  $grad(U)$  – gradient of the electric field potential,  $v$  – velocity vector of the electrolyte's convective transfer,  $div$  – vector divergence.

It follows from the equation (1) that the concentration changes within the flow are determined by the value of the potential's gradient  $U$  and the electrolyte's velocity vector  $v$ , which do not depend directly on the concentrations and current densities of the partial electrochemical reactions. These functions are determinative with regard to the distribution of electrochemical process within the flow-through three-dimensional electrode. In accordance with this point, the mathematical model was proposed, concerning the distribution of polarization, current density and concentrations of substances, involved in the electrode reaction, for the electrochemical systems with two or more electroactive components. Thus, in [10] a mathematical model is proposed of metal electrodeposition on the FTE considering the hydrogen emission reaction:

$$\frac{d^2U}{dx^2} = S \cdot V \left( \frac{1}{\chi_S(x)} + \frac{1}{\chi_L(x)} \right) \left( j_M(x) + j_H(x) \right) \quad (2)$$

$$|v|zF \frac{\partial C}{\partial x} = -S \cdot V \cdot j_M(x), \quad (3)$$

where  $S_V$  (cm<sup>2</sup>/cm<sup>3</sup>) – reaction surface,  $j_M$  (A/cm<sup>2</sup>) – density of polarizing current with regard to metal,  $j_H$  (A/cm<sup>2</sup>) – density of polarizing current with regard to hydrogen;  $\chi_S$  and  $\chi_L$  – specific electroconductivity of solid and liquid phases of the system involved,  $x$  – coordinate along the electrode depth.

Having transformed the Eq.(1), we shall receive the following system of differential equations for the stationary case:

$$\frac{\partial(\chi \frac{dU}{dx})}{\partial x} + vF \sum_i z_i \frac{\partial C_i}{\partial x} + \frac{\partial v}{\partial x} F \sum_i z_i C_i = 0, \quad (4)$$

$$|v| \frac{\partial C_i}{\partial n} = -\frac{S}{z_i F} J_{Si}. \quad (5)$$

Here  $J_{Si}$  (A/cm<sup>2</sup>) – polarizing current density with regard to the  $i$ -th component,  $n$  – direction of electrolyte movement,  $\chi$  (Ω/cm) – a value specifying the electroconducting properties of the system.

The system of Eqs.(4) and (5) can be completed with the polarization kinetic equations [11, 12], linking the values of current densities and potentials at the point  $x$ :

$$J_{Si}(x) = j_{0i} \frac{\exp\left(\frac{\alpha_i z_i F((U - \varphi_{Ri}) / RT)}{RT}\right) - \exp\left(\frac{(\alpha_i - 1) z_i F(U - \varphi_{Ri}) / RT}{RT}\right)}{1 + j_{0i} \frac{\exp(\alpha_i z_i F(U - \varphi_{Ri}) / RT) / z_i F K_{mi} C_i}{z_i F K_{mi} C_i}}, \quad (6)$$

(where  $\alpha_i$  – reductive symmetry factor,  $\varphi_{Ri}$  – equilibrium compromise potential,  $K_{mi}$  – mass transfer coefficient,  $R=8.31$  J/molK – universal gas constant), with the initial and boundary conditions applied to the unknown functions:

$$\frac{\partial U}{\partial x}(0) = I \cdot \rho_S; \quad \frac{\partial U}{\partial x}(L) = -I \cdot \rho_L; \quad C_i(0) = C_{i,0}. \quad (7)$$

Here  $I$  (A/cm<sup>2</sup>) – overall current density, passing through the electrode,  $L$  – depth of FTE.

It is to be noted that the Eq.(5) for the concentration of the second electroactive component (Fe<sup>+2</sup>) of the studied system Fe(III)/Fe(II)/Fe should be essentially converted, as soon as due to the electrode reaction Fe<sup>+3</sup>→Fe<sup>+2</sup>, the concentration of bivalent iron in the electrolyte will be changed with time.

In the studied case of electrolysis running on FTE, the direction of electrolyte flow coincides with the direction of current density distribution –  $x$ , therefore, the Eq.(5) can be written in the form:

$$|v| \frac{dC_i}{dx} = -\frac{S}{z_i F} J_{Si}.$$

To calculate the changes in the concentration of the first component of electrode reaction (Fe<sup>+3</sup>), the expression can be written:

$$|v| dC_1 = -\frac{S}{z_1 F} J_{S1} dx$$

or, in the final difference form:

$$\Delta C_1(x_i) = -\frac{S}{|v|z_1 F} J_{S1} \Delta x_i.$$

Apparently, the negative increment of trivalent iron concentration at the electrode point  $x_i$  is equal to the increment of bivalent iron concentration at the same point. Therefore, the differential equation for the bivalent iron concentration from the group (5) can be written in the following form:

$$\Delta C_2(x_i) = \left( \frac{S}{|v|z_1 F} J_{S1} + \frac{S}{|v|z_2 F} J_{S2} \right) \Delta x_i.$$

In this case the Eq.(5), modeling the  $Fe^{+2}$  concentration distribution on the FTE, will take the following form:

$$|v| \frac{dC_2}{dx} = \frac{S}{F} \left( \frac{J_{S1}}{z_1} + \frac{J_{S2}}{z_2} \right).$$

The system of Eqs. (4)–(7) is enclosed with regard to the unknown functions  $U(t,x)$ ,  $C_i(t,x)$ , which can be solved by the method described in the work [13], using the algorithms of the distribution calculation of the electrochemical parameters of process and electrode, changing during the electrolysis, specifically, electrode electroconductivity, specific reaction surface, porosity of CFM, solution flow velocity etc. [7,14]. However, during the numerical realization of this model, the essential difficulties appear, connected with the determination of the compromise potentials  $\varphi_{Ri}$  and mass transfer coefficients  $K_{mi}$ .

In this connection, to perform the calculations, we have chosen the values of the equilibrium compromise potentials  $\varphi_{Ri}$  from the reference literature available [15] and then have defined them more exactly using the method described in the work [16]. Such approach did not cause any difficulties, as the procedure of values  $\varphi_{Ri}$  specifying was not resulted in the values which were drastically different from those given in the literature [15].

The essential differences in the calculations results from the experimental data were observed while using the equations of polarization characteristics (6) under the insignificant (within 10%) changes in  $K_{mi}$  values.

The exact calculation of mass transfer coefficients is complicated, as the appropriate formula:

$$K_{mi}(x,t) = \frac{a_i \left( \frac{\rho m}{V} \right)^b}{\left( \rho \varepsilon_0 - M(x,t) \right)^b}, \tag{8}$$

contains  $a_i$ ,  $b_i$  – constants reflecting the properties of electrode, electrolyte and hydrodynamic properties of the process, which can be modified within the broad enough limits:  $10^{-3} \leq a_i \leq 1.9 \cdot 10^{-2}$ ,  $0.33 \leq b_i \leq 0.71$  [17-21]. In the formula (8)  $\rho$  denotes the density of metal deposit,  $M(x,t)$  is the amount of the deposited metal within the layer of solitary section in the point  $x$  at the time moment  $t$ .

It is naturally to suppose that with the sufficient values of the electrolyte's flow velocity, close to those, really used in practice ( $0.1 \leq |v| \leq 1$ ), the diffusion component of substance transfer towards the carbon-graphite fibers of CFM electrode will be less significant, than the convection component. This makes it possible to apply the approach, implying the determination of the type of polarization dependence, considering the process hydrodynamics. So, the transfer of  $i$ -th electroactive substance within the elementary volume, identified with the point  $(x)$  of homogeneous space (Figure 2) is described with the Eq. (9) [13]:

$$\Delta c_i = Pe_i \cdot (v \cdot \text{div}) c_i, \tag{9}$$

here  $\Delta$  – Laplace operator,  $Pe_i$  – Peclet number for  $i$ -th electroactive component.

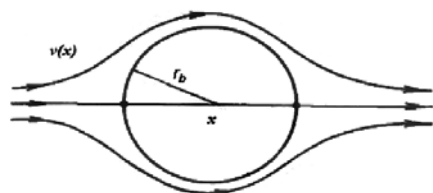


Figure 2. The scheme of the elementary volume of FTE, in which the electrolyte flows round the cylindrical CFM thread, having  $R_b$  radius.

At a rough approximation, the Eq.(9) has the following form:

$$\frac{\partial^2 c_i}{\partial w^2} + Pe_i \frac{\partial c_i}{\partial w} = 0, \tag{10}$$

where  $w$  – linear coordinate within the chosen elementary volume,  $c_i(w) = \frac{C_{ix} - C_i}{C_{ix}}$ ;  $Pe_i = \frac{r v}{D_i}$ ;  $C_{ix}$  – concentration of  $i$ -th component in the point of FTE, which is identified with the selected elementary volume of porous space – point  $x$  on the electrode with the depth  $L$ ,  $0 \leq x \leq L$ ,  $r_b$ - radius of carbon-graphite thread.

The Eq.(10) is complemented with the condition of  $C_i$  concentration change on the surface of CFM fiber, i.e. under  $w=0$  the following equation is applied:

$$\frac{\partial c_i}{\partial w} = -k_{iS} f_{iS}(c_i). \tag{11}$$

Coefficient  $k_{iS}$  corresponds to the rate constant of the  $i$ -th surface electrochemical reaction, and  $k_{iS} f_{iS}(c_i)$  – are the dimensionless functions corresponding to the rate of the  $i$ -th surface electrochemical reaction, which in the dimensionless form are given by the following formula:

$$k_{iS} = \frac{r_b j_{i0} (e^{M_{i1}} - e^{M_{i2}})}{z_i F D_i C_{ix}}$$

$$M_{i1} = \frac{\alpha_i z_i F (E(x) - E_i^p(x))}{RT}$$

$$M_{i2} = \frac{(1 - \alpha_i) z_i F (E(x) - E_i^p(x))}{RT}$$

$$F(c_i(w)) = j_{i0} \left[ \frac{c_i(w)}{C_{ix}} e^{M_{i1}} - e^{M_{i2}} \right];$$

$$F(C_{ix}) = j_{i0} \left[ e^{M_{i1}} - e^{M_{i2}} \right];$$

$$f_{iS}(c_i) = \frac{F(c_i(w))}{F(C_{ix})}$$

The solving of the Eq.(10), on condition (11), has the following form:

$$c_i = A_i e^{-Pe_i \cdot w}, \tag{12}$$

with  $A_i$  equal to:

$$A_i = \frac{\frac{r_b}{z_i F D_i C_{ix}} \left[ e^{M_{i1}} - e^{M_{i2}} \right]}{Pe_i + e^{M_{i1}} \frac{r_b}{z_i F D_i C_{ix}}}. \tag{13}$$

Substituting all the values determined into the well-known expression for the polarization curve [5]:

$$j_i(x) = \frac{j_{i0} [e^{M_{i1}} - e^{M_{i2}}]}{1 + j_{i0} e^{M_{i1}} / j_{i,lim}}$$

we shall receive the equation:

$$j_i(x) = \frac{j_{i0} [e^{M_{i1}} - e^{M_{i2}}]}{1 + j_{i0} e^{M_{i1}} / z_i F C_i(x) v(x)} \quad (14)$$

where  $j_i(x)$  – current density of the  $i$ -th reaction in the electrode point  $x$ ,  
 $j_{i0}$  – exchange current density of  $i$ -th reaction,  
 $j_i$  – polarizing current density,  
 $z_i$  – charge of the  $i$ -th electroactive component ( $i=1, \dots, 4$ ),  
 $F$  – Faraday's number ( $\text{C mol}^{-1}$ ),  
 $D$  – diffusion coefficient,  $\text{cm}^2/\text{s}$ ,  
 $C_i(x)$  – concentration of  $i$ -th electroactive component ( $i=1, \dots, 4$ ) in the point  $x$  of pseudo-homogeneous space,  
 $v(x)$  – velocity vector of convection transfer of electrolyte along the axes, or the linear velocity of electrolyte flow,  
 $r_a$  – degree of substance transformation.

The Eq. (14) can be written in another form, if we consider the value  $j_{i,\text{lim}}(x) = \frac{z_i F D_i C_{ix}}{r_a}$ , which in the first approximation reflects the value of the limited diffusion current:

$$j_i(x) = \frac{Pe_i j_{i0} \left[ e^{M_{i1}} - e^{M_{i2}} \right]}{Pe_i + j_{i0} e^{M_{i1}} / j_{i,\text{lim}}(x)} \quad (15)$$

In this way, the Eq. (14) contains easily determinable dynamic parameters, such as the diffusion coefficient, thickness of the diffusion layer, etc., explicitly described by us earlier in [7, 14]. This equation was used for carrying out the numerical calculations.

### Numerical calculations of electrolysis on FTE and the discussion of results

As it was already mentioned, the electrochemical processes occurring within the flow-through three-dimensional electrodes (FTE) made of the carbon-graphite fibrous materials (CFM) during the electroreduction of Fe(III) to Fe(II) and Fe(II) to metal phase ( $\text{Fe}^0$ ), are accompanied with the secondary electrochemical reactions with the involvement of hydrogen ions and molecular oxygen. Therefore, such electrochemical system should be regarded as a polycomponent one, which fluid phase contains four components that can be involved in the electrode reactions:  $\text{Fe}^{+3}$ ,  $\text{Fe}^{+2}$ ,  $\text{H}^+$ ,  $\text{O}_2$  [22].

To perform the numerical calculations in accordance with the mathematical model proposed, one needs to know the values of certain physical and kinetic parameters, characterizing the studied system, in which the following reactions can take place:  $\text{Fe(III)} \xrightarrow{+e} \text{Fe(II)}$ ;  $\text{Fe(II)} \xrightarrow{+2e} \text{Fe}^0$ ;  $2\text{H}^+ \xrightarrow{+2e} \text{H}_2$ ;  $\text{O}_2 \xrightarrow{2e+2\text{H}^+} \text{H}_2\text{O}_2$ ;  $\text{H}_2\text{O}_2 \xrightarrow{2e+2\text{H}^+} 2\text{H}_2\text{O}$ .

The initial values of electrochemical parameters of studied processes were taken from the reference literature [15]. The values of the main parameters and constants used for the numerical calculations are summarized in the Table 1.

Table 1

**Kinetic parameters used for the numerical calculations of electrochemical processes taking place during the electrolysis of iron-containing electrolyte.**

Electrode reaction	Reaction parameter, FTE				
	$C_0$	$D$	$j_0$	$\alpha$	$E_p$
$\text{Fe(III)} \rightarrow \text{Fe(II)}$	$0.5 \cdot 10^{-4}$	$0.5 \cdot 10^{-5}$	$0.1 \cdot 10^{-3}$	0.5	0.6
$\text{Fe(II)} \rightarrow \text{Fe}$	$0.5 \cdot 10^{-3}$	$0.6 \cdot 10^{-5}$	$0.1 \cdot 10^{-5}$	0.43	0.5
$2\text{H}^+ \rightarrow \text{H}_2$	–	–	$0.1 \cdot 10^{-5}$	0.5	0.5
$\text{O}_{\text{ads}} + 2\text{H}^+ + 2e \rightarrow \text{H}_2\text{O}$	$0.2 \cdot 10^{-4}$	$0.3 \cdot 10^{-5}$	$0.1 \cdot 10^{-7}$	0.4	0.8

The process parameters given above, served as a basis for carrying out the computer calculations in accordance with the program elaborated. The results were obtained in a numerical form, and on their base the diagrams were drawn reflecting the regularities of the electrolysis processes on the CFM. Further on, the calculated values were compared with the experimental data with the scope to estimate their convergence.

In Figures 3-7 the diagrams are presented of the main electrochemical functions distribution within the depth of the FTE for the different values of governing parameters: overall current density  $J$  (A/cm<sup>2</sup>) and input linear flow rate of electrolyte  $u$  (cm/s), obtained as a result of the numeric calculations.

The analysis of data obtained, presented in Figures 3-7, testifies that with the increase in the electrolyte flow velocity, all the electrochemical reactions studied are shifted to the front side of the FTE (nearest to the counter-electrode). This is the best pronounced under the high densities of the overall current and is insignificant under the low current densities.

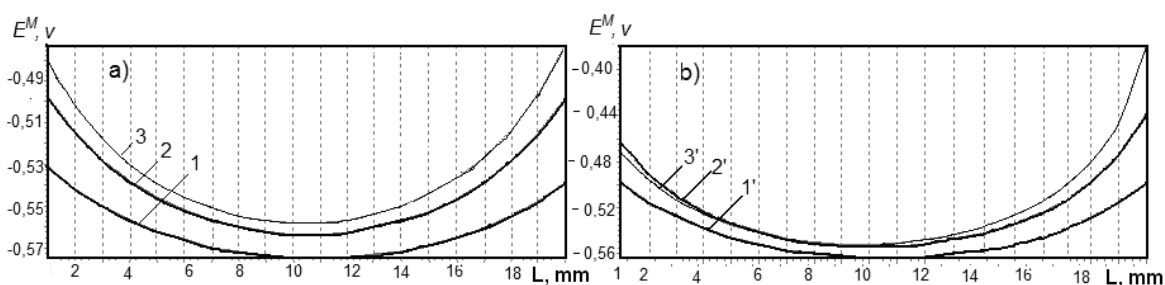


**Figure 3. Potential distribution within the depth of FTE under the different densities of overall current and the electrolyte flow velocity: a) – 0.5 cm/s; b) – 1 cm/s. Current densities, A/cm<sup>2</sup>: 1 – 0.05, 2 – 0.1, 3 – 0.15; 1' – 0.1, 2' – 0.25, 3' – 0.6.**

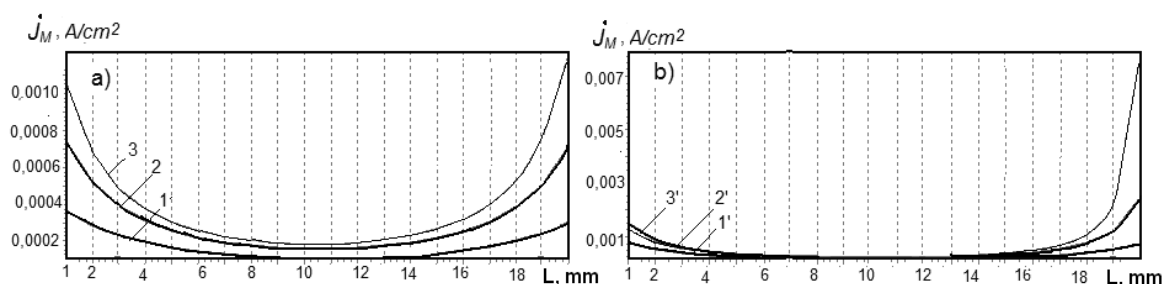


**Figure 4. Current density distribution of the reaction Fe(III) → Fe(II) within the FTE under the different densities of overall current and the electrolyte flow velocity: a) – 0.5 cm/s; b) – 1 cm/s. Current densities, A/cm<sup>2</sup>: 1 – 0.06, 2 – 0.1, 3 – 0.15; 1' – 0.1, 2' – 0.26, 3' – 0.5.**

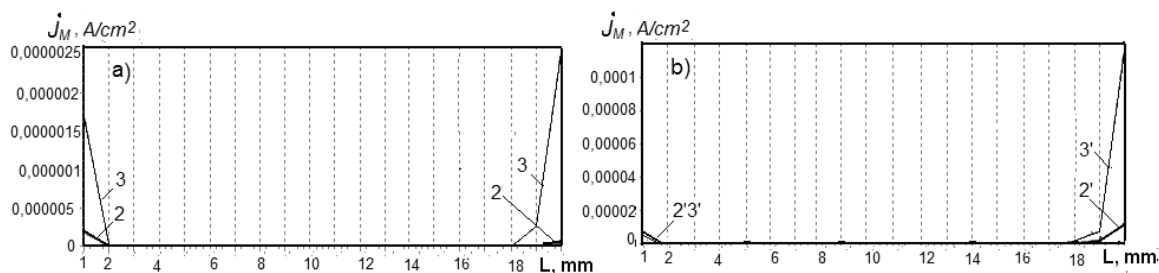


**Figure 5. Current density distribution of the reaction Fe(II) → Fe within the FTE under the different densities of overall current and the electrolyte flow velocity: a) – 0.5 cm/s; b) – 1 cm/s. Current densities, A/cm<sup>2</sup>: 2 – 0.1, 3 – 0.15; 2' – 0.25, 3' – 0.6.**

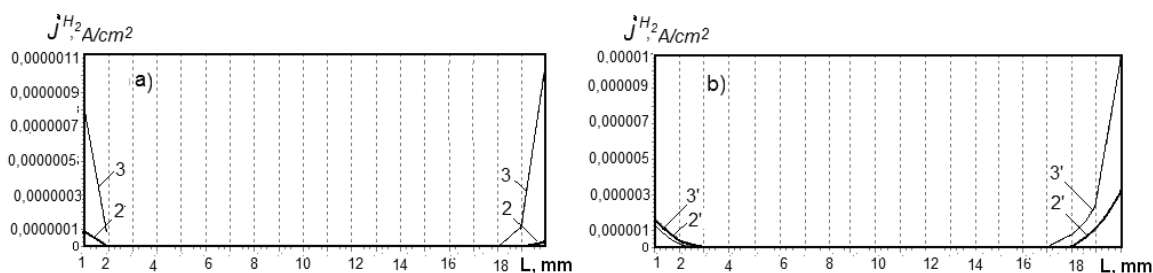


**Figure 6. Current density distribution of the reaction  $2\text{H}^+ \rightarrow \text{H}_2$  within the FTE under the different densities of overall current and the electrolyte flow velocity: a) – 0.5 cm/s; b) – 1 cm/s. Current densities, A/cm<sup>2</sup>: 2 – 0.1, 3 – 0.15; 2' – 0.25, 3' – 0.6.**

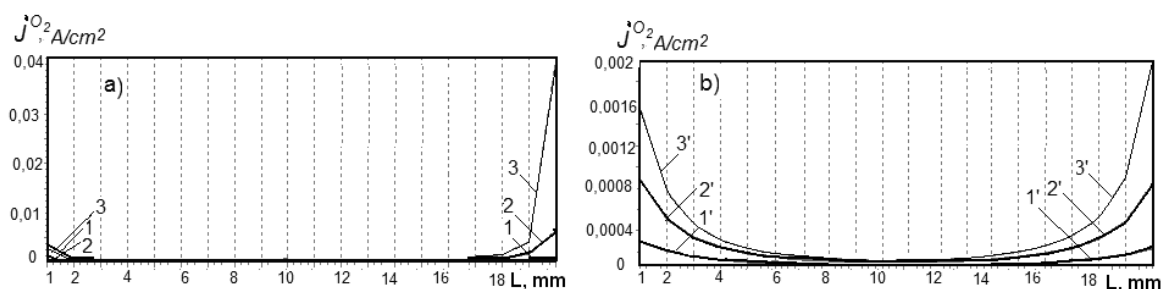


**Figure 7. Current density distribution of the molecular oxygen reduction within the FTE under the different densities of overall current and the electrolyte flow velocity: a) – 0.5 cm/s; b) – 1 cm/s. Current densities, A/cm<sup>2</sup>: 1 – 0.5, 2 – 0.1, 3 – 0.15; 1' – 0.1, 2' – 0.25, 3' – 0.6.**

For all the used values of the overall current density, the increase of the electrolyte flow velocity causes the increase in the FTE polarization within the entire depth. Thus, under the high values of the electrolyte flow velocity the approaching occurs of the potential distributions for various overall current densities. The distribution of the process  $\text{Fe(III)} \rightarrow \text{Fe(II)}$  intensity within the electrode thickness (Figure 4) is more uniform under the high values of electrolyte flow velocity and the average values of the overall current density.

Under the high values of the overall current density and the solution flow velocity, the processes  $\text{Fe(II)} \rightarrow \text{Fe}$  and  $2\text{H}^+ \rightarrow \text{H}_2$  are localized on the front side of the electrode. Under the less flow velocity, both processes take place both on the front and back side of the FTE. It is to be noted, that under the current densities less than 0.1 A/cm<sup>2</sup>, the processes of bivalent iron reducing to metal and hydrogen emission do not occur.

The partial current density of oxygen reduction reaction is practically symmetrically distributed within the thickness of FTE under the electrolyte flow velocity, equal or less than 0.5 cm/s and almost completely is shifted to the frontal side under the flow velocity, equal to or higher than 1 cm/s.

Generally, the distribution of electrochemical functions – potential and partial current densities within the electrode depth, is in line with the results of theoretical studies of the processes within the three-dimensional flow-through electrodes [23-26], which indirectly confirms the workability/efficiency of the mathematical model applied.

## Conclusions

The application of the mathematical model considered allows to study the cathode reactions connected with the regeneration of the iron plating solutions due to the reaction  $\text{Fe(III)} \rightarrow \text{Fe(II)}$ , within the flow-through three-dimensional electrode. The target reaction is accompanied by the parallel reactions of metal iron deposition, reduction of hydrogen ions and the molecular oxygen.

## References

1. Petrov, Yu.N. Effect of electrolysis conditions on iron coatings properties. Tadjikizdat: Dushanbe, 1957, 156 p. (in Russian).
2. Varentsov, V.K.; Covaliova, O.V. Application of carbonic fibrous materials for the reduction of “oxidized” plating iron solutions. Surface Engineering and Applied Electrochemistry. 1988, pp. 55-58 (in Russian).
3. Beck, R.Yu. Perspectives of application of the electrodes with extended surface in hydrometallurgy. Proceedings of Siberian Branch of Academy Sciences USSR, Chemical Series, 1977, 4(6), pp. 11-20 (in Russian).



4. Covaliova, O.V.; Varentsov, V.K. The study of the reduction of rapidly oxidizing iron plating electrolytes on the carbonic fibrous electrodes. Proceedings of Academy of Sciences MSSR, Physico-Technical and Mathematical Series, 1987, 3, pp. 33-37 (in Russian).
5. Damaskin, B.B.; Petrii, O.A. Introduction in Electrochemical Kinetics. Vyschaia Shkola: Moscow. 1975, 275 p. (in Russian).
6. Varentsov, V.K.; Koshev, A.N. Mathematical modeling of electrochemical processes in flow-through three-dimensional electrodes. Proceedings of Siberian Branch of Academy Sciences USSR, Chemical Series, 1988, 17, pp. 117-125 (in Russian).
7. Koshev, A.N.; Varentsov, V.K.; Chirkina, M.A.; Kamburg, V.G. Mathematical modeling and the theory of polarization distribution in the electrochemical reactors with flow-through three-dimensional cathodes. Mathematical Modeling, 2011, 23(8), pp. 110-126 (in Russian).
8. Koshev, A.N.; Kuzina, V.V. Elaboration and study of mathematical models on non-stationary processes in electrochemical reactors with flow-through three-dimensional electrodes. PSUAC: Penza. 2011, 119 p. (in Russian).
9. Newman, J. Electrochemical Systems. Mir: Moscow. 1977, 463 p. (in Russian).
10. Alkire, R.; Gould, R. Analysis of multiple reaction sequences in flow-through porous electrodes. Journal of the Electrochemical Society, 1976, 123(11), pp. 1842-1849.
11. Daniel-Beck, V.S. On the polarization of porous electrodes. 4. Effect of the solid phase resistance on the potential and current distribution in the electrode. Electrochemistry, 1966, 2(6), pp. 672-677 (in Russian).
12. Saleh, M.M. Mathematical modeling of gas evolving flow-through porous electrodes. Electrochimica Acta, 1999, 45(6), pp. 959-967.
13. Frumkin, A.N. On the distribution of corrosion process along the pipe length. Journal of Physical Chemistry, 1949, 23, pp. 1477-1482 (in Russian).
14. Kohshev, A.N.; Chirkina, M.A.; Varentsov, V.K. Non-stationary mathematical models of electrochemical processes in the reactors with the flow-through three-dimensional electrodes. Electrochemistry, 2007, 43(11), pp. 1372-1378 (in Russian).
15. Sukhotin A.M. Ed. Reference Book on Electrochemistry. Chemistry: Leningrad. 1981, 488 p. (in Russian).
16. Beck, R.Yu.; Zamyatin, A.P. Mass-transfer coefficient and surface of the flow-through fibrous electrodes, available for electrolysis. Electrochemistry, 1978, 14(18), pp. 1196-1201 (in Russian).
17. Newman, J.S. Tobias, C.W. Theoretical analysis of current distribution in porous electrodes. Journal of Electrochemical Society, 1962, 109, pp. 1183-1191.
18. Schmal, O., Ercel, J., Van Puin, P. Mass transfer at carbon fibrous electrodes. Journal of Applied Electrochemistry, 1986, 16, pp. 422-430.
19. Beck, R.Yu.; Zamyatin, A.P.; Koshev, A.N.; Poddubny, N.P. Mathematical modeling of the electrolytic deposition of metal within the pores of the flow-through three-dimensional electrode. Proceedings of Siberian Branch of Academy Sciences USSR, Chemical Series, 1980, 1(2), pp. 110-125 (in Russian).
20. Doherty, T.; Sunderland, J.G.; Roberts, P.L.; Pickett, D.J. An improved model of potential and current distribution within a flow-through porous electrode. Electrochimica Acta, 1996, 41(4), pp. 519-526.
21. Kuzina, V.V.; Zamyatin, A.P.; Koshev, A.N. Mathematical models in the tasks of voltammetric analysis. Ecological systems and equipment. Nauchtechlytizat: Moscow. 2006, 8, pp. 37-41 (in Russian).
22. Covaliova, O.V. The study of kinetic regularities of Fe(III) ions reduction to Fe(II) in concentrated electrolytes. Studia Universitatis, Natural Sciences Series, 2013, 6(26), pp. 195-203 (in Russian).
23. Varentsov, V.K.; Jerebilov, A.F.; Malei, M.D. Carbonic graphite fibrous materials – new electrodes for metals extraction from the diluted solutions. 1. Nonwoven carbonic graphite fibrous materials. Proceedings of Siberian Branch of Academy Sciences USSR, Chemical Series, 1984, 17(6), pp. 120-127 (in Russian).
24. Koshev, A.N.; Kuzina, V.V. Modeling and calculation of the electroactive component concentration during the electrolysis. Management of Large Systems, IPU RAN: Moscow. 2011, vol. 33, pp. 233-253 (in Russian).
25. Maslyi, A.I.; Poddubny, N.P.; Medvedev, A.J. The dynamics of metal deposition on the porous electrode with the low initial conductivity under the direct-flow regime of electrode operation and high rate of solution flow. Electrochemistry, 2006, 42(10), pp. 1237-1244 (in Russian).
26. Koshev, A.N.; Gleizer, G.N.; Varentsov, V.K. On the gas formation effect in the pores of flow-through cathode on the electroconductivity of electrolyte. Electrochemistry, 1992, 28(8), pp. 1160-1170 (in Russian).

## APPLICATION OF FLOW-THROUGH THREE-DIMENSIONAL ELECTRODES FOR REGENERATION OF PLATING IRON ELECTROLYTES: 2. STUDY OF PROCESS REGULARITIES BY MATHEMATICAL MODELING

Olga Covaliova<sup>a\*</sup>, Alexandr Koshev<sup>b</sup>, Valery Varentsov<sup>c</sup>

<sup>a</sup>State University of Moldova, Research Center of Applied and Ecological Chemistry, 60, A. Mateevici str., Chisinau MD 2009, Republic of Moldova

<sup>b</sup>Penza State University of Architecture and Construction, 28, G. Titova str., Penza 440028, Russian Federation

<sup>c</sup>Institute of Solid and Mechanochemistry of the Siberian Branch of RAS, 18, Kutateladze str., Novosibirsk 630128, Russian Federation

\*e-mail: covaleva.olga@yahoo.com; phone / fax: (+373 22) 57 75 56

**Abstract.** The main regularities of the electroactive components distribution, polarization and local current density within the depth of the three-dimensional flow-through electrode have been studied using the calculation method, in dependence on the overall current density, electrode thickness and degree of its compression, solution flow velocity through the electrode, initial concentration of Fe(III) ions in the solution and electrodes brand.

**Keywords:** three-dimensional flow-through electrode, mathematical modeling, numerical calculations, polarization, local current density.

### Introduction

Mathematical modeling [1,2] is one of the efficient methods allowing to research the regularities of the flow-through three-dimensional electrodes operation, including those made of the carbon fibrous materials (CFM). It makes it possible to study the processes occurring within the bulk such electrodes. In addition, this method offers a possibility to predict the effect of the main technological parameters on the studied process and to optimize the electrolysis conditions.

The mathematical model is based on the solution of the system of equations [3], which describe the distribution of the reacting substances concentration, polarization and current inside the pores of the three-dimensional electrode, and involve a series of parameters, which are partly known from the literature data (reaction equilibrium potentials, mass-transfer and diffusion coefficients, amount of electrons transmitted during the reaction). Another part of parameters, among which the characteristics of CFM electrodes, their reaction surface, porosity [4,5] can be determined by the experimental methods.

The analytical resolving of the differential equations system is usually difficult and is limited by consideration of some particular cases only. Therefore, in our research the numerical computational calculations were carried out, which results made it possible to reveal the regularities of the processes running within the bulk of carbon fibrous electrodes (CFE) during the electrochemical regeneration of iron plating solutions.

### Method and conditions of the numerical calculations at the modeling of electrolysis on CFE

During the occurrence of the processes on CFE, the principal mass and charge transfer takes place by the forced convection, when the diffusion and natural convection are negligibly low. Then, according to the mathematical description given in [6], the process of  $n$  components reduction within the bulk of porous electrode is described by the following Eq.:

$$j_i(X) = \frac{j_{i0} [e^{M_{i1}} - e^{M_{i2}}]}{1 + \frac{j_{i0} e^{M_{i1}}}{z_i F C_i(x) v(x)}}, \quad (1)$$

where  $j_{i0}$  – exchange current density;  $j_i$  – polarizing current density;  $z_i$  – charge of  $i$ -th electroactive component ( $i=1, \dots, 4$ );  $F$  – Faraday's number,  $C \text{ mol}^{-1}$ ;  $D$  – diffusion coefficient,  $\text{cm}^2/\text{s}$ ;  $C_i(x)$  – concentration of  $i$ -th electroactive component ( $i=1, \dots, 4$ );  $v(x)$  – velocity vector of the convection transfer of electrolyte along the axes or linear velocity of electrolyte flow,

$$M_{i1} = \frac{\alpha_i z_i F (E(x) - E_{ip}(x))}{RT} \quad \text{and}$$
$$M_{i2} = \frac{(1 - \alpha_i) z_i F (E(x) - E_{ip}(x))}{RT}$$

Here  $E(x)$  and  $E_{ip}(x)$  is a potential and equilibrium potential for  $i$ -th component in a point "x", accordingly.

Eq.(1) can be presented in another form, once the value  $j_{i,\text{lim}}(x) = \frac{z_i F D C_{ix}}{r_e}$  is introduced in consideration, which in the first approximation reflects the value of limited diffusion density:

$$j_i(x) = \frac{Pe_i j_0 [e^{M_{i1}} - e^{M_{i2}}]}{Pe_i + j_{i0} e^{M_{i1}} / j_{i,\text{lim}}(x)} \quad (2)$$

where  $Pe_i$  – Peclet number for  $i$ -th electroactive component.

As it was mentioned earlier, to perform the numerical calculations according to the mathematical model involved, it is necessary to know the values of certain physical and kinetic factors, characterizing the studied system, in which the following reactions can take place:  $\text{Fe(III)} \xrightarrow{+e} \text{Fe(II)}$ ;  $\text{Fe(II)} \xrightarrow{+2e} \text{Fe}^0$ ;  $2\text{H}^+ \rightarrow \text{H}_2$ .

The calculations were performed with regard to the electrolyte, broadly used in practical applications, containing Fe(II) ions ( $0.5 \cdot 10^{-3}$  mol/L) and Fe(III) ions ( $0.5 \cdot 10^{-4}$  mol/L). The measured value of the solution electroconductivity made  $c_1 = 0.14$   $\Omega/\text{cm}$ . As cathodes, the CFM types VINN-250 (ВИНН-250), NTM-100 (HTM-100), NTM-200 (HTM-200), VVP-66-95 (BBП-66-95), KNM (KHM), VNG-50 (BHГ-50), TGN (TГH) and TVS (TBIII) were used, for which the known parameters were taken: specific reaction surface ( $S_v$ ,  $\text{cm}^2/\text{cm}^3$ ), electrode electroconductivity ( $c$ ,  $\Omega/\text{cm}$ ) and electrode material porosity ( $\hat{I}$ ) [5,6], and their change with the 2-fold compression was taken in consideration. Such parameters as current density ( $j$ ,  $\text{A}/\text{cm}^2$ ) and linear flow velocity ( $u$ ,  $\text{cm}/\text{s}$ ) were varied within the defined limits for obtaining of the appropriate dependencies.

For the reaction  $\text{Fe(III)} \xrightarrow{+e} \text{Fe(II)}$  the diffusion coefficient  $D^{\text{Fe(II)}}$  and exchange current  $j_0$  of Fe(II) ions determined from the data of our polarization studies [7, 8], made, accordingly,  $0.535 \cdot 10^{-5}$   $\text{cm}/\text{s}$  and  $0.019$   $\text{A}/\text{cm}^2$ . According to the same studies results, the stationery potential of the reaction considered makes  $E^{\text{Fe(III)}} = +0.643$  V. The amount of electrons during the transfer of Fe(III) into Fe(II) is 1, and the transfer coefficient of Fe(III) ions, according to [9], is equal to 0.59.

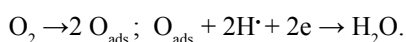
For the reaction of metal iron reducing  $\text{Fe(II)} \xrightarrow{+2e} \text{Fe}^0$ , the kinetic parameters are:  $D^{\text{Fe(II)}} = 0.6 \cdot 10^{-5}$   $\text{cm}/\text{s}$  [9];  $\alpha^{\text{Fe(II)}} = 0.43$  [9];  $z^{\text{Fe(II)}} = 2$ . The value of stationery potential  $E^{\text{Fe(II)}} = -0.620$  V was determined during the polarization studies on the graphite surface [7]. As to the exchange current of Fe(II) ions ( $j_0^{\text{Fe(II)}}$ ), for the process limited by the charge transfer stage it was necessary to consider the increase of its value, due to the high CFE surface with the fibers micro-roughness, with the coefficient equal to 100 [4]. Therefore, the value of  $j_0^{\text{Fe(II)}}$  taken from the literature data [10], was considered to be 2 orders higher and made  $1 \cdot 10^{-6}$   $\text{A}/\text{cm}^2$ .

For the third of possible reactions in the studied system – hydrogen emission, the kinetic parameters were taken as follows:  $E^{\text{H}_2}$ , according to the polarization studies on the graphite surface [7], made  $-0.83$  V; transfer coefficient was  $\alpha^{\text{H}_2} = 0.49$  [9]. The exchange current was calculated considering the aforementioned correction with regard to the data [10] and made  $j_0^{\text{H}_2} = 2 \cdot 10^{-6}$   $\text{A}/\text{cm}^2$ .

Therefore, the processes taken place on the CFE during the electrochemical regeneration of iron plating solution, are accompanied with the formation of the products in the ionic (Fe(II)) or gaseous state ( $\text{H}_2$ ). However, as it was shown [7], with the polarization increase, the electrode potential is shifted to the electronegative field, reaching the values, at which the metal iron is deposited.

It was earlier shown that the presence of oxygen, the reduction-oxidation system is formed in the iron electrolyte, which under the dynamic conditions causes the rapid oxidation of Fe(III) ions to Fe(II) [11]. Our polarization studies has shown [8], that the dependence the of limiting diffusion current value of the reaction  $\text{Fe(III)} \xrightarrow{+e} \text{Fe(II)}$  from the Fe(III) ions concentration is a straight line, which do not pass through the origin of coordinates, but clipping/cutting of a certain segment on the currents' axis, which may correspond to the current consumed for the reduction of oxygen. (Once the oxygen is removed from the electrolyte solution by the blowing of inert gas, the analogous straight line passes through the origin of coordinates). It is possible that a part of dissolved oxygen which did not react with Fe(III) ions, is involved in this reaction.

Thus, in our calculations we have considered possible electrochemical evolving of oxygen dissolved in water [12]. For the studied process it was supposed that the following electrode reaction with oxygen participation occurs, in which the intermediate product is the adsorbed oxygen atom:



The mechanism of this reaction was studied by A.N. Frumkin [13] with regard to the carbon electrodes, possessing high adsorption properties. For this reaction the kinetic parameters are as follows:  $E_p^{\text{O}_2} = 1.1$  V;  $j_0^{\text{O}_2} = 10^{-8}$   $\text{A}/\text{cm}^2$ ;  $z^{\text{O}_2} = 2$  [14]. Oxygen concentration was thus taken to be equal to its solubility in water ( $T=295$  K), which makes  $C_0^{\text{O}_2} = 2 \cdot 10^{-4}$  mol/L [14].

The calculations were made in the conditions of uniflow system, i.e. for the one-time pass of the treated solution through the electrode.

The results were received in the numerical form, and on their base the graphs have been created, reflecting the regularities of the electrolysis processes on CFE. Further, the calculated values were compared to the experimental data in order to estimate their convergence.

## The results of numerical calculations and their discussions

### Effect of current density

Current density is one of the main technological parameters which allow ensuring the high efficiency of electrochemical process on CFE. The data obtained by the calculation method (Figure 1) demonstrate that with the increase of the overall current density to 1000 A/m<sup>2</sup> the process rate increases sharply and then is stabilized on a certain level. At the same time, the current efficiency of the target reaction  $\text{Fe(III)} \xrightarrow{+e} \text{Fe(II)}$ , starting with these current densities, is decreasing. Such character of the dependencies indicates that equally with the target reaction, the secondary ones occur, resulting in the evolving of hydrogen and depositing of metal iron.

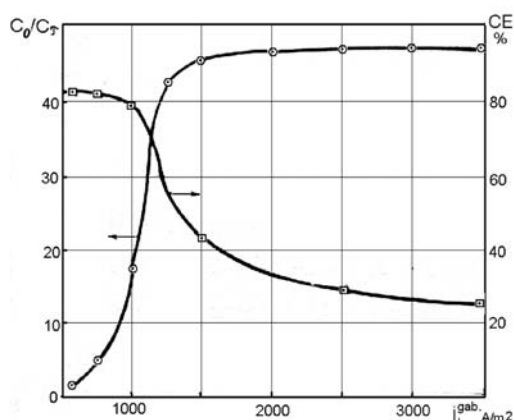


**Figure 1. Dependence of the rate of electrochemical reductions of Fe(III) ions to Fe(II) and current efficiency on the current density.**

**Conditions: electrode material VINN-250;  
S<sub>v</sub> = 560 cm<sup>2</sup>/g; ε = 0.925;**

**χ<sub>s</sub> = 0.4 Ω/cm; L = 0.1 cm; u = 0.1 mL/s;  
C<sub>initial</sub><sup>Fe(III)</sup> = 8.9 · 10<sup>-3</sup> mol/L.**

The work of CFE under the conditions of the solution flow is connected with the non-uniform distribution of the reacting substances concentration within the electrode depth that is testified by the data on Figure 2.

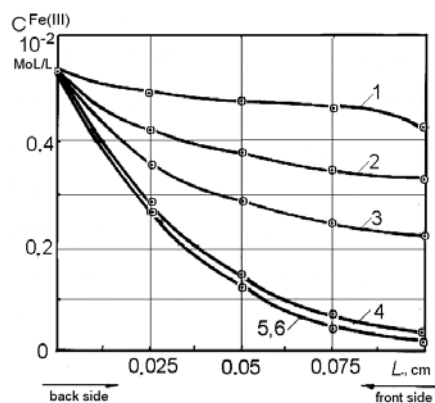


**Figure 2. Distribution of ions Fe(III) concentration along the depth of TDE in dependence on current density, A/m<sup>2</sup>:**

**1 – 200; 2 – 300; 3 – 500; 4 – 1000; 6 – 1500 and 2000, accordingly.**

**The conditions are the same as related to Figure 1.**

The polarization distribution of reaction  $\text{Fe(III)} \xrightarrow{+e} \text{Fe(II)}$  shown in Figure 3A demonstrates that under the low overall current densities for the low depth electrode, there is a uniform decrease in this value from the back side of the electrode towards the front one. With the increase in  $j_{\text{overall}}$  appears the polarization minimum, which shifts towards the front side. The calculations show that at the  $j_{\text{k}} \approx 1200 \text{ A/m}^2$  the limiting current is reached for the reaction  $\text{Fe(III)} \xrightarrow{+e} \text{Fe(II)}$ , hence, the subsequent increase of  $j_{\text{overall}}$  under the other equal conditions, will not provoke the increase in this reaction rate.

It was interesting to compare the given dependencies with the polarization distribution for the reaction  $\text{Fe(II)} \xrightarrow{+2e} \text{Fe}^0$ . It follows from the data of Figure 3B that, as well as for the previous case, the polarization distribution curve is characterized with maximum, which is however located closer to the back side of the electrode. The maximal polarization values are thus reached on the front side of it.

At the same time the distribution of the local current densities along the electrode depth was considered (Figure 4). For the reaction  $\text{Fe(III)} \xrightarrow{+e} \text{Fe(II)}$  these values on the back side of electrode surface were essentially higher than on the front one; this difference increases with the increase of the overall current density to 1000-1500 A/m<sup>2</sup>, remaining unchanged with its further increasing.

For the reaction  $\text{Fe(II)} \xrightarrow{+2e} \text{Fe}^0$  the highest values of the local current densities were characteristic for the front side of the electrode. Within the range  $j_k^{\text{overall}} = 1500\text{-}2000 \text{ A/m}^2$  this difference between the values of the current on the front and back side of the electrode is insignificant, but essentially increases with the increase of  $j_k^{\text{overall}}$  up to  $3000 \text{ A/m}^2$  and higher which corresponds to the conditions of the deposition of metal iron.

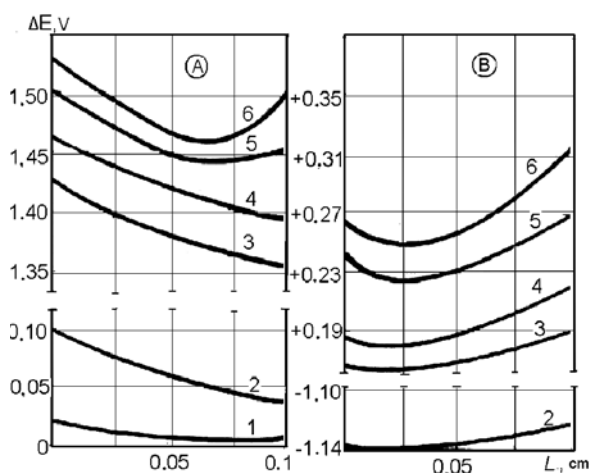


**Figure 3. Profiles of polarization distribution for the reactions  $\text{Fe(III)} \xrightarrow{+e} \text{Fe(II)}$  (A) and  $\text{Fe(II)} \xrightarrow{+2e} \text{Fe}^0$  (B) along the depth of TDE in dependence on current density,  $\text{A/m}^2$ : 1-300; 2-500; 3-700; 4-1000; 5-3000; 6-5000. The conditions are the same as related to Figure 1.**

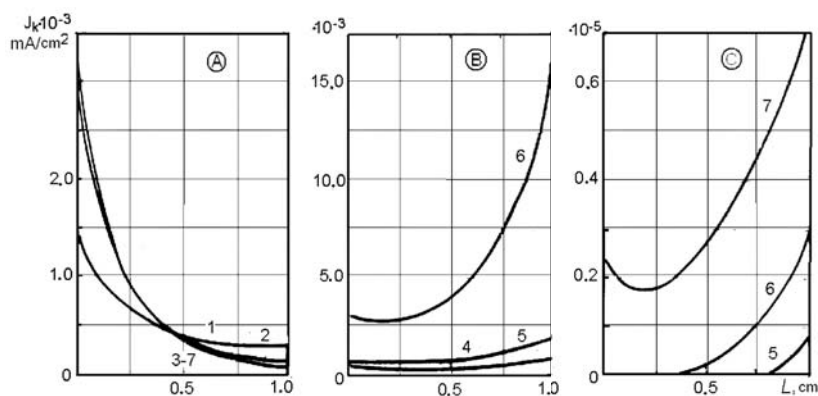


**Figure 4. Profiles of the local current densities distribution of the reactions  $\text{Fe(III)} \xrightarrow{+e} \text{Fe(II)}$  (A),  $\text{Fe(II)} \xrightarrow{+2e} \text{Fe}^0$  (B) and  $2\text{H}^+ + 2e \rightarrow \text{H}_2$  (C) along the TDE depth in dependence on the current densities,  $\text{A/m}^2$ : 1-500; 2-700; 3-1000; 4-1500; 5-2000; 6-3000; 7 - 5000. Conditions: electrode material VINN-250 (2-times compressed);  $S_v = 560 \text{ cm}^2/\text{g}$ ;  $\epsilon = 0.925$ ;  $\chi_s = 0.4 \text{ } \Omega/\text{cm}$ ;  $u = 0.1 \text{ mL/s}$ .**

As it was shown by calculations (Figure 4B), under  $j_k^{\text{overall}} \approx 2000 \text{ A/m}^2$  and higher under the selected conditions, the hydrogen emission begins, which causes the current consumption for this process. As for the case of the  $\text{Fe}^0$  deposition, the current density value is higher on the front side than on the back one, which indicates on the more intensive hydrogen emission on this side of the electrode.

#### **Effect of the electrode thickness and degree of its compression**

An important factor influencing the process efficiency on the CFE, is the high reaction surface. The increase of the total surface of these electrodes can be reached by two ways: increase of either their overall size or of their depth.

The second way is rational, as it makes it possible to develop the small-size equipment. However, the increase of the CFE depth has limitations connected with a number of factors, first of all, with the non-uniform distribution of the electrochemical process intensity within the electrode depth, which can be explained by the Ohmic losses. The maximal value of the electrochemical processes efficiency is determined by the electrode surface working under the conditions of the limiting diffusion current with regard to the ions of the main electroactive component [15].

Experimental study of the distribution of polarization, as well as substance concentration and local current densities along the CFE depth is difficult from the methodical point of view. However, there are publications in this field in which the experimental results are in agreement with the theoretical data obtained by calculations [16]. It can be concluded that the mathematical model can describe the real processes with certain reliability.

The dependence  $C_0/C_\tau$  from  $L$  obtained by calculations (Figure 5) testifies that the efficiency of Fe(III) ions reduction to Fe(II) increases with the electrode depth. Once the electrode depth values reach the value of  $L = 0.1-0.3$  cm,  $C_0/C_\tau$  remains constant. This regularity can be explained, knowing the distribution of the reacting ions concentration, current density and polarization within the porous electrode.

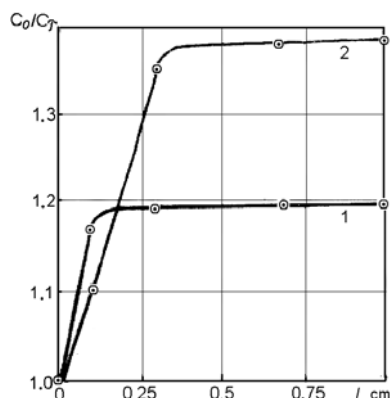


**Figure 5. Effect of the TDE depth on the change in  $C_0/C_\tau$  values in dependence on the overall current density,  $A/m^2$ : 1 – 500; 2 – 1000.**

**Conditions: electrode material VINN-250;**

$$u = 0.36 \text{ mL/s}; C_{initial}^{Fe(III)} = 8.9 \cdot 10^{-3} \text{ mol/L.}$$

At the low electrode thickness of 0.05 cm (Figure 6, curve 1), the polarization values on the back and front sides are almost the same, inside the electrode being the minimum of polarization. With the increase of  $L$ , the non-uniformity of  $\Delta E$  distribution is increased, but in all the cases the polarization on the front side is higher than on the back one. At the same time,  $\Delta E$  values at the internal part of electrode are reduced, approaching to zero. The higher  $L$  value, the higher part of the internal surface of electrode has the minimal  $\Delta E$  values, or absence of polarization. The latter fact testifies that there is no reaction of Fe(III) reaction running on this part of the electrode.

Further increase of the electrode thickness to 2 cm provokes the polarization shift inside the electropositive side, with the appearance of anodic zone (Figure 6, curve 5). Occurrence of the similar anodic zones is described in [17], where their formation is explained with the uniformity worsening of polarization distribution inside the electrode due to the Ohmic losses. In this case in the internal part of electrode the reverse process of Fe(II) ions oxidation to Fe(III) can be running. The calculation results obtained make it possible to suppose that the increase of the electrode thickness above some optimal value will result in the undesired processes, worsening the operation of CFE during the regeneration of iron plating electrolytes.

The curves of polarization distribution for the reaction  $Fe(II) \xrightarrow{+2e} Fe^0$  (Figure 6B) have the character similar to the appropriate curves for the reaction  $Fe(III) \xrightarrow{+e} Fe(II)$ . In follows from these data that under the low thicknesses of electrodes the probability of Fe(II) ions reduction to metal is increasing, especially on the front side of the electrode, where the polarization is higher.

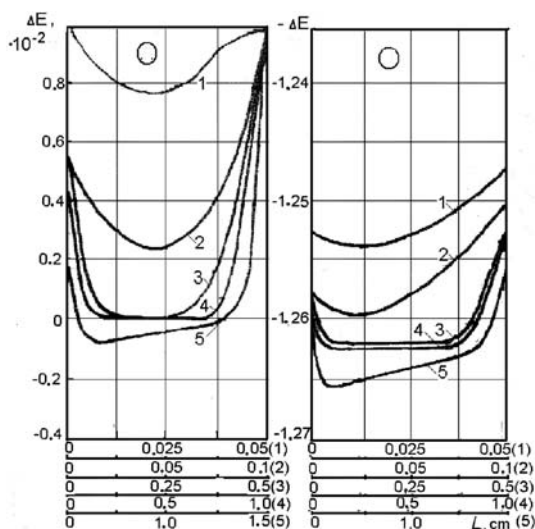


**Figure 6. Profiles of polarization distribution of the reactions  $Fe(III) \xrightarrow{+e} Fe(II)$  (A) and  $Fe(II) \xrightarrow{+2e} Fe^0$  (B) with the change of three-dimensional electrode depth (TDE), cm: 1-0.05; 2-0.1; 3-0.5; 4-1.0; 5-2.0.**

With the increase of  $L$  values, the polarization distribution for the reaction considered  $Fe(III) \xrightarrow{+e} Fe(II)$  becomes more non-uniform. The profiles of local current density distribution (Figure 7A) are also characterized with the essential decrease of these values in the depth of electrode with the increase of its thickness.

So, with the polarization and current density decrease inside the electrode, the part of its internal surface, on which the target reaction runs with the high sufficient rate, is decreasing with the increase of the electrode thickness.

This is confirmed with the data on Fe(III) ions concentration distribution inside the electrode (Figure 7B). It follows from the calculated dependencies that for the conditions selected by us, the maximal value of electrode thickness should not exceed 0.15-0.30 cm. However, in view of the fact that the kinetic and other parameters chosen for the calculations, can differ from the real values, it can be considered that for the practical scopes the electrode thickness can be increased to 0.6-0.9 cm, when its internal surface works intensively enough, or at least is not connected with the decrease in the process rate of Fe(III) ions reducing.

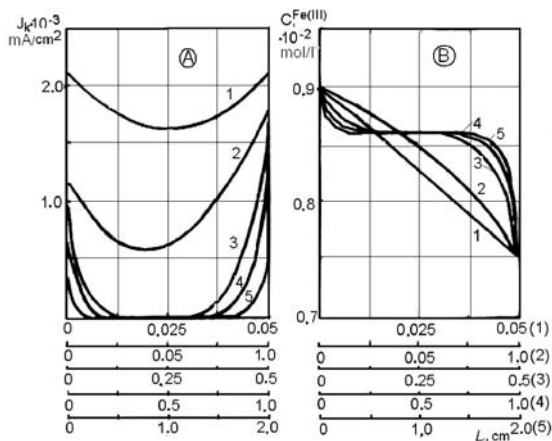


**Figure 7. Profiles of the local current densities distribution of the reactions  $\text{Fe(III)} \xrightarrow{+e} \text{Fe(II)}$  (A) and change in Fe(III) ions concentration (B) with the change in TDE depth, cm: 1-0.05; 2-0.1; 3-0.5; 4-1.0; 5-2.0.**

It was of specific interest to assess, with the help of the calculations by the mathematical model, the influence of CFE compression degree on studied process. It was found that the maximum process efficiency is reached when the CFE were 2.0-2.2 times compressed, and above this value the efficiency was decreased. At the 5-times compression, in spite of the appropriate increase in the reaction surface from 280 to 1400 cm<sup>2</sup>/g of the material VINN-250 and increase of its electroconductivity from 0.1 to 0.9 Ω/cm, the rate of the process  $\text{Fe(III)} \xrightarrow{+e} \text{Fe(II)}$  turned out to be even low, than for this material in the initial state. In this case the porosity of the material was decreased from 0.97 to 0.83.

With the increase of compression up to 2.0-2.2 times, the part of the internal surface, working efficiently enough, was decreased, and polarization in the depth of the electrode was reduced. The current density distribution is similar to the appropriate polarization changes. However, the values of polarization and current density on the back side are thus increased, which causes the acceleration of the target process under these conditions.

With the 3-times and more increase in the compression degree, the polarization distribution inside the electrode becomes more non-uniform, at the same time its values on the CFE sides are decreased. Correspondingly, the total electrode surface on which the target process runs with the sufficient rate is reduced.

In this way, the data obtained by calculation method, have shown that the optimal is 2-times compression of CFE, which ensures the highest rates of Fe(III) ions reduction to Fe(II).

### **Effect of the cathode material**

It is known from the literature [5,6], that the commercially produced carbonic-fibrous materials possess various properties, which may render the essential effects on the rates of electrochemical processes, including those running during the regeneration of iron-containing electrolytes. To compare the operation of electrodes made of various types of CFM, it is necessary to study the distribution of polarization, current and concentration within their body.

The results of the numerical calculations of concentration changes within the electrode body (Figure 8A) under the selected electrolysis conditions testify that the most uniformly the studied process runs when the TVS brand of CFM was used. For the other materials the highest process intensity was detected in the proximity of the external sides of electrode. For such materials as VNG-50, VINN-250, NTM-200 the back side was working worse than the front one, whereas for the materials KNM and BBP-66-95 – on the contrary. The materials brands TGN and NTM-100 have demonstrated the intermediate position in this line, and the curves of concentration distribution are symmetric. The central part of the electrodes, like for the other studied materials (except of TVS), is practically not working.

The comparison of polarization distribution curves on studied materials (Figure 8B) has also demonstrated the essential difference of CFM of TVS brand from the other materials. For the other materials the polarization was changed on the depth of 0.1÷0.12 cm on each of the sides, and its value makes on the electrode surface from 4·10<sup>-3</sup> to 15-20·10<sup>-3</sup> V. In case of TVS brand, under these conditions, the polarization was changes from 7.6·10<sup>-2</sup> to 11.1·10<sup>-2</sup> V on the lateral surfaces and does not decrease below 6.6·10<sup>-2</sup> V in the electrode depth. The front side is thus polarized more then the back one. The distribution of local current densities, like in the previous cases, has the character similar to the polarization distribution.

The calculated data obtained give rise to assumption that the rate of the studied process will be the highest for TVS brand of CFM. For the other studied materials it would be possible to slightly reduce the electrode thickness, without causing the essential effect on process rate, as soon as the internal zones with the insignificant polarization were observed for them. This, in its turn, will make it possible to reduce the hydraulic resistance during the electrolyte pumping.

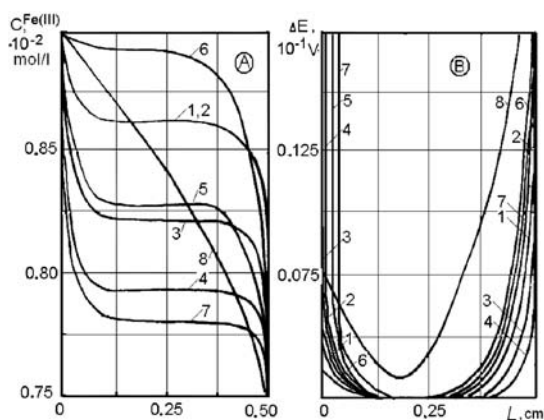


**Figure 8. Profiles of Fe(III) ions concentrations (A) and polarization (B) along the TDE depth in dependence on the electrode material type: 1-VINN-250; 2-NTM-200; 3-NTM-100; 4-VVP-66-95; 5-TNG; 6-VNG-50; 7-KNM; 8-TVS. Conditions:  $C_{initial}^{Fe(III)} = 8.9 \cdot 10^{-3}$  mol/L;  $u = 0.36$  mL/s;  $j_{overall} = 500$  A/m<sup>2</sup>.**

**Effect of the initial concentration of Fe(III) ions**

The studies of metals electrochemical reducing from low-concentrated solutions has shown [18], that process efficiency decreases with the increase of the electroactive component concentration. At the same time, there is a range of concentrations specific for each process, in which the rate of metal reducing is the highest. Like in the previous cases, this can be confirmed with the data of polarization and metal ions concentration, as well as current density distribution within the electrode body. It is important to determine these dependencies on the base of the numerical calculations using the mathematical model, as it allows determining the optimal conditions of iron plating solutions regeneration. With the increase of Fe(III) ions concentration up to  $8.9 \cdot 10^{-3} \div 1.8 \cdot 10^{-2}$  mol/L, the rate of the studied process is decreasing (Figure 9). However, with the increase of the overall current density to  $1500 \div 3000$  A/m<sup>2</sup> even under the high concentrations of Fe(III) ions, the high enough reaction rate is reached.

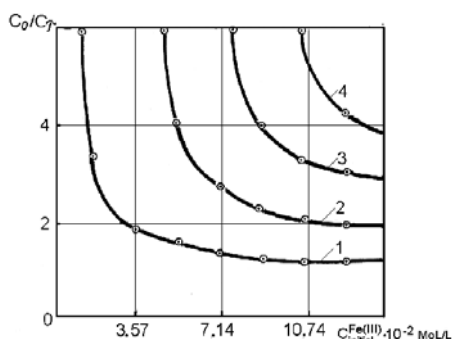


**Figure 9. Change of Fe(III) ions concentration (during the one-time pass through the CFE) in dependence on their initial contents in the electrolyte under the current densities, A/m<sup>2</sup>: 1-500; 2-700; 3-1000; 4-2000. Conditions: electrode material VINN-250 (2-times compression);  $u = 0.1$  mL/s;  $L = 0.5$  cm.**

Distribution of the cathode polarization within the electrode body (Figure 10) also demonstrates the essential influence of metal initial concentration: it's the lower  $C_{initial}^{Fe(III)}$  in the solution, the higher is the level of cathode polarization within the CFE depth, and the higher is the efficiency of these electrodes work. Under the high enough concentration of Fe(III) ions in electrolyte, in the central part of the electrode the minimum polarization is observed, where Fe(III) reduction to Fe(II) practically do not occur. This area is broadening with the increase in  $C_{initial}$ .

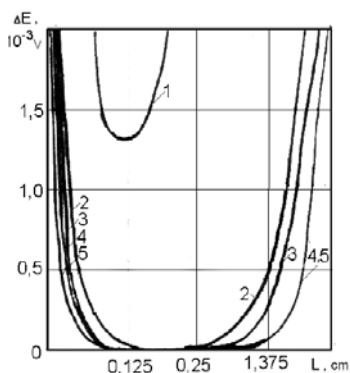


**Figure 10. Polarization distribution for the reaction  $Fe(III) + e \rightarrow Fe(II)$  under the initial contents in Fe(III) ions, mol/L: 1- $1.8 \cdot 10^{-3}$ ; 2- $8.9 \cdot 10^{-3}$ ; 3- $1.8 \cdot 10^{-2}$ ; 4- $8.9 \cdot 10^{-2}$ ; 5- $1.8 \cdot 10^{-1}$ .**



The study of Fe(III) ions distribution within the electrode has shown that the reduction processes occur only in the near-surface electrode layers, more intensively at the front side. With the decrease of Fe(III) ions concentration, the internal area of electrode, where the reduction of Fe(III) to Fe(II) occurs, is making broader, and under  $C^{\text{Fe(III)}} = 1.8 \cdot 10^{-3} \div 5.36 \cdot 10^{-3} \text{ mol/L}$  and  $j = 500\text{-}1500 \text{ A/m}^2$  the entire depth of the electrode is working at  $L = 0.5 \text{ cm}$ .

As follows from the data obtained, at the concentrations of Fe(III) ions of  $8.9 \cdot 10^{-2} \text{ mol/L}$  and higher, the thickness of CFE needs to be diminished up to 0.2-0.3 cm, thus decreasing the electrode area where Fe(III) are reduced. At the same time, electrolyte regeneration occurs with the permanent decrease of  $C^{\text{Fe(III)}}$ , and with time the internal part of electrode is broadening in which the studied reaction runs. In its turn, this requires to increase the total electrode up to 0.5 cm and higher.

### Influence of the solution flow rate

The rate of the electrolyte flow through the three-dimensional electrode is one of the technological parameters, which can be varied in order to modify the rate of the targeted process. With the increase of  $u$  values, the rate of Fe(III) reduction to Fe(II) is decelerating (Figure 11), which is caused by the one-time pass of the solution through the electrode body.

However, the results of polarization studies allow supposing that under the conditions of repeated pumping of treated solution through the electrode, the rate of target reaction should be increased, as it is controlled by the diffusion. Therefore, the acceleration of flow rate, like the agitation, results in the increase in the limiting diffusion current, thus accelerating the electrode process. The opposite influence of this factor detected at the calculations in accordance with the mathematical model, may be connected with the fact that not all the solution flowing during one-time pass through the CFE, interacts with the electrode surface.

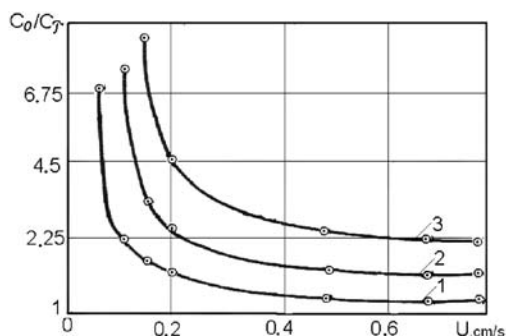


Figure 11. Effect of the solution flow velocity on the reduction of Fe(III) ions to Fe(II) with the change in current density,  $\text{A/m}^2$ : 1-500; 2-1000; 3-1500.

With the increase of the overall current density up to  $1000\div 1500 \text{ A/m}^2$  the reduction efficiency of Fe(III) ions is increasing, although the character of dependencies remains the same. At certain part of CFE the limiting current for the target reaction is reached.

It was of special interest to consider the work of the internal area of the electrode (Figure 12). At the flow rate  $0.05\div 0.10 \text{ cm/s}$ , the profile of concentration distribution has a tendency to the continuous decrease from the back to the front side of the electrode, but on a certain portion inside the electrode the rate of Fe(III) ions reducing becomes slower. At the flow rate of  $0.15 \text{ cm/s}$  and higher, the horizontal portions are discernible on the curves, which size increases with the increase in  $u$  values. This dependence is correlating with the polarization distribution data along the electrode depth. Thus, at the flow rate of  $0.07 \text{ cm/s}$  through the  $0.5 \text{ cm}$  electrode, the value of polarization for the reaction  $\text{Fe(III)} \xrightarrow{+e} \text{Fe(II)}$  is decreased to minimal, equal to  $0.2 \cdot 10^{-3} \text{ V}$ , and the minimum is on the  $1/4$  distance of electrode thickness from its back side. With the increase in  $u$  values from  $0.15 \text{ cm/s}$  and higher, the shift of the polarization minimum is observed to the center of electrode, with the simultaneous decrease of its values close to zero. The similar changes undergo also the profiles of current density distribution, consumed for the reaction  $\text{Fe(III)} \xrightarrow{+e} \text{Fe(II)}$ .

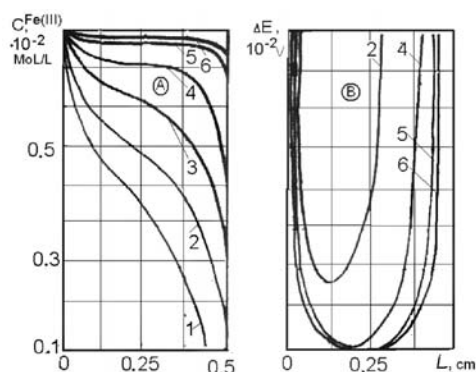
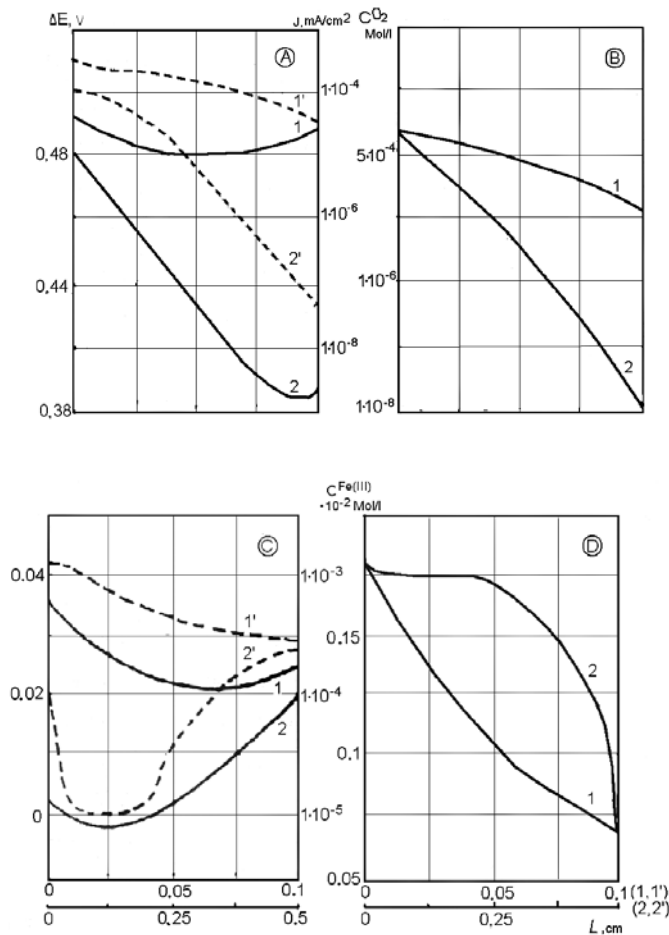


Figure 12. Profiles of Fe(III) ions concentration (A) and polarization (B) within the TDE depth in dependence on the flow velocity,  $\text{cm/s}$ : 1 – 0.05; 2 – 0.07; 3 – 0.1; 4 – 0.15; 5 – 0.5; 6 – 1.0.

In this way, the calculation data show that by decreasing the flow rate to certain values it is possible to increase the internal area of electrode where the target process occurs with the sufficient intensity. From the practical viewpoint, the reducing of flow rate makes it possible to reduce the energy consumption for the electrolyte pumping, as well as to reduce its turbulization, so as to prevent the reduction of Fe(II) ions to Fe(III) in the regenerated iron-containing electrolyte by air oxygen.

The data given in Figure 13 demonstrate the joint reduction of oxygen and Fe(III). The polarization distribution curve, corresponding to the reaction  $\text{Fe(III)} \xrightarrow{+e} \text{Fe(II)}$  (Figure 13B, curves 1,2), at the electrode thickness of 0.1 cm has a maximum, which at the increase of L values to 0.5 cm is shifted from the front to the back side of the electrode, which is similar to the current density change under these conditions (Figure 13D). With the increase in L values on the part of the electrode, corresponding to the decrease in polarization and local current density, the  $C^{\text{Fe(III)}}$  values are not changed, but then they sharply decrease with the increase of  $\Delta E$  and  $j$  values towards the back side of the CFE.



**Figure 13. Change in the polarization distribution (dotted line) - (A, B) and concentration (C,D) during the reaction of oxygen reducing (A,B) and Fe(III) within the CFE depth, cm: 1,1' – 0.1; 2,2' – 0.5.**

**Conditions: electrode material VINN-250 (2-fold compression);  $u = 0.36 \text{ mL/s}$ ;  
 $j_k = 500 \text{ A/m}^2$ ;  
 $E_p^{O_2} = 1.1 \text{ V}$ ;  $j_o^{O_2} = 10^{-8} \text{ A/cm}^2$ ;  $z^{O_2} = 2$ ;  
 $C_o^{O_2} = 2 \cdot 10^{-4} \text{ mol/L}$ .**

The values of polarization and current, consumed for the oxygen reduction reaction (Figure 13A), are reduced from the back side of CFE to the front one, the polarization distribution having the minimum shifting towards the front side with the increase in L value. With the increase of the electrode thickness, the more intensive oxygen reduction is observed (Figure 14B).

Another side the process with regard to the target reaction of Fe(III) ions reduction to Fe(II) in the iron-plating electrolyte is hydrogen emission. The calculation made for the three-component system, including the reduction of hydrogen ions, shows that the polarization distribution at the reaction occurrence  $\text{Fe(III)} \xrightarrow{+e} \text{Fe(II)}$  is characterized with the decrease of its values from the back to the front side of the electrode (Figure 14). At the low current densities, the polarization changes uniformly the electrode depth, and with the increase of  $j_{\text{overall}}$  values, the minimum appears in the internal area of the electrode.

The curves of polarization distribution for the reaction  $\text{Fe(II)} \xrightarrow{+2e} \text{Fe}^0$  (Figure 15B) show that the polarization is higher on the front side of the electrode than on the back one. At the same time, the numerical polarization values for this reaction is lower than for the reaction  $\text{Fe(III)} \xrightarrow{+e} \text{Fe(II)}$ , which indicates its easier occurrence in the negative potentials area, in which these two processes run simultaneously.

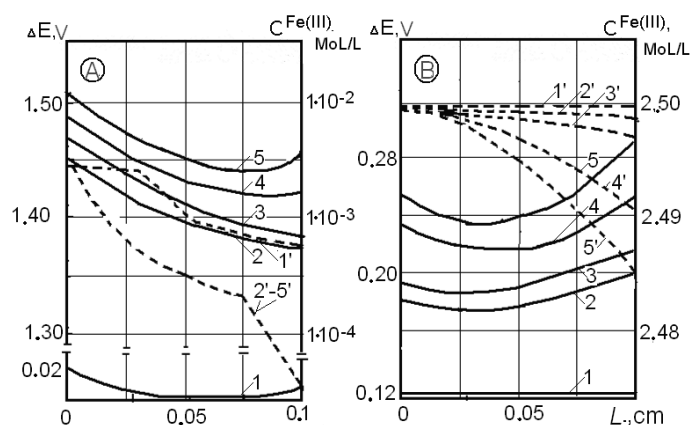


**Figure 14. Distribution of polarization (curves 1-5) and concentration (curves 1'-5') for the reaction  $\text{Fe(III)} \rightarrow \text{Fe(II)}$  (A) and  $\text{Fe(II)} \rightarrow \text{Fe}^0$  (B) with change in current density,  $\text{A/m}^2$ : 1,1' – 100; 2,2' – 500; 3,3' – 700; 4,4' – 1500; 5,5' – 3000. The conditions are similar to those shown on Figure 13.**

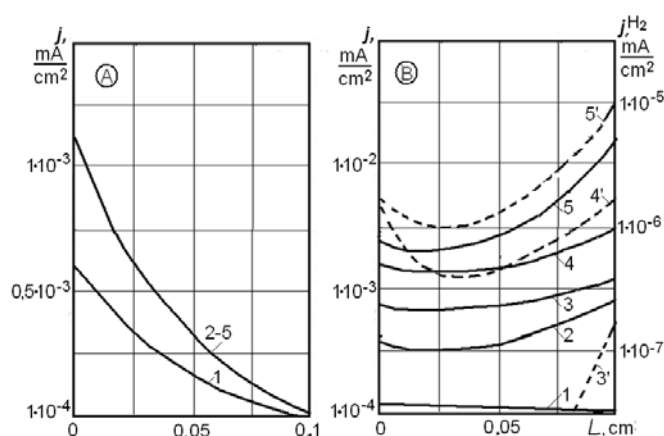


**Figure 15. Distribution of current for the reaction  $\text{Fe(III)} \xrightarrow{+e} \text{Fe(II)}$  (A) and  $\text{Fe(II)} \xrightarrow{+2e} \text{Fe}^0$  and hydrogen emission (dotted line) (B) in dependence on current density,  $\text{A/m}^2$ : 1 – 100; 2 – 500; 3,3' – 700; 4,4' – 1500; 5,5' – 3000. The conditions are similar to those shown on Figure 13.**

Under these conditions, the concentration of  $\text{Fe(III)}$  is distributed uniformly within the CFE body. With the current density increase, when the side processes start to occur, the  $C^{\text{Fe(III)}}$  distribution within the electrode body is practically not changed. The data of Figure 14B demonstrate that the change of the  $\text{Fe(II)}$  ions in the electrolyte proceeds uniformly, with the increase in the overall current density, from back to the front side of the electrode.

At the low electrode thickness (0.1 cm), used in our calculations, the curves of the current density distribution, consumed for the reaction  $\text{Fe(III)} \xrightarrow{+e} \text{Fe(II)}$ , have a tendency to decrease from the back to the front side of the CFE, although starting with  $j_{\text{overall}} = 500 \text{ A/m}^2$  and higher, the current density distribution remains unchanged (Figure 15).

It was also found that under the current densities below  $500 \text{ A/m}^2$  under the considered conditions, according to calculations, the hydrogen emission is not running, that can be explained by high overvoltage of its emission on the graphite surface [7]. At  $j_{\text{overall}} = 700 \text{ A/m}^2$  hydrogen starts evolving mainly on the back side of the electrode, and with the further increase in current density it is reduced within the entire electrode body, on the front side more than on the back one. The curves of current density distribution for hydrogen release reaction have minimum which is placed closer to the back side of the CFE. In this way, running of all the considered reactions has an independent character, the reduction of  $\text{Fe(III)}$  ions to  $\text{Fe(II)}$  running more intensively on the back side of the CFE, whereas two other processes connected with the evolving of metal iron and hydrogen on the front side of the electrode.

## Conclusions

The calculation results using the mathematical model, regarding the reduction processes in the iron plating electrolytes on the three-dimensional electrodes made it possible to study the effect of the overall current density, CFE thickness and degree of its compression, solution flow rate through the electrode, initial concentration of  $\text{Fe(III)}$  ions in the solution and CFM type on the efficiency of  $\text{Fe(III)}$  reduction.

The results obtained make it possible to select more purposely the conditions of iron electrolytes regeneration. Selecting the appropriate regimes, it would be possible to ensure the best conditions for the reduction of  $\text{Fe(III)}$  ions to  $\text{Fe(II)}$  in these electrolytes. The trends revealed require the experimental tests related to the real practical regeneration of such electrolytes.

## References

1. Varentsov, V.K.; Koshev, A.N. Mathematical modeling of the electrochemical processes in the flow-through three-dimensional electrodes. Proceedings of Siberian Branch of Academy of Sciences of USSR, Chemical Series, 1988, 17, pp. 117-125 (in Russian).
2. Koshev, A.N.; Kuzina, V.V. Elaboration and study of mathematical models on non-stationery processes in electrochemical reactors with flow-through three-dimensional electrodes. PSUAC: Penza, 2011, 119 p. (in Russian).
3. Koshev, A.N.; Varentsov V.K.; Kamburg, V.G. Mathematical modeling of metals electrodeposition from the multicomponent systems on flow-through three-dimensional electrodes. Proceedings of Siberian Branch of Academy of Sciences of USSR, Chemical Series, 1984, 6(5), pp. 24-27 (in Russian).
4. Daniel-Beck, V.S. On the polarization of porous electrodes. 4. Effect of the solid phase resistance on the potential and current distribution in the electrode. Electrochemistry, 1966, 2(6), pp. 672-677 (in Russian).
5. Varentsov, V.K.; Jerebilov, A.F.; Malei, M.D. Carbonic graphite fibrous materials – new electrodes for metals extraction from the diluted solutions. 1. Nonwoven carbonic graphite fibrous materials. Proceedings of Siberian Branch of Academy of Sciences of USSR, Chemical Series, 1984, 6(17), pp. 120-127 (in Russian).
6. Beck, R.Yu.; Zamyatin, A.P. Mass-transfer coefficient and surface of the flow-through fibrous electrodes, available for electrolysis. Electrochemistry, 1978, 14(18), pp. 1196-1201 (in Russian).
7. Covaliova, O.V. Electrochemical study of the redox processes in the iron-containing water solutions. Studia Universitatis, Natural Sciences Series, 2009, 21(1), pp. 195-203 (in Russian).
8. Covaliova, O.V. The study of kinetic regularities of Fe(III) ions reduction to Fe(II) in concentrated electrolytes. Studia Universitatis, Natural Sciences Series, 2013, 26(6), pp. 195-203 (in Russian).
9. Sukhotin, A.M. Ed. Reference Book on Electrochemistry. Chemistry: Leningrad, 1981, 488 p. (in Russian).
10. Fetter, K. Electrochemical kinetics. Chemistry: Moscow. 1967, 856 p. (in Russian).
11. Melkov, M.P.; Namakonov, B.V. On the cathode process of iron electrodeposition. Electrochemistry, 1974, 10(10), pp. 1555-1557 (in Russian).
12. Tarasevich, R.M. Electrochemistry of carbonic materials. Nauka: Moscow. 1984, 253 p. (in Russian).
13. Frumkin, A.N.; Bagotsky, V.S.; Iofa, Z.A.; et al. Kinetics of electrode processes. MSU: Moscow. 1952, 321 p. (in Russian).
14. Bagotsky, V.S. The bases of electrochemistry. Chemistry: Moscow. 1988, 400 p. (in Russian).
15. Beck, R.Yu. Perspectives of application of the electrodes with extended surface in hydrometallurgy. Proceedings of Siberian Branch of Academy of Sciences of USSR, Chemical Series, 1977, 6(4), pp. 11-20 (in Russian).
16. Jerebilov, A.F.; Varentsov, V.K. Experimental study of the polarization distribution along the depth of the flow-through three-dimensional electrodes made of the carbonic fibrous materials on the metals electrodeposition. Proceedings of Siberian Branch of Academy of Sciences of USSR, Chemical Series, 1987, 1, pp.19-24 (in Russian).
17. Jerebilov, A.F.; Varentsov, V.K. Experimental prove of the anodic zones presence on the cathode made of the carbonic graphite fibrous materials. Proceedings of Siberian Branch of Academy of Sciences of USSR, Chemical Series, 1985, 3(8), pp. 35-39 (in Russian).
18. Varentsov, V.K. Electrolysis with the three-dimensional flow-through electrodes in the hydrometallurgy of noble metals. Proceedings of Siberian Branch of Academy of Sciences of USSR, Chemical Series, 1984, 6(17), pp. 106-120 (in Russian).

## SOIL POLLUTION LEVEL OF ECOLOGICALLY VULNERABLE AREAS AROUND KAJARAN TOWN AND WAYS OF THEIR IMPROVEMENT

Karen Ghazaryan\*, Hasmik Movsesyan, Naira Ghazaryan, Gor Gevorgyan, Karlen Grigoryan

*Department of Ecology and Nature Protection, Faculty of Biology, Yerevan State University,*

*1, Alex Manoogian str., Yerevan 0025, Republic of Armenia*

*\*e-mail: ghazaryank@mail.ru; phone: + (37491) 34 29 19*

**Abstract.** Kajaran town is situated in the south-east of the Republic of Armenia in Syunik Marz. Developed mining and smelting industries can be observed in this area. This economic sphere is one of the main sources of soil pollution with heavy metals causing desertification of soils. Taking into consideration the location of the main sources of pollution six the most risky sites in this area and an unpolluted site as a control were selected for the study of pollution by heavy metals. The content of metals was determined by means of ELAN 9000 ICP-MS System. Study results revealed the increase up to 17 times in contents of following metals: Co, Ni, Cu, Zn, Cr, Sr, Mo, Cd, Pb, As. Based on Geoaccumulation index ( $I_{geo}$ ) classification, the soils from all sites may be classified between “practically uncontaminated” and “uncontaminated to moderate”. The pollution level for Cu ( $I_{geo} = 0.031-2.468$ ) was higher than for other metals. The sites adjacent to Kajaran ore-dressing and processing enterprise are classified as “moderately to strongly” contaminated by Cu. Experiments have led us to the assumption that pollution of soils with heavy metals in the studied territory is conditioned by human activities, particularly by mining and smelting industry.

**Keywords:** mining, heavy metals, soil pollution, soil improvement.

### Introduction

The prime emphasis among environmental advocates has always been the protection of human health, with the implicit recognition that human well-being is inextricably intertwined with the health and stability of natural ecosystems of which we form an integral part. Some of today's most prevalent ills are increasingly blamed on toxic environmental contaminants – heavy metals that become pollutants as a result of previous industrial, mining or other activities [12]. Contamination of soils by heavy metals is a significant problem, which leads to negative influence on soil characteristics and limitation of productive and environmental functions [2, 6, 7, 9, 10, 11, 13-16]. The accumulation of these contaminants in the environment has become a concern due to the health risks to humans and animals [4, 8, 17].

Mining industry is a developed branch of the Armenian economy. Since the last decades of the 20th century, mining and beneficiation of a variety of minerals, in particular copper and gold, have been the driving force behind economic development, particularly in RA Marzes (administrative districts) of Syunik and Lori.

The aim of our studies was the evaluation of soil pollution level (particularly by heavy metals) of ecologically vulnerable mining territories around Kajaran town in the RA Marz of Syunik and suggestion of ways for their improvement. The problem under study in this region is very urgent and actual because it concerns the preservation of sensitive natural resources, prevention of inadmissible contamination of food products and the protection of the health of inhabitants in this region. Appropriate management of surroundings of open mines, active tailing dams, sites adjacent to ore-dressing and processing enterprises as well as suggestion of ways for preventing pollution in the surrounding territories are very important. Preventing heavy metal pollution is critical because the cleaning of contaminated soils is extremely expensive and difficult.

### Materials and methods

The lands of the area belong to the type of mountain cambisol. In Armenia this soil type is distributed 500-1700 meters above sea level, and on arid southern slopes it reaches up to 2400 meters [1, 3]. The objective of this research was the analysis of soils of six the most risky sites of this region (Figure 1).

It should be noted that the tailing dam of Artsvanik is rather far from Kajaran town nevertheless this site was also chosen as far as it is now the only active tailing dam of the enterprise.

Taking into account the above-mentioned, 18 sections of only horizon A of soil (0-20 cm) were performed in selected sites. The control section on distance 4 km from enterprise in a western ward direction was also done (approximately on distance 1 km westward from Kajaran village). Sections were performed manually. The sampling of soils was carried out in a traditional way, well-known in soil science. All labware and sampling apparatus were pre-soaked in 5% nitric acid solution followed by distilled water for a day prior to sampling for removing trace concentrations of metals.

Samples of soils were taken from a depth of 0-20 cm at 5 m intervals on a grid measuring 20 m x 20 m and with the center point of the grid at the sample location. After homogenization and removal of unwanted content (stones, plant material etc.) samples were air-dried at room temperature, ground, sieved to pass a 1 mm mesh and stored in an all-glass jar for analysis of their properties.

The content of heavy metals was determined by means of ELAN 9000 ICP Mass Spectrometer (Perkin Elmer, Inc).

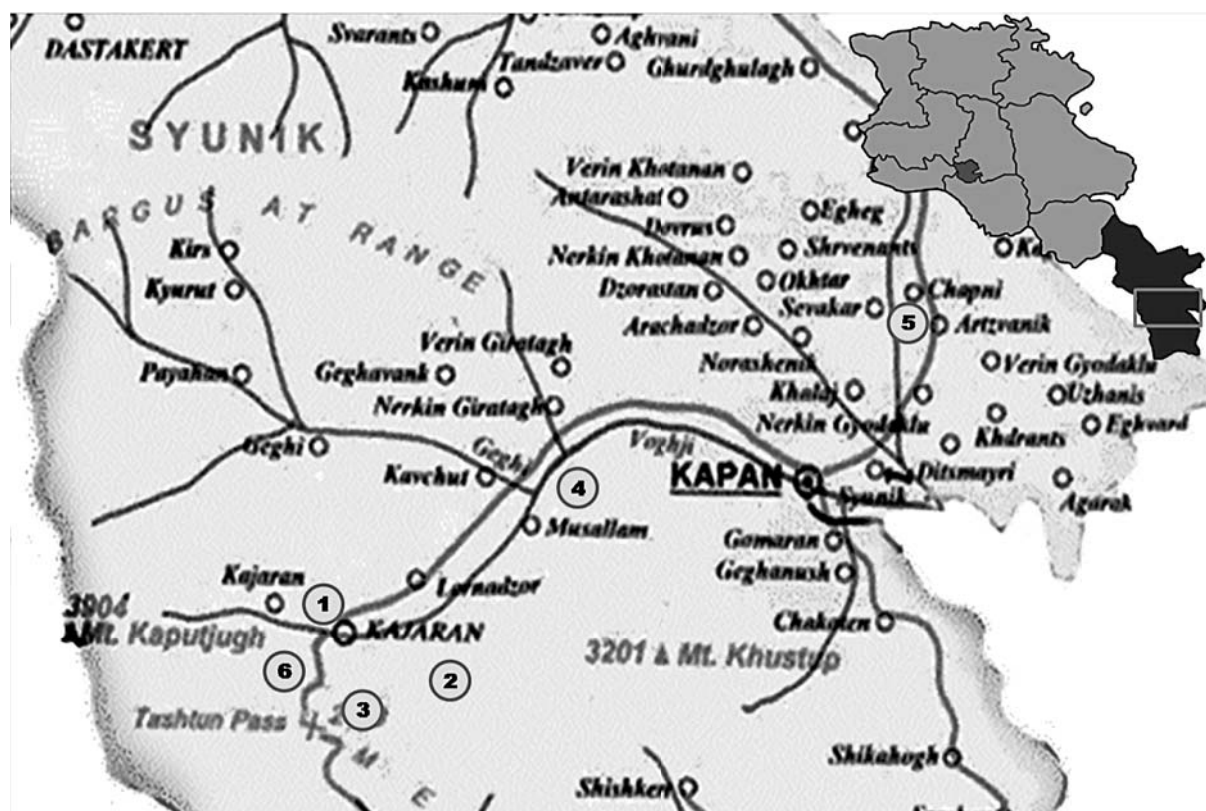


**Figure 1. The map of Syunik Marz of Armenia showing six sampling areas:**

1. the sites adjacent to Kajaran ore-dressing and processing enterprise (samples no. 1-6),
2. recultivated tailing dam of Pkhrut (sample no. 7),
3. recultivated tailing dam of Darazam (sample no. 8),
4. recultivated tailing dam of Voghji (sample no. 9),
5. surroundings of Artsvanik active tailing dam (samples no. 10-12),
6. surroundings of open mine near the Kajaran town (samples no. 13-18).

To quantify the degree of pollution of soils with heavy metals the Geoaccumulation index,  $I_{geo}$ , was used [5]:

$$I_{geo} = \ln(C_n / 1.5 \times B_n),$$

where:

$C_n$  – measured concentration of heavy metals in the soils from risky sites ( $\mu\text{g/g}$ );

$B_n$  – background value of heavy metals in the soil from control section ( $\mu\text{g/g}$ );

1.5 – background matrix correction factor.

The coordinates of sampling sites having been recorded with GPS receiver as well as their pollution with heavy metals have been described in registration book for general evaluation of soil pollution level.

## Results and discussion

The data of field studies indicate that the 19 sections of soil can be classified into types and subtypes. The main soil type in studying sites was the mountain cambisol with its subtypes:

1. a) mountain cambisol, decalcified, rubble-stony, with weak capacity, weakly eroded in some places (samples no. 1-3, 13, 17 and the control);
- b) mountain cambisol, decalcified, with medium capacity, weakly eroded (samples no. 4-6, 8, 14-16, 18);
2. mountain cambisol, calcareous, steppificated (samples no. 7, 9, 10-12).

The content ( $\mu\text{g/g}$ ) of some heavy metals in the studied samples of soil is presented in Table 1. Since the contents of metals and non-metals in soils are specific and depend on the compound of rocks producing the soil and the conditions of soil formation, for determination of pollution level the obtained results were compared with control sample which was considered as a background. Our study revealed the appreciable increase (1.5 to 17 times) in contents

of following heavy metals: Co (samples no. 4, 7-9, 10, 16, 17), Ni (samples no. 7-11), Cu (samples no. 1-8, 14-18), Zn (samples no. 6-9, 14, 16), Cr (samples no. 7, 9-11, 15, 18), Sr (samples no. 4, 6-8, 13, 14, 16), Mo (samples no. 3-6, 18), Cd (samples no. 4, 5, 14, 18), Pb (samples no. 1, 7, 14), As (samples no. 5, 7, 9, 10). Compared to the control sample the significant increase (approximately 17 times) in the content of heavy metals was observed only for copper which was due to the high content of this metal in ores (Table 2). In general the soil samples no.1-6, 8, 14, 16-18 were highly polluted by Cu and to some extent - by other metals, while the sample 12 was unpolluted.

Table 1

**The content ( $\mu\text{g/g}$ ) of some heavy metals in the studied samples of soil.**

Sample number	Co	Ni	Cu	Zn	Sr	Mo	Cd	Pb	Cr	As
1	1.607	1.092	36.082	7.196	29.444	3.822	0.032	7.002	2.558	0.224
2	1.634	1.535	44.840	5.943	30.939	6.937	0.025	2.359	2.621	**
3	1.162	1.145	37.498	4.547	23.005	18.436	0.042	1.834	1.955	**
4	2.130	2.226	44.980	8.285	53.383	14.745	0.045	3.144	3.583	0.199
5	1.512	1.586	131.573	5.047	14.741	24.848	0.052	1.242	2.105	0.941
6	1.526	1.860	104.975	11.255	44.037	11.850	0.034	3.264	2.579	0.802
7	2.456	4.784	11.500	8.877	43.028	0.291	0.028	6.358	6.985	1.234
8	2.030	4.071	17.853	9.880	45.541	2.389	0.031	3.565	5.276	0.730
9	2.367	6.150	7.287	8.460	29.518	0.698	0.035	2.861	9.116	2.148
10	2.090	6.697	3.526	7.039	27.820	**	0.027	1.551	12.619	1.170
11	1.553	5.106	3.421	6.630	14.080	**	0.032	1.770	7.791	0.578
12	1.611	2.824	3.074	6.497	22.135	**	0.020	1.091	3.994	**
13	1.348	2.892	8.737	5.285	47.217	1.403	0.024	2.156	4.466	0.705
14	1.458	1.429	41.246	8.419	47.583	4.081	0.047	4.994	1.572	**
15	1.326	3.370	11.879	5.473	24.932	0.935	0.027	2.217	6.749	**
16	2.309	1.772	20.978	8.661	50.155	0.736	0.018	2.126	2.515	0.452
17	1.995	1.846	49.894	7.836	23.607	2.271	0.017	1.024	2.772	0.862
18	1.387	3.794	48.187	7.191	19.062	29.699	0.076	2.739	6.317	0.837
Control	1.179	2.521	7.431	5.791	25.508	6.733	0.030	2.535	3.839	0.598

\*\* - Trace quantities

Table 2

**Degree of content exceeding of heavy metals (experimental variant/control).**

Sample number	Co	Ni	Cu	Zn	Sr	Mo	Cd	Pb	Cr	As
1	1.4	0.4	4.9	1.2	1.2	0.6	1.1	2.8	0.7	0.4
2	1.4	0.6	6.0	1.0	1.2	1.0	0.8	0.9	0.7	-
3	1.0	0.5	5.0	0.8	0.9	2.7	1.4	0.7	0.5	-
4	1.8	0.9	6.1	1.4	2.1	2.2	1.5	1.2	0.9	0.3
5	1.3	0.6	17.7	0.9	0.6	3.7	1.7	0.5	0.5	1.6
6	1.3	0.7	14.1	1.9	1.7	1.8	1.1	1.3	0.7	1.3
7	2.1	1.9	1.5	1.5	1.7	0.0	0.9	2.5	1.8	2.1
8	1.7	1.6	2.4	1.7	1.8	0.4	1.0	1.4	1.4	1.2
9	2.0	2.4	1.0	1.5	1.2	0.1	1.2	1.1	2.4	3.6
10	1.8	2.7	0.5	1.2	1.1	-	0.9	0.6	3.3	2.0
11	1.3	2.0	0.5	1.1	0.6	-	1.1	0.7	2.0	1.0
12	1.4	1.1	0.4	1.1	0.9	-	0.7	0.4	1.0	-
13	1.1	1.1	1.2	0.9	1.9	0.2	0.8	0.9	1.2	1.2
14	1.2	0.6	5.6	1.5	1.9	0.6	1.6	2.0	0.4	-
15	1.1	1.3	1.6	0.9	1.0	0.1	0.9	0.9	1.8	-
16	2.0	0.7	2.8	1.5	2.0	0.1	0.6	0.8	0.7	0.8
17	1.7	0.7	6.7	1.4	0.9	0.3	0.6	0.4	0.7	1.4
18	1.2	1.5	6.5	1.2	0.7	4.4	2.5	1.1	1.6	1.4

Table 3

Geoaccumulation index ( $I_{geo}$ ) and degree of pollution.

Sample number	Co	Ni	Cu	Zn	Sr	Mo	Cd	Pb	Cr	As
1	-0.096 /0/	-1.242 /0/	1.175 /2/	-0.188 /0/	-0.262 /0/	-0.972 /0/	-0.341 /0/	0.611 /1/	-0.811 /0/	-1.387 /0/
2	-0.079 /0/	-0.902 /0/	1.392 /2/	-0.380 /0/	-0.212 /0/	-0.376 /0/	-0.588 /0/	-0.477 /0/	-0.787 /0/	- /0/
3	-0.420 /0/	-1.195 /0/	1.213 /2/	-0.647 /0/	-0.509 /0/	0.602 /1/	-0.069 /0/	-0.729 /0/	-1.080 /0/	- /0/
4	0.186 /1/	-0.530 /0/	1.395 /2/	-0.047 /0/	0.333 /1/	0.378 /1/	0.000 /0/	-0.190 /0/	-0.474 /0/	-1.506 /0/
5	-0.157 /0/	-0.869 /0/	2.468 /3/	-0.543 /0/	-0.954 /0/	0.900 /1/	0.145 /1/	-1.119 /0/	-1.006 /0/	0.048 /1/
6	-0.147 /0/	-0.710 /0/	2.243 /3/	0.259 /1/	0.141 /1/	0.160 /1/	-0.280 /0/	-0.153 /0/	-0.803 /0/	-0.112 /0/
7	0.328 /1/	0.235 /1/	0.031 /1/	0.022 /1/	0.117 /1/	-3.547 /0/	-0.474 /0/	0.514 /1/	0.193 /1/	0.319 /1/
8	0.138 /1/	0.074 /1/	0.471 /1/	0.129 /1/	0.174 /1/	-1.442 /0/	-0.373 /0/	-0.064 /0/	-0.088 /0/	-0.206 /0/
9	0.291 /1/	0.486 /1/	-0.425 /0/	-0.026 /0/	-0.259 /0/	-2.672 /0/	-0.251 /0/	-0.284 /0/	0.459 /1/	0.873 /1/
10	0.167 /1/	0.572 /1/	-1.151 /0/	-0.210 /0/	-0.319 /0/	- /0/	-0.511 /0/	-0.897 /0/	0.785 /1/	0.266 /1/
11	-0.130 /0/	0.300 /1/	-1.181 /0/	-0.270 /0/	-1.000 /0/	- /0/	-0.341 /0/	-0.765 /0/	0.302 /1/	-0.439 /0/
12	-0.093 /0/	-0.292 /0/	-1.288 /0/	-0.290 /0/	-0.547 /0/	- /0/	-0.811 /0/	-1.249 /0/	-0.366 /0/	- /0/
13	-0.272 /0/	-0.268 /0/	-0.244 /0/	-0.497 /0/	0.210 /1/	-1.974 /0/	-0.629 /0/	-0.567 /0/	-0.254 /0/	-0.241 /0/
14	-0.193 /0/	-0.973 /0/	1.308 /2/	-0.031 /0/	0.218 /1/	-0.906 /0/	0.043 /1/	0.273 /1/	-1.298 /0/	- /0/
15	-0.288 /0/	-0.115 /0/	0.064 /1/	-0.462 /0/	-0.428 /0/	-2.380 /0/	-0.511 /0/	-0.540 /0/	0.159 /1/	- /0/
16	0.267 /1/	-0.758 /0/	0.632 /1/	-0.003 /0/	0.271 /1/	-2.619 /0/	-0.916 /0/	-0.581 /0/	-0.828 /0/	-0.685 /0/
17	0.121 /1/	-0.717 /0/	1.499 /2/	-0.103 /0/	-0.483 /0/	-1.492 /0/	-0.973 /0/	-1.312 /0/	-0.731 /0/	-0.040 /0/
18	-0.243 /0/	0.003 /1/	1.464 /2/	-0.189 /0/	-0.697 /0/	1.079 /2/	0.524 /1/	-0.328 /0/	0.093 /1/	-0.069 /0/

The degree of pollution of soils with metals was assessed (Table 3) using the Geoaccumulation index ( $I_{geo}$ ) classification (Table 4) by Förstner et al. [5].

Based on the classification, the soils from all sites may be classified between “practically uncontaminated” and “uncontaminated to moderate” by heavy metals Co, Ni, Zn, Sr, Mo, Cd, Pb, Cr and As except the site 18 where the soil was moderately polluted with Mo. The pollution level for Cu ( $I_{geo} = 0.031$ -2.468) was higher than for other metals. Soils from different sites were found to be polluted with copper somehow, and may be classified as “practically uncontaminated” (sites 9-13), “uncontaminated to moderate” (sites 7, 8, 15, 16), “moderate” (sites 1-4, 14, 17, 18) and “moderate to strong” (sites 5 and 6).



It should be noted that such kind of pollution of soils with heavy metals in studied territory is directly due to human activities, particularly to mining and smelting industry. The variation of high pollution with Cu and some heavy metals near the open mine and in territories that are adjacent to enterprise is due to the character of industrial activities, moving direction of airstreams as well as physical-chemical peculiarities of soils. According to classification the soil from site 12 is the least polluted with the metals. The low rate of soil pollution in the surroundings of Artsvanik tailing dam is conditioned by correct exploitation of tailing dam.

As was mentioned above, comparatively high rate of soil pollution was also observed near the no operating recultivated tailing dams of Pkhrut, Darazam and Voghji. Although the content of copper considering as main pollutant was small in these recultivated soils other heavy metals (Co, Ni, Zn, Sr, Pb, Cr, As) by their content exceeded control samples 1.5 and more times. Thereby the inhabitants of these territories are not recommended to use these territories for agricultural purposes even as pastures and hayfields.

Table 4

**Geoaccumulation index classification.**

Geoaccumulation index, $I_{geo}$	$I_{geo}$ class	Contamination intensity
> 5	6	very strong
> 4-5	5	strong to very strong
> 3-4	4	strong
> 2-3	3	moderate to strong
> 1-2	2	moderate
> 0-1	1	uncontaminated to moderate
< 0	0	practically uncontaminated

**Conclusions**

Taking into consideration the above-mentioned it is necessary to implement recultivation activities in the areas around Kajaran town that constitute the main source of pollution by heavy metals. The recultivation works are advisable to implement by the method of hydroseeding which is considered as a subtype of biological recultivation. The main goal of biological recultivation is the recovery of soil formation natural process, the stimulation of soil self-purification properties and biocenosis self-recovery process. Biological recultivation results in the formation of a landscape with satisfactory biodiversity on disturbed and polluted areas.

As the area of our studies is polluted especially with heavy metals it is also desirable to add to seed mixture using in hydroseeding method the seeds of plants which have the ability of removing selectively some heavy metals from the soil (rose (Cu, Fe), chalk plant (Cu), violet, penny cress (Zn), joint weed (Zn, Pb, Cd), mustard (Pb, Cr), hibiscus (Co), buckwheat (Ni)) making the process of recultivation more effective.

In addition to the above-mentioned approaches it is also suggested using ameliorants, particularly the mixture of organic fertilizers (manure, biohumus) and natural ameliorants (zeolite, dacite tuff) for utilization of heavy metals or at least for reducing their toxic impact on living organisms and the environment on the whole. It is scientifically proved that it is possible to improve the condition of soils polluted by heavy metals and to decrease the content of mobile forms of these elements by the joint use of natural ameliorants and organic fertilizers.

**Acknowledgements**

This work was supported by State Committee of Science MES RA, in frames of the research project No. SCS 13-4C202.

**References**

1. Baghdasaryan, A.B.; Abrahamyan, G.S.; Aleksandryan, G.A.; Aslanyan, A.A.; Zohrabyan, L.N. Physical Geography of Armenian SSR; National Academy of Armenian SSR: Yerevan, 1971, 471 p. (in Armenian).
2. CEC Commission of the European Communities Communication of 16 April 2002 from the Commission to the Council, the European Parliament, the Economic and Social Committee and the Committee of the Regions: Towards a Thematic Strategy for Soil Protection; Brussels, 2002, 35 p.
3. Edilyan, R.A. Atlas of Soils of the Republic of Armenia. Yerevan, 1990, 70 p. (in Russian).
4. Huber, S.; Prokop, G.; Arrouays, D.; Banko, G.; Bispo, A.; Jones, R.J.A.; Kibblewhite, M.G.; Lexer, W.; Möller, A.; Rickson, R.J.; Shishkov, T.; Stephens, M.; Toth, G.; Van den Akker, J.J.H.; Varallyay, G.; Verheijen, F.G.A.; Jones, A.R. ENVASSO Environmental Assessment of Soil for Monitoring: Volume I Indicators & Criteria., Eds. EUR 23490 EN/1., Office for the Official Publications of the European Communities: Luxembourg, 2008; 339 p.

5. Förstner, U.; Ahlf, W.; Calmano, W. Sediment quality objectives and criteria development in Germany. *Water Science and Technology*, 1993, 28, pp. 307-316.
6. Friedlová, M. The influence of heavy metals on soil biological and chemical properties. *Soil and Water Research*, 2010, 5(1), pp. 21-27.
7. Ghazaryan, K.; Movsesyan, H.; Ghazaryan, N.; Grigoryan, K. The ecological assessment of soils around Agarak town. *Biological Journal of Armenia*, 2013, 65(1), pp. 39-43.
8. Maxwell, N.I. *Understanding Environmental Health: How We Live in the World*; Jones & Bartlett Learning: Burlington, 2009, 378 p.
9. Mikanová, O. Effects of heavy metals on some soil-biological parameters. *Journal of Geochemical Exploration*, 2006, 88, pp. 220-223.
10. Ross, S.M., Ed. *Toxic Metals in Soil-Plant Systems*; John Wiley & Sons: Chichester, 1994; 469 p.
11. SQ Soil quality - Guidance on the determination of background values (ISO 19258:2005), 2007, 30 p.
12. USDA United States Department of Agriculture Heavy Metal Soil Contamination. Natural Resources Conservation Service. Soil Quality Institute. 411 S. Donahue Dr. Auburn. AL 36832 334-844-4741 X-177, Urban Technical Note No.3, 2000; 7 p.
13. Vodyanitskii, Yu.N. Contamination of soils with heavy metals and metalloids and its ecological hazard (analytic review). *Eurasian Soil Science*, 2013, 46(7), pp. 793-801.
14. Povar, I.; Spinu O. Buffer properties of soil minerals. Part 1. Theoretical aspects. *Chemistry Journal of Moldova*, 2013, 8(2), pp. 67-72.
15. Leah, T.; Povar, I.; Lupascu, T.; Andries, S.; Filipciuc, V. Studying the research results regarding fertilizers used in the Republic of Moldova. *Chemistry Journal of Moldova*, 2013, 8(1), pp. 14-22.
16. Leah, T. Ecological peculiarities of copper chemical forms content in the eroded soils. *Chemistry Journal of Moldova*, 2013, 8(1), pp. 33-36.
17. Walker, C.H.; Sibly, R.M.; Hopkin, S.P.; Peakall, D.B. *Principles of Ecotoxicology*; CRC Press: New York, 2012, 386 p.

## REMOVAL OF DIVALENT IRON AND MANGANESE IONS AND HYDROGEN SULFIDE FROM GROUNDWATER

Tudor Lupascu\*, Mihail Ciobanu, Victor Botan

*Institute of Chemistry of Academy of Sciences of Moldova, 3, Academiei str., Chisinau MD-2028, Republic of Moldova*  
*\*e-mail: lupascut@gmail.com; phone: (+373 22) 72 54 90; fax: (+373 22) 73 99 54*

**Abstract:** Processes of removal of divalent ions of iron and manganese and hydrogen sulfide from groundwater at various pH values and temperature were studied. Obtained results have been used in order to elaborate a process of groundwater purification from the mentioned pollutants. The use of elaborated process for natural water leads to the decrease of the content of iron, manganese and hydrogen sulfide below the maximum allowable concentrations.

**Keywords:** divalent iron, divalent manganese, hydrogen sulfide, oxidation, coagulation.

### Introduction

According to the Ministry of Health, the groundwaters of Moldova are of low quality. Around 50% of groundwater from Moldova is polluted with ions of fluorine, manganese, iron, strontium, ammonium, sulfides etc. Divalent ions of iron and manganese remain common in deep water beyond the permissible concentration. As a result of the oxidation of these ions with airborne oxygen, the water becomes colorized and the problems arise with its use in laundry and deposits within water supply networks. Iron and manganese may be present in one of the basic forms: (1) dissolved - the divalent ions of ( $\text{Fe}^{2+}$ ) and ( $\text{Mn}^{2+}$ ) and (2) suspended particles of small size corresponding to trivalent iron hydroxides ( $\text{Fe}(\text{OH})_3$ ) and tetravalent manganese hydroxides ( $\text{Mn}(\text{OH})_4$ ). The nature of these forms depends on the value of pH, Eh (redox potential) and the water temperature. Hydrogen sulfide is found in groundwater in its dissolved form ( $\text{H}_2\text{S}$ ) or as metal sulfides ( $\text{Me}_n\text{S}_m$ ). The knowledge of the species and the oxidation state of iron, manganese and hydrogen sulfide contribute to the elaboration of the water treatment process.

Scientific literature describes the procedure of removal of divalent ions of iron, manganese and hydrogen sulfide from various types of water [1-3]. In [1] for the removal of iron and manganese ions from water the MFO-47 filter was used, which contains a material of natural origin ( $\text{CaC}_n$ ). On the surface of this material, a catalytically active layer was applied, which consisting of a mixture of oxides  $\text{MnO}$ ,  $\text{Mn}_2\text{O}_3$  and  $\text{MnO}_2$ . This filter material removes only iron and manganese ions from water. In [2] there is mentioned that the treatment with reagents of this natural disperse material leads to material changes. On the surface of the natural material, a mixture of manganese hydroxide and oxides ( $\text{Mn}(\text{OH})_2$ ,  $\text{Mn}_2\text{O}_3$ ,  $\text{MnO}_2$ ) is formed. The presence of manganese hydroxide on catalyst surface contributes to the efficient oxidation of hydrogen sulfide, forming a weak dibasic acid. In [4] there is mentioned that for the removal of iron and manganese ions and hydrogen sulfide from groundwater, a mineral adsorbent surface was used, which has incorporated a catalytically active layer, containing the same mixture of  $\text{Mn}(\text{OH})_2$ ,  $\text{Mn}_2\text{O}_3$  and  $\text{MnO}_2$ , in a mass ratio (1-0.5):(3-2):(6-5), respectively. The filter material is obtained using two solutions that contain salts of manganese, the first salt containing bivalent manganese sulfate and sodium sulfate and the second - sodium permanganate solution.

The aim of this research was to study the processes and mechanisms of removal of divalent iron and manganese ions and hydrogen sulfide from groundwater. Manganese is present as  $\text{Mn}^{2+}$  at the value of pH between 0 and 8.4 and as  $\text{Mn}(\text{OH})_4$  when  $8.4 \leq \text{pH} \leq 14$ , while  $\text{Fe}^{3+}$  at  $\text{pH} = 9.5$  is present in the form of  $\text{Fe}(\text{OH})_3$  [5]. Based on these data, the possibility to remove the iron and manganese divalent ions as a result of pH change was studied.

### Experimental

The chemical composition of groundwater from village Sculeni (Ungheni district) and the maximum allowable concentrations (MAC) of detected chemical components, according to the current regulations, are presented in Table 1.

As shown in Table 1, the content of iron exceeds the maximum allowable concentration by 4.3 times, manganese - by 9 times and hydrogen sulfide slightly exceeds the MAC.

The treatment processes (adsorption/catalytic oxidation and precipitation) of water polluted by the bivalent ions of manganese and iron, as well as hydrogen sulfide were carried out using the installation presented in Figure 1. The model solution, which contained  $\text{Fe} - 1.24 \text{ mg/dm}^3$ ,  $\text{Mn} - 0.47 \text{ mg/dm}^3$  and  $\text{H}_2\text{S} - 0.12 \text{ mg/dm}^3$ , appropriate to the real water from the village Sculeni, was used in the experimental tests. In order to oxidize only hydrogen sulfide to sulfate, the  $1.8 \text{ cm}^3$  of 35%  $\text{H}_2\text{O}_2$  was added to the volume of  $10 \text{ dm}^3$ , by mixing for 10 minutes. The value of pH was then adjusted to 10.25. The removal process of iron and manganese ions was carried out by stirring for 20 minutes at a temperature of  $15^\circ\text{C}$ . During this time the precipitation floccules appear which representing three valence iron hydroxide and four valence manganese hydroxide. The water from the reactor was passed through a sand filter, fraction 0.8 to 1.3 mm by means of a pump. The filtration speed was 7 m/h. After filtration, the water was subjected to laboratory analysis in order to establish the concentrations of iron, manganese and sulfur.

**Chemical composition of groundwater from village Sculeni and maximum allowable concentration (MAC) of mentioned components.**

Parameter name and unit	Determined	MAC
Total hardness, mol/dm <sup>3</sup>	6.16	5.0
Dry residue (110°C), mg/dm <sup>3</sup>	498.4	1500
Nitrites (NO <sub>2</sub> <sup>-</sup> ), mg/dm <sup>3</sup>	0.0075	0.5
Nitrates (NO <sub>3</sub> <sup>-</sup> ), mg/dm <sup>3</sup>	<0.5	50
Iron (Fe) total, mg/dm <sup>3</sup>	1.29	0.3
Ammonia (NH <sub>4</sub> <sup>+</sup> ), mg/dm <sup>3</sup>	0.37	0.5
Sodium (Na <sup>+</sup> ), mg/dm <sup>3</sup>	45.7	200
Fluorine (F <sup>-</sup> ), mg/dm <sup>3</sup>	<0.2	1.5
Copper (Cu), mg/dm <sup>3</sup>	<0.1	1.0
Cadmium (Cd), mg/dm <sup>3</sup>	<0.001	0.003
Chromium (Cr), mg/dm <sup>3</sup>	<0.01	0.05
Manganese (Mn), mg/dm <sup>3</sup>	0.45	0.05
H <sub>2</sub> S, mg/dm <sup>3</sup>	0.12	0.1

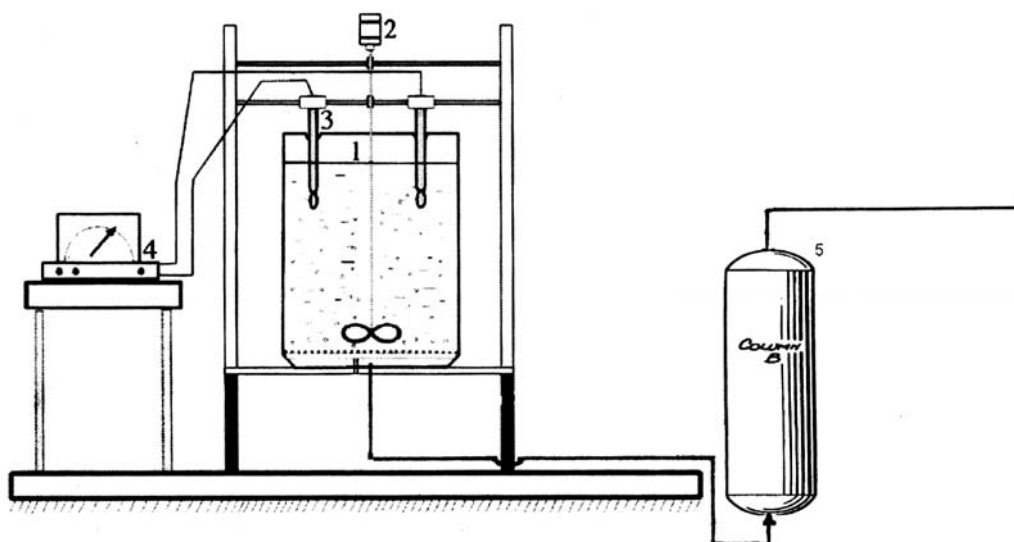
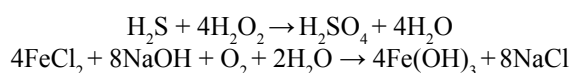


**Figure 1. Scheme of the installation for the testing of the process of removal of Fe, Mn, H<sub>2</sub>S from groundwater.**

- 1**–reactor;
- 2**–agitator;
- 3**–electrodes;
- 4**–pH/mV-meter;
- 5**–sand filter.

### Results and discussion

The results of the analyzes of purified water is as follows: (i) the concentration of sulfate ions initially was 60.1 mg/dm<sup>3</sup> and after the treatment increased to 63.3 mg/dm<sup>3</sup> due to the oxidation of 1.2 mg/dm<sup>3</sup> of hydrogen sulfide; (ii) the concentration of hydrogen sulfide after treatment became 0; the initial pH of the water was 10.25 and after filtration became 9.9; (iii) the concentration of iron and manganese after treatment was 0.12 mg/dm<sup>3</sup> and <0.05 mg/dm<sup>3</sup>, respectively. Test results allow us to conclude that the developed method allows treating the groundwater contaminated with bivalent ions of iron, manganese and hydrogen sulfide. These processes can be described by the following chemical reactions:





Groundwater is used daily throughout the year at various temperatures. In these conditions, it is necessary to perform the scientific research, regarding the influence of temperature and the value of pH on the process of removal of iron and manganese ions and hydrogen sulfide, as these factors are changing in dependence on the season.

The data on the removal of iron, manganese ions and hydrogen sulfide from groundwater at various values of pH and temperature are presented in the Table 2.

Table 2

**Removal of iron, manganese and hydrogen sulfide from groundwater at various values of pH and temperature.**

Temperature, °C	Volume of H <sub>2</sub> O <sub>2</sub> , cm <sup>3</sup>	Value of pH		Final amount, mg/dm <sup>3</sup>			Amount of SO <sub>4</sub> <sup>2-</sup> , mg/dm <sup>3</sup>	
		initial	final	H <sub>2</sub> S	Fe <sup>2+</sup>	Mn <sup>2+</sup>	initial	final
10°C	1.80	9.45	8.85	0.0	0.086	0.000	65.56	70.80
15°C	1.80	9.45	8.85	0.0	0.052	0.084	65.56	71.50
15°C	1.80	9.80	9.25	0.0	0.086	0.000	65.60	70.40
15°C	4.00	10.25	10.15	0.0	0.100	0.020	65.50	71.60
22.5°C	1.80	9.50	9.45	0.0	0.070	0.078	67.20	72.50
32°C	1.80	9.40	8.70	0.0	0.084	0.105	65.50	69.60

The data presented in this table show that the optimal conditions for removal of such pollutants from water are: temperature of 10–15 °C, the hydrogen peroxide concentration - 1.8 mg/dm<sup>3</sup>, and its initial pH is adjusted to 9.45. The value of pH after treatment is equal to 8.85, which is below the drinking water standard, according to current regulations in the Republic of Moldova. The technological flowsheet for the treatment of groundwater in the village Sculeni is shown in Figure 2.

The total content of sulfides in many places of Moldova is more than 10 mg/dm<sup>3</sup>. Taking this fact into account, the identification of the treatment solutions for groundwater with a high content of sulfides is of interest. During the removal of hydrogen sulfide, into the 10 dm<sup>3</sup> of water, which contained the 10 mg/dm<sup>3</sup> H<sub>2</sub>S and 70.1 mg/dm<sup>3</sup> SO<sub>4</sub><sup>2-</sup>, the 4 cm<sup>3</sup> of 35% H<sub>2</sub>O<sub>2</sub> were added and stirred. Samples were removed every 5 min for the determination of the sulfides concentration. The kinetics of sulfides removal from the studied water is illustrated in Figure 3.

The presented data show an increase of sulfates concentration from 70.1 mg/dm<sup>3</sup> to ~100 mg/dm<sup>3</sup> in a short time (~8 min), which proves that the oxidation of hydrogen sulfide occurred and the all hydrogen sulfide present in water was transformed to sulfates.

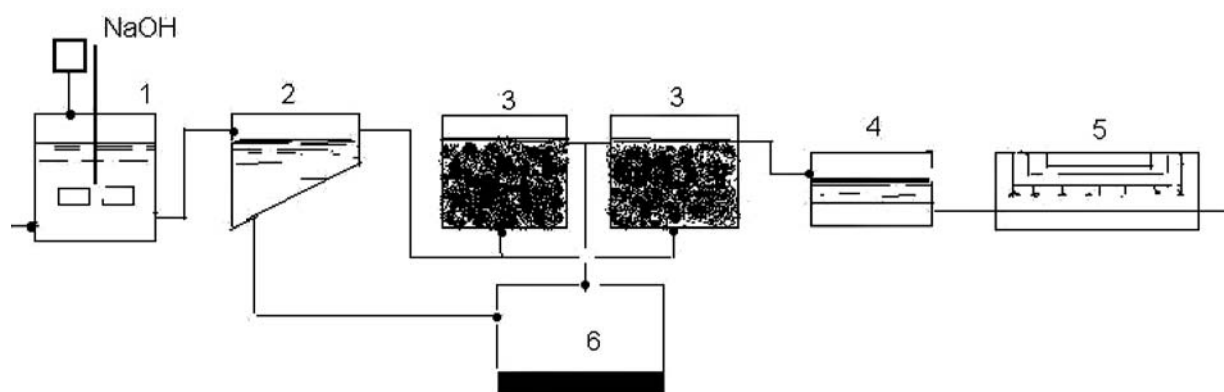


**Figure 2. Technological scheme of the removal of iron and manganese divalent ions and of hydrogen sulfide from the groundwater of village Sculeni, district Ungheni.**

1-reactor-agitator;  
2-decanter;  
3-sand filter;

4-water reservoir;  
5-UV disinfection unit;  
6- wastewater reservoir.

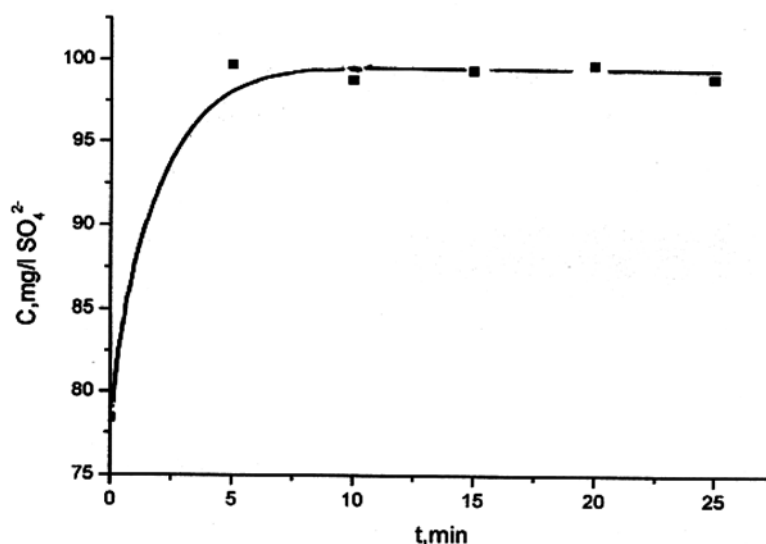


Figure 3. Kinetics of sulfides oxidation from modeled water (10 mg/dm<sup>3</sup> sulfides, 4 cm<sup>3</sup> H<sub>2</sub>O<sub>2</sub> in 10 dm<sup>3</sup> water).

### Conclusions

Processes and mechanisms of divalent ions of iron and manganese and hydrogen sulfide removal from groundwater have been studied.

The maximum efficiency of the removal of divalent ions of iron and manganese and hydrogen sulfide from the studied water was established at a temperature of 10 - 15 °C and pH adjusted to 9.45.

After filtration of purified water, the value of pH is 8.85, this value being at the upper limit of pH of drinking water standard.

Hydrogen sulfide and sulfides are oxidized to sulfates using as oxidant concentrated hydrogen peroxide.

### References

1. Goncikov, V.C.; Gubaidullina, V.C.; Kaminskaia, P.A.; Apcarian, A.C. Filtering material for water purification from iron, manganese and hydrogen sulfide. Buletine of Poliutechnik University from Tomsk, 2012, 320(3), pp. 37-40 (in Russian).
2. Gubaidullina, T.A.; Melnikov, A.G. Proceedings of the IX International Scientific-Practical Conference. Kemerovo, Russian Federation, May 16-17, 2006. pp. 204-206 (in Russian).
3. Lupascu, T.; Ciobanu, M.; Botan, V.; Gromovoy, T.; Cibotaru, S.; Petuhov, O.; Mitina T. Study of hydrogen sulfide removal from groundwater. Chemistry Journal of Moldova, 2013, 8(1), pp. 37-42.
4. Gubaidullina, T.A.; Kaminskaia, P.A.; Apcarian, A.C. Filtering material for purification water from iron, manganese and hydrogen sulfide and the method for its preparation. Russian Federation Patent, 2010, No. 2447922 (in Russian).
5. Fistic, I.F.; Vataman, I.I. Thermodynamics of the hydrolysis of metal ions. Kisinev, Stiinta, 1988. 294 p. (in Russian).

## DINUCLEAR NICKEL(II) PIVALATE WITH $\mu$ -AQUA AND DI- $\mu$ -PIVALATO BRIDGES SHOWING A FERROMAGNETIC INTERACTION

Masahiro Mikuriya<sup>a\*</sup>, Melissa Schumacher<sup>a</sup>, Chinatsu Kawano<sup>a</sup>, Takahiro Akihara<sup>a</sup>,  
Kenta Ono<sup>a</sup>, Daisuke Yoshioka<sup>a</sup>, Hiroshi Sakiyama<sup>b</sup>, Makoto Handa<sup>c</sup>

<sup>a</sup>Department of Chemistry and Research Center for Coordination Molecule-based Devices, School of Science and Technology, Kwansei Gakuin University, 2-1 Gakuen, Sanda 669-1337, Japan

<sup>b</sup>Department of Material and Biological Chemistry, Faculty of Science, Yamagata University, 1-4-12 Kojirakawa, Yamagata 990-8560, Japan

<sup>c</sup>Department of Chemistry, Interdisciplinary Graduate School of Science and Engineering, Shimane University, 1060 Nishikawatsu, Matsue 690-8504, Japan

\*e-mail: junpei@kwansei.ac.jp; phone: (+81 79) 565 83 65; fax: (+81 79) 565 90 77

**Abstract.** Dinuclear nickel(II) complex,  $[\text{Ni}_2\{\text{O}_2\text{CC}(\text{CH}_3)_3\}_4(\text{OH}_2)\{\text{HO}_2\text{CC}(\text{CH}_3)_3\}_4]$  (**1**), was synthesized and characterized by elemental analysis, IR and UV-Vis-NIR spectroscopy, and temperature dependence of magnetic susceptibilities (4.5–300 K). Single-crystal X-ray crystallography revealed a dinuclear core with  $\mu$ -aqua and di- $\mu$ -pivalato bridges having monodentate pivalato and monodentate pivalic acid molecules. Magnetic data analysis showed a ferromagnetic interactions between the two nickel atoms with  $g = 2.251$ ,  $J = 2.78 \text{ cm}^{-1}$ ,  $D = 3.75 \text{ cm}^{-1}$ , and  $tip = 184 \times 10^{-6} \text{ cm}^3 \text{ mol}^{-1}$ ;  $g = 2.253$ ,  $J = 2.73 \text{ cm}^{-1}$ ,  $D = -3.26 \text{ cm}^{-1}$ , and  $tip = 176 \times 10^{-6} \text{ cm}^3 \text{ mol}^{-1}$ .

**Keywords:** nickel complex, dinuclear complex, magnetic property, ferromagnetic interaction.

### Introduction

Copper(II) acetate is a well-known dinuclear metal complex, having a lantern-type (or paddlewheel-type) core composed of two copper(II) atoms and four acetato bridges as shown in Figure 1 (a) [1-9]. On the other hand, nickel(II) acetate is known as a mononuclear metal complex composed of one nickel(II) atom and two acetato and four aqua ligands shown in Figure 1 (b).

Although a lantern-type dinuclear core was also found in some adducts of nickel(II) pivalate [10-12], the structure of the parent complex, nickel(II) pivalate, has not been elucidated yet. Therefore, we tried to reveal the

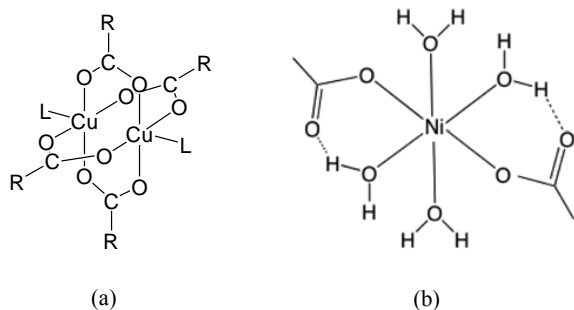


**Figure 1. Molecular structures of copper(II) acetate monohydrate (R = CH<sub>3</sub>) and nickel(II) acetate tetrahydrate.**

molecular structure of nickel(II) pivalate by crystallizing the parent complex using various kinds of organic solvents. In this study, we isolated a crystalline material by recrystallizing the product from hexane. The isolated complex was characterized by elemental analysis, IR and UV-Vis-NIR spectroscopy, measurement of temperature dependence of magnetic susceptibilities (4.5-300 K), and single-crystal X-ray crystallography. The X-ray structure analysis of the complex revealed a different dinuclear core from the lantern-type dinuclear copper(II) complexes. Interestingly temperature dependence of magnetic susceptibilities (4.5-300 K) of the complex showed a ferromagnetic property. Herein, we report on the crystal structure, spectral features, and magnetic property of this complex.

### Experimental

All reagents and solvents were obtained from commercial sources and were used without further purification.  $[\text{Ni}_2\{\text{O}_2\text{CC}(\text{CH}_3)_3\}_4(\text{OH}_2)\{\text{HO}_2\text{CC}(\text{CH}_3)_3\}_4]$  (**1**).

Nickel(II) carbonate hydroxide (0.358 g, 1.17 mmol) and pivalic acid (0.966 g, 9.45 mmol) were mixed at room temperature and then heated at 60°C with stirring for 1 hr. The resulting green product was dissolved in hexane (200 mL) and the solution was filtrated. The solution was concentrated by rotary evaporator to 5 mL and left in a refrigerator overnight. Green crystals that deposited were collected by filtration, washed with small amount of petroleum ether. Yield: 0.458 g (27.5%). Anal. Found: C, 51.08; H, 7.96%. Calcd for  $\text{C}_{40}\text{H}_{78}\text{Ni}_2\text{O}_{17}$ : C, 50.66; H, 8.29%. IR (KBr):  $\nu(\text{OH})$  3350sh, 3140sh;  $\nu_{\text{as}}(\text{CO}_2^-)$  1607, 1482;  $\nu_{\text{s}}(\text{CO}_2^-)$  1407, 1362. Diffuse reflectance spectrum:  $\lambda_{\text{max}}$  390, 664, 740 sh, 1132 nm.

Measurements: Elemental analyses for carbon, hydrogen, and nitrogen were done using a Thermo-Finnigan FLASH EA1112 series CHNO-S analyzer. Infrared spectra were measured with a JASCO MFT-2000 FT-IR Spectrometer in the 4000–600  $\text{cm}^{-1}$  region. Electronic spectra were measured with a Shimadzu UV-Vis-NIR Recording Spectrophotometer (Model UV-3100). Magnetic susceptibilities were measured with a Quantum Design MPMS-XL7 SQUID susceptometer operating at a magnetic field of 0.5 T over a range of 4.5–300 K. The susceptibilities were corrected for the diamagnetism of the constituent atoms using Pascal's constants. The effective magnetic moments were calculated from the equation  $\mu_{\text{eff}} = 2.828\sqrt{\chi_M T}$ , where  $\chi_M$  is the molar magnetic susceptibility per mole of dinuclear nickel molecule.

X-Ray crystallography: X-Ray diffraction data were collected on a Bruker SMART APEX CCD diffractometer (Mo  $K\alpha$  radiation) at 90 K and indexed using the SMART software. Crystal data and details concerning data collection are given in Table 1. The cell parameters were refined by full-matrix least-squares on  $F^2$ . Integrated intensity information for each reflections was obtained and corrected using the SAINT+ program package including the reduction program SAINT and the empirical absorption correction program SADABS. The structure was solved using the SHELXTL program. The structure was solved by direct methods, and the residual non-hydrogen atoms were located by D-Fourier synthesis. All of non-hydrogen atoms were refined by full-matrix least-squares on  $F^2$ . The hydrogen atoms except for those of water molecules were inserted at their ideal positions and fixed there. All of the calculations were carried out on a Pentium IV Windows 2000 computer utilizing the SHELXTL software package. CCDC 997144 for **1** contains supplementary crystallographic data for this paper. The data can be obtained free of charge at [www.ccdc.cam.ac.uk/conts/retrieving.html](http://www.ccdc.cam.ac.uk/conts/retrieving.html) [or from the Cambridge Crystallographic Data Centre, 12 Union Road, Cambridge CB12 1EZ, UK; fax: (internet.) +44 1223 336033; E-mail: [deposit@ccdc.cam.ac.uk](mailto:deposit@ccdc.cam.ac.uk)].

Table 1

## Crystal and experimental data.

Parameter	Value
Chemical formula	$\text{C}_{40}\text{H}_{78}\text{Ni}_2\text{O}_{17}$
Formula weight	948.44
Temperature, (K)	90
Crystal system	Monoclinic
Space group	$P2_1/n$
Z	4
a, (Å)	11.920(3)
b, (Å)	19.811(4)
c, (Å)	22.746(5)
$\beta$ , (°)	103.523(4)
V, (Å <sup>3</sup> )	5222(2)
$D_x$ , (g/cm <sup>3</sup> )	1.206
Radiation: Mo $K\alpha$ , $\lambda$ , (Å)	0.71073
$\mu$ (Mo $K\alpha$ ), (mm <sup>-1</sup> )	0.781
F, (000)	2040
Crystal size, (mm <sup>3</sup> )	0.66 × 0.39 × 0.34
No. of reflections collected	31122
No. of independent reflections	12083
$\theta$ range for data collection, (°)	1.78 - 28.44
Data/Restraints/Parameters	12083/0/551
Goodness-of-fit on $F^2$	0.974
R indices [ $I > 2\sigma(I)$ ]	$R1 = 0.0368$ , $wR2 = 0.0874$
R indices (all data)	$R1 = 0.0536$ , $wR2 = 0.0921$
$(\Delta/\sigma)_{\text{max}}$	0.000
$(\Delta\rho)_{\text{max}}$ , (eÅ <sup>-3</sup> )	0.711
$(\Delta\rho)_{\text{min}}$ , (eÅ <sup>-3</sup> )	-0.233
Measurement	Bruker Smart APEX CCD diffractometer
Program system	SHELXTL
Structure determination	Direct methods (SHELXS-97)
Refinement	full matrix least-squares (SHELXL-97)
CCDC deposition number	997144



## Results and discussion

Reaction of nickel(II) carbonate hydroxide with excess amount of pivalic acid gave green product. Successive recrystallization of the product from hexane afforded green crystals. The formulation of dinuclear species,  $[\text{Ni}_2\{\text{O}_2\text{CC}(\text{CH}_3)_3\}_4(\text{OH}_2)\{\text{HO}_2\text{CC}(\text{CH}_3)_3\}_4]$ , was confirmed by the elemental analysis, infrared and electronic absorption spectroscopies, single-crystal X-ray structure analysis, and magnetic susceptibility measurement. In the infrared spectra of **1**, two strong bands assignable to antisymmetric  $\nu_{\text{as}}(\text{CO}_2)$  stretching vibrations were observed at 1608 and 1483  $\text{cm}^{-1}$ , whereas another two bands attributable to symmetrical  $\nu_{\text{s}}(\text{CO}_2)$  stretching vibrations appear at 1407 and 1360  $\text{cm}^{-1}$ . The  $\Delta$  values of  $\nu_{\text{as}}(\text{CO}_2) - \nu_{\text{s}}(\text{CO}_2)$ ,  $1607 - 1362 = 245 \text{ cm}^{-1}$  and  $1482 - 1407 = 75 \text{ cm}^{-1}$ , are in the ranges of monodentate and *syn-syn* bridging pivalato, respectively [7,13,14] (Figure 2). The shoulder bands at 3350 and 3140  $\text{cm}^{-1}$  in **1** may be attributed to  $\nu(\text{OH})$  stretching bands of pivalic acid and water molecules [13].

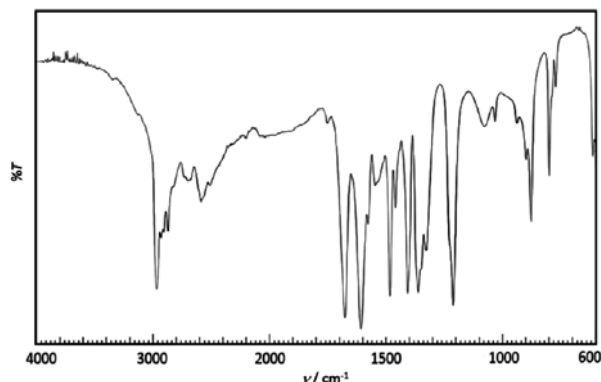


Figure 2. Infrared spectra of **1**.

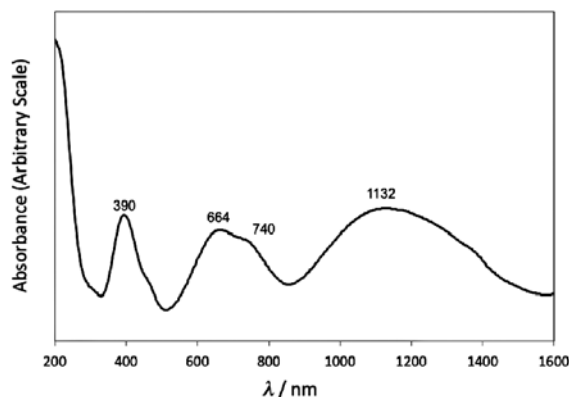


Figure 3. Diffused reflectance spectra of **1**.

The diffused reflectance spectra of **1** are shown in Figure 3. Four absorption bands appear at around 390, 664, 740 sh, and 1132 nm in solid. These bands can be attributed to d-d transitions of octahedral nickel(II) complex in origin. The first band at 1132 nm may be assigned to spin-allowed  ${}^3\text{A}_{2g}({}^3\text{F}) \rightarrow {}^3\text{T}_{2g}({}^3\text{F})$  transition, a shoulder at 740 nm to a spin-forbidden  ${}^3\text{A}_{2g}({}^3\text{F}) \rightarrow {}^1\text{E}_g({}^1\text{D})$  transition, a band at around 664 nm to spin-allowed  ${}^3\text{A}_{2g}({}^3\text{F}) \rightarrow {}^3\text{T}_{1g}({}^3\text{F})$  transition, and a band at 390 nm to spin-allowed  ${}^3\text{A}_{2g}({}^3\text{F}) \rightarrow {}^3\text{T}_{1g}({}^3\text{P})$  transition [15]. The spectral feature is in harmony with the presence of two octahedral nickel(II) ions.

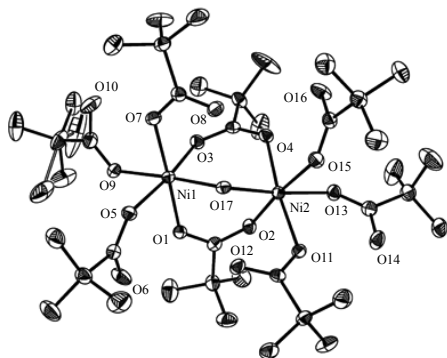


Figure 4. ORTEP drawing of the structure of the dinuclear nickel complex showing the 50% probability level thermal ellipsoids.

Selected bond lengths (Å) and angles (°):  
 Ni1···Ni2 3.3969(7), Ni1-O1 2.0336(14), Ni1-O3 2.0194(13), Ni1-O5 2.0832(13), Ni1-O7 2.0577(14), Ni1-O9 2.0640(14), Ni1-O17 2.0319(13), Ni2-O2 2.0140(14), Ni2-O4 2.0284(13), Ni2-O11 2.0532(13), Ni2-O13 2.0715(14), Ni2-O15 2.0935(14), Ni2-O17 2.0823(13), Ni1-O17-Ni2 113.57(6).

Single crystals of **1** were obtained by recrystallization of the reaction product from hexane. X-ray crystal structure analysis revealed that the present complex has a dinuclear nickel(II) core being different a little from the lantern-type dinuclear metal complexes. The structure of the dinuclear complex drawn by ORTEP is shown in Figure 4. The Ni1 atom is coordinated by two pivalato-oxygen atoms (O1 and O3) of *syn-syn*-bridging, one monodentate pivalato-oxygen atom (O7), two oxygen atoms (O5 and O9) of monodentate pivalic acid molecules, and bridging aqua-oxygen atom (O17) in an octahedral geometry, whereas the Ni2 atom is coordinated by two bridging pivalato-oxygen atoms (O2 and O4), one monodentate pivalato-oxygen atom (O11), two oxygen atoms (O13 and O15) of monodentate pivalic acid molecules and  $\mu$ -aqua-oxygen atom (O17) in an octahedral geometry. The Ni1···Ni2 distance is 3.3969(7) Å. There are hydrogen bonds between the monodentate pivalato ligand and the  $\mu$ -aqua molecule [O17(H)···O8 2.539(2) Å, O17(H)···O12 2.526(2) Å]. Another hydrogen bonds can be found between the coordinating pivalic acid molecule and the bridging pivalato group or the neighboring pivalic acid molecule [O6(H)···O1 2.564(2) Å, O10(H)···O7 2.534(2) Å, O14(H)···O11 2.567(2) Å, O16(H)···O4 2.578(2) Å]. Almost same structure was reported by Eremenko et al. [16] and Winpenny et al. [17,18], although the preparative methods are different from the present preparation. The Eremenko's crystal structure was measured

at 230 K and is almost same as the present crystal structure taken at 90 K, whereas the Winpenny's structure at 150 K belongs to different crystal system and space group, orthorhombic *Pbca*, irrespective of the similar dinuclear structure.

Temperature dependence of effective magnetic moment of **1** is shown in Figure 5. The magnetic moment is 4.65  $\mu_B$  at 300 K per dinuclear nickel(II) molecule, which is significantly higher than the spin-only value (4.00  $\mu_B$ ). The magnetic moment gradually increases with lowering of temperature until reaching 5.36  $\mu_B$  at 4.5 K, being typical of ferromagnetic behavior [19]. The magnetic data were analyzed with magnetic susceptibility Eq.(1) based on the Heisenberg model  $H = -2J\mathbf{S}_{\text{Ni1}} \cdot \mathbf{S}_{\text{Ni2}}$  considering zero-field-splitting (*D*) by the Ginsberg's method [20].

$$\chi_M = (2Ng^2\mu_B^2/3)[F_1/(kT) + 2F_5] + tip \quad (1)$$

where

$$\delta = [(3J+D)^2 - 8JD]^{1/2}$$

$$c_1 = 2(2)^{1/2}D/[(9J-D+3\delta)^2 + 8D^2]^{1/2}$$

$$c_2 = (9J-D+3\delta)/[(9J-D+3\delta)^2 + 8D^2]^{1/2}$$

$$F_0 = 2 + \exp[D/(kT)] + \exp[J/(kT)] \exp[-\delta/(kT)] + \exp[J/(kT)] \exp[\delta/(kT)] + 2\exp[4J/(kT)] + 2\exp[4J/(kT)] \exp[D/(kT)]$$

$$F_1 = \{1 + \exp[4J/(kT)] + 4\exp[4J/(kT)] \exp[D/(kT)]\} / F_0$$

$$F_2 = \{2\exp[4J/(kT)] \exp[-D/(kT)] + \exp[D/(kT)] - 1 - 2\exp[4J/(kT)]\} / F_0$$

$$F_3 = \{\exp[4J/(kT)] - \exp[J/(kT)] \exp[\delta/(kT)]\} / F_0$$

$$F_4 = \{\exp[4J/(kT)] - \exp[J/(kT)] \exp[-\delta/(kT)]\} / F_0$$

$$F_5 = F_2/D + 3c_2^2F_3/(3J-\delta) + 3c_1^2F_4/(3J+\delta).$$

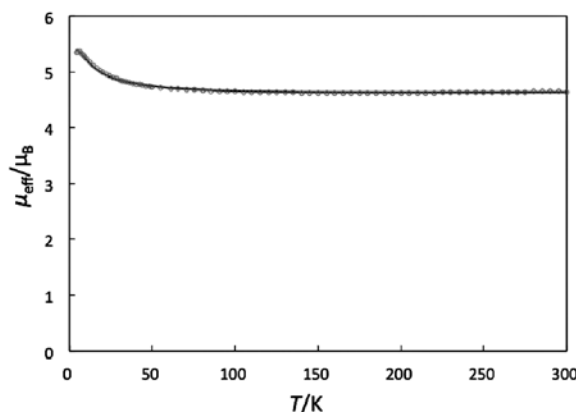


Figure 5. Temperature dependence of magnetic moment of **1**.

Best fitting curve was obtained for positive and negative *D* values, respectively:  $g = 2.251$ ,  $J = 2.78 \text{ cm}^{-1}$ ,  $D = 3.75 \text{ cm}^{-1}$ , and  $tip = 184 \times 10^{-6} \text{ cm}^3 \text{ mol}^{-1}$ ;  $g = 2.253$ ,  $J = 2.73 \text{ cm}^{-1}$ ,  $D = -3.26 \text{ cm}^{-1}$ , and  $tip = 176 \times 10^{-6} \text{ cm}^3 \text{ mol}^{-1}$  [15,21]. This result shows that a considerable ferromagnetic interaction is operating between the two nickel atoms. Similar magnetic behavior was also reported by Eremenko [16] and Winpenny [17], although a smaller *D* value was found. The bridging angle between the two nickel atoms is  $113.57(6)^\circ$  for Ni1-O17-Ni2 in the present crystal structure. The corresponding Ni-O-Ni angle is  $112.8(2)^\circ$  in Eremenko's crystal structure [16], whereas  $111.24(11)^\circ$  [17] or  $111.53(10)^\circ$  [18] in Winpenny's crystal structures. From the magneto-structural relationship between exchange interaction and Ni-O-Ni angle, the observed Ni-O-Ni angles prefer antiferromagnetic interaction rather than ferromagnetic interaction [15,19]. In this regard, we should notice that a DFT calculation showed a positive *J* value of  $3.6 \text{ cm}^{-1}$  for the Ni-O-Ni angle of  $111.53^\circ$  [18]. This may come from the combination of the hydrogen-bonded aqua and two pivalato bridges.

## Conclusions

Recrystallization of reaction product of pivalic acid and nickel(II) carbonate hydroxide from hexane gave a dinuclear nickel(II) complex,  $[\text{Ni}_2\{\text{O}_2\text{CC}(\text{CH}_3)_3\}_4(\text{OH}_2)\{\text{HO}_2\text{CC}(\text{CH}_3)_3\}_4]$ . The crystal structure revealed a unique dinuclear core with  $\mu$ -aqua- and di- $\mu$ -pivalato-bridges having monodentate pivalato and monodentate pivalic acid molecules. In contrast with the structural feature, a considerable ferromagnetic interaction was observed for the present complex.

## Acknowledgements

During the course of publication, we became aware of the literatures on the present complex. We thank the referees for their pointing out. The present work was partially supported by Grant-in-Aid for Scientific Research No. 26410080 from the Ministry of Education, Culture, Sports, Science and Technology (MEXT, Japan) and the MEXT-Supported Program for the Strategic Research Foundation at Private Universities, 2010-2014.

## References

1. Mikuriya, M. Copper(II) acetate as a motif for metal-assembled complexes. *Bulletin of the Japanese Society of Coordination Chemistry*, 2008, 52, pp. 17-28 (in Japanese).
2. Nukada, R.; Mori, W.; Takamizawa, S.; Mikuriya, M.; Handa, M.; Naono, H. Microporous structure of a chain compound of copper(II) benzoate bridged by pyrazine, *Chemistry Letters*, 1999, pp. 367-368.
3. Mikuriya, M.; Azuma, H.; Nukada, R.; Sayama, Y.; Tanaka, K.; Lim, J.-W.; Handa, M. Antiferromagnetic adducts of copper(II) propionate with pyridyl nitronyl nitroxides, *Bulletin of the Chemical Society of Japan*, 2000, 73, pp. 2493-2498.
4. Mikuriya, M.; Azuma, H.; Sun, J.; Yoshioka, D.; Handa, M. Dinuclear copper(II) complexes of free radical carboxylic acids. *Chemistry Letters*, 2002, pp. 608-609.
5. Horikoshi, R.; Mikuriya, M. One-dimensional coordination polymers from the self-assembly of copper(II) carboxylates and 4,4'-dithiobis(pyridine), *Bulletin of the Chemical Society of Japan*, 2005, 78, pp. 827-834.
6. Lorinc, S.; Koman, M.; Melnik, M.; Mikuriya, M. Mono-, di-, and polymeric copper(II) complexes with diclofenic acid (NSAID drug), structures, spectral and magnetic properties, *Advances in Coordination, Bioinorganic and Inorganic Chemistry*. ed. by Melnik, M.; Sima, J.; Tatarko, M. Slovak Technical University Press: Bratislava, 2005; pp. 176-186.
7. Mikuriya, M.; Azuma, H.; Nukada, R.; Handa, M. Synthesis, X-ray structures, and magnetic properties of  $[\text{Cu}_2(\text{piv})_4(\text{Et}_3\text{N})_2]$  and  $[\text{Cu}_6(\text{piv})_6(\text{EtO})_6]$  (Hpiv = pivalic acid): role of base for dinuclear adduct and oligonuclear formation. *Chemistry Letters*, 1999, pp. 57-58.
8. Nukada, R.; Mikuriya, M.; Yamashita, A.; Handa, M. Mononuclear and polynuclear chain compounds of copper(II) pivalate with *N,N'*-didentate ligands, *Challenges for Coordination Chemistry in the New Century*. ed. by Melnik, M.; Sirota, A. Slovak Technical University Press: Bratislava, 2001; pp. 83-88.
9. Mikuriya, M.; Azuma, H.; Handa, M. Coordination polymers of copper(II) propionate with linkage ligands, *Molecular Crystal and Liquid Crystals*, 2002, 379, pp. 205-210.
10. Kirillova, N. I.; Struchkov, Y. T.; Porai-Koshits, M. A.; Pasynskii, A. A.; Antsyshkina, A. S.; Minacheva, L. K.; Sadikov, G. G.; Idrisov, T. C.; Kalinnikov, V. T. Steric effects of nonbonded interligand interactions in dimeric adducts, Ni(II) quinaldinetrimeethylacetate and Cu(II) acridinetrimeethylacetate. *Inorganica Chimica Acta*, 1980, 40, pp. 115-119.
11. Hirashima, N.; Husebye, S.; Kato, M.; Maartmann-Moe, K.; Muto, Y.; Nakashima, M.; Tokii, T. The Magnetic Properties of Nickel(II) 2,2-Dimethylpropanoate Dimers and the Crystal Structure of Di-2,4-lutidinetetrakis( $\mu$ -2,2-dimethylpropanoate)dinickel(II). *Acta Chemica Scandinavica*, 1990, 44, pp. 984-989.
12. Morooka, M.; Ohba, S.; Nakashima, M.; Tokii, T.; Muto, Y.; Kato, M.; Steward, O. W. Dimeric nickel(II) carboxylates and a silanecarboxylate:  $[\text{Ni}(\text{Me}_3\text{CCOO})_2(2,5\text{-lutidine})_2]$ ,  $[\text{Ni}(\text{MePh}_2\text{CCOO})_2(\text{quinoline})_2] \cdot 2\text{CHCl}_3$ ,  $[\text{Ni}(\text{Me}_2\text{PhCCOO})_2(\text{quinoline})_2]$ ,  $[\text{Ni}(\text{Me}_3\text{CCOO})_2(2\text{-ethylpyridine})_2]$ ,  $[\text{Ni}(\text{Me}_3\text{CCOO})_2(2\text{-picoline})_2]$  and  $[\text{Ni}(\text{MePh}_2\text{SiCCOO})_2(\text{Ph}_3\text{P})_2]$ , *Acta Crystallographica*, 1992, C48, pp. 1888-1894.
13. Nakamoto, K. *Infrared and Raman Spectra of Inorganic and Coordination Compounds Part B*; John Wiley & Sons: Hoboken, 2009, 424 p.
14. Wada, S.; Saka, K.; Yoshioka, D.; Mikuriya, M. Synthesis, Crystal Structures, and Magnetic Properties of Dinuclear and Hexanuclear Copper(II) Complexes with Cyclam-Based Macrocyclic Ligands Having Four Schiff-Base Pendant Arms. *Bulletin of the Chemical Society of Japan*, 2010, 83, pp. 364-374.
15. Sakiyama, H.; Tone, K.; Yamasaki, M.; Mikuriya, M. Electronic spectrum and magnetic properties of a dinuclear nickel(II) complex with two nickel(II) ions of  $C_2$ -twisted octahedral geometry. *Inorganica Chimica Acta*, 2011, 365, pp. 183-189.
16. Mikhailova, T. B.; Fomina, I. G.; Sidorov, A. A.; Golovaneva, I. F.; Aleksandrov, G. G.; Novotortsev, V. M.; Ikorskii, V. N.; Eremenko, I. L. A study of magnetic properties in binuclear complexes with  $\{\text{M}_2(\mu\text{-OH}_2)(\mu\text{-OCCMe}_3)_2\}$  moiety (M = Co(II), Ni(II)). *Russian Journal of Inorganic Chemistry*, 2003, 48, pp. 1505-1512.
17. Chaboussant, G.; Basler, R.; Gudel, H.-U.; Ochsenein, S.; Parkin, A.; Parsons, S.; Rajaraman, G.; Sieber, A.; Smith, A. a.; Timco, G. A.; Winpenny, R. E. P. Nickel pivalate complexes: structural variations and magnetic susceptibility and inelastic neutron scattering studies, *Dalton Transactions*, 2004, pp. 2758-2766.
18. Rajaraman, G.; Christensen, K. E.; Larsen, F. K.; Timco, G. A.; Winpenny, R. E. P. Theoretical studies on di- and tetra-nuclear Ni pivalate complexes, *Chemical Communications*, 2005, pp. 3053-3055.
19. Mikuriya, M.; Minowa, K.; Nagao, N. Ferromagnetic coupling between an alkoxo-bridged dinickel(II) pair in a mixed-spin tetranuclear nickel(II) complex. *Inorganic Chemical Communications*, 2001, 4, pp. 441-443.
20. Ginsberg, A. P.; Martin, R. L.; Brookers, R. W.; Sherwood, R. C. Magnetic exchange in transition metal complexes. IX. Dimeric nickel(II)-ethylenediamine complexes. *Inorganic Chemistry*, 1972, 11, pp. 2884-2889.
21. Mautner, F. A.; Mikuriya, M.; Ishida, H.; Sakiyama, H.; Louka, F. R.; Humphrey, J. W.; Massoud, S. S. Dicyanamido-metal(II) complexes. Part 4: Synthesis, structure and magnetic characterization of polynuclear Cu(II) and Ni(II) complexes bridged by  $\mu$ -1,5-dicyanamide. *Inorganica Chimica Acta*, 2009, 362, pp. 4073-4080.

## SUBSTITUTED 1,3-PHENYL(PYRIDYL) PROPENONES AND DERIVATIVES WITH THIOSEMICARBAZIDIC GROUPS. STRUCTURE – (HL-60) ANTILEUKEMIA ACTIVITY RELATIONSHIP

Ana Popusoi<sup>a\*</sup>, Nicanor Barba<sup>a</sup>, Aurelian Gulea<sup>a</sup>, Jenny Roy<sup>b</sup>, Donald Poirier<sup>b</sup>

<sup>a</sup>Moldova State University, 60, Mateevici str., Chisinau, MD-2009, Republic of Moldova

<sup>b</sup>Laboratory of Medicinal Chemistry, CHUQ (CHUL) - Research Center and Université Laval, 2705 Boulevard Laurier, Québec City, G1V 4G2, Canada

<sup>\*</sup>e-mail: popusoi.ana@gmail.com; phone: (+373 22) 57 76 96

**Abstract.** 3-(4-(Dimethylamino)phenyl)-1-(4-isothiocyanatophenyl)prop-2-en-1-one was obtained from the corresponding N,N-dimethylthioureas by elimination of dimethylamine at heating with gaseous hydrogen chloride in chloroform and 1-(4-isothiocyanatophenyl)-3-(pyridin-2-yl)prop-2-en-1-one by treating 1,1-dimethyl-3-(4-(3-(pyridin-2-yl)acryloyl)-phenyl)thiourea with acetic anhydride. The difference in the reactivity of the groups >C=O and NCS in the synthesis with hydrazine hydrate and its derivatives allows the synthesis of some 1,3-disubstituted propenones with thiosemicarbazide groups (4- and 1,4-disubstituted) in good yields. From 4-substituted thiosemicarbazides and 2-formilpyridine thiosemicarbazones were obtained. In the case of some derivatives, the propenone group in the reaction with hydrazine hydrate allows the formation of pyrazole derivatives. All obtained compounds were investigated for antileukemia activity. It was found that this activity is more pronounced for thiosemicarbazide derivatives with two pyridine nuclei at concentrations 10<sup>-5</sup>-10<sup>-7</sup> mol/L.

**Keywords:** chalcones, isothiocyanatopropenones, thioureas, antileukemia activity.

### Introduction

3-(4-(Dimethylamino)phenyl)-1-(4-isothiocyanatophenyl)prop-2-en-1-one was obtained from the corresponding amine treated with triphosgene [1] in 80% yield. The authors [2] obtained this chalcone by the elimination of dimethylamine from 3-(4-(3-(4-(dimethylamino)phenyl)acryloyl)phenyl)-1,1-dimethylthiourea at heating with acetic anhydride, with an yield of 92%. This compound shows high fluorescence and can be used as marker for proteins [3] and for the synthesis of luminescence polymer nanocomposites [4].

Thiosemicarbazides 4- and 1,4-disubstituted can be obtained at the addition of hydrazine and its derivatives to isothiocyanates [5,6], or directly from N-aryl-N,N-dimethylthiourea [7]. The purpose of this study was to obtain biologically active compounds.

In the paper [8], the anticancer activity (for 5 types of cancer) was investigated for a class of chalcones with different substituents (H, CH<sub>3</sub>, OH, OCH<sub>3</sub>, N(CH<sub>3</sub>)<sub>2</sub>, Cl) for both aromatic nuclei (A and B). In some cases the chalcones with OCH<sub>3</sub> and N(CH<sub>3</sub>)<sub>2</sub> groups show higher anticancer activity. The thiosemicarbazones of some chalcones show antitumor activity for HepG2 cell line [9]. The authors [10] investigated the anticancer activity for some thiosemicarbazones with the structures depicted in Figure 1.

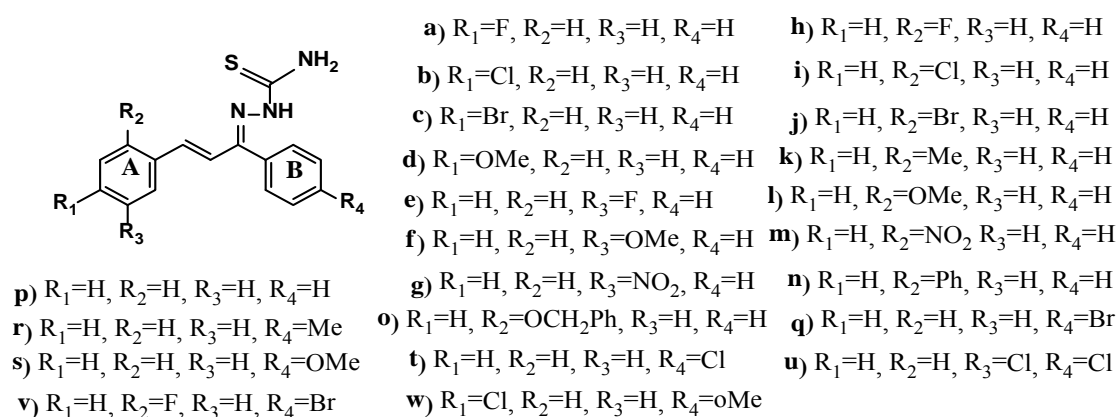


**Figure 1. The structure of chalcone thiosemicarbazide derivatives (a-w).**

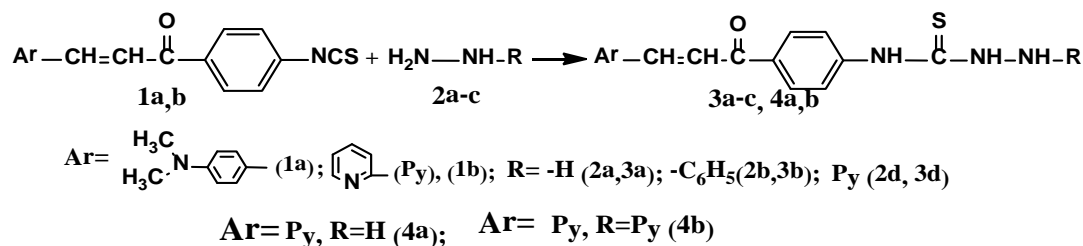
It was demonstrated that the anticancer activity depends on the nature and the position of the substituents in the structure. The 1,3-aryl(heteryl)-2-prop-1-ones chalcones at heating in a basic medium allow the formation of 1-thiocarbamoil-3-phenyl-5-heteroaril-2-pyrazoline with anticonvulsant and antidepressant properties [11].

The (1,3-aryl(heteryl)propen-2-one) chalcones with thiosemicarbazidic groups (4- and 1,4-disubstituted) and respectively thiosemicarbazones are lacking in the literature and they became our object of study.

## Results and discussion

### Chemistry

Introduction of groups 4- and 1,4-thiosemicarbazide in chalcones structure was performed by treating isothiocyanato-1,3-prop-2-one **1a, b** with hydrazine or with their derivatives **2a-d** following the Scheme 1.

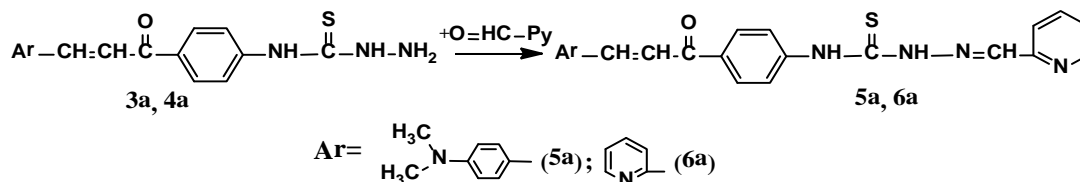


**Scheme 1. General synthesis of chalcone thiosemicarbazide derivatives (3a-c, 4a,b).**

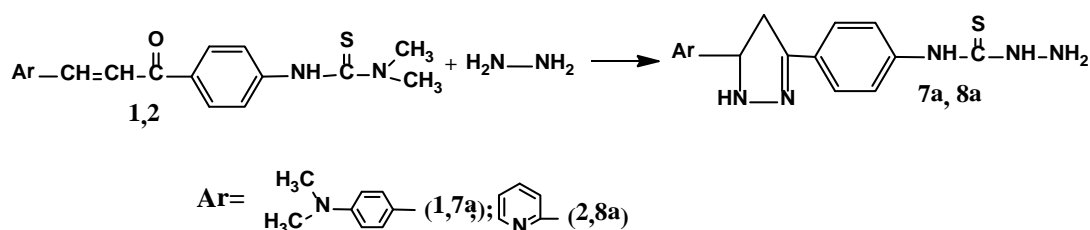
Taking into account the high activity of NCS group in the reaction with nucleophile agents, the synthesis was realized at room temperature with a molar ratio of reagents of 1:1, to exclude the participation of the carbonyl group at condensation with hydrazine hydrate and its derivatives. Benzene was used as solvent, from which the hydrazinecarbothioamides **3a-c** and **4a,b** crystallized during the synthesis. Hydrazinecarbothioamides **3a** and **4a** which condense at heating were filtrated and washed first with benzene and after with water. They were used without further recrystallization. The other compounds can be recrystallized from corresponding solvents in a yield of 60-92%.

The synthesis of N-(4-(3-(4-(dimethylamino)phenyl)acryloyl)phenyl)-2-(pyridin-2-ylmethylene)-hydrazinecarbothioamide **5a** and N-(4-(3-(pyridin-2-yl)acryloyl)phenyl)-2-(pyridin-2-ylmethylene)-hydrazinecarbothioamide **6a** (Scheme 2) is more efficient in the presence of acetic acid, when the solution of 2-formylpyridine is in excess. The solution of thiosemicarbazides **3a** or **4a** was added droplet by droplet. Thus, the interaction of chalconic >C=O group with thiosemicarbazidic group was excluded. The yields of thiosemicarbazones **5a** and **6a** reached a value of 83% and 77% (Scheme 2).

4,5-Dihydro-1H-pyrazol-3-yl)phenyl)hydrazinecarbothioamides **7a** and **8a** were obtained through the sequence of reactions that is indicated in Scheme 3.



**Scheme 2. Synthesis of hydrazinecarbothioamide (5a, 6a).**



**Scheme 3. Synthesis of chalcone derivatives (1, 7a, 2, 8a).**

First the N,N-dimethylthioureas **1,2** with hydrazine at room temperature transforms in hydrazones in pyridine, which without being isolated at heating it will cyclise in pyrazole derivatives [7]. In parallel, dimethylamine is substituted by hydrazine [11] with the formation of compounds **7a** and **8a** in good yields. Compound **7a** was also obtained by an alternative method, from isothiocyanatophenylprop-2-en-1-one **1a**, pyridine and hydrazine at room temperature, after that the mixture was heated. It could be possible that the same intermediate is formed, which is transformed into the final product **7a**.

Compounds **9a** and **10a** (Figure 2) were obtained from **7a** and **8a** at heating in ethanol with 2-formylpyridine.

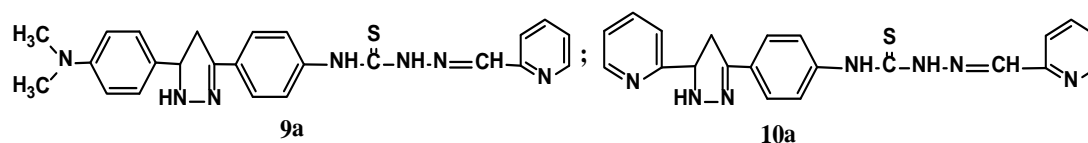


Figure 2. Structure of chalcone derivatives (9a, 10a).

### Biological Activity

#### Antiproliferative Activity of Human Leukemia HL-60 Cells

For all obtained compounds the antileukemia activity was investigated. It is more pronounced for thiosemicarbazide derivatives with two pyridine nuclei at concentrations  $10^{-5}$ - $10^{-7}$  mol/L (see Table 1).

The aryl isothiocyanates with different substituents in their structure are inactive against leukemia [12]. Isothiocyanatochalcone **1a** and 1-(4-isothiocyanatophenyl)-3-(pyridine-2-yl)prop-2-en-1-one **1b** are also inactive. Similarly, the N-phenylhydrazinecarbothioamide **11a** is inactive. It was found that the modification of the -NCS fragment in compounds **1a** and **1b** by the addition of the hydrazine and its derivatives, leads to anticancer activity for all the chalcones **3a-d**. Chalcone **3c**, which contain residues of pyridine in the first position of the thiosemicarbazidic fragment, shows an inhibition of the antileukemia of 92% at concentration of  $10^{-5}$  mol/L. It can be concluded that the introduction of the fragment  $(\text{CH}_3)_2\text{N}-\text{C}_6\text{H}_4-\text{CH}=\text{CH}-\text{CO}-$  or  $\text{Py}-\text{CH}=\text{CH}-\text{CO}-$  in the molecule of N-phenylhydrazinecarbothioamide **11a** plays an important role to increase the anticancer activity. This activity increases when the fragment  $(\text{CH}_3)_2\text{N}-\text{C}_6\text{H}_4-$  of the chalcone **3c** is replaced by rest of pyridine, propenone **4b** (100%,  $\text{C} = 10^{-5}$  mol/L).

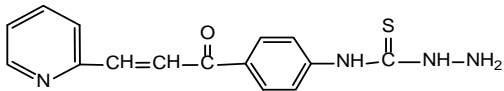
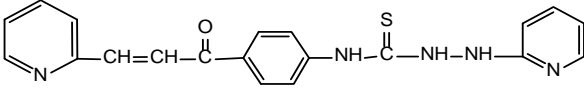
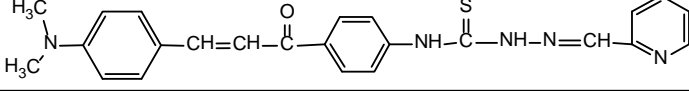
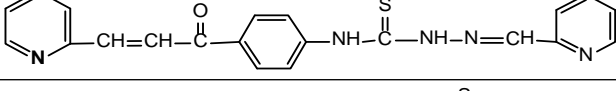
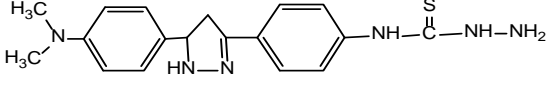
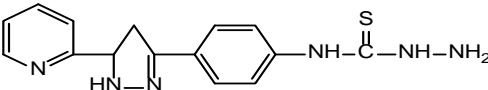
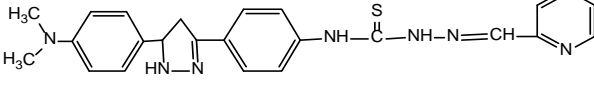
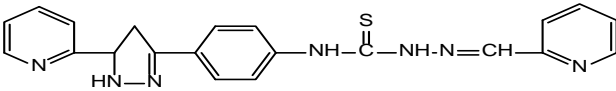
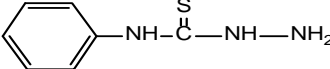
To highlight the role of the propenonic group on the anticancer activity on the propenones **3a**, **4a**, **5a** and **6a** the fragment  $-\text{CH}=\text{CH}-\text{CO}-$  was transformed in pyrazole heterocycle. For all obtained and studied samples **7a**, **8a**, **9a** and **10a** a sudden decrease of anticancer activity was observed (see Table 1). It was identified that for compound **10a** with two pyridine nuclei the inhibitor activity decrease slower when is diluted and achieves ~60% at concentration of  $10^{-7}$  mol/L. The high anticancer activity for compound **10a** can be explained by the formation of the strong hydrogen bonds between the inhibitor and the nucleic acid of the cancer cells [13].

Table 1

#### Antiproliferative activity of compounds on human leukemia (HL-60) cells at three concentrations.

No	Compound	Inhibition of cell proliferation, (%)		
		Concentration, mol/L		
		$10^{-5}$	$10^{-6}$	$10^{-7}$
1a		0	0	0
1b		0	0	0
3a		34.2	26.7	19.2
3b		52.2	6.0	0
3c		92.4	34.2	22.0

Continuation of the Table 1

4a		48.9	21.6	14.3
4b		100.0	25.1	24.6
5a		55.9	26.0	11.8
6a		100	46.7	28.5
7a		20.8	11.5	6.0
8a		30.4	24.1	20.5
9a		46.8	20.5	9.4
10a		-	62.5	58.1
11a		0	0	0

## Conclusions

Ten new propenones and thiosemicarbazidic groups have been synthesized and characterized. The IR,  $^1\text{H-NMR}$  and  $^{13}\text{C-NMR}$  data were successfully used to elucidate the formation of the structure of compounds. All obtained compounds were investigated for antileukemia activity. It was found that this activity is more pronounced for thiosemicarbazide derivatives with two pyridine nuclei at concentrations  $10^{-5}$ - $10^{-7}$  mol/L.

## Experimental

The structure of compounds **1a**, **b**, **3a-c**, **4a**, **b**, **5a**, **6a**, **7a**, **8a**, **9a** and **10a** was confirmed by elemental and spectral analysis ( $^1\text{H}$  and  $^{13}\text{C}$  NMR). The  $^1\text{H}$  and  $^{13}\text{C}$  NMR spectra were recorded on a Bruker Avance III-400 spectrometer at room temperature. All chemical shifts ( $^1\text{H}$ ,  $^{13}\text{C}$ ) are given in ppm versus  $\text{SiMe}_4$  using  $\text{DMSO-d}_6$  as solvent. Elemental analyses (C, H and N) were performed on an Elemental Analyzer Vario EL (III). Compounds **3a** and **4a** form insoluble in organic solvents polycondensed compounds at heating until the melting point. The melting points were determined with a Melting point meter A. KRUSS OPTRONIC Germany KSP-1N 90-26V/Al.

**3-(4-(Dimethylamino)phenyl)-1-(4-isothiocyanatophenyl)prop-2-en-1-one 1a.** 0.7 g (0.002 mol) of 3-(4-(3-(4-(Dimethylamino)phenyl)acryloyl)phenyl)-1,1-dimethylthiourea **1** and 6 mL of chloroform were placed in one flask. After this, the solution was cooled and gaseous hydrogen chloride was passed through it. Once the mass of the mixture increase with 0.15 g, the ampoule was welded and heated at  $70^\circ\text{C}$  for 3 hours. The resulting product was neutralized to  $\text{pH}=7$ , the organic solution was dried with  $\text{Na}_2\text{SO}_4$  and a part of the solvent was distilled. The final product was purified by chromatography on Silicagel (eluent hexane/benzene, 1/5). It was obtained 0.54 g (88%) of propenone **1a** m.p.  $136$ - $138^\circ\text{C}$  which corresponds with the literature results [2].

**Elemental analysis and NMR data:** Calculated of  $\text{C}_{18}\text{H}_{16}\text{N}_2\text{OS}$  (**1a**), %: C-70.26, H-5.28, N-9.26. Found, %: C-70.10, H-5.23, N-9.08.  $^1\text{H-NMR}$  ( $\text{DMSO-d}_6$ ), ppm: 3.02 (s, 6H,  $\text{N}(\text{CH}_3)_2$ ), 6.74-8.20 (m, 10H,  $=\text{CH}$  and  $\text{C}_6\text{H}_4$ ).  $^{13}\text{C-NMR}$  ( $\text{DMSO-d}_6$ ), ppm: 187.82 (C=O), 181.39 (C=S), 152.42 (C-N), 145.14 ( $-\text{C}_6\text{H}_4-\text{CH}=\text{C}=\text{S}$ ), 137.11 ( $-\text{C}_6\text{H}_4-\text{N}=\text{C}=\text{S}$ ), 145.14, 134.39, 131.45, 131.15, 129.46, 126.67, 122.59, 122.01, 111.54, 40.65, 40.44.

**N-(4-(3-(4-(Dimethylamino)phenyl)acryloyl)phenyl)hydrazinecarbothioamide 3a.** The mixture formed by 0.61 g (0.002 mol) 3-(4-(Dimethylamino)phenyl)-1-(4-isothiocyanatophenyl)prop-2-en-1-one **1a**, 0.13 g (0.0025 mol) hydrazine hydrate and 5 mL of ethanol was kept at room temperature for 30 min. After, it was heated at 40°C for 5 min. The CCM (silufol) show the total consumption of isothiocyanatochalcone **1a**. The reacting mixture was cooled and the resulting crystals were filtrated and washed with ethanol. Yield 0.63 g (92 %) of hydrazinecarbothioamide **3a**, m.p. >155°C (is polycondensation).

**Elemental analysis and NMR data:** Calculated of C<sub>18</sub>H<sub>20</sub>N<sub>4</sub>OS (**3a**), %: C-63.50, H-5.92, N-16.47. Found, %: C-63.53, H-6.01, N-16.84. <sup>1</sup>H-NMR (DMSO-d<sub>6</sub>), ppm: 4.89 (m, 2H, NH<sub>2</sub>), 6.71-8.82 (m, 10H, =CH, Ar-H), 10.10 (s, -NH-CS), 9.45 (s, -NH-NH<sub>2</sub>), 3.46 (s, 6H, -N(CH<sub>3</sub>)<sub>2</sub>). <sup>13</sup>C-NMR (DMSO-d<sub>6</sub>), ppm: 179.39 (C=S), 187.75 (C=O), 152.35 ((CH<sub>3</sub>)<sub>2</sub>N-Ar-CH=CH), 145.02 (Ar-CH=CH), 122.59 (Ar-CH=CH), 40.74 (CH<sub>3</sub>), 131.13, 129.09, 128.93, 124.42, 123.83, 116.53, 112.22.

**N-(4-(3-(4-(Dimethylamino)phenyl)acryloyl)phenyl)-2-phenylhydrazinecarbothioamide 3b.** To a solution of 0.61 g (0.002 mol) 3-(4-(Dimethylamino)phenyl)-1-(4-isothiocyanatophenyl)prop-2-en-1-one **1a** and 4 mL of benzene was added by droplet a solution of 0.21 g (0.002 mol) phenylhydrazine in 2 mL of benzene. The reacting mixture was let at room temperature for 1 hour and after heated at 40-45°C for 20 min. The end of the reaction was followed by chromatography by the consumption of isothiocyanatochalcone **1a**. The resulting crystals were filtrated and recrystallized from ethanol. Yield 0.73 g (88%) of thioamide **3b**, m.p. 219-221°C.

**Elemental analysis and NMR data:** Calculated of C<sub>24</sub>H<sub>24</sub>N<sub>4</sub>OS (**3b**), %: C-69.20, H-5.81, N-13.45. Found, %: C-69.32, H-5.61, N-13.65. <sup>1</sup>H-NMR (DMSO-d<sub>6</sub>), ppm: 6.73-8.10 (m, 15H, =CH, Ar-H), 10.12 (s, NH-CS), 9.96 (s, -NH-NH-Py), 8.16 (s, -NH-NH-Ar), 3.42 (s, 6H, -N(CH<sub>3</sub>)<sub>2</sub>). <sup>13</sup>C-NMR (DMSO-d<sub>6</sub>), ppm: 187.93 (C=O), 181.32 (C=S), 148.34 (-NH-NH-Ar), 143.71 (-C<sub>6</sub>H<sub>4</sub>-NH), 152.41 ((CH<sub>3</sub>)<sub>2</sub>N-Ar-CH=CH), 145.18 (Ar-CH=CH), 122.58 (Ar-CH=CH), 40.92 (CH<sub>3</sub>), 134.65, 131.16, 129.39, 124.20, 116.56, 112.24.

**2-Benzoyl-N-(4-(3-(4-(dimethylamino)phenyl)acryloyl)phenyl)hydrazinecarbothioamide 3c.** The mixture of 0.61 g (0.002 mol) 3-(4-(Dimethylamino)phenyl)-1-(4-isothiocyanatophenyl)prop-2-en-1-one **1a**, 0.23 g (0.0021 mol) 2-hydrazinylpyridine and 6 mL of benzene was kept at room temperature for 1 hour and after heated at 40°C for 5 min. The total consumption of isothiocyanatochalcone **1a** was checked by chromatography. The resulting mixture was cooled and the resulting crystals were filtered out. Yield 0.76 g (92 %) of hydrazinecarbothioamide **3d** with m.p. 178-180°C, (from ethanol).

**Elemental analysis and NMR data:** Calculated of C<sub>23</sub>H<sub>23</sub>N<sub>5</sub>OS (**3d**), %: C-66.16, H-5.55, N-16.77. Found, %: C-66.18, H-5.52, N-16.79. <sup>1</sup>H-NMR (DMSO-d<sub>6</sub>), ppm: 6.68-8.16 (m, 13H, =CH, Ar-H, Py-H), 10.10 (s, NH-CS), 9.97 (s, NH-NH-Py), 8.65 (s, NH-NH-Py), 3.42 (s, 6H, -N(CH<sub>3</sub>)<sub>2</sub>). <sup>13</sup>C-NMR (DMSO-d<sub>6</sub>), ppm: 187.92 (C=O), 181.36 (C=S), 159.47 (-NH-NH-Py), 139.26 (-C<sub>6</sub>H<sub>4</sub>-NH), 152.42 ((CH<sub>3</sub>)<sub>2</sub>N-Ar-CH=CH), 145.14 (Ar-CH=CH), 122.59 (Ar-CH=CH), 131.16, 124.33, 116.58, 112.24, 107.94, 40.65 (CH<sub>3</sub>).

**N-(4-(3-(pyridin-2-yl)acryloyl)phenyl)hydrazinecarbothioamide 4a.** The mixture of 0.53 g (0.002 mol) 1-(4-isothiocyanatophenyl)-3-(pyridine-2-yl)prop-2-en-1-one **1b**, 0.13 g (0.0025 mol) of hydrazine hydrate and 2 mL of benzene was stirred at room temperature for 2 hours until the total consumption of isothiocyanate **1b**. After the mixture was cooled down and the formed crystals were filtrated, washed with water and dried. Yield 0.38 g (64%) of carbothioamide **4a**, m.p. 169-171°C.

**Elemental analysis and NMR data:** Calculated of C<sub>15</sub>H<sub>14</sub>N<sub>4</sub>OS (**4a**), % C-60.38, H-4.73, N-18.78. Found, %: C-60.47, H-4.84, N-18.97. <sup>1</sup>H-NMR (DMSO-d<sub>6</sub>), ppm: 3.89 (m, 2H, NH<sub>2</sub>), 7.36-8.70 (m, 10H, =CH, Ar-H), 10.50 (s, -NH-CS), 9.48 (s, -NH-NH<sub>2</sub>). <sup>13</sup>C-NMR (DMSO-d<sub>6</sub>), ppm: 180.39 (C=S), 188.09 (C=O), 152.39 (Py-CH=CH), 144.96 (Ar-CH=CH), 122.59 (Ar-CH=CH), 137.42, 133.72, 126.58, 122.31.

**2-(Pyridin-2-yl)-N-(4-(3-(pyridin-2-yl)acryloyl)phenyl)hydrazinecarbothioamide 4b.** The solution of 0.53 g (0.002 mol) 1-(4-isothiocyanatophenyl)-3-(pyridine-2-yl)prop-2-en-1-one **1b**, 0.22 g (0.002 mol) 2-hydrazinylpyridine and 4mL of benzene was stirred at room temperature for 2 hours. After, the solution was cooled down and the resulting crystalline product was filtered and recrystallized from ethanol. Yield 0.64 g (85%) m.p. 198-200°C.

**Elemental analysis and NMR data:** Calculated of C<sub>20</sub>H<sub>17</sub>N<sub>5</sub>OS (**4b**), %: C-63.98, H-4.56, N-18.65. Found, %: C-63.96, H-4.58, N-18.64. <sup>1</sup>H-NMR (DMSO-d<sub>6</sub>), ppm: 6.78-8.36 (m, 13H, =CH, Ar-H, Py-H), 10.12 (s, NH-CS), 9.91 (s, NH-NH-Py), 8.68 (s, NH-NH-Py). <sup>13</sup>C-NMR (DMSO-d<sub>6</sub>), ppm: 187.92 (C=O), 181.36 (C=S), 159.47 (-NH-NH-Py), 139.26 (-C<sub>6</sub>H<sub>4</sub>-NH), 154.42 (Py-CH=CH), 145.17 (Ar-CH=CH), 122.56 (Ar-CH=CH), 131.16, 124.33, 116.58, 112.24, 107.94.

**N-(4-(3-(4-(Dimethylamino)phenyl)acryloyl)phenyl)-2-(pyridin-2-ylmethylene)hydrazinecarbothioamide 5a.** To the solution of 0.24 g (0.0023 mol) 2-formylpyridine, 0.1 g of CH<sub>3</sub>COOH and 1 mL of dimethylformamide was



added under stirring droplet by droplet to a of 0.68 g (0.002 mol) N-(4-(3-(4-(Dimethylamino)phenyl)acryloyl)phenyl)hydrazinecarbothioamide **3a** in 2 mL of dimethylformamide during 30 min at room temperature and after heated at 40°C. After, the reacting mixture was heated at 70°C for 3 hours (the consumption of carbothioamide **3a** was verified by chromatography), diluted with small amount of water and cooled. Yield 0.71 g (83%) of final product **5a** with m.p. 133-135°C, (from dimethylformamide).

**Elemental analysis and NMR data:** Calculated of  $C_{24}H_{23}N_5OS$  **5a**, %: C-67.11, H-5.40, N-16.30. Found, %: C-67.10, H-5.42, N-16.33. **<sup>1</sup>H-RMN** (DMSO- $d_6$ ), ppm: 6.74-8.61 (m, 14H, =CH, Ar-H, Py-H), 3.42 (s, 6H, -N(CH<sub>3</sub>)<sub>2</sub>), 10.46 (s, **NH**-CS), 12.24 (s, **NH**-N=CH). **<sup>13</sup>C-NMR** (DMSO- $d_6$ ), ppm: 187.26 (C=S), 188.02 (C=O), 153.41 (**Py**-CH=N-NH-), 152.47 (-NH-N=CH-Py), 145.36 (Ar-CH=CH), 122.18(Ar-CH=CH-), 144.58 (-C<sub>6</sub>H<sub>4</sub>-**NH**), 40.92 (CH<sub>3</sub>), 130.46, 128.87, 121.3.

Similar procedure was used for the synthesis of **N-(4-(3-(pyridin-2-yl)acryloyl)phenyl)-2-(pyridin-2-ylmethylene)hydrazinecarbothioamide 6a** with an yield of 77%, m.p. 192-194°C.

**Elemental analysis and NMR data:** Calculated of  $C_{21}H_{17}N_5OS$  **6a**, %: C-65.10, H-4.42, N-18.08. Found, %: C-65.72, H-4.62, N-18.33. **<sup>1</sup>H-RMN** (DMSO- $d_6$ ), ppm: 7.43-8.68 (m, 14H, =CH, Ar-H, Py-H), 3.42 (s, 6H, -N(CH<sub>3</sub>)<sub>2</sub>), 10.64 (s, **NH**-CS), 12.25 (s, **NH**-N=CH). **<sup>13</sup>C-NMR** (DMSO- $d_6$ ), ppm: 188.94 (C=O), 176.37 (C=S), 153.08 (**Py**-CH=N-NH-), 150.48 (-NH-N=CH-Py), 145.47 (Ar-CH=CH), 125.57 (Ar-CH=CH-), 143.66 (-C<sub>6</sub>H<sub>4</sub>-**NH**), 134.15, 125.57, 122.33.

**N-(4-(5-(4-(Dimethylamino)phenyl)-4,5-dihydro-1H-pyrazol-3-yl)phenyl)hydrazinecarbothioamide 7a. a)** The mixture of 0.70 g (0.002 mol) 3-(4-(3-(4-(Dimethylamino)phenyl)acryloyl)phenyl)-1,1-dimethylthiourea **1**, 0.22 g (0.0044 mol) hydrazine hydrate and 5 mL of pyridine was let at room temperature for 24 hours and after heated at 90-95°C for 3 hours. The resulting crystals were filtered and recrystallized from methanol. Yield 0.54 g (77%) of thioamide **7a** with m.p. 173-174°C.

**b)** The mixture of 0.61 g (0,002 mol) 3-(4-(Dimethylamino)phenyl)-1-(4-isothiocyanatophenyl)prop-2-en-1-one **1a**, 0.26 g (0.0025 mol) hydrazine hydrate and 5 mL of pyridine was left to stand at room temperature for 24 hours. The consumption of propenone **1a** was, verified by chromatography. After the reacting mixture, was heated at 90-95°C for 3 hours. The resulting product was isolated like in the case "a". Yield 0.58 g (82%) of thioamide **7a**, m.p. 172-174°C.

**Elemental analysis and NMR data:** Calculated of  $C_{18}H_{22}N_6S$  **7a**, %: C-60.99, H-6.26, N-23.71. Found, %: C-61.07, H-6.21, N-23.74. **<sup>1</sup>H-NMR** (DMSO- $d_6$ ), ppm: 4.73 (m, 2H, NH<sub>2</sub>), 6.69-7.66 (m, 8H, =CH, Ar-H), 3.39 (m, 2H, CH<sub>2</sub>), 10.39 (s, **NH**-CS), 9.89 (s, **NH**-NH<sub>2</sub>). **<sup>13</sup>C-NMR** (DMSO- $d_6$ ), ppm: 176.55 (C=S), 153.45 (Ar-CH-NH=N), 139.26 (-C<sub>6</sub>H<sub>4</sub>-**NH**), 63.86 (-CH<sub>2</sub>-C(-C<sub>6</sub>H<sub>4</sub>-)=N), 40.95 (CH<sub>3</sub>), 130.44, 129.46, 127.69, 125.54, 112.92, 63.82.

The **N-(4-(5-(pyridin-2-yl)-4,5-dihydro-1H-pyrazol-3-yl)phenyl)hydrazinecarbothioamide 8a** was obtained similarly from 1,1-dimethyl-3-(4-(3-(pyridin-2-yl)-acryloyl)-phenyl)thiourea **2** and hydrazine hydrate with an yield of 77%, with m.p. 199-201°C (from ethanol).

**Elemental analysis and NMR data:** Calculated of  $C_{15}H_{16}N_6S$  **8a**, %: C-57.67, H-5.16, N-26.90. Found, %: C-57.62, H-5.20, N-26.91. **<sup>1</sup>H-NMR** (DMSO- $d_6$ ), ppm: 4.95 (m, 2H, NH<sub>2</sub>), 7.27-8.58 (m, 8H, =CH, Ar-H, Py-H), 3.42 (m, 2H, CH<sub>2</sub>), 9.19 (s, **NH**-CS), 8.53 (s, **NH**-NH<sub>2</sub>). **<sup>13</sup>C-NMR** (DMSO- $d_6$ ), ppm: 179.70 (C=S), 162.16 (**Py**-CH-NH=N), 150.05 (**Py**-CH(CH<sub>2</sub>)NH-N=), 139.74 (-C<sub>6</sub>H<sub>4</sub>-**NH**), 64.89 (-CH<sub>2</sub>-C(-C<sub>6</sub>H<sub>4</sub>-)=N), 149.44, 129.28, 125.85, 122.49, 64.89.

**N-(4-(5-(4-(dimethylamino)phenyl)-4,5-dihydro-1H-pyrazol-3-yl)phenyl)-2-(pyridin-2-ylmethylene)hydrazinecarbothioamide 9a.** To a solution of 0.7g (0.002 mol) N-(4-(5-(4-(dimethylamino)phenyl)-4,5-dihydro-1H-pyrazol-3-yl)phenyl)hydrazinecarbothioamide **7a** and 8 mL of CH<sub>3</sub>COOH was added under stirring 0.22 g (0.002 mol) of 2-formylpyridine. The reacting mixture was let at room temperature for 24 hours and after heated at 70-80°C for 2 hours. After, the resulting mixture was neutralized with a solution of NaHCO<sub>3</sub>. The resulting crystalline product was filtered and recrystallized from acetone. Yield 0.53 g (60%) of final product with m.p. 168-169°C.

**Elemental analysis and NMR data:** Calculated of  $C_{22}H_{26}N_6S$  (**9a**), %: C-67.84, H-5.92, N-18.99. Found, %: C-67.65, H-5.75, N-18.41. **<sup>1</sup>H-NMR** (DMSO- $d_6$ ), ppm: 6.52-8.63 (m, 13H, =CH, Ar-H, Py-H), 3.73 (m, 2H, CH<sub>2</sub>), 10.34 (s, **NH**-CS), 12.18 (s, **NH**-N=CH), 3.62 (s, 6H, -N(CH<sub>3</sub>)<sub>2</sub>). **<sup>13</sup>C-NMR** (DMSO- $d_6$ ), ppm: 178.26 (C=S), 156.26 (**Py**-CH=N-NH-), 152.73 (-NH-N=CH-Py), 52.03 (Ar-CH-(CH<sub>2</sub>)NH-N=), 140.16 (-C<sub>6</sub>H<sub>4</sub>-**NH**), 64.95 (-CH<sub>2</sub>-C(-C<sub>6</sub>H<sub>4</sub>-)=N), 149.98, 133.89, 129.20, 127.30, 122.90.

**N-(4-(5-(pyridin-2-yl)-4,5-dihydro-1H-pyrazol-3-yl)phenyl)-2-(pyridin-2-ylmethylene)hydrazinecarbothioamide 10a.** To the solution of 0.62g (0.002 mol) N-(4-(5-(pyridin-2-yl)-4,5-dihydro-1H-pyrazol-3-yl)phenyl)hydrazinecarbothioamide **8a** and 8 mL of dimethylformamide was added under stirring 0.22 g (0.002 mol) of 2-formylpyridine, previously dissolved in 1 mL of ethanol. The reacting mixture was heated at 70-80°C for 2 hours, after diluted with water and cooled to room temperature. The resulting crystalline product was filtered and recrystallized from ethanol. Yield 0.48 g (63%) of final product **10a** with m.p. 140-142°C.

**Elemental analysis and NMR data:** Calculated of  $C_{21}H_{19}N_7S$  (**10a**), %: C-62.82, H-4.77, N-24.42. Found, %: C-62.85,

H-4.75, N-24.41. <sup>1</sup>H-NMR (DMSO-d<sub>6</sub>), ppm: 6.10-8.67 (m, 13H, =CH, Ar-H, Py-H), 3.33 (m, 2H, CH<sub>2</sub>), 10.42 (s, NH-CS), 12.22 (s, NH-N=CH). <sup>13</sup>C-NMR (DMSO-d<sub>6</sub>), ppm: 176.66 (C=S), 158.18 (Py-CH=N-NH-), 152.16 (-NH-N=CH-Py), 152.07 (Py-CH-(CH<sub>2</sub>)-NH-N=), 139.30 (-C<sub>6</sub>H<sub>4</sub>-NH), 64.95 (-CH<sub>2</sub>-C(-C<sub>6</sub>H<sub>4</sub>-)=N), 143.98, 138.89, 129.28, 127.79.

### Cytotoxicity Assay

**Cell culture.** Human promyelocytic leukemia cells HL-60 (ATCC, Rockville, MD, USA) were routinely grown in suspension in 90% RPMI-1640 (Sigma, Saint Louis, USA) containing L- glutamine (2 mM), antibiotics (100 IU penicillin/mL, 100 mg streptomycin/mL) and supplemented with 10% (v/v) foetal bovine serum (FBS), in a 5% CO<sub>2</sub> humidified atmosphere at 37°C. Cells were currently maintained twice a week by diluting the cells in RPMI 1640 medium containing 10% FBS.

**Cell proliferation assay.** The cell proliferation assay for compounds and ligands was performed using 3-(4,5-dimethylthiazol-2-yl)-5-(3-carboxymethoxyphenyl) 2-(4-sulfophenyl)-2H-tetrazolium (MTS) (Cell Titer 96 Aqueous, Promega, USA), which allowed us to measure the number of viable cells. In brief, triplicate cultures of 10,000 cells in a total of 100 mL medium in 96-well microtiter plates (Becton Dickinson and Company, Lincoln Park, NJ, USA) were incubated at 37°C, 5% CO<sub>2</sub>. All compounds were dissolved in ethanol to prepare the stock solution of 1 J 1022 M. These compounds and doxorubicin (Novapharm, Toronto, Canada) which was used as a positive control were diluted at multiple concentrations (1 and 10 μM) with culture media and added to each well and incubated for 3 days. Following each treatment, MTS (20 μL) was added to each well and the mixture was incubated for 4 hours. MTS is, converted to water-soluble colored formazan by dehydrogenase enzymes present in metabolically active cells. Subsequently, the plates were read at 490 nm using a microplate reader (Molecular Devices, Sunnyvale, CA).

### References

- Dzurilla, M.; Kristian, P. The synthesis infrared and ultraviolet absorption spectra of 4-substituted 3'- and 3'-isothiocyanatochalcones. Collection of Czechoslovak Chemical Communications, 1970, 35, pp. 417-429.
- Barbă, N.; Luchita, G.; Barbă, A.; Vieru, R. Process for isothiocyanatochalcones preparation, Patent for invention MD 2985, 2004 (in Romanian).
- Kessler, M.A.; Meinitzer, A.; Wolfbeis, O.S. Albumin Blue 580 fluorescence assay for Albumin. Analytical Biochemistry, 1997, 248, pp.180-182.
- Popusoi, A.; Barba, N.; Dragalina, G.; Culeac, I.; Robu, Ș. Synthesis and study of materials of copolymers of luminophores 4-aminostiren grafted with isothiocyanatochalcones. The XXXI-st Romanian Chemical Conference, Romania, 2010, p. 141 (in Romanian).
- Pelkis, P.S.; Pereteajco M.Z. Synthesis of substituted 1,4-diphenylthiosemicarbazides. Russian Journal of General Chemistry, 1961, XXXI(11), pp. 3726-3728 (in Russian).
- Yousef, T.A.; Badria, F.A.; Ghazy, S.E. In vitro and in vivo antitumor activity of some synthesized 4-(2-pyridyl)-3-Thiosemicarbazides derivatives. International Journal of Medicine and Medical Sciences, 2011, 3, pp. 37-46.
- Gutu, Ia.; Boi, L.V.; Barba, N. Process for 4-aryl and 1,4-diarylthiosemicarbazides preparation. Inventor's certificate USSR 1643533, 15, 1991 (in Russian).
- Suvitha, S.; Siddig, I. A. Synthesis of Chalcones with Anticancer Activities. Molecules, 2012, 17, pp. 6179-6195.
- Hu, K.; Yang, Z.H.; Pan, S.S.; Xu, H.J.; Ren, J. Synthesis and antitumor activity of liquiritigenin thiosemicarbazone derivatives. European Journal of Medicinal Chemistry, 2010, 45, pp. 3453-3458.
- Hong-Jia, Z.; Yong, Q.; Di-Di, Z.; Xu-Guang, Y. Synthesis, molecular modeling and biological evaluation of chalcone thiosemicarbazide derivatives as novel anticancer agents. European Journal of Medicinal Chemistry, 2011, 46, pp. 4702-4708.
- Ozan, R.; Zuhail, O.; Unsal, C. Synthesis of and Pharmacological Studies on The Antidepressant and Anticonvulsant Activites of Some 1,3,5-trisubstituted pyrazolines. Arzneimittel-Forsch. Drug Research, 2005, 55(8), pp. 431-436.
- Robinson, T.P.; Hubbard, R.B.; Ehlers, T.J.; Arbiser, J.L.; Goldsmith, D.J.; Bowena, J.P. Synthesis and biological evaluation of aromatic enones related to curcumin. Bioorganic Medicinal Chemistry, 2005, 13, pp. 4007-4013.
- Gulea, A.; Poirier, D.; Roy, J.; Stavila, V.; Bulimestru, I.; Țapecov, V.; Bârcă, M.; Popovsch, L. In vitro antileukemia, antibacterial and antifungal activities of some 3d metal complexes: Chemical synthesis and structure-activity relationships. Journal of Enzyme Inhibition and Medicinal Chemistry, 2008, 23, pp. 806-818.

## POLYMER NANOCOMPOSITE BASED ON STYRENE WITH BUTYL METHACRYLATE AND INORGANIC SEMICONDUCTOR CdS

Mihail Iovu<sup>a</sup>, Mihai Enachescu<sup>b</sup>, Ion Culeac<sup>a\*</sup>, Victor Verlan<sup>a</sup>, Stefan Robu<sup>c</sup>,  
Dionezie Bojin<sup>b</sup>, Iurie Nistor<sup>a</sup>, Ion Cojocaru<sup>a</sup>

<sup>a</sup>Institute of Applied Physics of Academy of Sciences of Moldova, 5, Academiei str., Chisinau MD 2028, Republic of Moldova

<sup>b</sup>CSSNT, University Politehnica of Bucharest, 313, Splaiul Independentei, sector 6, Bucharest, RO-060042, Romania

<sup>c</sup>Moldova State University, 60, Mateevici str., Chisinau MD 2009, Republic of Moldova

\*e-mail: ionculeac@gmail.com

**Abstract.** We present experimental results on copolymer-based nanocomposite made of styrene with butyl methacrylate (1:1) and inorganic semiconductor CdS. Thin film composite samples have been characterized by UV-Vis absorption and photoluminescent spectroscopy, as well as by transmission electron microscopy. Transmission electron microscope examination confirms a relatively narrow distribution of CdS nanoclusters in the SBMA matrix, which covers the range 2-10 nm. On the other side, the average CdS particles size estimated from the position of first excitonic peak in the UV-Vis absorption spectrum was found to be 2.8 nm and 4.4 nm for two samples with different duration of thermal treatment, which is in good agreement with PL experimental data. The PL spectrum for CdS nanocrystals is dominated by near-band-edge emission. The relatively narrow line width (40-45 nm) of the main PL band suggests the nanoparticles having narrow size distribution. On the other side, relatively low PL emission from surface trap states at longer wavelengths were observed in the region 500-750 nm indicating on recombination on defects.

**Keywords:** nanocomposite, polymer matrix, photoluminescence, exciton.

### Introduction

Nanocomposite (NC) materials belong to one of the most dynamic domain of research and development, and they occupy an important place in the field of nanotechnology [1-6]. Nanocomposite materials made of a polymer matrix and an inorganic semiconductor have become a prominent area of research and technology because of their attractive properties [4-6]. NCs offer a variety of new possibilities beyond those of conventional materials as well as compared to NCs constituent components. The basic feature of nanoscale materials resides in the possibility of tuning of their physical and chemical properties through varying the size of incorporated nanoparticles. This actually means obtaining different properties within the same chemical composition just by changing the size of nanoparticles [7-10].

Among existing variety of nanocomposite materials polymer based NCs attract a lot of research efforts because of many advantages, compared to conventional materials. These advantages refer to their relatively simple technology, low cost, easy tuning, etc. Polymer NCs can be obtained in the form of thin films, bulk, or fiber samples, etc., by relatively simple technological methods, among them drop-wise deposition, spin coating, extrusion, etc. Polymer based NC materials with inorganic semiconductors comprise a polymer material as a matrix and incorporated inorganic semiconductor nanoparticles as fillers [11-12]. The role of the polymer matrix in nanocomposites is to assemble the nanoparticles into clusters, avoiding agglomeration, inducing ordering and orientation in self-assembling structures, etc.

As one of the most important II-VI group semiconductors CdS nanoparticles have received great attention because of their attractive properties and potential for application in photonics and optoelectronics [14-16]. In the present work we report preparation and characterization of photoluminescent polymer-inorganic nanocomposite thin films based on styrene-butylmethacrylate copolymer (SBMA) (1:1) and inorganic semiconductor CdS.

### Experimental

The technology of preparation of the nanocomposite thin films made of styrene with butylmethacrylate (SBMA) (1:1) and inorganic semiconductor CdS was described elsewhere [17-18]. At the first step a solution of cadmium nitrate  $Cd(NO_3)_2$  was mixed with a solution of thiocarbamide,  $SC(NH_2)_2$ , taken in equimolar ratio. In this way we obtain a complex compound  $Cd(NO_3)_2 \times SC(NH_2)_2$ , well soluble in distilled water. The SBMA copolymer, which is used as a matrix, was dissolved in an organic solvent, partially hydrophilic (e.g. dimethylformamide). In this way a copolymer solution with concentration 10 g of polymer in 100 ml solvent was prepared. At the next step an appropriate quantity of  $Cd(NO_3)_2 \times SC(NH_2)_2$  related to CdS concentration of 20 and 40 mass% relative to SBMA copolymer was added in the solution. All this composition was mixed by vigorous stirring. For preparation of the nanocomposite thin films the final solution was cast onto a clean, flat glass plate, and heated at 100 °C during 30-60 min.

The composite layers were obtained on clean glass substrates for measuring of optical transmission and photoluminescence. The thickness of the thin film layers was in the range 5-15 μm. Nanocomposite thin films were characterized by measuring UV-Vis transmission and photoluminescent (PL) spectra, and by transmission electron microscopy (TEM EM 410). Optical transmission spectra of the samples were registered in the range 400–800 nm on a

Specord UV-Vis spectrophotometer or M40 photospectrometer. PL spectra of nanocomposite thin films were measured at room temperature under excitation of a laser beam 337 or 405 nm using a MDR-23 monochromator and a Hamamatsu photomultiplier module H9319-12 operating in a photon counting regime.

## Results and discussion

Examination of prepared thin films suggests that they contain clusters of CdS of different sizes. This can be seen on nanocomposite thin films *SBMA + 40%CdS* deposited on glass substrate (Figure 1). Transmission electron microscope images indicate on a relatively narrow distribution of the CdS nanoclusters in the SBMA matrix, which covers the range  $\sim 2$ -10 nm (Figure 1a). The small nanoparticle diameter correlates with the strong shift of the PL maximum at  $\sim 383$  nm. On the other hand, in the case of larger thermal treatment time one can observe a less dispersed but larger nanoclusters diameter (Figure 1b). From the image in Figure 1b the nanoparticles size can be estimated to be in the range  $\sim 20$ -30 nm. The UV-Vis absorption spectra of nanocomposite thin-film samples deposited on glass substrates are presented in Figure 2. The position of the main excitonic peak one can clearly distinguish on these spectra. These peaks are situated at 381 nm (2.97 eV) and 429 nm (3.28 eV) respectively.

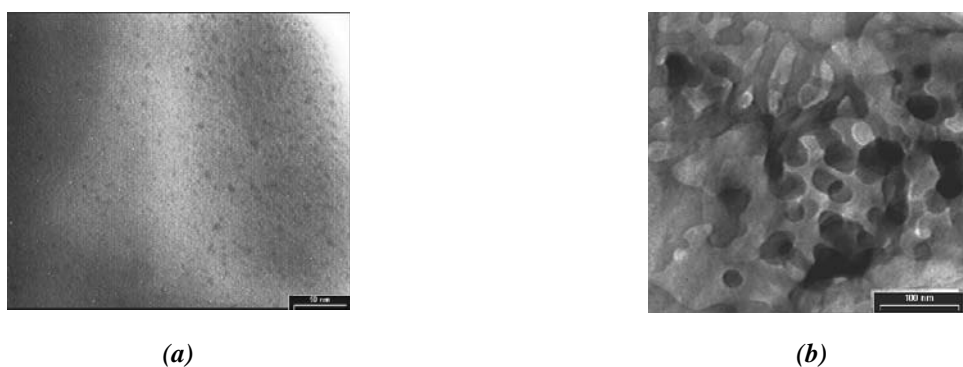


**Figure 1. TEM image of the nanocomposite thin films SBMA+40%CdS obtained at different thermal treating time 30 (a) and 60 (b) min.**

The size of nanoparticles has been evaluated from the position of the first excitonic peak from the data in Figure 2 through the empirical relation [19-21]:

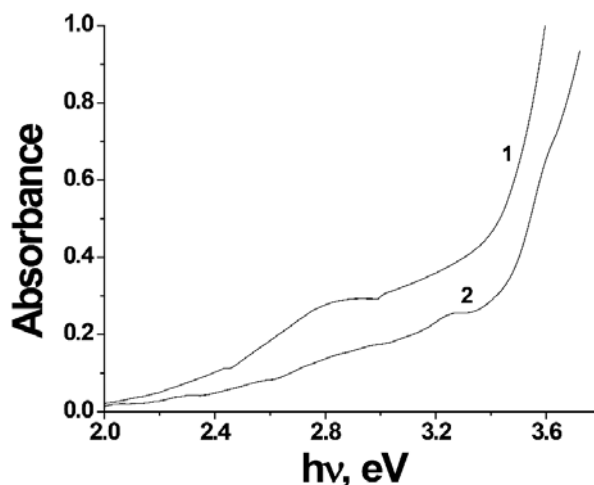
$$D = (-6.6521 \times 10^{-8})\lambda^3 + (1.9557 \times 10^{-4})\lambda^2 - (9.2352 \times 10^{-2})\lambda + (13.29), \quad (1)$$

where  $D$  (nm) is the diameter of the nanoparticles and  $\lambda$  (nm) is the wavelength of the first excitonic peak of the corresponding sample. In this way we can evaluate the diameter of the nanoparticles as 2.8 nm and 4.4 nm. Such nanoparticles size implies a strong confinement of the charge carriers, while the confinement energies of the electron and hole are much larger than the energy of Coulomb interaction [22,24]. The position of the first excitonic energy can be estimated from the relation, which connects the size of the nanocrystal and the excitonic energy  $E$  [21-23]:

$$E = E_g + \frac{\hbar^2 \pi^2}{2R^2} \left( \frac{1}{m_e^*} + \frac{1}{m_h^*} \right) - \frac{1}{R} \left( \frac{1.8e^2}{4\pi\epsilon_0\epsilon_r} \right), \quad (2)$$

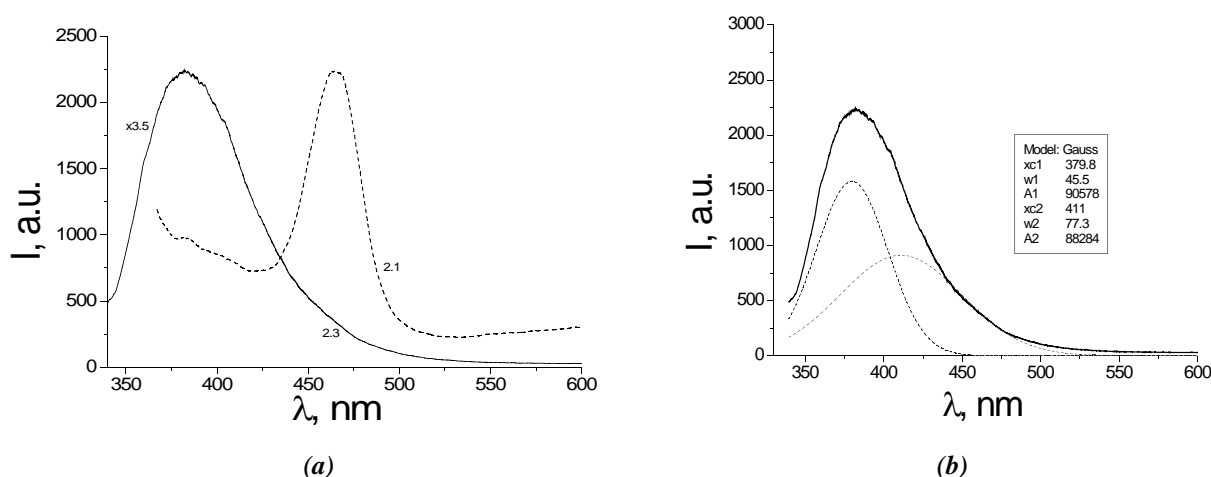
where  $E_g$  is the energy gap of bulk CdS,  $R$  is the size of the nanoparticle,  $m_e^*$  and  $m_h^*$  are the effective masses of the electron and hole. The corresponding values for the effective masses are as reported elsewhere [24-26]:  $\frac{m_e^*}{m_0} = 0.19$  and  $\frac{m_h^*}{m_0} = 0.8$ ; and the dielectric constant  $\epsilon_r = 5.7$ ;  $\epsilon_0$  is the permittivity of free space and  $e$  is the electron charge. If we take

the particles diameter as determined from the absorption spectra in Figure 2 as  $D_1 = 2.8$  nm and  $D_2 = 4.4$  nm, then the calculated exciton energies are respectively 2.72 eV and 3.36 eV. On the other side the positions of the main excitonic peak determined from the absorption spectra in Figure 2 are 2.97 eV (curve 1) and 3.28 eV (curve 2) respectively. These values are higher than the energy gap  $E_g$  of the bulk CdS (2.42 eV at 300 K [24-26]) which indicates on a blue shift of the absorption edge. The increase of the band gap is determined by the quantum size effect of these small crystallites, and the calculated diameter of the nanocrystals (2.8 nm and 4.4 nm) is comparative to the excitonic Bohr radius  $\sim 3$  nm of CdS [21-23].



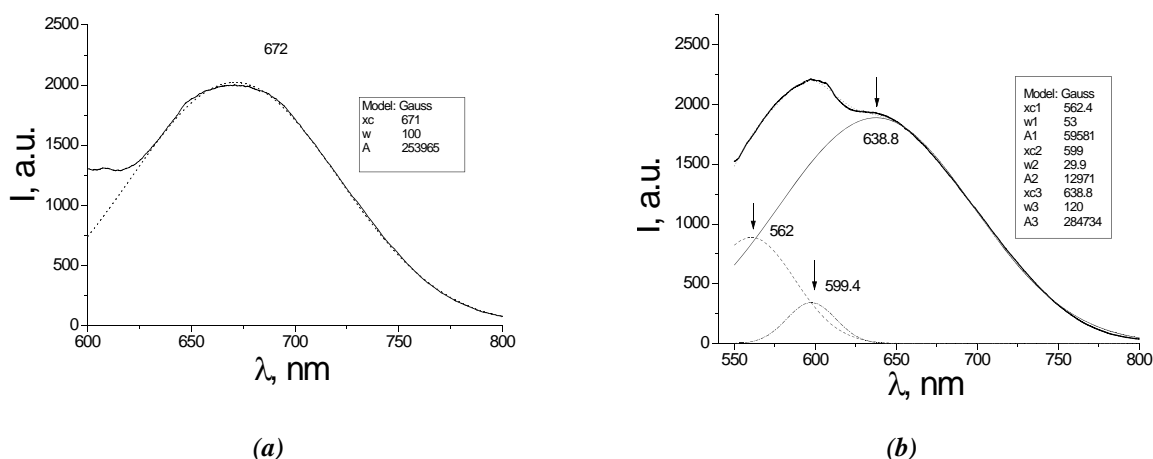
**Figure 2. Absorbance spectrum of SBMA+40%CdS nanocomposite samples with different nanoparticles size: (1) 2.8 nm and (2) 4.4 nm.**

Figure 3 represents the PL spectra of nanocomposites SBMA/CdS measured in two different samples SBMA/CdS characterized by different nanoparticles size [27]. Nanocomposite samples SBMA/CdS exhibit a luminescent signal in the range 350–600 nm, with the position of PL maximums varying in dependence of the dimensions of the CdS nanoparticles in polymer matrix. Variation of the thermal treatment time leads to variation of the size of CdS nanoparticles and shifts the maximum of the photoluminescence peak in the high energy region. The PL emission peaks of the nanocomposites SBMA/CdS are found to be located at 383 nm and 463 nm respectively (samples 2.3 and 2.1 in Figure 3a). The excitonic energy for the corresponding nanocomposite samples (Figure 2) corresponds to 2.97 and 3.28 eV respectively. These values indicate that the luminescence peaks are Stokes-shifted from their band gap energy. The full width at half maximum (FWHM) of the PL peak in Figure 3a represents 45 (2.3) and 40 nm (2.1). The full width of  $\sim 40$  nm suggests the size dispersion of the nanoparticles around the mean diameter value is relatively narrow. The broadening of the PL spectra for the sample 2.3 of approximately  $\sim 45$  nm can be attributed basically to nanoparticle size dispersion and less to the presence of charges on the surface of the nanoparticles [24–27]. The PL maximums can be attributed to direct transitions from the conduction band to valence band.



**Figure 3. PL spectra of NC SBMA+40% CdS measured at room temperature under excitation 337 nm: (a) sample 2.3 – nanoparticles size 2.4 nm; sample 2.1 – nanoparticles size 4.2 nm; (b) deconvolution of PL spectra for sample 2.3.**

In addition to blue-violet PL main bands nanocomposite samples exhibit several weaker red peaks positioned at 562 nm, 599 and 639 nm (Figure 4). While the PL maxima in the visible range can be attributed to direct transitions from the conduction band to valence band, the PL emission in the red range can be associated to the transitions from the donor levels to the valence band of CdS [25–27].



**Figure 4. PL spectra of nanocomposite samples SBMA/CdS under excitation of light beam 405 nm: (a) SBMA+20% CdS (sample 1.1); (b) SBMA+40% CdS (sample 2.1).**

Figure 5 illustrates the scheme of optical absorption in CdS nanoparticles incorporated in the copolymer matrix SBMA. In the case of confinement the absorption spectrum of the nanocrystallites exhibits a quasi discrete character versus the photon energy and the density of states in quantum dots peaks at certain energies. As a result of the confinement the energetic QDs gap increases compared to bulk semiconductor. The nanocrystallite energetic spectrum behaves like an isolate hydrogen atom with the energetic levels  $1s$ ,  $1p$ ,  $1d$ , etc.

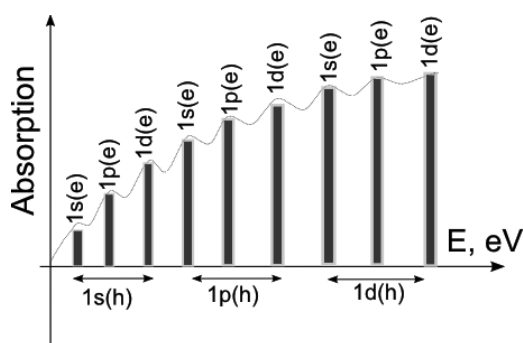


**Figure 5. A simplified scheme of QDs energy levels and their absorption bands in the SBMA/CdS nanocomposite.**

When a photon is absorbed by the CdS semiconductor an electron is excited from the valence into the conduction band, and a positively-charged hole is created in the valence band. When the excitation energy corresponds to optical transition  $1s(h) - 1s(e)$  one or two electrons can appear on the energetic level  $1s(e)$  (Figure 5). In the later case the level  $1s(e)$  is split into two sublevels  $1s_{1/2}(e)$  and  $1s_{3/2}(e)$  with anti-parallel spins. In this way, as a result of optical excitation an exciton is created – a bound state of electron and hole, which are attracted to each other by the electrostatic Coulomb force. The onset of the optical absorption can be considered as the threshold of optical absorption of the CdS nanocrystals. At each absorption event an exciton appears, consequently because of many different energetic levels there are many different groups of excitons. The smallest excitonic energy can be determined from the relation (2), and this energy can be attributed to the absorption threshold of confined nanoparticle.

PL mechanism is illustrated in Figure 6. Under UV radiation the electrons from the holes levels  $1s$ ,  $1p$  and  $1d$  are excited to the electrons levels  $1s$ ,  $1p$  and  $1d$ . When the photon energy is absorbed in CdS material excitons appear. In the case of annihilation of these excitons a photon is emitted, according to the transitions  $1s(e) - 1s(h)$ ,  $1p(e) - 1s(h)$ ,  $1d(e) - 1s(h)$ , etc. In the case of CdS incorporated in the copolymer SBMA matrix, additional to the transitions described above, there are other transitions with energy transfer from the singlet and triplet levels in the copolymer to the energy levels of CdS nanocrystal  $1s(e)$ ,  $1p(e)$ ,  $1d(e)$  (Figure 6). Because of the dispersion of the size of CdS nanoparticles in the matrix of SBMA the magnitude of FWHM is a bit larger. Besides, there are PL bands shifted to red, and which can be related to the defects within the bulk of CdS as well as on the surface of nanocrystalites.

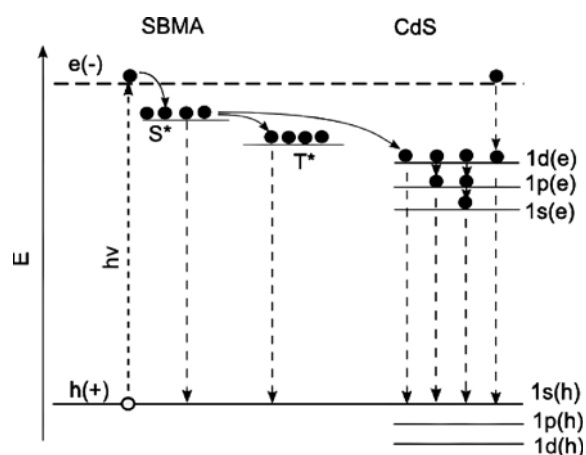


Figure 6. Illustration of the mechanism of energy transfer and photoluminescence in NC.

## Conclusions

Copolymer-based nanocomposites made of styrene with butyl methacrylate and inorganic semiconductor CdS have been investigated. Nanocomposite samples with the concentration of CdS semiconductor 20 and 40% have been studied. The average CdS particle size estimated from TEM correlates with the particle size estimated from the UV-Vis absorption spectrum and was found to be in the range 2-10 nm. The nanocomposite samples exhibit a major PL band in the visible range 350-500 and a weak PL signal in the range 600-800 nm.

## Acknowledgement

This research was supported by the Academy of Sciences of Moldova (research grants 11.817.05.03A, 13.820.05.15/RoF and 14.819.02.20A).

## References

- Paul, D.R.; Robeson, L.M. Polymer nanotechnology: Nanocomposites, *Polymer*, 2008, 49, pp. 3187-3204.
- Wang, Y. Fiber-Optic Sensors for Fully-Distributed Physical, Chemical and Biological Measurement. PhD Thesis, Virginia Polytechnic Institute, Blacksburg, Virginia, 2012.
- Jorge, P.; Martins, M.A.; Trindade, T.; Santos, J.L.; Farahi F. Optical Fiber Sensing Using Quantum Dots, *Sensors*, 2007, 7, pp. 3489-3534.
- Li, S.; Lin, M.M.; Toprak, M.S.; Kim, D.K.; Muhammed, M. Nanocomposites of polymer and inorganic nanoparticles for optical and magnetic applications, *Nano Reviews*, 2010, 1, doi:10.3402/nano.v1i0.5214.
- Shenhar, R.; Norsten, T.B. Polymer-Mediated Nanoparticle Assembly: Structural Control and Applications, *Advanced Materials*, 2005, 17, pp. 657-669.
- Godovsky, D.Y. Device applications of polymer-nanocomposites. *Advances in Polymer Sciences*, Springer-Verlag, Berlin Heidelberg, 2000, 153, pp. 163-205.
- Wang, Y.; Herron, N. Nanometer-sized semiconductor clusters: materials synthesis, quantum size effects, and photophysical properties. *Journal of Physical Chemistry*, 1991, 95, pp. 525-532.
- Chouksey, P.; Tiwari, M.; Chandra, B.P. Luminescence Studies of Nanoparticle/Polymer Nano-Composites, *International Journal of Advanced Mechanical Engineering & Applications*, 2011, 1, pp. 106-111.
- Murray, C.B.; Noms, D.J.; Bawendi, M.G. Synthesis and Characterization of Nearly Monodisperse CdE (E = S, Se, Te) Semiconductor Nanocrystallites, *Journal of the American Chemical Society*, 1993, 115, pp. 8706-8715.
- Chen, X.; Yu, Z.T.; Chen, J.S.; Yang, B. In situ hydrothermal preparation of CdS/polymer composite particles with cadmium-containing polymer latexes. *Materials Letters*, 2004, 58, pp. 384-386.
- Lakowicz, J.R.; Gryczynski, I.; Gryczynski, Z.; Murphy, C.J. Luminescence Spectral Properties of CdS Nanoparticles, *Journal of Physical Chemistry B*, 1999, 103, pp. 7613-7620.
- Yoon, H.; Rhym, Y.-M.; Shim, S.E. Optical properties of core/shell typed PMMA/CdS nanoparticles prepared by in situ and ex situ surfactant-free emulsion polymerization, *Colloid Polymer Sciences*, 2011, 289, pp. 1185-1189.
- Sounderya, N.; Zhang, Y. Use of Core/Shell Nanoparticles for Biomedical Applications, *Recent Patents on Biomedical Engineering*, 2008, 1, pp. 34-42.
- Mondal, S.P.; Mullick, H.; Lavanya, T.; Dhar, A.; Ray, S.K.; Lahiri, S.K. Optical and dielectric properties of junctionlike CdS nanocomposites embedded in polymer matrix, *Journal of Applied Physics*, 2007, 102(6), 064305(7p).
- Rong, M.Z.; Zhang, M.Q.; Liang, H.C.; Zeng, H.M. Surface derivatization of nano-CdS clusters and its effect on

- the performance of CdS quantum dots in solvents and polymeric matrices, *Applied Surface Science*, 2004, 228, pp. 176–190.
16. Prabhu R. R.; Abdul Khadar, M. Characterization of chemically synthesized CdS nanoparticles, *PRAMANA Journal of Physics*, 2005, 65, pp. 801-807.
  17. Popusoi, A.; Barba, N.; Dragalina, G.; Cuculescu, E.; Caraman, M.; Robu, S. Photoluminescent polymeric nanocomposites based on aromatic chalcones derivatives (Nanocompozite polimerice fotoluminescente din derivati ai chalconelor aromatice). *PRIOCHIM*, 2009, Sinaia, Romania, p. 44.
  18. Iovu, M.; Tiginyanu, I.; Culeac, I.; Robu, S.; Nistor, Iu.; Dragalina, G.; Enachi, M.; Petrenko, P. Nanostructured Polymer/CdS Photoluminescent Thin Films, *Journal of Nanoelectronics and Optoelectronics*, 2013, 7, pp. 1-5.
  19. Wang, Y.; Suna, A.; Mahler, W.; Kasowski, R. PbS in polymers. From molecules to bulk solids. *The Journal of Chemical Physics*, 1987, 87, pp. 7315-7322.
  20. Yu, W. W.; Qu, L.; Guo, W.; Peng, X. Experimental Determination of the Extinction Coefficient of CdTe, CdSe, and CdS Nanocrystals, *Chemistry of Materials*, 2003, 15, pp. 2854-2860.
  21. Brus, L. Quantum crystallites and nonlinear optics, *Applied Physics A*, 1991, 53(6), pp. 465-474.
  22. Chukwuocha, E. O.; Onyeaju, M. C.; Harry, T. S. T. Theoretical Studies on the Effect of Confinement on Quantum Dots Using the Brus Equation, *World Journal of Condensed Matter Physics*, 2012, 2, pp. 96-100.
  23. Chukwuocha, E. O.; Onyeaju, M. C. Effect of Quantum Confinement on The Wavelength of CdSe, ZnS and GaAs Quantum Dots (QDs), *International Journal of Scientific & Technology Research*, 2012, 1(7), pp. 21-24.
  24. Zou, Y.; Li, D.; Yang, D. Noninjection Synthesis of CdS and Alloyed CdS<sub>x</sub>Se<sub>1-x</sub> Nanocrystals Without Nucleation Initiators, *Nanoscale Research Letters*, 2010, 5, pp. 966–971.
  25. Pilla, V.; Munin, E.; Dantas, N. O.; Silva A. C. A.; Andrade, A. A. Photothermal Spectroscopic Characterization in CdSe/ZnS and CdSe/CdS Quantum Dots: A Review and New Applications, *Quantum Dots - A Variety of New Applications*, Dr. Ameenah Al-Ahmadi (Ed.), ISBN: 978-953-51-0483-4, InTech, DOI: 10.5772/36814. <http://www.intechopen.com/books/quantum-dots-a-variety-of-new-applications/photothermal-spectroscopic-characterization-in-cdse-zns-and-cdse-cds-quantum-dots-a-review-and-new-applications>.
  26. Murphy, C. J.; Coffey, J. L. Quantum Dots: A Primer, *Applied Spectroscopy*, 2002, 56(1), pp. 16A-27A.
  27. Iovu, M.; Tighineanu, I.; Culeac, I.; Robu, S.; Nistor, Iu.; Dragalina, G.; Enachi, M.; Petrenko, P.; Verlan, V. Preparation and Characterization of Polymer/CdS Nanostructured Photoluminescent Films, *Proceedings of the International Congress ARA37, Chisinau 4-9 June, 2013*, pp. 558-561.



# ELECTRONIC CONTROL OF MOLECULAR CONFIGURATION INSTABILITY VIA VIBRONIC COUPLING. PSEUDO JAHN-TELLER STABILIZATION OF VERTICALLY EXCITED STATES OF F<sub>2</sub>CO, N<sub>2</sub>H<sub>2</sub> AND H<sub>2</sub>C<sub>2</sub>O MOLECULES

Natalia Gorinchoy

*Institute of Chemistry of Academy of Sciences of Moldova, 3, Academiei str., Chisinau MD-2028, Republic of Moldova  
e-mail: ngorinchoy@yahoo.com*

**Abstract.** The pseudo Jahn-Teller effect is employed to explain the origin of distortions of carbonyl fluoride, diazene and ketene molecules in the lowest singlet and triplet excited states. The ground state and the excited electronic states of considered molecules were calculated by *ab initio* SCF CI method with the use of the 631G-type basis set. The corresponding pseudo Jahn-Teller coupling constants are estimated by fitting the *ab initio* data for the adiabatic potential curves of the molecules to the general formula, obtained from the vibronic theory. With these data an explanation of both the larger instability of the triplet excited states as compared with the singlet ones and the elongation of the corresponding bond distances in the excited states is obtained.

**Keywords:** Pseudo Jahn-Teller effect, stereochemistry, excited states, carbonyl fluoride, diazene, ketene.

## Introduction

The stereochemistry of molecular systems is determined by their electronic structure and the permutation symmetry of identical atoms. The latter means that from the viewpoint of symmetry any molecule must possess the spatial structure with the highest possible symmetry. However, depending on the electronic state the high-symmetry nuclear configuration can become unstable, and the molecule is distorted. Any perturbation of molecular system (excitation, ionization, coordination to transition metal complexes etc.) changes its electronic state and, as a consequence, may lead to distortion of its nuclear configuration.

The problem of electronic control on nuclear configuration instability has already some history. In the case of degenerate electronic states the configuration instability is a direct consequence of the Jahn-Teller effect (See, e.g. in [1-3]). It has also been shown that the only reason of instability of the high-symmetry nuclear configurations and structural distortions of any molecular system in the non-degenerate state is the pseudo Jahn-Teller effect (PJTE), that is the vibronic mixing of considered state with the appropriate by symmetry excited states [1, 2, 4-7]. Hence the instabilities should be sought for in the electronic states which mix strongly under nuclear displacements, and vice versa. If there is instability, there should be corresponding excited states that cause the instability of the reference configuration. The electronic control of the instabilities via vibronic coupling has been considered in detail in a series of papers [4-13].

One of the examples of electronic control on nuclear configuration instability is the stabilization of vertically excited states. The available experimental and theoretical data indicate that in the electronically excited states molecules may adopt equilibrium geometries very different from those in the ground states. Moreover, the distortions of some molecules in the lowest triplet state are stronger than in the excited singlet state of the same symmetry. In [14] the pseudo Jahn-Teller effect was used to explain the origin of the carbonyl group bending in the lowest excited states of formaldehyde molecule. It was shown that the larger distortion of formaldehyde in the triplet excited state as compared with the singlet one can be explained by the larger vibronic contribution to the curvature of the adiabatic potential (AP) for the triplet state. However, the non-vibronic contribution to the curvature of the AP has not been evaluated, and the resulting values of the curvature along the distortion coordinate in these two states were not obtained.

In the present work the pseudo Jahn-Teller effect is employed to reveal the origin of geometry peculiarities of carbonyl fluoride F<sub>2</sub>CO, diazene N<sub>2</sub>H<sub>2</sub> and ketene H<sub>2</sub>C<sub>2</sub>O molecules in the excited states. These molecules are rather well studied. All of them are planar in the ground electronic states, but have distorted geometry of lower symmetry in the excited states. Thus, for the tetraatomic carbonyl molecules X<sub>2</sub>CO (X=H, F, Cl) it was shown experimentally and by quantum chemical calculations that electronic excitation from the ground to the lowest excited singlet and triplet states results in lengthening of C-O distance and pyramidalization of the carbonyl fragment, which is planar in the ground state (See, for example [15-17] and references herein). Moreover, in the triplet excited state distortion is stronger than in the singlet one (Figures 1b, 1c).

The diimide molecule N<sub>2</sub>H<sub>2</sub> (also referred to as 1,2-diazene) has a *trans*-planar shape of C<sub>2h</sub> symmetry in the ground <sup>1</sup>A<sub>g</sub> state, but the lowest excited singlet and triplet states are predicted to have nonplanar "skewed" anticline (C<sub>2</sub>) structures, the dihedral angle being by ≈10° smaller for the triplet state compared with the singlet one (Figure 2) [18-20].

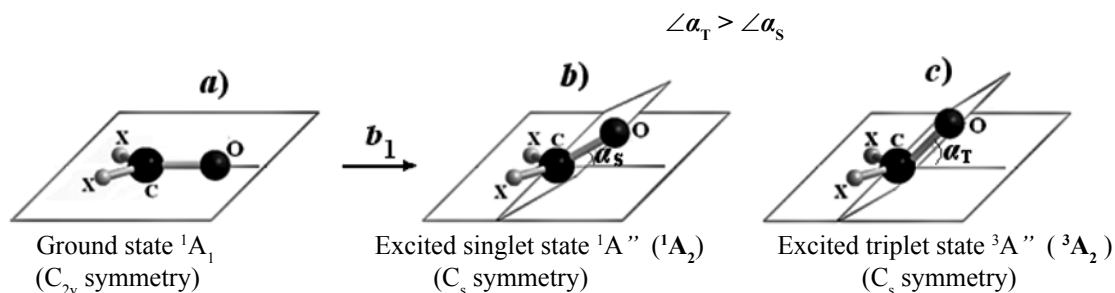


**Figure 1.** Geometry of  $X_2CO$  molecules in (a) the ground state  ${}^1A_1$ , (b) the excited singlet state  ${}^1A_2$ , and (c) the excited triplet state  ${}^3A_2$ .

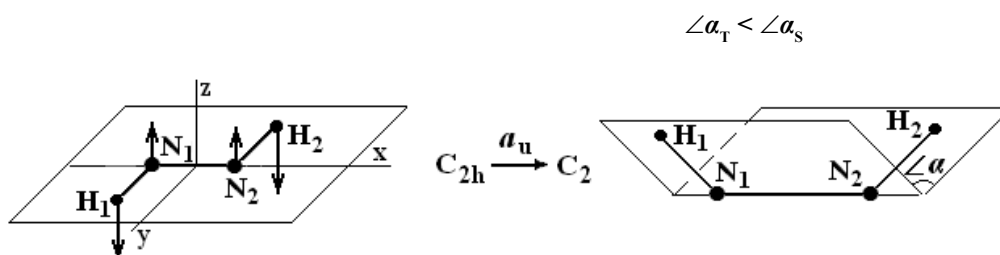


**Figure 2.** Geometry of  $N_2H_2$  molecule in the ground  ${}^1A_g$  and excited  ${}^{1,3}B_g$  state singlet states. The arrows show the displacement of  $a_u$  type leading to the nonplanar  $C_2$  structure.

Ketene molecule in the ground  ${}^1A_1$  electronic state is also planar with the nuclear configuration of  $C_{2v}$  symmetry, while it has peculiar geometries in the excited states. It was established that in the first excited triplet state the molecule undergoes the in-plane distortion leading to the in-plane  $C_s$  structure ( $C_s^{\parallel}$  in Figure 3) with the elongated C-C bond, while in the second triplet state it has the out-of-plane distorted nuclear configuration ( $C_s^{\perp}$  in Figure 3), also with the elongated C-C bond [21, 22].

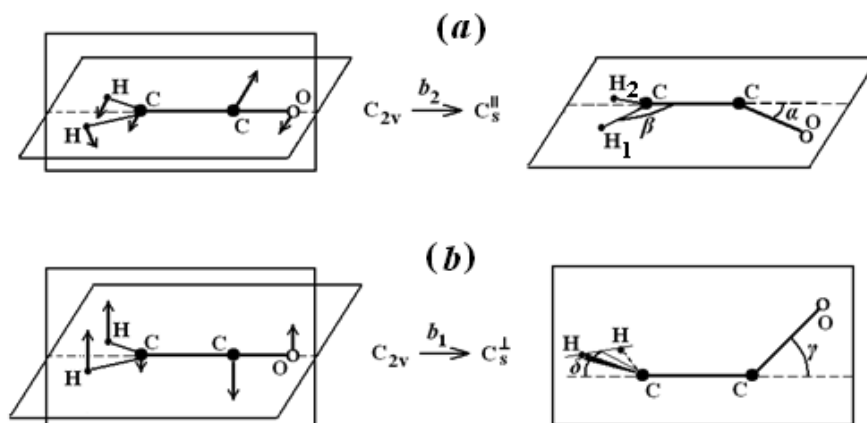


**Figure 3.** Ketene geometries in the ground ( $C_{2v}$ ) and low-lying  ${}^3A_2$  ( $C_s^{\parallel}$ ) and  ${}^3A_1$  ( $C_s^{\perp}$ ) excited states. In what is designated  $C_s^{\parallel}$ , the molecule is planar but the oxygen and the  $CH_2$  group are bent from the C-C axis at the angles  $\alpha$  and  $\beta$ , respectively. In configuration designated as  $C_s^{\perp}$ , the reflection plane is perpendicular to the molecular plane of the  $C_{2v}$  structure.

Many studies of molecules under consideration were devoted to the determination of their equilibrium geometries in the ground and the lowest excited states, vertical excitation energies, potential barriers to inversion, the harmonic frequencies calculations etc. [15-22]. However, the origin of stabilization of their vertically excited states, accompanied by changes in molecular geometry, as well as the reasons of the larger distortion in the triplet state compared with the excited singlet one were not considered at all.

In all the cases the electronic structure calculations were carried out, the PJTE parameters (non-vibronic contribution to the curvature of the AP, the vibronic coupling constants, the resulting values of the curvature) were estimated, and it was shown that structural distortions of the molecules in the excited states are due to the vibronic mixing of considered states with the appropriate by symmetry higher-lying excited states.

### Methods and computational details

The theory of the PJTE is well developed (See, e.g. in [1-3]). We present here the basic formulas that will be needed in further discussion of the results. In this approach the problem of the stability or instability of molecular nuclear configuration is reduced to the estimation of the curvature  $K$  of the adiabatic potential energy surface (APES) of the molecular system in the arbitrary direction  $Q_r$  at the high-symmetry configuration  $Q_0$  for which the first derivatives are zero. The exact expression for  $K$  of any molecular system in the state  $|\Gamma_1\rangle$ , ground or excited, can be obtained in the second order perturbation theory with respect to small nuclear displacements  $Q_r$ :

$$K_{\Gamma}^{\Gamma_1} = K_{0\Gamma}^{\Gamma_1} + K_{v\Gamma}^{\Gamma_1} = \langle \Gamma_1 | (\partial^2 H / \partial Q_r^2)_0 | \Gamma_1 \rangle - 2 \sum_i \frac{|\langle \Gamma_1 | (\partial H / \partial Q_r)_0 | \Gamma_i \rangle|^2}{(E_{\Gamma_i} - E_{\Gamma_1})}. \quad (1)$$

Here  $H$  is the adiabatic electronic Hamiltonian of the system which includes all Coulomb interactions between electrons and nuclei, and  $|\Gamma_i\rangle$  and  $E_{\Gamma_i}$  are the electronic wave functions and the total energies for the equilibrium nuclear configuration, respectively. The first term in Eq.(1),  $K_{0\Gamma}^{\Gamma_1}$ , is the so-called primary force constant. It determines the restoring force arising when the nuclei are displaced with respect to the “frozen” electronic distribution. The second term,  $K_{v\Gamma}^{\Gamma_1}$ ,

$$K_{v\Gamma}^{\Gamma_1} = -2 \sum_{\Gamma_i} |F_{\Gamma}^{\Gamma_1 \Gamma_i}|^2 / (E_{\Gamma_i} - E_{\Gamma_1}) \quad (2)$$

results from the vibronic contribution. It takes into account the reduction of  $K$  due to the partial “floating” of electrons, their relaxation. This term is always negative if the vibronic mixing takes place only with the higher states. In Eq.(2)  $F_{\Gamma}^{\Gamma_1 \Gamma_i}$  is the constant of vibronic coupling between the states  $|\Gamma_1\rangle$  and  $|\Gamma_i\rangle$  under the distortion  $Q_r$ :

$$F_{\Gamma}^{\Gamma_1 \Gamma_i} = \langle \Gamma_1 | (\partial H / \partial Q_r)_0 | \Gamma_i \rangle. \quad (3)$$

Note that the vibronic constants  $F_{\Gamma}^{\Gamma_1 \Gamma_i}$  and therefore the vibronic contribution  $K_{v\Gamma}^{\Gamma_1}$  to the curvature of the AP are nonzero only if two states  $\Gamma_1$  and  $\Gamma_i$  obey the symmetry restriction:  $\Gamma_1 \otimes \Gamma_i$  contains  $\Gamma$ .

It was proved analytically and confirmed by a series of numerical calculations [4-7] that for any molecular system

$$K_{0\Gamma}^{\Gamma_1} \geq 0. \quad (4)$$

This means that structural instabilities and distortions of high-symmetry nuclear configurations of any polyatomic system in non-degenerate states are only due to the PJTE, i.e. the vibronic mixing of the electronic state under consideration with appropriate higher in energy states under the nuclear displacements in the direction of distortion. The instability takes place if the inequality

$$|K_{v\Gamma}^{\Gamma_1}| \geq K_{0\Gamma}^{\Gamma_1} \quad (5)$$

holds, i.e. when the vibronic coupling is strong enough and/or the energy gap between the mixing states is relatively small.

The curvature operator in Eq.(1) contains the part of the Hamiltonian dependent on nuclear coordinates only, i.e.  $\partial^2 H / \partial Q^2 = \partial^2 V / \partial Q^2$ , where

$$V = - \sum_{\alpha=1}^N \sum_{i=1}^n \frac{Z_{\alpha}}{|\vec{r}_i - \vec{R}_{\alpha}|} + \frac{1}{2} \sum_{\alpha > \beta}^N \frac{Z_{\alpha} Z_{\beta}}{|\vec{R}_{\alpha} - \vec{R}_{\beta}|}. \quad (6)$$

Here  $N$  is the number of atoms,  $Z_\alpha$  are the nuclear charges, and  $\mathbf{R}_\alpha$  and  $\mathbf{r}_i$  are the nuclear and electron coordinates respectively. It follows that the operator  $\partial^2 H / \partial Q^2$  is a sum of one-electron operators, and hence in the one-electron approximation the value of  $K_0$  equals the sum (over the occupied MOs) of one-electron matrix elements:

$$K_{0\Gamma}^{\Gamma_1} = \sum_l^{\text{occ}} n_l \left\langle l \left| \left( \frac{\partial^2 h(l)}{\partial Q_\Gamma^2} \right) \right| l \right\rangle + \frac{\partial^2}{\partial Q_\Gamma^2} \left( \sum_{\alpha>\beta}^N \frac{Z_\alpha Z_\beta}{R_{\alpha\beta}} \right)_0 \quad (7)$$

where  $n_l$  is the occupation number of the  $l$ -th MO, and  $h(l)$  is the one-electron Coulomb operator.

If both the lowest singlet and triplet excited states are formed by one-electron excitation  $i \rightarrow \alpha$  from the occupied MO  $|i\rangle$  to the unoccupied MO  $|\alpha\rangle$ , that is the corresponding singlet ( $|S_i^\alpha\rangle$ ) and triplet ( $|T_i^\alpha\rangle$ ) wave functions differ from each other only by the spin factor, then  $K_0(|S_i^\alpha\rangle) = K_0(|T_i^\alpha\rangle)$ . Hence, the difference in curvature, and therefore in the degree of distortion of the molecule in these excited states is due to the difference in the second term in (1), i.e. in the vibronic contributions to the curvature,  $K_{v\Gamma}^{\Gamma_1}$ . In its turn, the value of the latter depends on the vibronic coupling constant  $F_\Gamma^{\Gamma_1\Gamma_i}$ . In the "frozen orbital" approximation the wavefunctions of mixing states  $\Gamma_1$  and  $\Gamma_i$  differ from each other by only one spin-orbital ( $\alpha \leftrightarrow m$ ). In this case the vibronic constants can be calculated as one-electron matrix elements:

$$F_\Gamma^{\Gamma_1\Gamma_i} = f_\Gamma^{(am)} = \langle \varphi_\alpha | (\partial V / \partial Q_\Gamma)_0 | \varphi_m \rangle, \quad (8)$$

$\varphi_\alpha$  and  $\varphi_m$  are molecular orbitals. Again, if  $|S_1\rangle = |S_i^\alpha\rangle$  and  $|T_1\rangle = |T_i^\alpha\rangle$ , and higher states  $|S_2\rangle = |S_j^\beta\rangle$  and  $|T_2\rangle = |T_j^\beta\rangle$  are pairwise different from each other only by the spin factor, then from Eq.(8) it follows that

$$F_\Gamma^{S_1S_2} = F_\Gamma^{T_1T_2}. \quad (9)$$

Therefore, the difference in the vibronic contributions to the curvature of the AP for considered  $|S_i^\alpha\rangle$  and  $|T_i^\alpha\rangle$  states depends only on the energy gaps between the mixing states,  $\Delta E_S = E(|S_2\rangle) - E(|S_1\rangle)$  and  $\Delta E_T = E(|T_2\rangle) - E(|T_1\rangle)$ .

Thus, to answer the questions whether the system in the reference nuclear configuration is stable or not with respect to any low-symmetry coordinate  $Q_\Gamma$ , the wave functions, energy gaps ( $E_{\Gamma_i} - E_{\Gamma_1}$ ), and the matrix elements  $F_\Gamma^{\Gamma_1\Gamma_i}$  and  $K_{0\Gamma}^{\Gamma_1}$  should be calculated for the states that are mixed under the considered displacement. Direct calculation of the vibronic coupling matrix elements involved in the PJT model is rather difficult mathematically. In the present work the numerical values of parameters (primary force constants  $K_0$  and vibronic coupling constants  $F$ ) were estimated by fitting the *ab initio* data for the APES of the molecules to the general formula, obtained from the vibronic theory. In the case of the two-level problem the AP curves as the functions of  $Q_\Gamma$  can be expressed as [1, 2]:

$$\varepsilon_0(q_\Gamma) = 1/2 K_{0\Gamma}^{\Gamma_1} q_\Gamma^2 + \Delta/2 - 1/2 \sqrt{\Delta^2 + F^2 q_\Gamma^2} \quad (10)$$

and the minima of the APES in this case are given by

$$\pm Q_{\min} = \left[ (F^2 / K_0^2) - (\Delta^2 / F^2) \right]^{1/2}, \quad (11)$$

where  $\Delta$  is the energy gap between the mixing states.

Electronic structure calculations of all considered species were performed using the GAMESS quantum chemistry package [23, 24], and the split-valence basis sets 6-31G [25]. The geometry optimization was carried out in the frame of the Hartree-Fock-Roothaan method. The potential energy curves for the molecules in the lowest excited states as the functions of corresponding low-symmetry displacements were calculated taking into consideration configuration interaction with single and double excitations (CISD). The active space of CI included three highest occupied and four lowest unoccupied MOs.

## Results and discussion

### Carbonyl fluoride $F_2CO$

In Figure 4 the MO energy levels scheme and the electronic terms of carbonyl fluoride molecule  $F_2CO$  are presented. It is seen that the lowest singlet and triplet excited states of  $A_2$  symmetry are formed by one-electron excitation from the HOMO of  $5b_2$  symmetry to the LUMO  $3b_1$ . Because the out-of-plane distortion, leading to pyramidalization, transforms according to the irreducible representation  $B_1$  (Figure 1), then in accordance with the selection rules for the vibronic coupling constants only the excited states of  $B_2$  symmetry can mix with the considered  $A_2$  states. It is also seen, that the triplet  $^3A_2$  and singlet  $^1A_2$  states differ from each other only by the spin factor. Hence from Eq. (7) it follows that the value of  $K_0$  is the same for both singlet and triplet  $A_2$  states,  $K_0^S = K_0^T$ . The  $^3B_2$  and  $^1B_2$  states also differ from each other

only by the spin factor. Then, from the Eq. (9) it follows that  $F_{b_1}^{A_2B_2}(S) = F_{b_1}^{A_2B_2}(T)$ . Therefore, the difference between the curvatures of the adiabatic potentials for the singlet and triplet excited states,  $K^S$  and  $K^T$ , is due to the difference in the energy gaps between the  $A_2$  states and the  $B_2$  states, i.e. between the  $\Delta E_T$  and  $\Delta E_S$  (Figure 4b).

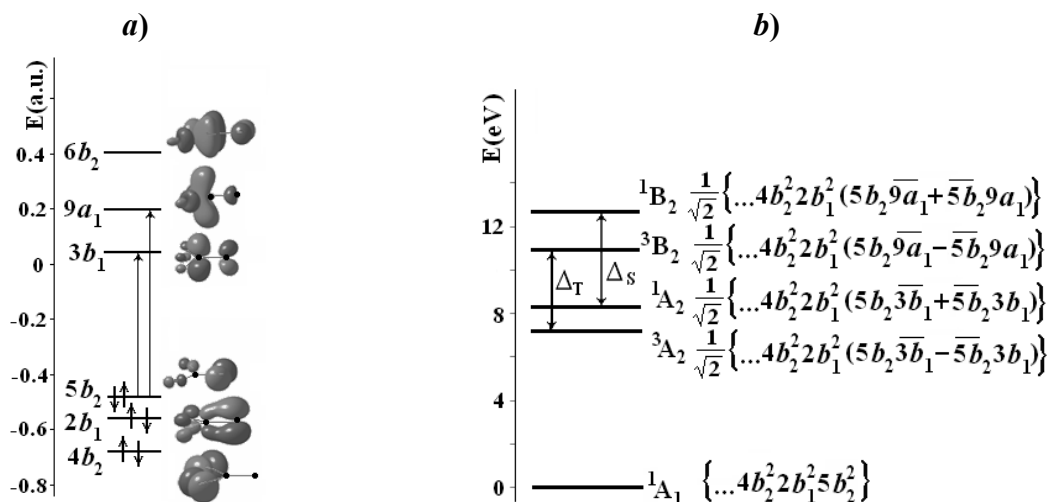


Figure 4. MO energy levels scheme (a) and electronic terms (b) of  $F_2CO$  in the ground state with planar ( $C_{2v}$ ) nuclear configuration. The arrows in (a) indicate the one-electron excitations that form the singlet and triplet  $A_2$  and  $B_2$  excited states which are mixed by the vibronic coupling under the  $B_1$  distortion.

In (b) the arrows show triplet-triplet and singlet-singlet vibronic coupled states.

To estimate the values of the PJT parameters according to Eq.(10), the potential energy curves along the out-of-plane distortion of  $b_1$ -type were calculated for the triplet excited state of  $F_2CO$  molecule, using two basis sets, 6-31G and tzv (Figure 5). As  $Q_{b_1}$ , we used the distance from the oxygen atom to the plane  $CH_2$ . Estimated in such a way values of  $K_0$  and  $F$  are presented in Figure 5.

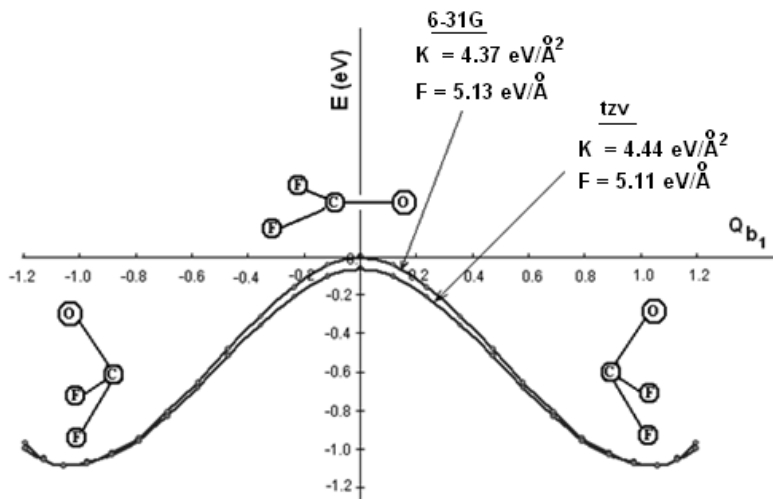
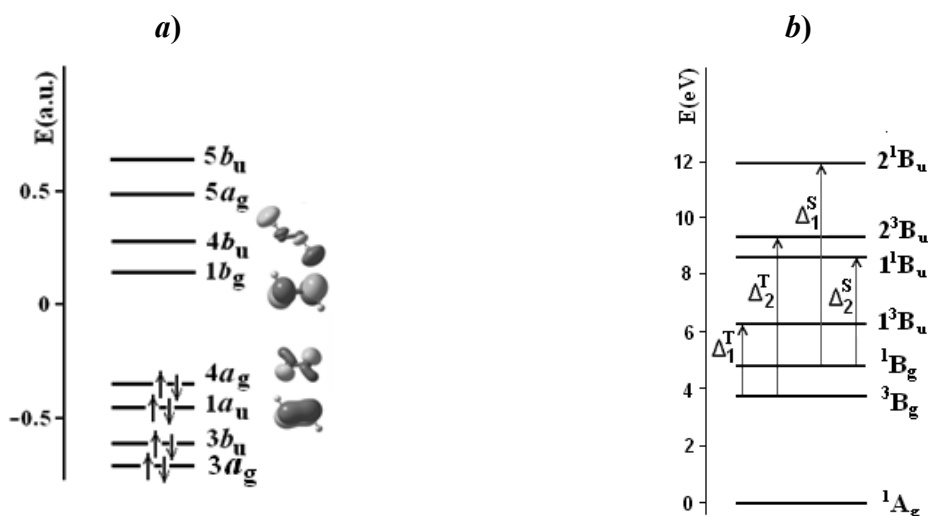


Figure 5. Calculated (marked by points) in the 6-31G and tzv basis sets and analytical (solid lines) AP curves for the  ${}^3A_2$  excited state of  $F_2CO$  along the  $Q_{b_1}$  coordinate.

It is seen that only a small difference is observed between these double minimum curves and respectively between the  $K_0$  and  $F$  calculated in different basis sets. Calculated values of the energy gaps are:  $\Delta E_T = 4.92\text{eV}$  and  $\Delta E_S = 5.34\text{eV}$ . With these parameters, we obtain following result values of curvature of the AP respectively for the triplet and singlet  $A_2$  excited states:  $K^T = -6.33\text{ eV}/\text{\AA}^2$  and  $K^S = -5.48\text{ eV}/\text{\AA}^2$ . It is seen that the absolute value of the curvature for the triplet state is larger than that for the singlet one:  $|K^T| > |K^S|$ . This explains the larger instability and the larger distortion of the triplet excited state as compared with the singlet one. Calculated values of the angles  $\alpha_T$  and  $\alpha_S$  (Figure 1) for this molecule are:  $\angle \alpha_T = 52.2^\circ$   $\angle \alpha_S = 48.7^\circ$ .

**Diimide  $N_2H_2$** 

The valence electron configuration of the ground state of  $N_2H_2$  molecule in the equilibrium *trans*-planar ( $C_{2h}$ ) nuclear configuration is  $(3a_g)^2(3b_u)^2(1a_u)^2(4a_g)^2(1b_g)^0(4b_u)^0$  (Figure 6a). The scheme of the electronic terms is shown in Figure 6b, calculated values of the total and relative energies of the states are given in Table 1.



**Figure 6. MO energy levels scheme (a) and electronic terms (b) of  $N_2H_2$  in the equilibrium *trans*-planar ( $C_{2h}$ ) nuclear configuration. In (b) the arrows show triplet-triplet and singlet-singlet vibronic coupled states.**

Table 1

**Total energies (hartree), relative energies (eV) and electronic configurations of the ground and low-lying excited states for planar ( $C_{2h}$ )  $N_2H_2$  calculated in tzv basis set.**

State	Total energy	Relative energy	Electronic configuration
$1A_g$	-110.01265	0	$[\dots 3b_u^2 1a_u^2 4a_g^2 1b_g^0 4b_u^0]$
$3B_g$	-109.88862	3.37	$1/\sqrt{2}[\dots 3b_u^2 1a_u^2 (4a_g \bar{1}b_g - \bar{4}a_g 1b_g) 4b_u^0]$
$1B_g$	-109.84542	4.55	$1/\sqrt{2}[\dots 3b_u^2 1a_u^2 (4a_g \bar{1}b_g + \bar{4}a_g 1b_g) 4b_u^0]$
$1^3B_u$	-109.78185	6.28	$1/\sqrt{2}[\dots 3b_u^2 4a_g^2 (1a_u \bar{1}b_g - \bar{1}a_u 1b_g) 4b_u^0]$
$1^1B_u$	-109.68997	8.78	$1/\sqrt{2}[\dots 3b_u^2 1a_u^2 (4a_g \bar{4}b_u + \bar{4}a_g 4b_u) 1b_g^0]$
$2^3B_u$	-109.65505	9.73	$1/\sqrt{2}[\dots 3b_u^2 1a_u^2 (4a_g \bar{4}b_u - \bar{4}a_g 4b_u) 1b_g^0]$
$2^1B_u$	-109.58435	11.65	$1/\sqrt{2}[\dots 3b_u^2 4a_g^2 (1a_u \bar{1}b_g + \bar{1}a_u 1b_g) 4b_u^0]$

Note that not all obtained excited states are listed in Table 1, but only those that participate in the singlet-singlet and triplet-triplet vibronic coupling. From Table 1 and Figure 6b it is seen that the lowest excited singlet and triplet  $1B_g$  and  $3B_g$  states are mainly formed by the electron excitation from the nonbonding HOMO  $4a_g$  ( $n_{N1} - n_{N2}$ ) to the antibonding LUMO  $1b_g$  ( $\pi^*$ ) (Figure 6a). The out-of-plane distortion leading to nonplanar  $C_2$  structure is of the  $a_u$  type. This means that the direct product of irreducible representations of the two mixing electronic states that contribute to the  $a_u$  type instability of the planar configuration must contain the  $A_u$  representation. For the first excited  $1^3B_u$  states, their mixing with the higher  $1^3B_u$  states yields the necessary  $A_u$  symmetry:  $B_g \times B_u = A_u$ . The two such excited states are  $1^{1,3}B_u$  ( $1a_u \rightarrow 1b_g$ ) and  $2^{1,3}B_u$  ( $4a_g \rightarrow 4b_u$ ). The next  $B_u$  states ( $4a_g \rightarrow 5b_u$ ) is much higher in energy ( $\Delta E > 20$  eV) and seems to be less important ones.

Since both the excited singlet  $1B_g$  and triplet  $3B_g$  states are calculated at the same geometry (of the ground state) and differ from each other only by the spin factor, it means that, as in the previous case,  $K_0(1B_g) = K_0(3B_g)$ . That is, the primary force constant  $K_0$  in the expression for the curvature  $K$  of the AP with respect to the symmetry coordinate  $Q_{au}$  is the same for both  $1B_g$  and  $3B_g$  states. Hence, the difference in curvature, and therefore in the degree of distortion of the molecule in these states is due to the difference in the vibronic contributions to the curvature. From the Eq.(2) it follows:

$$K_v(1B_g) = -2F_1^2/\Delta_1^S - 2F_2^2/\Delta_2^S$$

$$K_v(3B_g) = -2F_1^2/\Delta_1^T - 2F_2^2/\Delta_2^T$$

where the constants of the vibronic coupling  $F_1$  and  $F_2$  between the singlet-singlet and triplet-triplet excited states are also equal to each other:

$$F_1 = \langle {}^1B_g | (\partial H / \partial Q_{au})_0 | {}^1B_u \rangle = \langle {}^3B_g | (\partial H / \partial Q_{au})_0 | {}^1B_u \rangle$$

$$F_2 = \langle {}^1B_g | (\partial H / \partial Q_{au})_0 | {}^2B_u \rangle = \langle {}^3B_g | (\partial H / \partial Q_{au})_0 | {}^2B_u \rangle$$

Because the mixing  ${}^1B_g$  and  ${}^1B_u$  states, as well as the  ${}^3B_g$  and  ${}^3B_u$  states differ from each other by only one spin-orbital, then in accordance with Eq.(8) we obtain:

$$F_1 = f_1 = \langle 1a_u | (\partial H / \partial Q_{au})_0 | 4a_g \rangle,$$

$$F_2 = f_2 = \langle 1b_g | (\partial H / \partial Q_{au})_0 | 4b_u \rangle,$$

and for  $K_v$  we can write:  $K_v({}^1B_g) = -2f_1^2/\Delta_1^S - 2f_2^2/\Delta_2^S$ , and  $K_v({}^3B_g) = -2f_1^2/\Delta_1^T - 2f_2^2/\Delta_2^T$ .

To estimate the values of the orbital vibronic coupling constants  $f_1$  and  $f_2$  the following procedure is applied. From the *ab initio* calculations the curvature of the APES with respect to the  $a_u$  distortion is determined for the *trans*-planar nuclear configurations of  $C_{2h}$  symmetry of the neutral  $N_2H_2$  molecule, of the anion  $N_2H_2^-$  and the cation  $N_2H_2^+$ . Calculated values are:  $K(N_2H_2) = 12.60 \text{ eV/\AA}^2$  (the experimental value  $K = M\omega^2$  with  $\omega(a_u) = 1290 \text{ cm}^{-1}$  [26] is  $11.52 \text{ eV/\AA}^2$ ),  $K(N_2H_2^+) = 5.78 \text{ eV/\AA}^2$ , and  $K(N_2H_2^-) = 3.10 \text{ eV/\AA}^2$ . The softening of the  $N_2H_2^+$  with respect to the  $a_u$  distortion is due to the vibronic coupling between the double occupied  $1a_u$  MO and single occupied  $4a_g$  MO,  $\Delta K = f_1^2/\Delta E_{\text{cation}}$ ,  $\Delta E_{\text{cation}} = E({}^2A_u) - E({}^2A_g)$ , while the softening of the  $N_2H_2^-$  is due to the vibronic coupling between the single occupied  $1b_g$  MO and vacant  $4b_u$  MO,  $\Delta K = f_2^2/\Delta E_{\text{anion}}$ ,  $\Delta E_{\text{anion}} = E({}^2B_u) - E({}^2B_g)$ . Thus, we obtain the following values for the vibronic coupling constants in the  $N_2H_2$  molecule:  $f_1 = 4.25 \text{ eV/\AA}$  and  $f_2 = 4.73 \text{ eV/\AA}$ .

Using the values of  $\Delta E_i^{S,T}$  from Table 1, we obtain  $K_v({}^1B_g) = -15.67 \text{ eV/\AA}^2$  and  $K_v({}^3B_g) = -19.45 \text{ eV/\AA}^2$ . As the  $K_0$  we used the value of  $K$  for the ground state because the latter is not mixed with any excited states of  $A_u$  symmetry. Finally we get  $K({}^1B_g) = -3.07 \text{ eV/\AA}^2$  and  $K({}^3B_g) = -6.85 \text{ eV/\AA}^2$ . Calculations point-by-point give the following values of  $K$  in the neighborhood of  $Q_{au} = 0$ :  $K({}^1B_g) = -3.20 \text{ eV/\AA}^2$  and  $K({}^3B_g) = -6.48 \text{ eV/\AA}^2$ . Thus, in this case we also obtain  $|K^T| > |K^S|$ . That is why the distortion of  $N_2H_2$  in the triplet state is stronger than that in the singlet one. Calculated values of the dihedral angles  $\alpha_T$  and  $\alpha_S$  (Figure 2) for this molecule are:  $\leq \alpha_T = 95.5^\circ$  and  $\leq \alpha_S = 106.2^\circ$ , and the pseudo Jahn-Teller stabilization energies are equal to  $\Delta E_{PJT}^T = 0.67 \text{ eV}$  and  $\Delta E_{PJT}^S = 0.25 \text{ eV}$ .

### Ketene $H_2C_2O$

The five-atom ketene molecule ( $H_2CCO$ ) has nine vibrational degrees of freedom. In the planar configuration of  $C_{2v}$  symmetry (configuration of the ground electronic state) they transform according to the irreducible representations  $4a_1 + 2b_1 + 3b_2$ . Three symmetrized displacements of the  $b_2$ -type (the C-C-O in-plane bending, the  $CH_2$  fragment in-plane wagging, and the C-H asymmetric stretch) reduce the symmetry from  $C_{2v}$  to  $C_s$  and lead to the  $C_s^{\text{II}}$  structure (Figure 3). Two low-symmetry  $b_1$  modes (the C-C-O out-of-plane bending and the  $CH_2$  fragment out-of-plane wagging) correspond to the out-of-plane bending of the molecule and transform the planar nuclear configuration into the  $C_s^{\text{I}}$  one (Figure 3). Calculated parameters of the geometrical structure in the ground ( ${}^1A_1$ ) and excited ( ${}^3A''$  and  ${}^3A'$ ) states of ketene are presented in Table 2. They agree rather well with those of other authors [21, 22].

Table 2

Optimized geometry parameters in the ground ( ${}^1A_1$ ) and excited ( ${}^3A''$  and  ${}^3A'$ ) states of ketene<sup>a</sup>.

Symmetry	State	$R_{C-O}$	$R_{C-C}$	$R_{C-H}$	$\angle HCH$	$\alpha$	$\beta$	$\gamma$	$\delta$
$C_{2v}$	${}^1A_1$	1.167	1.303	1.069	119.98	-	-	-	-
$C_s^{\text{I}}$	${}^3A'$ ( ${}^3A_1$ )	1.191	1.482	1.072	122.38	-	-	55.3	22.7
$C_s^{\text{II}}$	${}^3A''$ ( ${}^3A_2$ )	1.193	1.449	1.073 (C-H <sub>1</sub> ) 1.069 (C-H <sub>2</sub> )	119.81	49.3	120.36	-	-

<sup>a</sup> Bond lengths are in Å, angles are in degrees; angles  $\alpha$ ,  $\beta$ ,  $\gamma$  and  $\delta$  are shown in Figure 3.

The MO energy level scheme and the electronic terms of ketene molecule in the equilibrium planar ( $C_{2v}$ ) nuclear configuration are presented in Figure 7. We see that the first excited  ${}^3A_2$  state is formed by the electron excitation from the HOMO  $2b_1$  which is the C-C bonding one, to the LUMO  $3b_2$ , the antibonding MO with respect to C-O bond. Because the in-plane distortion is of the  $b_2$  type, then only the higher excited  ${}^3B_1$  state contributes to the  $b_2$  type instability of the  $C_{2v}$  configuration:  $A_2 \times B_1 = B_2$ .

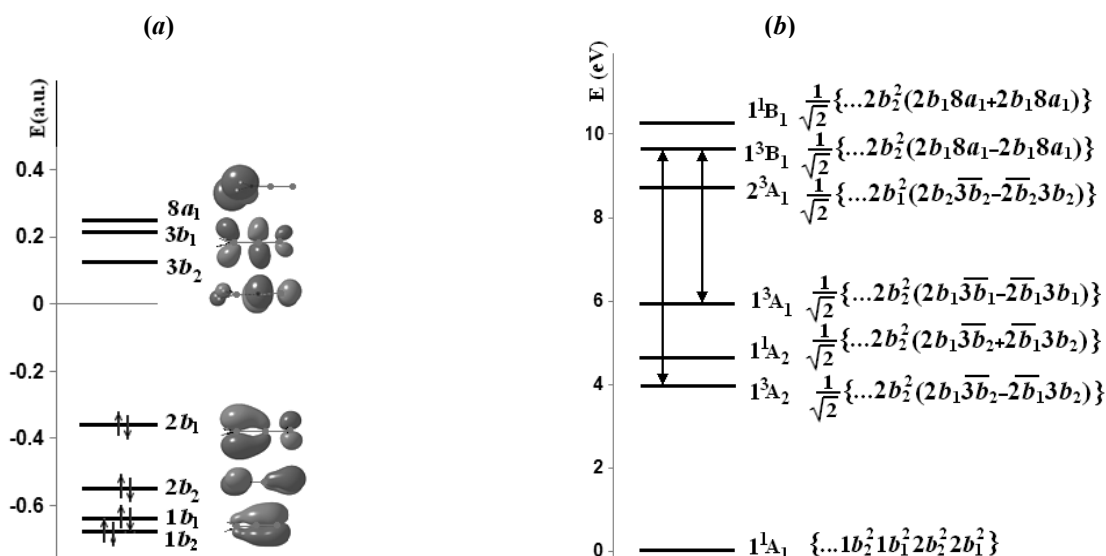


Figure 7. MO energy levels scheme (a) and electronic terms (b) of ketene molecule in the ground state with planar ( $C_{2v}$ ) nuclear configuration. The arrows indicate the vibronic coupled excited states.

The  $^3A_1$  state is formed by the one-electron excitation  $2b_1 \rightarrow 3b_1$ , the latter is the antibonding MO for both the C-C and C-O bonds. In this case the vibronic contribution to the curvature of the AP along the out-of-plane distortion of the  $b_1$  type is determined by the PJT mixing also with the  $^3B_1$  excited state:  $A_1 \times B_1 = B_1$ .

Generally speaking, in order to reveal the vibronic origin of the in-plane distortion of ketene molecule in the  $^3A_2$  state we must solve the three-mode  $(A_2 + B_1) \otimes (b_2 + b_2 + b_2)$  pseudo Jahn-Teller problem. For the out-of-plane distortion the two-mode  $(A_1 + B_1) \otimes (b_1 + b_1)$  problem arises. Then the resulting normal coordinates  $Q_{b_2}$  and  $Q_{b_1}$  of the  $b_2$ -type and  $b_1$ -type displacements are obtained as the eigenvectors of the matrices  $K_{ij}$  ( $i=1, 2, 3$  for the three symmetrized displacements of the  $b_2$ -type, and  $i=1, 2$  for those of the  $b_1$ -type)

$$K_{ij} = K_{ij}^{(0)} - 2 \frac{F^{(i)} F^{(j)}}{E(^3B_1) - E(^3A_2 \text{ (or } ^3A_1))},$$

corresponding to the negative eigenvalues of the latest. Fortunately, the problem can be simplified taking into account that the  $Q_{b_2}$  and  $Q_{b_1}$  coordinates coincides with the line of steepest decrease of the energy in the space of symmetrized coordinates that connects the  $C_{2v}$  and  $C_s^{II}$  ( $C_s^\perp$ ) minima. From Table 2 one can see that the  $Q_{b_2}$  is determined almost exclusively by the in-plane C-C-O bending, the  $CH_2$  fragment in-plane wagging and the C-H asymmetric stretch are negligibly small. That is why in further calculations of the AP curve along the in-plane distortion we used as the  $Q_{b_2}$  the deviation of the oxygen atom from the C-C axis. Calculations of the AP curve along the out-of-plane distortion showed that the  $CH_2$  fragment out-of-plane wagging (change of the angle  $\delta$  in Figure 3) has little effect on the value of the total energy (about 0.02 eV). Therefore, as  $Q_{b_1}$  we used the out-of-plane displacement of the oxygen atom.

Calculated adiabatic potential curves as the functions of  $Q_{b_2}$  for the first triplet state of ketene, and of  $Q_{b_1}$  for the second excited triplet state are shown in Figure 8. As in the case of carbonyl fluoride we evaluated parameters  $K_0$  and  $F$  by fitting the *ab initio* data for the AP curves to the general formula from Eq.(10). Estimated in such a way values of the PJT parameters are presented in Figure 8, where

$$F(b_2) = F_{b_2}^{A_2, B_1} = \left\langle ^3A_2 \left| \left( \frac{\partial H}{\partial Q_{b_2}} \right)_0 \right| ^3B_1 \right\rangle \text{ and } F(b_1) = F_{b_1}^{A_1, B_1} = \left\langle ^3A_1 \left| \left( \frac{\partial H}{\partial Q_{b_1}} \right)_0 \right| ^3B_1 \right\rangle.$$

From Figure 8 it is seen that calculated potential energy curves for the  $^3A_2$  (a) and  $^3A_1$  (b) excited states along the corresponding low-symmetry distortions ( $b_2$ -type in the first case and  $b_1$ -type in the second one) are fully coincide with those predicted from the general theory. Thus, we can conclude that the instability of high-symmetry  $C_{2v}$  nuclear configuration of ketene molecule in considered  $^3A_2$  and  $^3A_1$  excited states and the corresponding low-symmetry distortions are due to the pseudo Jahn-Teller mixing of these states with the higher excited  $^3B_1$  state.



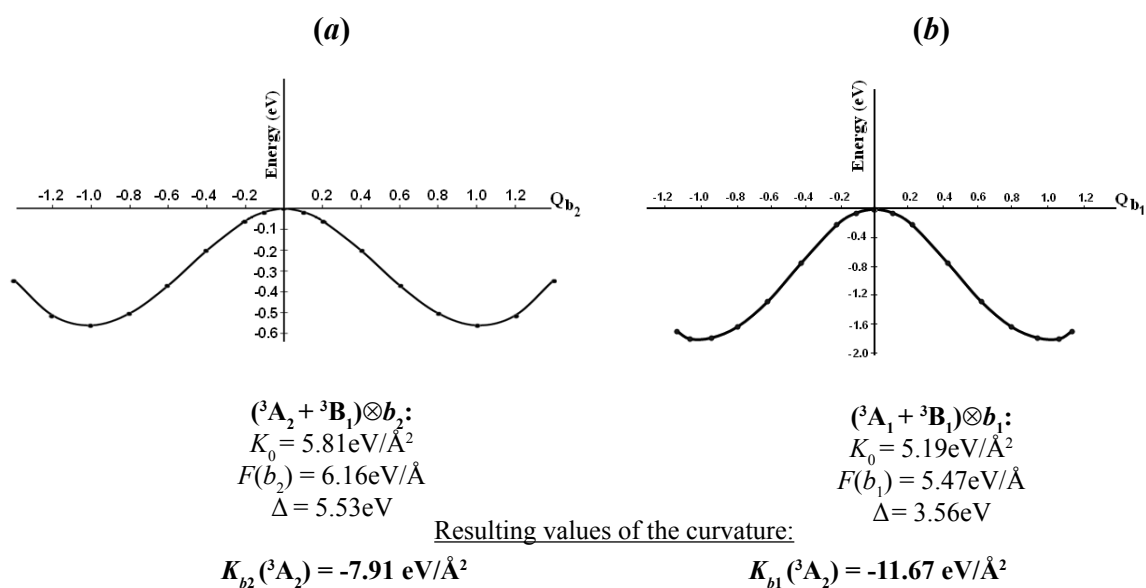


Figure 8. Calculated (marked by points) and analytical (solid lines) AP curves for the  $^3A_2$  (a) and  $^3A_1$  (b) excited states along the  $Q_{b_2}$  and  $Q_{b_1}$  coordinates.

#### Diagonal vibronic constants for the excited states

In the same approximation, by applying the above equations to the molecules with respect to the totally symmetric displacements, one can explain also the elongation of C-O, N-N, and C-C bonds in excited states of  $F_2CO$ ,  $N_2H_2$ , and  $H_2C_2O$  molecules, respectively. These distortions do not change the symmetry of the molecules, but change the interatomic distances. The diagonal vibronic coupling constant  $F_Q^{\Gamma\Gamma} = \langle \Gamma | (\partial H / \partial Q)_0 | \Gamma \rangle$  has the physical meaning of the force with which the electrons in the state  $|\Gamma\rangle$  affect the nuclei in the direction of  $Q$  [1, p. 340]. In the one-electron approximation this constant equals the sum of diagonal orbital vibronic coupling constants (OVCC) multiplied by the appropriate MO occupation numbers,  $n_i$ :

$$F_Q = \sum_i^{occ} n_i f_Q^{ii}, \quad (12)$$

where

$$f_Q^{ii} = \langle i | (\partial V / \partial Q)_0 | i \rangle \quad (13)$$

are the linear diagonal orbital vibronic constants. These values can be both positive and negative, depending on the character of the MO: for a bonding (relative to the considered bond) molecular orbital  $f_Q^{ii} > 0$ , for an antibonding MO  $f_Q^{ii} < 0$ , and for nonbonding MO  $f_Q^{ii} \cong 0$  [1, p. 342]. In the ground state equilibrium configuration  $F_Q^{\Gamma\Gamma}$  equals zero. However, any change of the electron structure of the molecule results in a nonzero distorting force  $\Delta F_Q \neq 0$ . If the excited state is formed by the one-electron excitation  $i \rightarrow a$ , then

$$\Delta F_Q = f_Q^{aa} - f_Q^{ii}. \quad (14)$$

In our cases, as shown above, the lowest excited states are formed by the one-electron excitation from the nonbonding ( $F_2CO$ ,  $N_2H_2$ ) or the bonding ( $H_2C_2O$ ) MOs to the antibonding MOs of corresponding molecules. Hence,  $f_Q^{ii} \geq 0$ ,  $f_Q^{aa} < 0$ , and we get that in all the cases  $\Delta F_Q < 0$ . Thus, for all the considered molecules their excitation induces a JTE distorting force which pushes away the nuclei and thereby increases the C-O, N-N, and C-C bond lengths.

#### Conclusions

From the results of this paper the following conclusions emerge.

The nonplanar geometry of carbonyl fluoride and diazene molecules in the lowest singlet and triplet excited states, as well as the in-plane and the out-of-plane distortions of ketene molecule in the first and the second triplet states respectively, are due to the pseudo Jahn-Teller mixing of these states with the higher excited states of appropriate

symmetry. This vibronic coupling produces the low-symmetry distortion of the planar nuclear configurations, as predicted by the general theory.

The elongation of C-O, N-N, and C-C bonds respectively in excited states of  $F_2CO$ ,  $N_2H_2$ , and  $H_2C_2O$  molecules, as compared with the bond lengths in their ground states is due to the change of the corresponding diagonal vibronic coupling constants induced by the electronic excitation.

## References

- Bersuker, I.B. *Electronic Structure and Properties of Transition Metal Compounds. Introduction to the Theory*, Second Ed.; Wiley: New York, 2010, 759 p.
- Bersuker, I.B. *The Jahn-Teller Effect*; Cambridge University Press: Cambridge (UK), 2006, 616 p.
- Bersuker, I.B.; Polinger, V. Z., *Vibronic Interactions in Molecules and Crystals*. Springer: New York, 1989, 422 p.
- Bersuker, I.B. Symmetry, instability, stereochemistry and phase transitions in coordination compounds. *Pure and Applied Chemistry*, 1988, 60, pp. 1167-1174.
- Bersuker, I. B. Proof of the vibronic origin of an instability in structural phase transitions occurring in condensed media. *Soviet Physics. Solid State*, 1988, 30, pp. 1000-1003.
- Bersuker, I.B.; Gorinchoi, N.N.; Polinger, V.Z. On the origin of dynamic instability of molecular systems. *Theoretica Chimica Acta*, 1984, 66, pp. 161-172.
- Bersuker, I.B.; Polinger, V.Z.; Gorinchoi, N.N. Pseudo Jahn-Teller origin of square-planar configuration instability of main-group-element hydrides. *Journal of Molecular Structure: THEOCHEM*, 1992, 270, pp. 369-380.
- Reinen, D.; Atanasov, M. Fluxionality and stereochemistry of 5-coordinated  $Cu^{2+}$  complexes. *Chemical Physics*, 1989, 136, pp. 27-46.
- Reinen D.; Atanasov M. Symmetry and vibronic coupling: The stereochemistry and the ground state potential surface of  $Cu^{2+}$  in five-coordination. *Chemical Physics*, 1991, 155, pp. 157-171.
- Gorinchoi, N.N.; Bersuker, I.B.; Polinger, V.Z. Electronic control of molecular configuration instability via vibronic coupling. Comparison of  $CuCl_5^{3+}$  with  $ZnCl_5^{3+}$ . *New Journal of Chemistry*, 1993, 17, pp. 125-130.
- Polinger, V.Z.; Gorinchoi, N.N.; Bersuker, I.B. MO LCAO analysis of the vibronic instability of the  $CuCl_5^{3-}$  trigonal bipyramidal configuration. Critical view on the angular overlap model in vibronic problems. *Chemical Physics*, 1992, 159, pp. 75-87.
- Gorinchoy, N.N.; Ogurtsov, I.Ya.; Arsene, I. Vibronic origin of the "skewed" anticline configuration of the hydrogen peroxide molecule. *Chemistry Journal of Moldova*, 2008, 3, pp. 105-111.
- Ogurtsov, I.; Gorinchoy, N.; Balan, I. Vibronic origin of the  $H_3O$  metastability. *Journal of Molecular Structure.*, 2007, 838, pp. 107-111.
- Ogurtsov, I.Ya.; Munteanu, G.; Bantush, L.; Bersuker, I.B. Pseudo Jahn-Teller origin of formaldehyde molecular in excited states. *Journal of Molecular Structure: THEOCHEM*, 2001, 541, pp. 141-148.
- Choi, H.; Baeck, K. K. Theoretical study of low-lying excited states of  $X_2CY$  ( $X=F, Cl; Y=O, S$ ) using the equation-of-motion coupled-cluster theory. *Molecular Physics*, 2005, 103, pp. 2247-2254.
- Godunov, I.A.; Abramnikov, A.V.; Bataev, V.A.; Pupyshchev, V.I. Potential functions of inversion of  $R_2CO$  molecules in the lowest excited electronic states. *Russian Chemical Bulletin*, 1999, 48, pp. 640-646.
- Bokarev, S.I.; Dolgov, E.K.; Bataev, V.A.; Godunov, I.A. Molecular parameters of tetraatomic carbonyls  $X_2CO$  and  $XYCO$  ( $X, Y=H, F, Cl$ ) in the ground and lowest excited electronic states, Part 1: a test of *ab initio* methods. *International Journal of Quantum Chemistry*, 2009, 109, pp. 569-585.
- Kim, K.; Shavitt, I.; Del Bene, J.E. Theoretical study of the di-imide ( $N_2H_2$ ) molecule in ground and  $n \rightarrow \pi^*$  excited states. *Journal of Chemical Physics*, 1992, 96, pp. 7573-7579.
- Tavernelli, I.; Röhrig, U.F.; Rothlisberger, U. Molecular dynamics in electronically excited states using time-dependent density functional theory. *Molecular Physics*, 2005, 103, pp. 963-981.
- Dhont, G.S.F.; van Lenthe, J.H.; Groenenboom, G.C.; van der Avoird, Ad. *Ab initio* calculation of the  $NH(\^3\Sigma^-) - NH(\^3\Sigma^-)$  interaction potentials in the quintet, triplet, and singlet states. *Journal of Chemical Physics*, 2005, 123, 184302.
- Dykstra, C.E.; Schaefer III, H.F. Excited electronic states of ketene. *Journal of American Chemical Society* 1976, 98, pp. 2689-2695.
- Szalay, P.G.; Császár, A.G.; Nemes, L. Electronic states of ketene. *Journal of Chemical Physics*, 1996, 105, pp. 1034-1044.
- Granovsky, A.A. <http://classic.chem.msu.su/gran/gamess/index.html>.
- Schmidt, M.W. et al. General atomic and molecular electronic structure system. *Journal Computational Chemistry*, 1993, 14, pp. 1347-1363.
- Hehre, W.J.; Ditchfield, R.; Pople, J.A. Self-Consistent Molecular Orbital Methods. XII. Further Extensions of Gaussian-Type Basis Sets for Use in Molecular Orbital Studies of Organic Molecules. *Journal of Chemical Physics*, 1972, 56, 2257.
- Hallin, K. E. J.; Johns, J. W. C.; Trombetti, A. The infrared spectrum of di-imide near 7.6  $\mu m$ . *Canadian Journal of Physics*, 1981, 59, pp. 663-672.

## IODIDE IONS SORPTION ON POLYMER AV-17(Cl) AND SORBENT AV-17(Bi)

Vasile Gutsanu

Moldova State University, 60, A. Mateevici str., Chisinau MD-2009, Republic of Moldova  
e-mail: gutsanu@gmail.com

**Abstract.** The iodide ions sorption from solutions of KI and KI in excess of KCl has been investigated. The strongly basic anion exchangers AV-17 in Cl<sup>-</sup> form and Varion AD in NO<sub>3</sub><sup>-</sup> form was used as sorbents. Also AV-17 polymer modified with Bi(III)-containing compounds were used. The sorption was performed in static and dynamic conditions. Isotherms are approximated with BET sorption model. The sorption value of iodide ions in the KI solutions with KCl in excess is quite high. It was established that sorption of iodide ions in the form of polyiodide occurs both as a result of anion exchange and as a result of chemisorption.

**Keywords:** strongly basic anion exchanger, iodide ions, sorption, Bi(III) compounds.

### Introduction

It is well known that iodine is a very important element for normal function of the human organism. In many countries, including Republic of Moldova, the population suffers from iodine deficiencies in the nutrients. Therefore the obtaining of elemental iodine is an actual problem. There are two main sources of iodine: (i) the marine flora and fauna and (ii) the water of the oil wells. The iodine content in water from getting oil drilling is relatively high, ranging between 10-60 mg/L [1].

Basically there are two following methods of extraction of iodine from aqueous solutions: (i) extraction and (ii) sorption methods. Adsorption methods are based on the use of anion-exchangers. The process of iodide ions interaction with strongly basic anion exchangers was investigated in a number of scientific papers [1-5]. The authors have been mentioned that sorption of iodide ions from different solutions by polymers containing strongly basic functional groups is over equivalent. Although sorption studies of iodide ions by strongly basic anion exchanger is carried out for a long time, sorbate-sorbent interaction mechanism is not yet fully elucidated. It is found that the sorption of iodide ions occurs as a result of the formation of polyiodide ions in polymer phase. This process is performed by the anion exchange and chemical sorbate-sorbent interactions.

Researches of iodide ions adsorption on anion exchangers modified with metal compounds have not yet been done. It is necessary to perform such research not only to recover iodide ions from solutions, but also in order to elucidate the mechanism of sorbate-sorbent interaction. It should also be noted that the polymers containing polyiodide ions can serve as sorbents for the removal of reductants from gaseous phase such as phosphine [6], hydrazine [7] and others.

### Experimental

The commercial strongly basic anion exchangers AV-17 and Varion-AD have been used. The exchangers are gel-type cross-linked polystyrene-divinylbenzene copolymers. The AV-17 have -N<sup>+</sup>(CH<sub>3</sub>)<sub>3</sub> and Varion-AD -N<sup>+</sup>(CH<sub>3</sub>)<sub>3</sub> and -OH functional groups. Their full anion-exchange capacity is 3.5-4.0 meq/g [10]. The exchanger AV-17 was in Cl<sup>-</sup> form, while Varion-AD was in NO<sub>3</sub><sup>-</sup> form. Polymer AV-17 modified with Bi(III) compounds also was investigated. The process of obtaining of the sorbent AV-17(Bi) takes place according to the method described elsewhere [11]. The AV-17(Cl) polymer dried sample (5 g) have been contacted with 0.014 M Bi(OH)<sub>2</sub>NO<sub>3</sub> solution (0.5 L) at a temperature of 60 ± 1°C for 5 h. The pH value of Bi(OH)<sub>2</sub>NO<sub>3</sub> solution was about 0.2. After 5 h of contacting time the polymer sample was separated by filtration, washed with distilled water and dried in air. The polymer modified with Bi(III) compounds contains crystalline BiOCl and amorphous BiOOH [9]. The Bi content (25.3 mg Bi/g) in the prepared sorbent AV-17(Bi) was determined photocolometrically [12] after desorption with HNO<sub>3</sub> solution.

Sorption of the iodide ions occurred in solutions containing (i) KI and (ii) mixture of KI and KCl. The investigation was carried out in static and dynamic conditions. In the static conditions the polymer samples of 0.2 g were contacted with 50 mL of solution. When was necessary, the pH value of solution was adjusted using solution of H<sub>2</sub>SO<sub>4</sub> or NaOH.

The sorption value was calculated with the Eq.(1):

$$S = \frac{(C_0 - C_e)V}{m}, \quad (1)$$

where,  $S$  is the sorption value, mmol I/g;  $C_0$  and  $C_e$  are the initial and, respectively, the equilibrium concentrations of I (mg I/mL),  $V$  is the solution volume in contact with polymer sample, mL;  $m$  is the mass of polymer sample, g.

The investigation of iodide ions sorption in the dynamic conditions was carried out using glass column with diameter of 10.7 mm. Solutions with pH 5.0 - 5.2 containing 0.64 mg I/mL have been passed through the column, containing 2 g of dried polymer, with different flow.

The parameters of sorption process have been calculated from the breakthrough curves: (i) dynamic sorption capacity ( $DSC$ , mg I/ g) corresponds to sorption value until the appearance of the iodide ions into effluents; (ii) total dynamic sorption capacity ( $TDSC$ , mg I/ g) - sorption value at the sorbent saturation.

The relative rate of sorption ( $W$ , %) was calculated according to Eq.(2):

$$W, \% = \frac{DSC}{TDSC} \cdot 100\% \quad (2)$$

## Results and discussion

### Iodide ions sorption by AV-17(Cl) in the static conditions

The results showed that at temperature of 19.5°C the equilibrium sorption of iodide ions (in solutions containing 0.25 mg KI/mL) is reached at 10 minutes of the contact with the polymer AV-17(Cl). It was also found that the sorption practically does not depend on the solution pH value in the range of 3-10.

Theoretically, iodide ions sorption on strongly basic anion exchanger should be a reversible process according to the Eq.(3):



But sorption isotherm obtained at 16.5°C, shows that iodide ions retention on AV-17(Cl) from KI solution is not determined by the anion exchange process only (see Figure 1). The shape of sorption isotherm is similar to the BET isotherm. This indicates that in the polymer phase take place processes of condensation of iodide ions as a result of forming of polyiodide ions  $I_2^-$ . This indicates that in the system containing polymer and KI solution, the redox processes take place, involving atmospheric oxygen. Polyiodide ions formation in the polymer phase is confirmed by the fact that the sorption value is much higher than the theoretical exchange capacity of the polymer.

The isotherm parameters using BET adsorption model were calculated by Eq. (4):

$$S = \frac{S_\infty B(C/C_s)}{(1 - C/C_s)[1 + (B - 1)C/C_s]}, \quad (4)$$

where,  $S$  is sorption value, mmol I/g;  $S_\infty$  is first layer capacity, mmol I/g;  $B$  is a constant,  $C$  – equilibrium I concentration, mmol I/L;  $C_s$  – pseudo saturated solution, mmol I/L (see Figure 1).

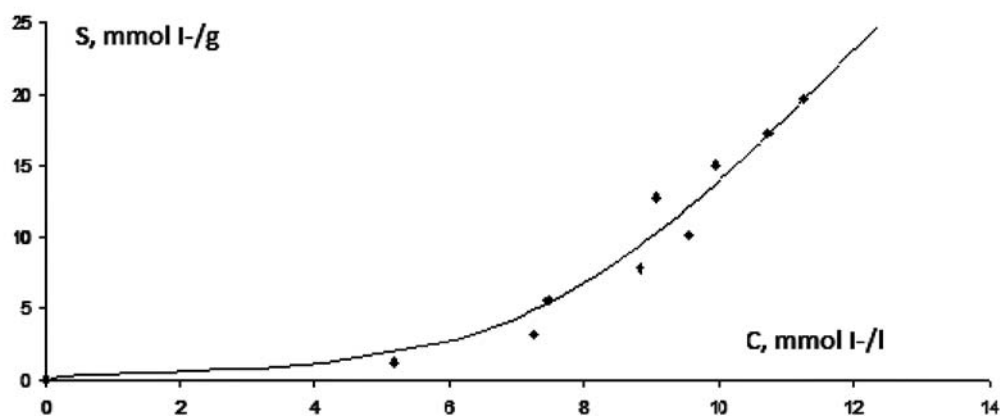


Figure 1. The isotherm of iodide ions sorption from KI solutions on AV-17(Cl).

It is known that BET isotherm describes adsorption of gases. But it can also be used to describe the sorption from solutions when in the sorbent phase the sorbate forms polymeric compounds [8]. Calculation of isotherm constants has been made using the linear form of the BET isotherm (Eq. 5):

$$\frac{C/C_s}{S \cdot (1 - C/C_s)} = \left( \frac{1}{S_\infty B} \right) + \left( \frac{(B - 1) \cdot C/C_s}{S_\infty B} \right) \quad (5)$$

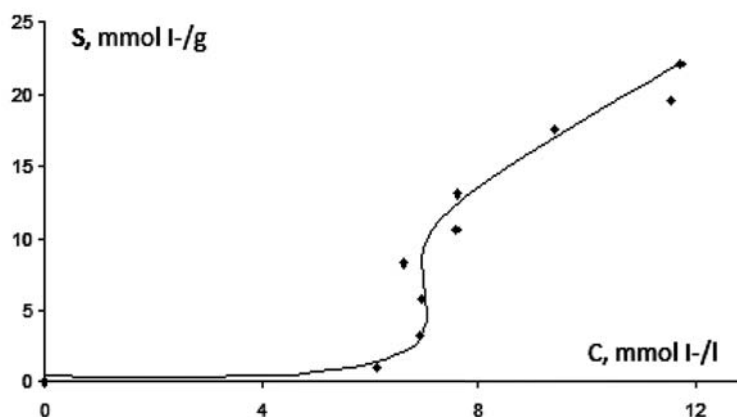


Figure 2. The isotherm of iodide ions sorption on AV-17(Cl) from solutions containing KI and KCl.

The linear form of the experimentally obtained isotherm (Figure 1) with  $C_s = 13.4$  mmol I-/L, is shown in Figure 3, and the constants values in the Table 1.

As shown in Figure 1, the forming of the polyiodide ions in the polymer phase begins at concentrations higher than 7 mmol I-/L. It would seem that sorption occurs in outcome (Eq. (6)), i.e. in the result of the anion exchange:

$$R_4NI + nI_2 \leftrightarrow R_4NI(I_2)_n \quad (6)$$

But the results of iodide ions sorption from solutions of KI with increased concentrations of KCl demonstrated that it is not so. The sorption isotherm of iodide ions from the KI solution containing 0.1 mol KCl/L on polymer AV-17(Cl) (at 16.5°C) is shown in Figure 2. The shape of this isotherm is similar to the shape of the sorption isotherm from KI solution in the absence of KCl (Figure 1). The linear form of the isotherm calculated using the BET model with  $C_s = 12.8$  mmol I-/L, is shown in Figure 3, and the constants values in the Table 1. It is possible that in the polymer phase takes place formation of  $I_2Cl^-$  ions and others [1]. According to [1], sorption of the iodine containing ions on the AV-17-8 increases in the following order:  $I^- < I_3^- < I_2Cl^-$ .

The  $S_\infty$  value of iodine ions sorption from KI solution containing KCl is much lower in comparison with solution without KCl (Table 1). This means that in solutions with low concentrations of KI ( $C < 7$  mmol KI/L), I<sup>-</sup> ions are in competitions with the Cl<sup>-</sup> ions. Given the much higher concentration of KCl than KI, iodide ions sorption from solutions containing KCl should be much lower than from solutions without KCl, if sorption would be determined by anion exchange. But the results show that sorption of iodide ions from solutions containing excess of KCl is no lower than from solutions without KCl. These results suggest that a part of iodide ions and polyiodide is retained by AV-17(Cl) due to the anion exchange process and another as a result of a chemical interaction with polymer matrix.

Table 1

Isotherms constants of iodine ions sorption on AV-17(Cl) and AV-17(Bi).

Sorbent	Solution	Temperature, °C	$pH_{eq}$	$S_\infty$ , mmol/g	B, g/mmol
AV-17(Cl)	KI	16.5	4.85 – 5.65	0.74	48.5
AV-17(Cl)	KI + KCl	16.0	4.66 – 5.95	0.46	33.8

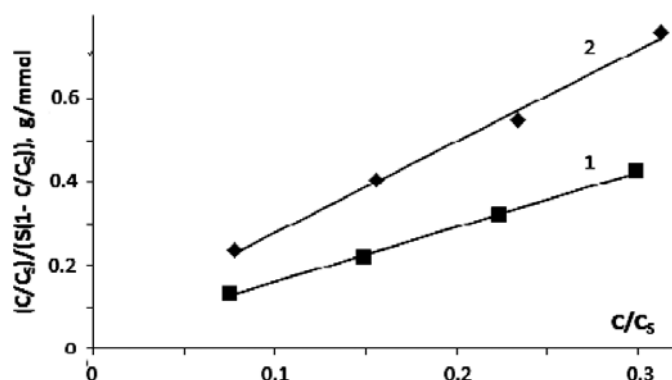
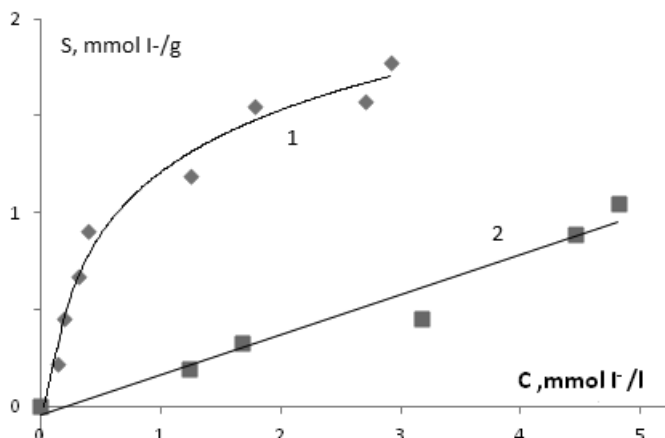


Figure 3. The linear BET isotherms of iodide ions sorption on AV-17(Cl) from KI solutions (1) and solutions containing KI and KCl (2).

It is known, that at low concentrations the BET isotherm turns to Langmuir isotherm. Indeed, sorption of iodide ions at 19.5°C in solutions with low concentrations of KI on the polymer Varion-AD(NO<sub>3</sub><sup>-</sup>) (strongly basic anion exchanger, analogue AV-17) is described by the Langmuir sorption model (Figure 4) according to Eq.(7):

$$S = \frac{S_{\infty} KC}{(1 + KC)}, \quad (7)$$

where,  $K$  is a constant (L/mmol),  $C$  – equilibrium concentration of iodide ions (mmol/L).



**Figure 4. The isotherms of iodide ions sorption by Varion-AD(NO<sub>3</sub><sup>-</sup>) from KI solutions (1) and solutions containing KI and KCl (2).**

Using linear form of the Langmuir isotherm (Figure 5), performed according to the Eq.(8), the constants  $S_{\infty}$  and  $K$  were calculated.

$$\frac{C}{S} = \frac{1}{(S_{\infty} K)} + \frac{C}{S_{\infty}} \quad (8)$$

The following values of the constants:  $S_{\infty} = 1.84$  mmol I/g and  $K = 2.134$  L/mmol were obtained. The sorption isotherm of iodide ions from 0.1 M KCl solutions on Varion-AD, obtained at 19.5°C, is approximately described by Henry sorption model (Figure 4) with  $K = 0.206$  L/g.

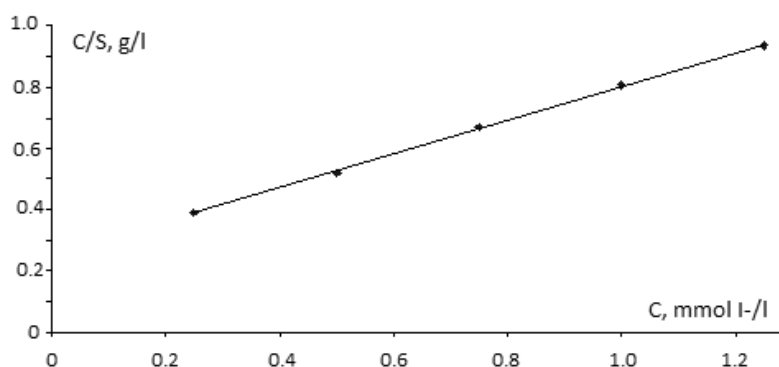


**Figure 5. The linear Langmuir isotherm of iodide ions sorption from KI solutions on Varion-AD(NO<sub>3</sub><sup>-</sup>).**

#### ***Iodide ions sorption on AV-17(Bi) in the static conditions***

As shown in Figure 6, the iodide ions sorption isotherm from KI solutions by sorbent AV-17(Bi), obtained at 12.5°C, also can be described by the BET sorption model. The isotherms of iodide ions sorption on AV-17(Bi) sorbent from solutions containing KI and KCl, obtained at 16°C and 60°C (Figure 7), also correspond to the BET adsorption model. From linear BET isotherms (Figure 8) considering  $C_s = 23.2$  mmol I/L (sorption from KI solutions),  $C_s = 21$

mmol I/L (sorption at 16°C from solutions containing KI and KCl) and  $C_s = 17$  mmol I/L (sorption at 60°C from solutions containing KI and KCl) were calculated constants shown in the Table 2.

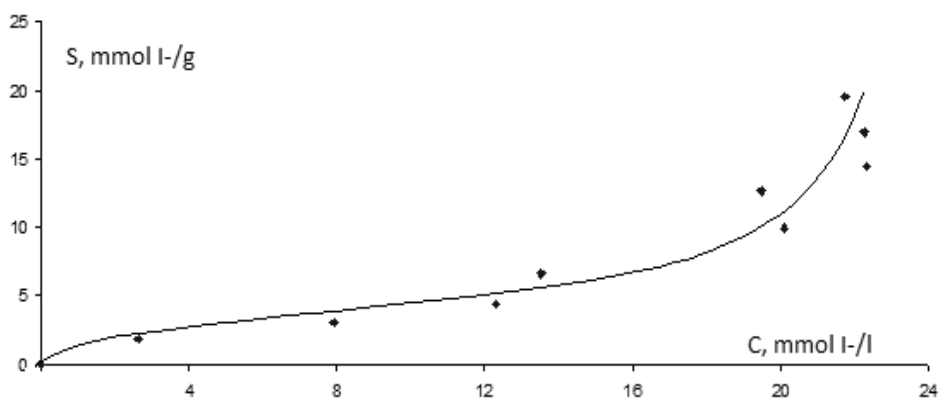


Figure 6. The isotherm of iodide ions sorption from KI solutions on AV-17(Bi).

Table 2

Isotherms constants of iodine ions sorption on AV-17(Cl) and AV-17(Bi).

Sorbent	Solution	Temperature, °C	$pH_{eq}$	$S_{\infty}$ , mmol/g	B, g/mmol
AV-17(Bi)	KI	12.5	5.0 – 6.15	2.23	15.2
AV-17(Bi)	KI + KCl	16.0	5.1 – 6.2	2.03	10.5
AV-17(Bi)	KI + KCl	60.0	4.54 – 6.1	1.87	7.8

From the Figures 6 and 7, and  $S_{\infty}$  values (Table 2) we can see that the monolayer sorption capacity of the sorbent AV-17(Bi) is much higher than of the polymer AV-17(Cl). It means that the compounds of Bi(III) in the polymer phase also are involved in the processes of iodide ions sorption. It is important to remark that the sorption of iodine ions slightly depends on the presence of KCl excess in the KI solution and on temperature. If to compare the data from the Figures 1 and 2, and Figures 6 and 7, we can see that the value of iodide ions sorption on AV-17(Cl) and AV-17(Bi) samples is almost the same.

It would seem that in the similar conditions maximal iodide ions sorption on AV-17(Bi) must be larger than on the AV-17(Cl) because in the first sorbent there are  $R_4NNO_3$  and Bi(III)-containing sorption centers and in the AV-17(Cl) there are only  $R_4NCl$  centers. It can be explained by the fact that a part of Bi(III) compounds are situated on  $R_4NNO_3$  groups and block the iodine ions access to them [9].

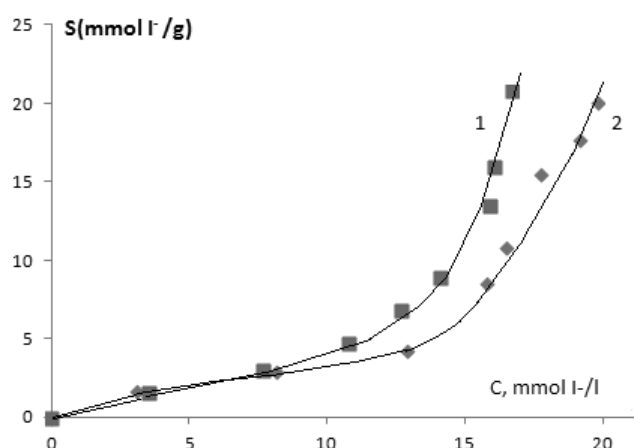


Figure 7. The isotherms of iodide ions sorption on AV-17(Bi) at 60°C (1) and 16°C (2) from solutions containing KI and KCl.

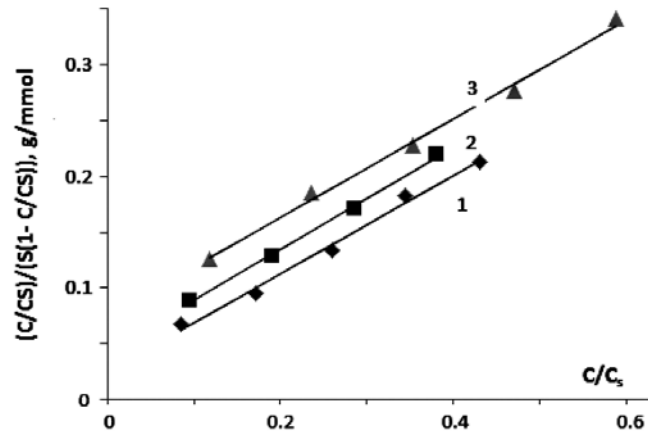


Figure 8. The linear BET isotherms of iodide ions sorption on AV-17(Bi) from KI solutions (1), from solutions containing KI and KCl at 16°C (2) and at 60°C (3).

*Iodide ions sorption on AV-17(Cl) and AV-17(Bi) in dynamic conditions*

Solution of KI with initial concentration of  $C_0 = 0.635$  mg I/mL,  $pH_0 = 5.0$  and a temperature of 14°C has been passed through the column containing 2 g of polymer AV-17(Cl) with a flow of 4.46 mL/min. In the effluents the concentration of I<sup>-</sup> ions and the value of pH were measured. From the obtained experimental data the dependencies  $C = f(V)$  and  $pH = f(V)$  were performed, where  $V$  is the volume of effluents. These dependencies are shown in Figures 9 and 10.

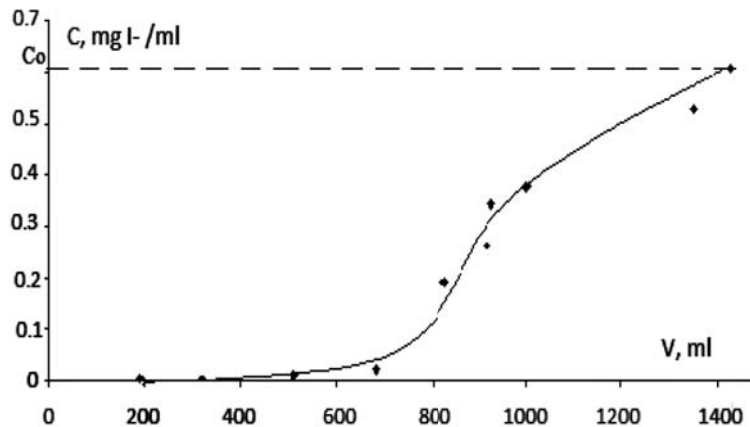


Figure 9. Breakthrough curves for sorption of iodine ions from KI solution on AV-17(Cl).

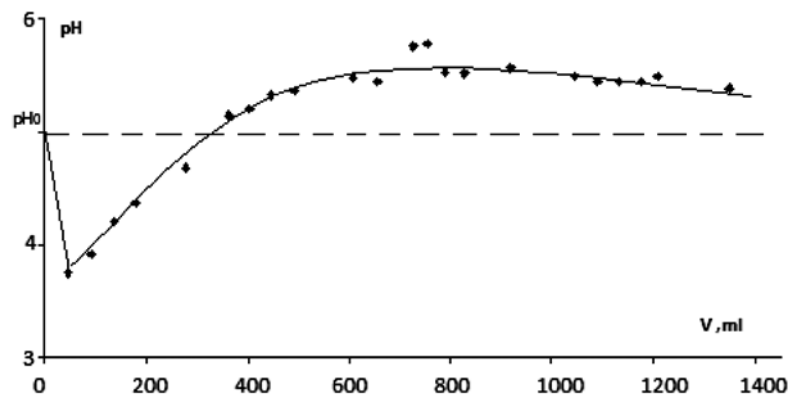


Figure 10. pH value of effluents during of iodide ions sorption on AV-17(Cl) from KI solution.



The dynamic sorption capacity (DSC), the total dynamic sorption capacity (TDSC) and the relative rate of sorption ( $W$ ) were calculated from Figure 9 and are presented in the Table 3. The values of these parameters are quite high.

Table 3

**Data of the iodide ions sorption in dynamic conditions.**

Sorbent	Solution	$t$ , °C	Flow rate, mL/min	DSC, mg I/g	TDSC, mg I/g	$W$ , %
AV-17(Cl)	KI	14	4.46	212.72	314.28	67.7
AV-17(Cl)	KI+KCl	16	5.00	124.46	167.10	74.5

In Figure 9 it can be seen that the speed of the sorption of iodide ions is quite high. This confirms the high rate of sorption that has been observed in the static conditions.

Sorption of iodide ions in 0.1M KCl solutions on polymer AV-17(Cl) at the same conditions of concentration of KI, temperature and initial pH, but at the flow rate of 5 mL/min, is lower than in the absence of KCl in solution (Figure 11, Table 3). But the relative rate of I<sup>-</sup> ions sorption from solution containing an excess of KCl is slightly larger (Table 3). Although the affinity of the polymer to the iodide ions is much greater than to chloride ions, these ions (Cl<sup>-</sup>) significantly affects I<sup>-</sup> ions sorption. The pH value of effluents during of iodide ions sorption on AV-17(Cl) from KI and KCl solution is presented in Figure 12.

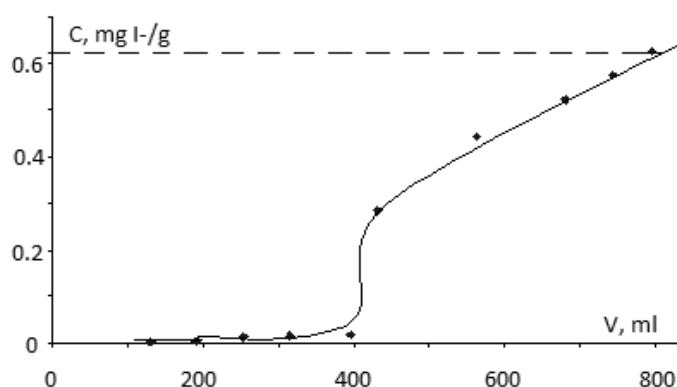


**Figure 11. Breakthrough curve for sorption of iodide ions on AV-17(Cl) from KI solution containing KCl.**

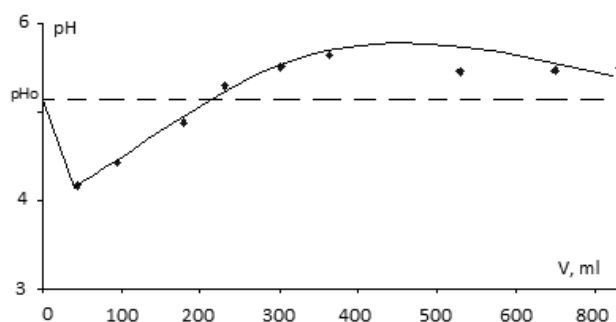


**Figure 12. pH value of effluents during of iodide ions sorption on AV-17(Cl) from KI and KCl solution.**

The breakthrough curves for sorption of iodide ions from solutions (containing 0.635 mg I/mL) on sorbent AV-17(Bi) and pH of the effluents are similar to those obtained using polymer AV-17(Cl) (Figures 13-16). The values of the sorption parameters are higher than for sorption on AV-17(Cl) in almost the same conditions. The data in Table 4 show that the iodide ions sorption parameters from solutions containing KI and KCl on the sorbent AV-17(Bi) are lower than those from solutions in absence of KCl. But they are quite high if to take in consideration that concentration of iodide ions is much lower than of the chloride ions. This confirms that the selectivity for iodide ions sorption on AV-17(Bi) is greater than that on the AV-17(Cl).

Decreases of iodide ions sorption from solutions containing excess of KCl can be explained by the fact that some of the Cl<sup>-</sup> ions can form I<sub>2</sub>Cl<sup>-</sup> which are retained less by the polymer. With increasing of temperature, concentration of I<sub>2</sub>Cl<sup>-</sup> ions also increases (Figure 7).

Table 4

Data of the iodide ions sorption in dynamic conditions.

Sorbent	Solution	<i>t</i> , °C	Flow rate, mL/min	DSC, mg I/g	TDSC, mg I/g	W, %
AV-17(Bi)	KI	16.5	4.9	263.52	377.62	69.8
AV-17(Bi)	KI+KCl	17.5	4.6	134.00	229.15	58.5

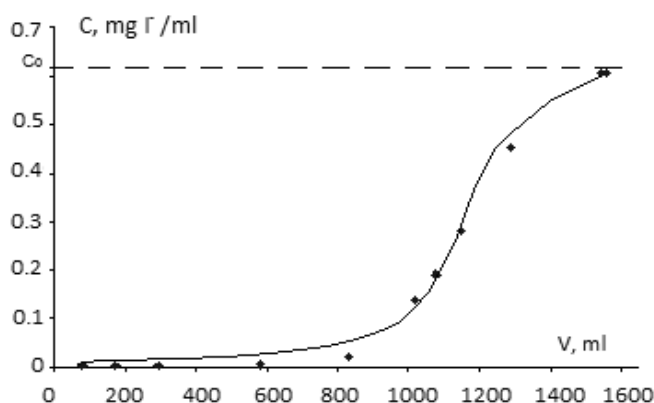


Figure 13. Breakthrough curve for sorption of iodide ions from KI solution on AV-17(Bi).

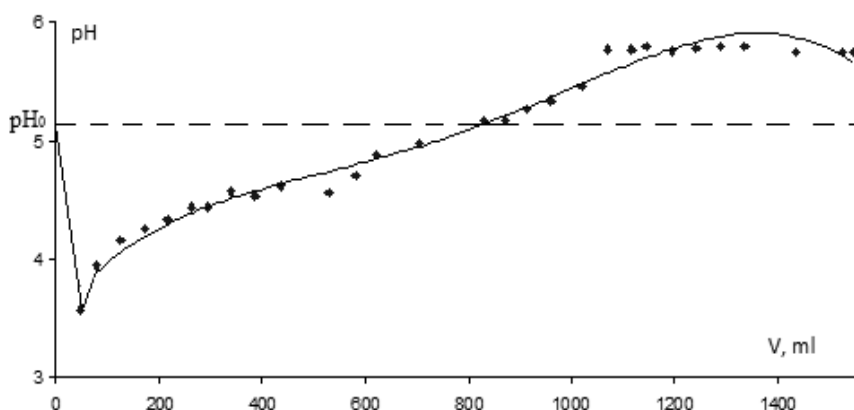


Figure 14. pH value of effluents during of iodide ions sorption on AV-17(Bi) from KI.

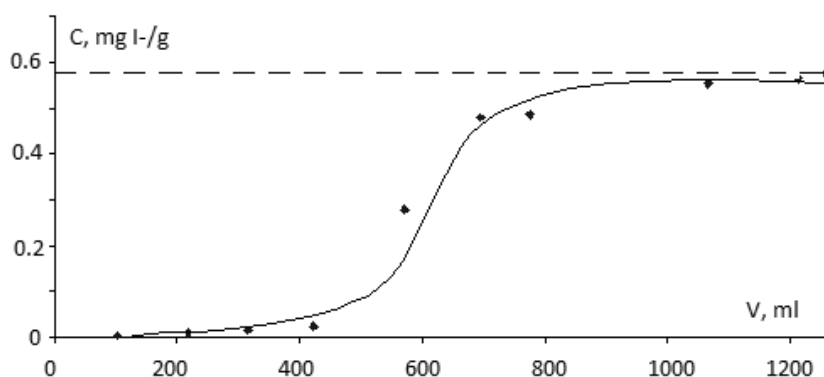
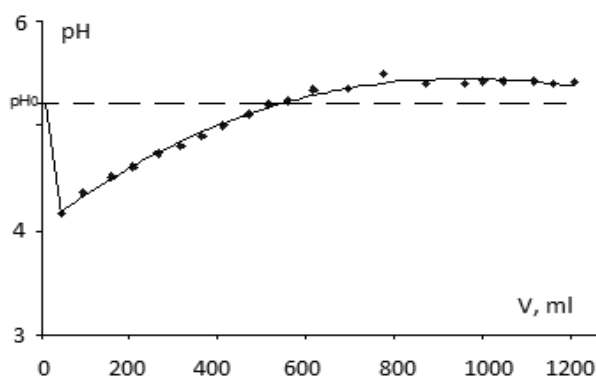


Figure 15. Breakthrough curve for sorption of iodide ions on AV-17(Bi) from solution containing KI and KCl.

Comparing the curves from Figures 10, 12, 14 and 16, it was established that in case of absorption from KI solutions and solutions containing KI and KCl, the variation of pH value in the effluents volume is almost the same for AV-17(Bi) or AB-17(Cl) samples.

Probably, at the beginning of the process, the polymer retains  $\text{OH}^-$  ions from solution, thus decreasing pH of the effluent. When promoting sorption layer of iodide ions along the column,  $\text{OH}^-$  ions are displaced in the effluents, increasing its pH. This can be explained by the increase of pH value in the effluents, which becomes higher than the initial pH of the solution.



**Figure 16.** pH value of effluents during of iodide ions sorption on AV-17(Bi) from KI and KCl.

**Note:** Additional qualitative experiments showed that sorbent AV-17(Bi) is able to retain compounds of iodine (and bromine) from Valeni drilling waters.

### Conclusions

Sorption of the iodide ions from solutions by strongly basic anion exchanger AV-17(Cl) and the AV-17(Bi) is a complex process. In the sorbent phase the polyiodide ions are formed. Polyiodide ions are retained by the sorbents in the result of anion exchange and chemisorption. The iodide ions sorption isotherms, obtained from KI and KI containing excess of KCl, can be described by BET sorption model. The iodide ions sorption, both in static and dynamic conditions, is super equivalent. The sorption selectivity of AV-17(Bi) in dynamic conditions is greater than that of AV-17(Cl).

### Acknowledgments

The author thanks to V. Lupan for his help in performing of some experiments.

### References

1. Stroeva, E.V. Physico-chemical bases of extracting iodine from solutions of highly mineralized Orenburg gas condensate. Ph.D. thesis, Mendeleev MCT University, Moscow, Russian Federation, 2004. (in Russian).
2. Myagkoy, O.N.; Krasova, K.N.; Serdiucova, M.I.; Meleshko, B.P. Theory and practice of the sorption processes. Voronezh State University: Voronezh, 1974, 9, pp. 86-91 (in Russian).
3. Myagkoy, O.N.; Serdiucova, M.I. Theory and practice of the sorption processes. Voronezh State University: Voronezh. 1977, 12, pp. 67-73 (in Russian).
4. Myagkoy, O.N.; Serdiucova, M.I.; Seryacenko, L.A. Theory and practice of the sorption processes. Voronezh State University: Voronezh, 1981, 16, pp. 36-41 (in Russian).
5. Serdiucova, M.I. Theory and practice of the sorption processes. Voronezh State University: Voronezh, 1984, 19, pp. 87-91 (in Russian).
6. Vulih, A.I.; Dubinina, E.G. Redox macromolecular compounds. Khimia: Leningrad, 1967, pp. 91-98 (in Russian).
7. Myagkoy, O.N.; Serdiucova, M.I.; Perunova, N.A. Theory and practice of the sorption processes. Voronezh State University: Voronezh, 1980, 15, pp. 73-77 (in Russian).
8. Zelentsov, V.; Datsko, T.Ya. Application of adsorption models in order to describe the equilibrium in the aluminum oxyhydroxide – fluor system. *Electronnaya obrabotka materialov*, 2012, 48(6), pp. 65-73 (in Russian).
9. Gutsanu, V.; Cojocaru, L.; Lisa, G.; Volodina, G.F. Some metal compounds in the phase of crosslinked ionic polymer- precursors for new sorbents and catalysts. *Journal of Applied Polymer Science*, 2012, 124, pp. 2582-2593.
10. Lurie, A.A. Sorbents and Chromatographic Carriers. Nauka: Moscow, 1972, 320 p. (in Russian).
11. Gutsanu, V.; Cojocaru, L. Process for obtaining selective sorbent containing Bi(III) compounds. MD Patent, 2007, No. 3295. (in Romanian).
12. Marcenko, Z. Photometrical Determination of Elements. Mir: Moscow, 1971, 502 p. (in Russian).

## LACTOFERRIN: ANALYSIS OF THE STRUCTURE PROFILE

Lilia Anghel

*Institute of Chemistry of the Academy of Sciences of Moldova, 3, Academiei str., Chisinau MD-2028, Republic of Moldova  
e-mail: anghel.lilia@gmail.com*

**Abstract.** The multitude of physiological processes in which the binding of iron ions takes part makes its mechanism worth investigating. The multiple sequence alignment method was applied to investigate the structure similarities of five lactoferrin X-ray crystallographic structures and outline the differences and similarities between lactoferrin and serum transferrin. The results of this study provide useful insights into the mechanism of iron-binding of lactoferrin protein molecule.

**Keywords:** iron, protein, lactoferrin, transferrin, multiple sequence alignment.

### Introduction

Intracellular iron plays an essential role in different physiological reactions such as metabolic oxidation/reduction reactions or building highly selective biological catalysts – enzymes [1]. Unbounded iron ions could initiate a multitude of deleterious processes in biological systems [2], therefore, cells have developed various systems for iron acquisition and intracellular transport. A common toolkit for iron transport is represented by the family of transferrin. The primary role of this protein family is to control the level of free iron ions in the body, protecting it from possible damages which free iron ions could initiate.

Lactoferrin is a protein that belongs to the family of transferrin. This protein also referred as lactotransferrin, originally was isolated from milk and later it was found in biological fluids such as blood plasma, tears, saliva, pancreatic juice, bile. In blood plasma lactoferrin derives from specific granules of neutrophils but there are evidences that it might be produced by other cells and even microorganisms [3].

### Structure of lactoferrin

Lactoferrin is a non-haem iron-binding glycosylated protein with a molecular mass of about 80 kDa. Its polypeptide chain consists of about 600-700 amino acid residues. The number of amino acids in the protein structure varies depending on the origin of the molecule. The structure of a lactoferrin molecule is composed of  $\alpha$ -helix and  $\beta$ -sheets which are presented in Figure 1 as ribbons and arrows, respectively.

The protein structure is divided in two lobes, referred as N- and C- lobes which are connected by a 3-turn-helix structure (see Figure1). Both protein lobes share a degree of similarity of about 40% [4]. Each lobe contains an iron-binding site consisting of an aspartic acid, a histidine and two tyrosine residues (Figure 2). Iron coordination in each protein cleft is finished through a carbonate / bicarbonate ion.

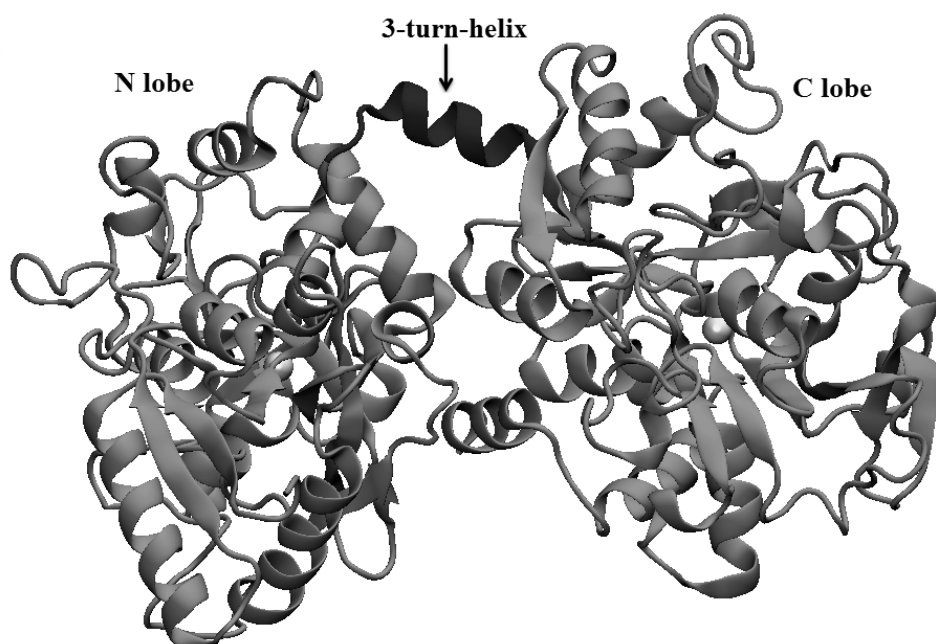


**Figure 1.** Structure representation of diferric human lactoferrin (1B0L Protein Data Bank code). The protein is presented in ribbon and ferric ions are presented as van der Waals spheres.

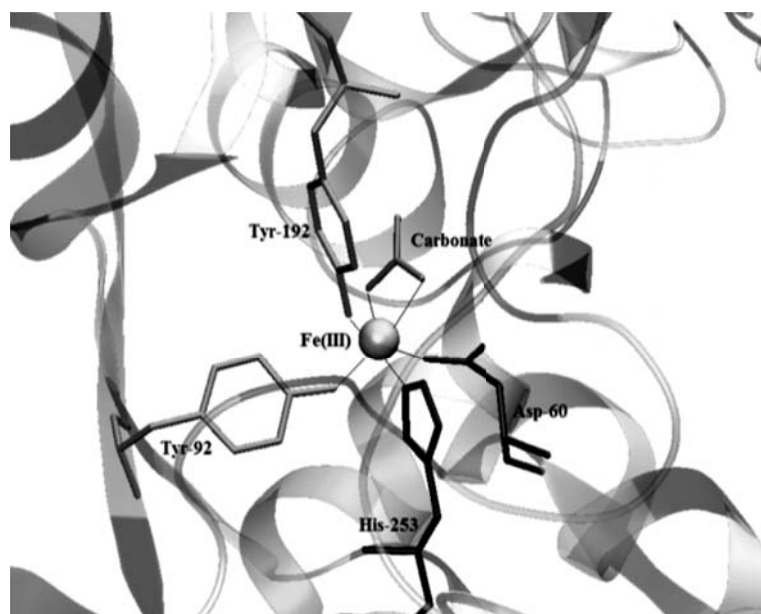


**Figure 2. Graphical representation of the active iron-binding site of the N-lobe of human lactoferrin (1B0L Protein Data Bank code).**

Table 1 presents the bond lengths of ferric ion to coordinated ligands measured on the basis of the X-ray crystallographic structure file of human lactoferrin (1B0L entry).

Even though subsequent studies have shown that lactoferrin molecule is capable of binding other metal ions its affinity for iron ions is greater in comparison to serum transferrin [5-6]. The primary biological role of lactoferrin is to bind iron in physiological fluids, but there is no evidence of transport function that is characteristic to the other members of the transferrin family. This indicates on the existence of a different mechanism of iron-binding. The process of iron binding and release from lactoferrin molecule depends on its molecular properties and on the location where it is expressed. To help gain more insights into the process of iron uptake, it is important to investigate the structure similarities of lactoferrin molecules isolated from different species (see Table 2) and outline the structure differences and similarities between lactoferrin [7] and serum transferrin [12].

*Table 1*

**The bond lengths (Å) of Fe(III) to coordinated ligands in human lactoferrin.**

<i>Bond</i>	<i>N lobe</i>	<i>C lobe</i>
Fe-O:Asp60 (Asp395)	2.146	2.008
Fe-O:Tyr92 (Tyr435)	2.035	2.004
Fe-O:Tyr192 (Tyr 528)	1.817	1.848
Fe-N:His253 (His597)	2.087	2.194
Fe-O1:CO <sub>3</sub> <sup>2-</sup> 695(CO <sub>3</sub> <sup>2-</sup> 696)	2.007	2.286
Fe-O2:CO <sub>3</sub> <sup>2-</sup> 695(CO <sub>3</sub> <sup>2-</sup> 696)	2.138	2.010

### Materials and methods

Multiple sequence alignment (MSA) method is used in sequence and structural assessment of sets of macromolecular biological molecules which have a common evolutionary relationship. The sequence assessment is performed using sequence alignment analysis, which makes use of the sequence information from the protein structure to perform the alignment of the protein molecules and for the evaluation of their degree of similarity. When making a sequence alignment it should also be considered the structural information. The effect of the substitution of an amino acid sometimes within the sequence can cause substantial effects of the function of the protein. Therefore, for a correct alignment, structural information should also be used. The structural assessment is performed using the structure alignment analysis. The output of the implementation of this method offers the possibility to build an accurate profile for structurally related proteins.

The multiple sequence alignment method was applied to investigate the structure similarities and differences of five lactoferrin X-ray crystallographic structures and outline the differences between lactoferrin and serum transferrin. The coordinate files of the investigated proteins were downloaded from Protein Data Bank (PDB) [13]. The PDB codes

are listed in Table 2. Visual Molecular Dynamics (VMD) software [14] was used for all graphical representations. The analysis was performed using MultiSeq 2.0, a unified analysis environment, included in the VMD. Multiseq 2.0 was developed for the analysis of sequence and structure of proteins and nucleic acids [15]. For the structural data, proteins were aligned using STAMP [16] plug-in and for sequence data, proteins were aligned using ClustalW [17] plug-in. As a result of the implementation of the algorithms include in STAMP and ClustalW plug-ins the following set of parameters was computed for each protein structure:  $Q_{res}$  (structure similarity per residue),  $Q_H$  (structural homology), Percent Identity and RMSD (root mean square deviation). The computed values for these parameters will differ as a result of a different alignment algorithm applied to the same set of proteins. Therefore these parameters can be used to assess the quality of the alignment and common similarities of the analyzed proteins.

$Q_{res}$  is the parameter used to measure the structural similarity of each residue in a set of aligned structures by measuring the backbone carbon distances between a residue and all other residues in the protein, excluding nearest neighbors, to the corresponding distances in a given set of proteins.

In the MultiSeq 2.0 this parameter is defined by the following formula:

$$Q_{res}^{(i,n)} = \aleph \sum_{\substack{\text{proteins} \\ (m \neq n)}} \sum_{\substack{\text{residue} \\ (j \neq i-1, i, i+1)}} \exp \left[ -\frac{\left( r_{ij}^{(n)} - r_{i'j'}^{(m)} \right)^2}{2\sigma_{ij}^2} \right] \quad (1)$$

where:  $Q_{res}^{(i,n)}$  is the structural similarity of the  $n^{\text{th}}$  amino acid residue in the  $n^{\text{th}}$  protein;

$r_{ij}^{(n)}$  is the  $C_\alpha - C_\alpha$  distance between residues  $i$  and  $j$  in protein  $n$ ;

$r_{i'j'}^{(m)}$  is the  $C_\alpha - C_\alpha$  distance between residues  $i'$  and  $j'$  in protein  $m$  that correspond to residues  $i$  and  $j$  in protein  $n$ ;

$\sigma_{ij}^2 = |i - j|^{0.15}$  is the variance related to the sequence separation between residues  $i$  and  $j$ ;

$\aleph = \left( (N_{seq} - 1)(N_{res} - k) \right)^{-1}$  is the normalization, with  $N_{seq}$  - the number of proteins in the set and  $N_{res}$  - the number of amino acid residues in protein  $n$ , and  $k = 3$  except when the residue  $i$  is the N or C-terminus of the protein, in this case  $k = 2$  [15].

$Q_H$  measures the homology of two structures by summing the similarity of all residues ( $Q_{res}$ ) and adds a term for each gap (structural deviation) in the alignment, its mathematical expression is presented elsewhere [18]. Percent Identity parameter is derived from the  $Q_H$ .  $Q$  values range from 0 to 1, for  $Q=1$  the proteins are identical. RMSD measures the distances in angstroms between the atoms  $C_\alpha$  of two aligned residues and indicates how well two structures were aligned [15].

Table 2

The PDB code of the X-ray structure files of the proteins used for this study.

PDB code	Description	Reference
1B0L	Diferric human lactoferrin	[7]
1BIY	Diferric buffalo lactoferrin	[8]
1BLF	Diferric bovine lactoferrin	[9]
1I6B	Diferric equine lactoferrin	[10]
1I6Q	Diferric camel lactoferrin	[11]
3QYT	Diferric human transferrin	[12]

## Results and discussion

### Conservation of lactoferrin across the species

The goal of this study was to detect the common similarities of several lactoferrin protein molecules from the alignments of their structures and sequences. A simple structure inspection in the VMD showed that in all five lactoferrin structures iron is bounded to the same four amino acid residues (Figure 2) and one carbonate ion. Each lactoferrin molecule consists of 689 amino acids, except human lactoferrin, which is composed of 691 amino acids.

Representation of the multiple sequence alignment of bovine, buffalo, equine and camel lactoferrin colored by sequence identity is depicted in Figure 3.

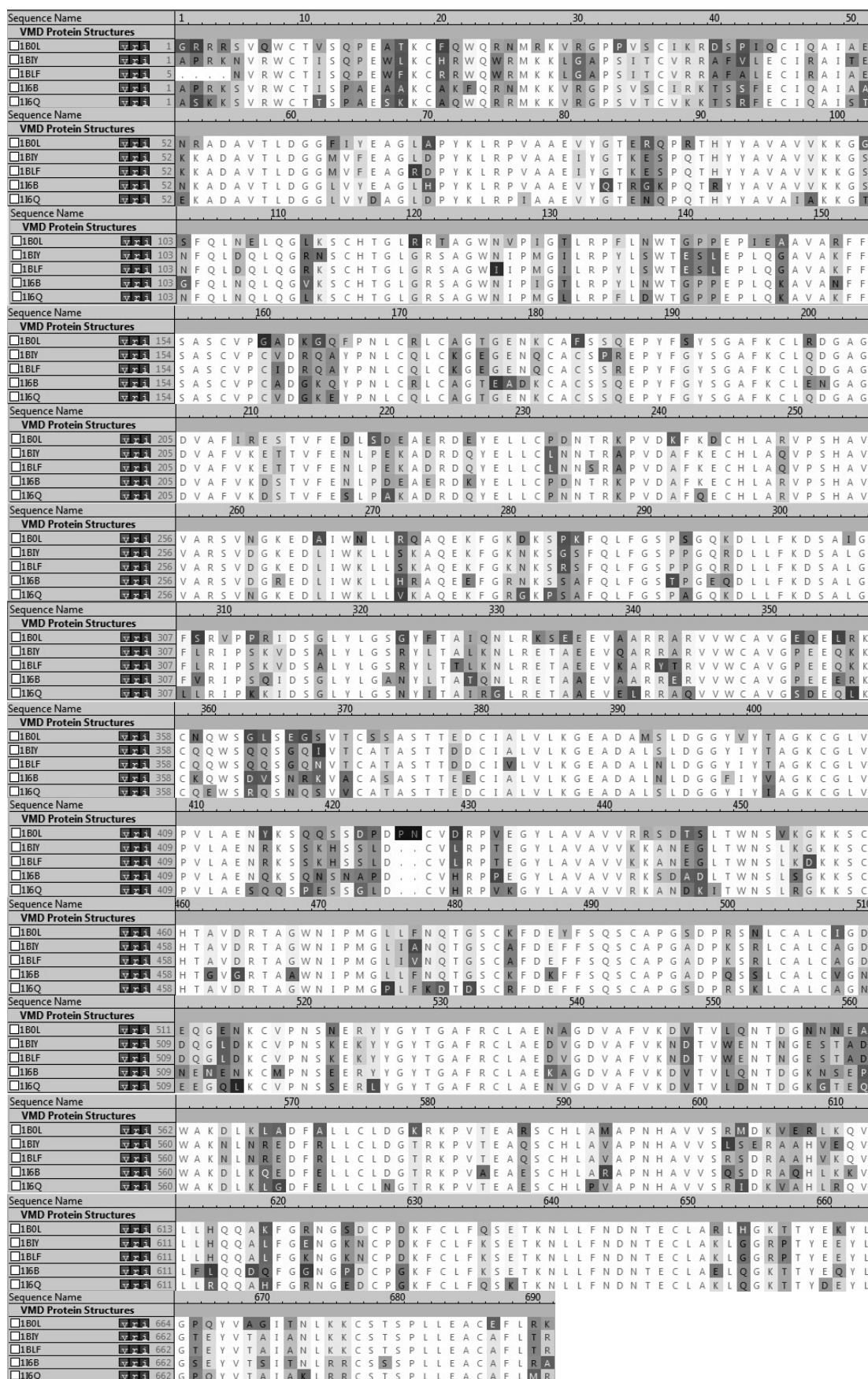


Figure 3. Representation of the multiple sequence alignment of the five studied lactoferrins colored by sequence identity. Variable residues are highlighted in grey.

The structure and sequence and identity parameters for the five studied lactoferrins structures were computed with respect to the structure of human lactoferrin and results of this study are presented in Table 3 and Table 4.

Parameters computed from the structural alignment show that overall the structure of lactoferrin is highly conserved across all species investigated in this study. Only in the case of camel lactoferrin the structural homology parameter is lower in comparison to the rest of proteins,  $Q_H$  is 0.3869 and the Percent Identity is 30.60%.

Table 3

**Structural alignment parameters computed for the studied lactoferrin structures.**

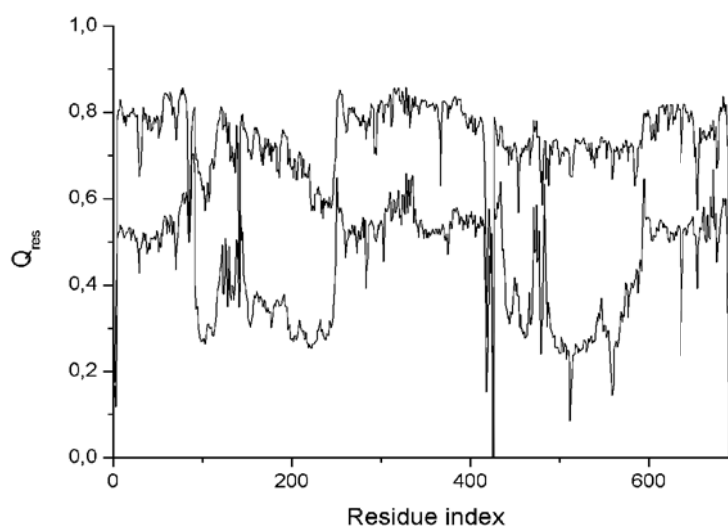
	<i>Buffalo lactoferrin</i>	<i>Bovine lactoferrin</i>	<i>Equine lactoferrin</i>	<i>Camel lactoferrin</i>
$Q_H$	0.8393	0.8160	0.8688	0.3869
RMSD (Å)	1.5354	1.8106	1.2773	1.6093
Percent Identity (%)	69.35	68.88	74.31	30.60

Table 4

**Sequence alignment parameters computed for the studied lactoferrin structures.**

	<i>Buffalo lactoferrin</i>	<i>Bovine lactoferrin</i>	<i>Equine lactoferrin</i>	<i>Camel lactoferrin</i>
$Q_H$	0.8356	0.8154	0.8634	0.4503
RMSD (Å)	1.6093	1.8616	1.1414	12.6343
Percent Identity (%)	70.19	69.61	74.96	73.81

The sequence alignment analysis showing that camel lactoferrin differs from the other structures not only chemically but also the arrangement of the residues in the protein structure differs a lot more (RMSD=12.6343). Figure 4 presents the plot of structure similarity ( $Q_{res}$ ) per residue of the human lactoferrin and camel lactoferrin, computed from the sequence alignment. Even though the  $Q_{res}$  values of both lactoferrins differ, the general pattern presented in Figure 4 is similar in both cases indicating a common structure profile.



**Figure 4. Plot of the structural similarity computed from the sequence alignment of each residue of the human lactoferrin (black) and camel lactoferrin (light grey).**

#### ***Structural comparison of human serum transferrin and human lactoferrin molecules***

Human serum transferrin and human lactoferrin are members of the transferrin family. These proteins are known for their ability of binding iron, although serum transferrin is also responsible for the iron transportation. Both proteins share a similar architecture, with a structure consisting of two lobes (N and C) attached by a linker region. In both proteins an iron ion is bounded to an aspartic acid, two tyrosine, a histidine residues and a carbonate or bicarbonate ion. Although these two proteins share many similarities, there are some structural differences that may influence the mechanism of iron-binding. The most prominent structural difference between these two proteins is the linker region between the two lobes. The lactoferrin linker is an uncompleted  $\alpha$ -helix structure whilst the transferrin linker is represented by an unstructured residue conformation (see Figure 5). Experimental studies [19] have shown that iron-binding process is pH-dependent, meaning that iron will bind to the protein only when the key-residues from the protein structure will have a certain protonation state. For example, in case of transferrin iron-binding is triggered by two lysine residues which are localized in the vicinity of the active site of the N lobe of protein. In acidic medium these two



lysine residues will become charged which will lead to repulsion and forcing the opening of the N lobe of transferrin, this mechanism is known as dilysine trigger. In the lactoferrin structure this mechanism is absent due to the fact that the first lysine is replaced by an arginine residue. The multiple sequence alignment was applied to investigate the degree of similarity between the structures of human lactoferrin and human serum transferrin. Results of this study are presented in Figure 6 and Table 5.

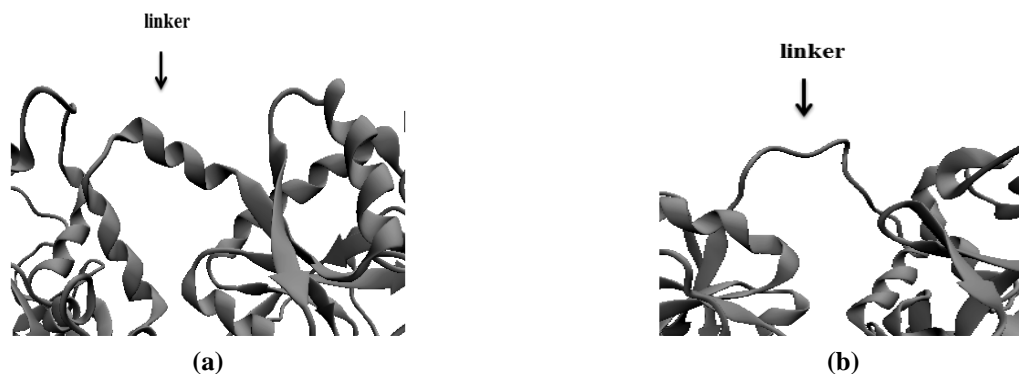


Figure 5. Graphical representation of the linker region in the structure of human lactoferrin (a) and human serum transferrin (b).

Sequence Name	1	10	20	30	40	50
<b>VMD Protein Structures</b>						
1B0L	1	G R R R S V Q W C T I V S Q P E A T K C F Q W Q R N M R K V R . . . G P P V S C I K R D S P I Q C I Q A				
3QYT	1	V P D K T V R W C A V S E H E A T K C Q S F R D H M K S V I P S D G P S V A C V K K A S Y L D C I R A				
Sequence Name	60	70	80	90	100	
<b>VMD Protein Structures</b>						
1B0L	49	I A E N R A D A V T L D G G F I Y E A G L A P Y K L R P V A A E V Y G T E R Q P R T H Y Y A V A V V K				
3QYT	52	I A A N E A D A V T L D A G L V Y D A Y L A P N N L K P V V A E F Y G S K E D P Q T F Y Y A V A V V K				
Sequence Name	110	120	130	140	150	
<b>VMD Protein Structures</b>						
1B0L	100	K G G S F Q L N E L Q G L K S C H T G L R R T A G W N V P I G T L R P F L N W T G P P E P I E A A V A				
3QYT	103	K D S G F Q M N Q L R G K K S C H T G L G R S A G W N I P I G L L . . . Y C D L P E P R K P L E K A V A				
Sequence Name	160	170	180	190	200	
<b>VMD Protein Structures</b>						
1B0L	151	R F F S A S C V P G A D K G Q F P N L C R L C A G T G E N K C A F S S Q E P Y F S Y S G A F K C L R D				
3QYT	152	N F F S G S C A P C A D G T D F P Q L C Q L C P G . . . . . C G C S T L N Q Y F G Y S G A F K C L K D				
Sequence Name	210	220	230	240	250	
<b>VMD Protein Structures</b>						
1B0L	202	G A G D V A F I R E S T V F E D L S D E A E R D E Y E L L C P D N T R K P V D K F K D C H L A R V P S				
3QYT	198	G A G D V A F V K H S T I F E N L A N K A D R D Q Y E L L C L D N T R K P V D E Y K D C H L A Q V P S				
Sequence Name	260	270	280	290	300	
<b>VMD Protein Structures</b>						
1B0L	253	H A V V A R S V N G K E D A I W N L L R Q A Q E K F G K D K S P K F Q L F G S P S G Q K D L L F K D S				
3QYT	249	H T V V A R S M G G K E D L I W E L L N O A Q E H F G K D K S K E F O L F S S P H G . K D L L F K D S				
Sequence Name	310	320	330	340	350	
<b>VMD Protein Structures</b>						
1B0L	304	A T G F S R V P P R I D S G L Y L G S G Y F T A I Q N L R K . . S E E E V A A R R A R V V W C A V G E				
3QYT	299	A H G F L K V P P R M D A K M Y L G Y E Y V T A I R N L R E G T C P E A P T D E C K P V K W C A L S H				
Sequence Name	360	370	380	390	400	
<b>VMD Protein Structures</b>						
1B0L	353	Q E L R L K C N Q W S G L S E G S V T C S S A S T T E D C I A L V L K G E A D A M S L D G G Y V Y T A G				
3QYT	350	H E R L L K C D E W S V N S V G K I E C V S A E T T E D C I A K I M N G E A D A M S L D G G F V Y I A G				
Sequence Name	410	420	430	440	450	
<b>VMD Protein Structures</b>						
1B0L	404	K C G L V P V L A E N Y K S Q Q S S D P D P N C V D R P V E G Y L A V A V V R R S D T S L T W N S V K				
3QYT	401	K C G L V P V L A E N Y N K . . . S D . . . N C E D T P E A G Y F A V A V V K K S A S D L T W D N L K				
Sequence Name	460	470	480	490	500	510
<b>VMD Protein Structures</b>						
1B0L	455	G K K S C H T A V D R T A G W N I P M G L L F N Q T G S C K F D E Y F S Q S C A P G S D P R S N L C A				
3QYT	446	G K K S C H T A V G R T A G W N I P M G L L Y N K I N H C R F D E F F S E G C A P G S K K D S S L C K				
Sequence Name	520	530	540	550	560	
<b>VMD Protein Structures</b>						
1B0L	506	L C I G D E Q G E N K C V P N S N E R Y Y G Y T G A F R C L A E N A G D V A F V K D V T V L Q N T D G				
3QYT	497	L C M G . . S G L N L C E P N N K E G Y Y G Y T G A F R C L V E K G D V A F V K H Q T V P Q N T G G				
Sequence Name	570	580	590	600	610	
<b>VMD Protein Structures</b>						
1B0L	557	N N E A W A K D L K L A D F A L L C L D G K R K P V T E A R S C H L A M A P N H A V V S R M D K V E				
3QYT	545	K N P D P W A K N L N E K D Y E L L C L D G T R K P V E E Y A N C H L A R A P N H A V V T R K D K E A				
Sequence Name	620	630	640	650	660	
<b>VMD Protein Structures</b>						
1B0L	608	R L K Q V L L H Q Q A K F G R N G S D C P D K F C L F Q S E T K N L L F N D N T E C L A R L H G K T T				
3QYT	596	C V H K I L R Q Q H L F G S N V T D C S G N F C L F R S E T K D L L F R D D T V C L A K L H D R N T				
Sequence Name	670	680	690			
<b>VMD Protein Structures</b>						
1B0L	659	Y E K Y L G P Q Y V A G I T N L K K C S T S P L L E A C E F L R K				
3QYT	647	Y E K Y L G E E Y V K A V G N L R K C S T S S L L E A C T F R R P				

Figure 6. Representation of the multiple sequence alignment of the human lactoferrin (1B0L pdb) and human serum transferrin (3QYT pdb). Variable residues are highlighted.

Structure alignment parameters indicate a visible structural similarity between proteins, and that 41.90% of residues from the structure are identical in both proteins. The sequence alignment parameters present a different picture. The RMSD value of 6.8932 Å, computed from the sequence alignment indicates that the structures of both proteins aren't well aligned and therefore the sequences of these two proteins differ, although the structural homology,  $Q_H$ , is approximately 0.5 and a Percent Identity of 60.49%.

Table 5

**Structure and sequence alignment parameters computed for the human lactoferrin and human serum transferrin structures.**

	$Q_H$	RMSD (Å)	Percent Identity (%)
Structure alignment analysis	0.5251	3.2254	41.90
Sequence alignment analysis	0.5501	6.8932	60.49

## Conclusions

The multiple sequence alignment method was applied to investigate the structure similarities of five lactoferrin X-ray crystallographic structures and outline the differences between lactoferrin and serum transferrin.

Given the obtained results, it can be concluded that overall the structure of lactoferrin is highly conserved across all species investigated in this study. It was identified that only camel lactoferrin structurally differs from other lactoferrins. General pattern of camel lactoferrin is similar to the other four structures, pointing on a common structure profile.

Comparison of the structure human lactoferrin and human serum transferrin has revealed some insights into the architecture of these two proteins. Structure alignment parameters indicate a visible structural similarity between proteins; both proteins share a similar architecture. Structural differences of human lactoferrin and human serum transferrin were assessed using the sequence alignment analysis. Sequence differences are dictated by nucleotide sequence of their genes pointing onto the existence of differences in the three-dimensional structure that determines the proteins activity.

Results of this study increase our understanding of the structural profile of lactoferrin protein and provide useful insights into the iron-binding process.

## Acknowledgements

I would like to acknowledge and express my sincere gratitude to my scientific adviser Acad. Gheorghe Duca for continuous guidance and encouragement throughout every process of my research.

I gratefully acknowledge the Programs of Collaboration JINR-Romania (projects No.81/18.02.2013-37 and No.95/17.02.2014-26 within the JINR Theme No.04-4-1069-2009/2014) and Moldovan State Programs (project No. 14.518.02.05A) for the support.

## References

- Duca, Gh. Homogeneous Catalysis with Metal Complexes: Fundamentals and Applications. Springer Series in Chemical Physics: Berlin Heidelberg, 2012, XII, 478 p.
- Duca, Gh.; Secara, N. The free radicals in biological systems: formation and protection mechanisms. Akademos: Journal of Science, Innovation, Culture and Art, 2010, 4(19), pp. 115-118.
- Levay, P.F.; Viljoen, M. Lactoferrin: a general review. Haematologica, 1995, 80, pp. 252-267.
- Baker, E.N.; Baker, H.M. Molecular structure, binding properties and dynamics of lactoferrin. Cellular and Molecular Life Sciences, 2005, 62, pp. 2531-2539.
- Smith, C.A.; Anderson, B.F.; Baker, H.M.; Baker, E.N. Metal substitution in transferrins: the crystal structure of human copper-lactoferrin at 2.1-Å resolution. Biochemistry, 1992, 31, pp. 4527-4533.
- Loehr, T.M. Ed. Iron Carriers and Iron Proteins, VCH Publishers: New York, 1989, 533 p.
- Sun, X.L.; Baker, H.M.; Shewry, S.C.; Jameson, G.B.; Baker, E.N. Structure of recombinant human lactoferrin expressed in *Aspergillus awamori*. Acta Crystallographica, Section D, 1999, 55, pp. 403-407.
- Karthikeyan, S.; Yadav, S.; Paramasivam, M.; Srinivasan, A.; Singh, T.P. Structure of buffalo lactoferrin at 3.3 Å resolution at 277 K. Acta Crystallographica, Section D, 2000, 56, pp. 684-689.
- Moore, S.A.; Anderson, B.F.; Groom, C.R.; Haridas, M.; Baker, E.N. Three-dimensional structure of diferric bovine lactoferrin at 2.8 Å resolution. Journal of Molecular Biology, 1997, 274, pp. 222-236.
- Kumar, P.; Khan, J.A.; Yadav, S.; Singh, T.P. Crystal structure of equine apolactoferrin at 303 K providing further evidence of closed conformations of N and C lobes. Acta Crystallographica, Section D 2002, 58, pp. 225-232.
- Khan, J.A.; Kumar, P.; Srinivasan, A.; Singh, T.P. Protein intermediate trapped by the simultaneous crystallization process. Crystal structure of an iron-saturated intermediate in the  $Fe^{3+}$  binding pathway of camel lactoferrin at 2.7 Å resolution. The Journal of Biological Chemistry, 2001, 276, pp.36817-36823.

12. Yang, N.; Zhang, H.; Wang, M.; Hao, Q.; Sun, H. Iron and bismuth bound human serum transferrin reveals a partially-opened conformation in the N-lobe. *Scientific Reports*, 2012, 2, doi:10.1038/srep00999.
13. Protein Data Bank – an information portal to biological macromolecules <http://www.rcsb.org/pdb/home/home.do>
14. Humphrey, W.; Dalke, A. Schülten, K. VMD - Visual Molecular Dynamics. *Journal of Molecular Graphics*, 1996, 14, pp. 33-38.
15. Roberts, E.; Eargle, J.; Wright, D.; Luthey-Schulten, Z. MultiSeq: unifying sequence and structure data for evolutionary analysis, *BMC Bioinformatics*, 2006, 7(382), pp. 1-11.
16. Russell, R.B.; Barton, G.J. Multiple protein sequence alignment from tertiary structure comparison: assignment of global and residue confidence levels. *Proteins*, 1992, 14(2), pp. 309-323.
17. Thompson, J.D.; Higgins, D.G.; Gibson, T.J. CLUSTAL W: improving the sensitivity of progressive multiple sequence alignment through sequence weighting, position-specific gap penalties and weight matrix choice. *Nucleic Acids Research*, 1994, 22(22), pp. 4673-4680.
18. O'Donoghue, P.; Luthey-Schulten, Z. On the evolution of structure in aminoacyl-tRNA synthetases. *Microbiology and Molecular Biology Reviews*, 2013, 67(4), pp. 550-573.
19. He, Q.Y.; Mason, A.B.; Tam, B.M. MacGillivray, R.T.A.; Woodworth, R.C. Dual role of Lys206-Lys296 interaction in human transferrin N-lobe: Iron-release trigger and anion-binding site. *Biochemistry*, 1999, 38, pp. 9704–9711.

## MALDI-TOF INVESTIGATION OF LYSOZYME-ALBUMIN INTERACTION

Marharyta Vasylieva, Taras Gromovoy\*

*O. Chuiko Institute of Surface Chemistry, National Academy of Sciences of Ukraine,  
17, General Naumov str., Kyiv 03164, Ukraine*

*\*e-mail: gromovoy@mail.md, phone: (+38 044) 42 494 56*

**Abstract.** Proteins are the main components of living systems therefore they are a subject of study from different points of view. Under certain conditions, proteins are capable of self-organization forming oligomeric structures of various composition and new properties. The investigations of these transformations were carried out on two well known proteins: albumin and lysozyme. It is shown that with increase in the concentration of lysozyme in relation to that of albumin the intensities of the peaks corresponding to associates, related to the intensities of the peaks corresponding to albumin and lysozyme, are also increased. Associates of albumin and lysozyme are forming in the stoichiometric ratios of 1:1, 1:2, 1:3, 1:4. A similar pattern is observed in the case of albumin dimer.

**Keywords:** MALDI-TOF, albumin, lysozyme, protein-protein interaction.

### Introduction

Proteins, as the main components of living systems, are an interesting object of study from different points of view. At the molecular level, with application of new physical and chemical methods, research on some aspects of the evolution of matter and the nature of the interaction of macromolecules with each other has become available [1]. It is known that proteins are capable of self-organization outside the living system. They form oligomeric structures of various composition new properties [2-4].

The study of self-organization of proteins is carried out by different methods and in different systems. This can be a chromatographic separation of the associates, changes in the intensity of scattered light, sedimentation analysis, IR spectroscopy, changing pH etc. [5]. All these methods indicate the emergence of new properties of associates, but quantitative characteristics of mentioned associates are unexplored, such as is the nature of quantitative and qualitative changes of associates formed at different concentrations of proteins in solution [6,7]. The important issue in this research is preserving of the native structure of proteins, which suggests the possibility of these processes to take place *in vivo* [8,9].

In the present study proteins albumin and lysozyme were selected, due to their simultaneous presence in biological fluids and their functions. Lysozyme and albumin are found in the contact with the environment - the mucous membrane of the nasopharynx, oral and gastrointestinal tract, lacrimal fluid. Lysozyme belongs to the class of hydrolases that destroy the cell walls of bacteria. Albumin belongs to a class of transport proteins that exhibit high binding effect to low-molecular-weight compounds and contains both hydrophilic and lipophilic areas. Also, the intensity of inflammation *in vivo* may vary with the strength of binding proteases (antimicrobial proteins) by albumin.

The study of such systems can be considered from different points: as a component of biological fluids (changes in the quantitative composition and properties) used as the base or the active ingredient in the pharmaceutical industry, the determination of constants of interaction with other macromolecules, modeling of protein- protein and protein-ligand (complex formation) interactions [10,11].

### Experimental

Lysozyme and human serum albumin (HSA) were dissolved in water at concentration of 1 mg/mL. Lysozyme solution was mixed with a solution of HSA in different ratios. Solution 1 consisted of 0.1 mL HSA and 0.4 mL of lysozyme, solution 2 - 0.2 mL HSA and 0.3 mL of lysozyme, solution 3 - 0.3 mL HSA and 0.2 mL lysozyme, and solution 4 - 0.4 mL HSA and 0.1 mL of lysozyme. After incubation under standard conditions for 2 h solutions were investigated by MALDI-TOF. We used this approach to mixing in order to maintain a uniform concentration of proteins in the mixture. This preserves the matrix to analyte ratio in all cases, which increases the reliability of the mass spectra and enables a comparative analysis.

### Results and discussion

In the Figure 1, the mass spectra of the starting compounds are presented. As Figure 1 shows, albumin (m/z 66000) forms homogenous dimers (m/z 132,000) and trimers (m/z 198000) under the conditions of our experiment. Lysozyme (m/z 14200) under these conditions forms homooligomers with high oligomerization number up to 5 (Figure 1).

For solutions 1-4 in all the mass spectra, the formation of heterocompositions of albumin and lysozyme with different stoichiometric ratios was observed (Figure 2). The solution 1 is characterized by presence of the heterostructures albumin - lysozyme and albumin dimer - lysozyme at stoichiometric ratios of (1:1, 1:2) and (1:1), respectively. With advance of lysozyme concentration relative to that of albumin (solution 2), peaks observed in the mass spectrum

correspond to the formation of the above-mentioned products along with (albumin - lysozyme) complex with ratio (1:3). With further increase in the concentration of lysozyme (solutions 3 and 4), the formation of the structures (albumin - lysozyme dimer), ratio 1:4 and (albumin - lysozyme), ratio 1:2 takes place. In all cases, we observed no changes in the values of  $m/z$  for peaks of lysozyme, albumin and their homo structures. Experimentally obtained values of  $m/z$  of the hetero structures correspond to the theoretically calculated ones. General trends in the studied systems are as follows: with increasing of lysozyme concentration relative to albumin not only qualitative changes of the mix composition are observed, but an increase in the relative intensities of the mass spectrometric peaks belonging to hetero structures (related to the intensities of peaks of albumin and its dimer) is also detected. These changes indicate a) the formation of new structures and b) the increase of their concentration in solution with the increase of lysozyme / albumin ratio in solution.

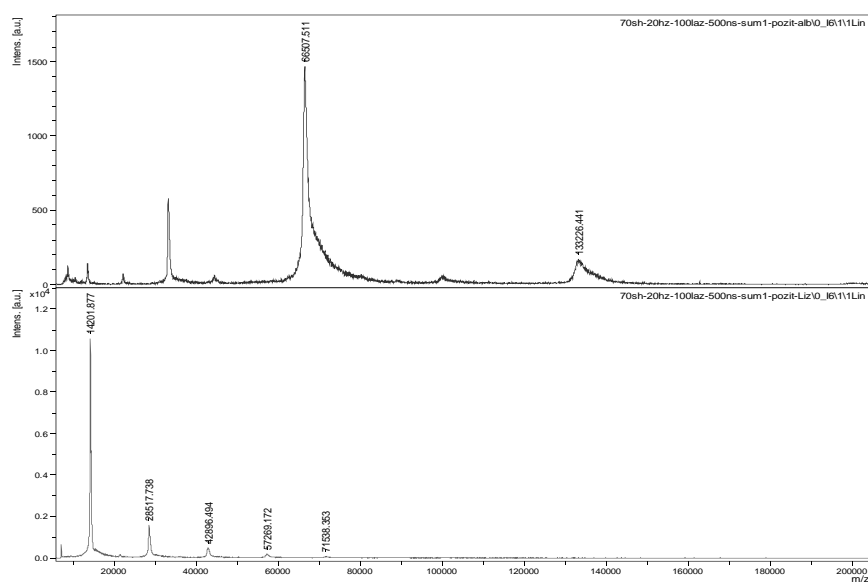


Figure 1. Mass spectra of individual substances albumin (top) and lysozyme (bottom).

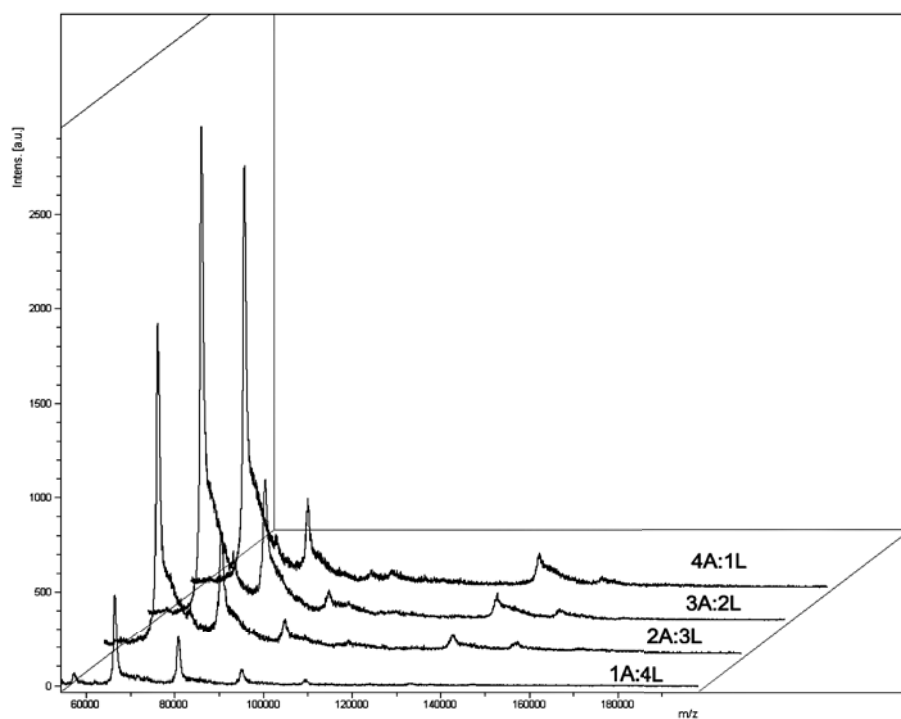


Figure 2. MALDI-ToF mass spectra of solutions 1-4.

In this paper, an attempt is made to evaluate the qualitative changes in the dynamics of heterostructures formation upon protein concentration. As an option, which corresponds to the dynamics of change in the systems, we have chosen the ratio of the relative intensities of the corresponding hetero structures in the mass spectrum for that of albumin and its dimer.

Description of these curves was performed according to the equation:

$$y = a \frac{kx^n}{1 + kx^n},$$

where,

$x$  - the ratio of the concentration of lysozyme to albumin in solution;

$k$  - apparent stability constant of the certain composition;

$a, n$  - empirical coefficients.

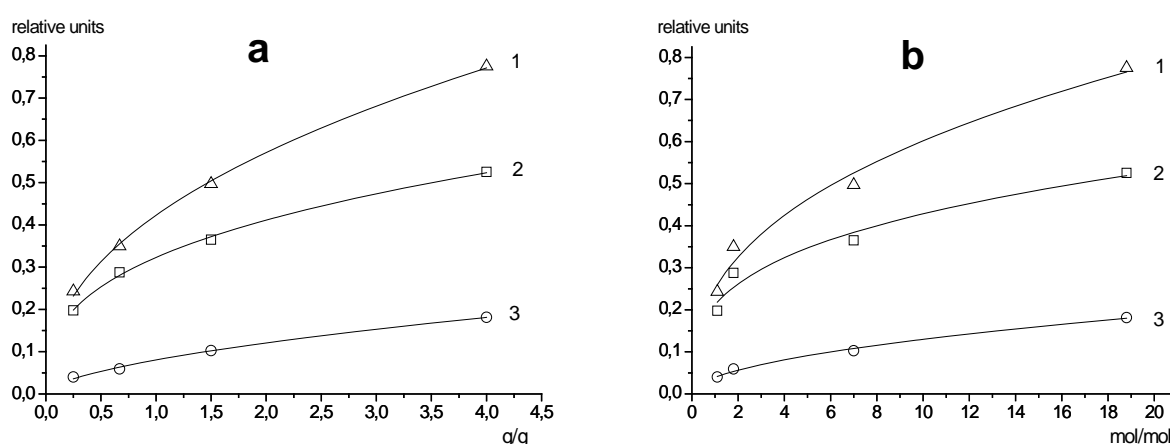


**Figure 3. Relative content of albumin and lysozyme oligomers depending on mass (a) and molecular (b) concentration.**

1- (AL+AL<sub>2</sub>)/A

2- AL/A

3- AL<sub>2</sub>/A

The calculated constants are characteristic (reflecting only a trend in the system). Their value may differ from the actual stability constants of associates (see Figure 3). For each system the stability row of the compounds (by the value of  $k$ ) is evaluated and listed in the Table 1.

It should be noted that the formation of equal weight oligomers can occur in different ways. This was illustrated by the associate AL<sub>2</sub>.

Table 1

Apparent stability constant of the oligomers.		
Oligomeric forms	g/g	mol/mol
A <sub>2</sub> L	2.85E+00	0.94 E+00
AL <sub>2</sub>	2.80E-05	2.69E-08
AL	3.70E-06	4.70E-09

For AL<sub>2</sub> formation we consider two mechanisms (Figure 4). It is logical to assume that an increase in the content of lysozyme in solution leads to the increase in the content of its dimer. But Figure 4 shows that the content of lysozyme dimer with increase of the lysozyme concentration passes through a maximum, indicating that AL<sub>2</sub> formation is more likely to occur by the second mechanism: the albumin molecule joins the molecule of lysozyme dimer.

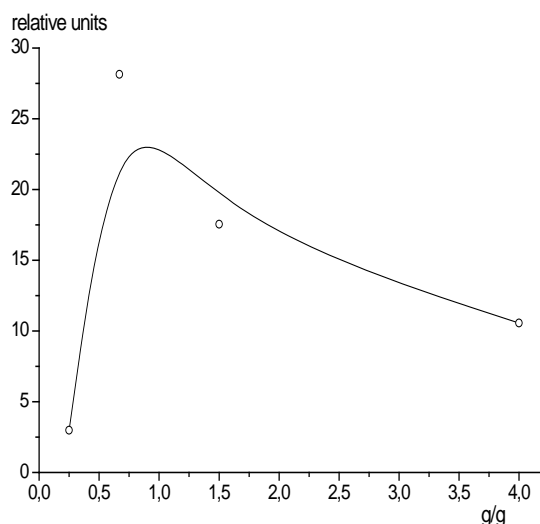


Figure 4. Relative content of lysozyme dimer in solutions versus concentration.

### Conclusions

It has been shown that the oligomerization processes of albumin and lysozyme can be studied by means of MALDI-TOF mass spectrometry. E. g., the mass spectrometric peaks corresponding to the formation of associates (albumin - lysozyme) in the stoichiometric ratios of 1:1, 1:2, 1:3, 1:4, also associates (lysozyme dimer - albumin) in the stoichiometric ratios of 1:1, 1:2.

It has been demonstrated that with increase in the concentration of lysozyme in relation to that of albumin the intensities of the peaks corresponding to associates, related to the intensities of the peaks corresponding to albumin and lysozyme, are also increased. A similar pattern is observed in the case of albumin dimer.

Usage of a modified Freundlich equation for mathematical description of the associates formation processes in albumin-lysozyme solution has been proposed, as the experimental data are well described by this equation.

The stability rows of the associates have been found based on the value of the apparent stability constants. It has been shown that the stability of AL complex is higher than that of  $A_2L$  and  $AL_2$  complexes.

### References

- Rapis, E. To the problem of nucleation (the formation of cells) with nanostructures self protein *in vitro* and *in vivo*. Journal of Technical Chemistry, 2005, 75(6), pp. 101-113 (in Russian).
- Nishikawa, T.; Akiyoshi, K.; Sunamoto, J. Macromolecular Complexation between Bovine Serum Albumin and the Self-Assembled Hydrogel Nanoparticle of Hydrophobized Polysaccharides. Journal of the American Chemical Society, 1996, 118(26), pp. 6110-6115.
- Rapis, E. Evolutionary aspect of protein folding. Journal of Technical Chemistry, 2008, 78(6), pp. 110-115 (in Russian).
- Rapis, E. On the nonequilibrium phase transition protein. Journal of Technical Chemistry, 2007, 77(6), pp. 109-115 (in Russian).
- Yeh, P.-R.; Tseng, W.-L. Human serum albumin-coated gold nanoparticles for selective extraction of lysozyme from real-world samples prior to capillary electrophoresis. Journal of Chromatography A, 2012, 1268, pp.166-172.
- Reynolds, C.; Damerell, D.; Jones, S. ProtorP: a protein-protein interaction analysis server. Structural bioinformatics, 2009, 25(3), pp. 413-414.
- Almeida, N.L.; Oliveira, C.L.P.; Torriani, I.L.; Loh, W. Calorimetric and structural investigation of the interaction of lysozyme and bovine serum albumin with poly(ethylene oxide) and its copolymers. Colloids and Surfaces B: Biointerfaces, 2004, 38, pp. 67-76.
- Steiner, R.F. Reversible Association Processes of Globular Proteins. II. Electrostatic Complexes of Plasma Albumin and Lysozyme. Global Proteins II, pp. 56-75.
- Steiner, R.F. Reversible Association Processes of Globular Proteins. IV. Fluorescence Methods in Studying Protein Interactions. Global Proteins, IV, pp. 291-311.
- Schreiber, G. Kinetic studies of protein-protein interactions. Current Opinion in Structural Biology, 2002, 12, pp. 41-47.
- Singh, M. Structural Interactions of Globular Proteins-Bovine Serum Albumin, Egg Albumin, and Lysozyme, in Aqueous Medium, Elucidated with Molar Volumes, Viscosities, Energy Functions, and IR Spectra from 293.15 to 303.15 K. Journal of Applied Polymer Science, 2007, 103, pp. 1420-1429.



(17.02.1947 – 28.07.2014)

## **IN MEMORY OF CORRESPONDING MEMBER OF ACADEMY OF SCIENCES OF MOLDOVA PROFESSOR MIHAIL REVENCO**

Mr. Mihail Revenco, corresponding member of the Academy of Sciences of Moldova, Professor, Dr. habilitate in chemistry, was born on 17<sup>th</sup> February 1947 in the village Badiceni, distinct Soroca. After graduating the secondary school in his native village in 1964, he was registered at the Faculty of Chemistry of the Moldova State University, in 1969. During the years 1969-1973 he followed the PhD studies at the Department of Inorganic Chemistry, Faculty of Chemistry of the Moldova State University. In 1973 he obtained the Ph.D. degree and the degree of Doctor Habilitate in Chemistry in 1991. Since 1992 he held the title of university professor.

The didactic activity began at the State Agrarian University of Moldova (1972-1987), then Mihail Revenco activated at the Hydrotechnical Institute from Blida, Algeria (1978-1982). Several years he worked at the Moldova State University, as head of the Department of Organic and Analytical Chemistry (1988-2006), Dean of the Faculty of Chemistry and Chemical Technology (2007-2008). Since 2008 he held the position of vice-rector for scientific activity. In 2012 he was elected the corresponding member of the Academy of Sciences of Moldova.

The chemist Mihail Revenco has worked many years also at the Institute of Chemistry of the Academy of Sciences of Moldova. Thus, in the period 1997-2006 he led the scientific activity of the Laboratory of Analytical Chemistry and during of 2006-2007 – of Laboratory of Coordination Chemistry.

Specialist in coordination and analytical chemistry, he was argued as a skillful organizer of the university process, the erudite professor, appreciated by colleagues and students, the talented scholar of international value, manager of scientific projects carried out with the participation of teams from Europe and the United States in programs NATO, INTAS, CRDF, SCOPES. His scientific interests were focused towards the assembly reactions and its application for analytical or medico-biological purposes. Contributed to the reform of secondary education, he was the author of the school curricula and textbook related to the bases of chemical analysis.

Professor Mihail Revenco, together with the late Academician Nicolae Garbalau, in the early 70's of the last century, discovered a new method of synthesis in coordination chemistry – *the assembly method of ligands based on the thiosemicarbazides in the presence of metal ions*. In this way, the template method of synthesis of this class of coordination compounds have been arose, which, at present, has been recognized and used worldwide and became the basis of the assembly method of the supramolecules.

Scientific research of chemist Mihail Revenco was focused on the application of the assembly reactions for analytical purpose, valorization of the coordination compounds in the sensitive methods of analysis. On the basis of these reactions, it has been proposed the original structures for membranes of potentiometric sensors, the convenient devices for the analysis and analytical control of the content of ionic species. The scientific basis of analytical coordination chemistry with polyfunctional derivatives was developed, the field which was promoted with passion together with his students.



The achievements of fundamental and applied scientific research performed by the chemist Mihail Revenco were the basis for the foundation of the scientific school in the field of coordination and analytical chemistry which was further recognized abroad. The rich scientific activity of Professor Mihail Revenco was eloquently described by the high number of scientific papers that exceeded 400, published in national and international journals with impact factor. He is also the author of 4 monographs, 8 patents, and 12 didactic materials. The achievements of the scientific school founded by corresponding member Mihail Revenco has been highly appreciated by various international scientific centers.

Scientific work and practical results of Professor Mihail Revenco were deservedly appreciated by superior bodies, being awarded the National Award in Science and Technology (1995), Order of “Emeritus” of the Republic of Moldova (1996), “Dimitrie Cantemir” Medal (2006), “Paisie Velcikovsky” Medal (Poland 2011), the Memorial Award “Yurii Simonov” (2012). In 2012, for outstanding results, through Presidential Decree, Professor Mihail Revenco was awarded the Order “Labour Glory”.

The famous French art historian and essayist Jacques Élie Faure said following “A man when he is gone, nothing is left of him if he took care to leave, at least, a trace on stones road”. This message is for us an urge to leave traces and good things throughout our life on Earth, as always took care to do our friend, scientist, professor and Personality Mihail Revenco.

Academician Gheorghe Duca,  
President of the Academy of Sciences of Moldova

Corresponding member Tudor Lupascu,  
Director of the Institute of Chemistry of A.S.M.